TRAVERSABLE WORMHOLES IN $f(R)$ GRAVITY SOURCED BY A CLOUD OF STRINGS

Parangam Goswami, **Anshuman Baruah**, **Atri Deshamukhya**[*]

Department of Physics, Assam University, Silchar, 788011, Assam, India
*Corresponding Author e-mail: atri.deshamukhya@aus.ac.in

Wormhole solutions in General Relativity (GR) require *exotic* matter sources that violate the null energy condition (NEC), and it is well-known that higher-order modifications of GR and some alternative matter sources can support wormholes. In this study, we explore the possibility of formulating traversable wormholes in $f(R)$ modified gravity, which is perhaps the most widely discussed modification of GR, with two approaches. First, to investigate the effects of geometrical constraints on the global characteristics, we gauge the rr–component of the metric tensor and employ Padè approximation to check whether a well–constrained *shape function* can be formulated in this manner. We then derive the field equations with a background of string cloud and numerically analyse the energy conditions, stability, and amount of exotic matter in this space-time. Next, as an alternative source in a simple $f(R)$ gravity model, we use the background cloud of strings to estimate the wormhole shape function and analyse the relevant properties of the space-time. These results are then compared with those of wormholes threaded by normal matter in the simple $f(R)$ gravity model considered. The results demonstrate that string cloud is a viable source for wormholes with NEC violations; however, the wormhole space-times in the simple $f(R)$ gravity model considered in this study are unstable.

Keywords: *Einstein equations, Wormhole solution, String cloud*

PACS: 04.60.Cf

1. INTRODUCTION

The governing equation of the theory of General Relativity (GR) is the Einstein field equation (EFE), and solutions to this set of coupled differential equations have been remarkably successful in accounting for phenomena ranging from black holes [1] to the evolution of the universe. Spherical symmetry is an important physically relevant constraint in solving the EFEs, and wormholes are an intriguing prospect among spherically symmetric solutions, explored since the early days of GR [2, 3]. Ellis [6] and Bronnikov [7] independently reported the first traversable Lorentzian wormhole solution, and the geometric requirements were established in detail by Morris & Thorne in 1988 [8]. Wormholes are exact solutions to the EFEs and can be interpreted as bridges connecting two different asymptotically flat regions of space-time via a *throat*. The topology of the wormhole interior is non-trivial, while the topology at the boundaries remains simple [9]. While theoretical as of now, wormholes are of crucial importance in fundamental physics, especially considering quantum entanglement [10] and quantum gravity. Moreover, it has recently been shown that wormholes may mimic astrophysical black holes in some observations [63, 5]. A fundamental problem in such spacetimes is that for the *throat* to remain open for signal propagation, the behavior of the matter sources supporting such a space-time is *exotic* in that the null energy condition (NEC) is violated [8]. Specifically, this implies that observers in an inertial frame measure negative energy densities at the throat, which is unphysical. Such behavior can be avoided in modified gravity theories.

Despite its success, GR fails to explain cosmological phenomena such as late–time accelerated cosmic expansion [11, 13] and the so-called 'inflationary epoch' [14]. Modified theories of gravity address these short-comings [15, 16, 17, 28, 29], and the extra degrees of freedom in modified gravity theories also enables one to evade NEC violations in wormhole space-times. Moreover, wormhole solutions are an inherent feature of most modifications of GR. One of the simplest modifications to GR is $f(R)$ modified gravity, where the Ricci scalar R in the Einstein–Hilbert action is replaced by some arbitrary function of it [18]. This simple modification to GR can lead to a host of models that can independently meet both cosmological and solar system tests [19]. It has been shown that the extra degrees of freedom in $f(R)$ gravity arising from higher order curvature terms may lead to scenarios where the matter content satisfies the NEC in wormhole spacetimes [20, 21]. Wormholes in the framework of $f(R)$ gravity have been studied extensively in different iterations of $f(R)$ gravity (for instance, in Refs. [22, 12, 23, 24, 25, 26, 27, 30, 31, 64, 32, 33]).

Another inherent limitation of GR is that it provides only a classical description of gravity, and the theory is non–renormalizable at high energy (small length) scales. String theory [34] is perhaps the strongest contender to

a unified paradigm of gravity with the other fundamental forces, and it posits that the fundamental constituent of matter and energy are extended objects, instead of point-like ones. Precisely, the extended objects are considered as one–dimensional relativistic strings, and the interactions of strings on a classical level provide better models of several fundamental interactions [35, 36, 37]. To this end, string clouds as a gravitational source have been studied extensively in literature. A general solution to the EFEs for a spherically symmetric cloud of strings was first reported in [38], with an emphasis on the energy conditions. Properties of compact objects such as black holes in the background of a string cloud have been reported previously [39, 40, 41, 42]. Traversable wormholes in the background of a string cloud have been reported [43], with an emphasis on the amount of exotic matter and stability of the wormhole configuration against radial perturbations. Recently, a detailed study of the properties of traversable wormholes surrounded by a string cloud in the framework of $f(R)$ gravity has been reported with analysis of the quasi-normal modes (QNMs) of the wormhole solutions [44].

In this study, we investigate traversable wormholes in $f(R)$ gravity with two motivations: First, to investigate the effects of geometrical constraints, we gauge the rr–component of the metric tensor and employ Padé approximation to check whether a well–constrained *shape function* can be formulated in this manner. We then derive the field equations with the background of a string cloud and numerically analyse the energy conditions, stability, and amount of exotic matter in this space-time. Next, we use a background of string cloud to estimate the wormhole shape function in a simple $f(R)$ gravity model, with $f(R) = \alpha R^m - \beta R^n$ [45], and analyse the relevant properties of the space-time as in the previous case. These results are then compared with those of wormholes threaded by normal matter in the same modified gravity model considered.

The remainder of this manuscript is organized as follows. In Sec. 2, we discuss the traversable wormhole geometry. A novel shape function is proposed using Padé approximation in Sec. 2.1. In Sec. 3, we present the modified EFEs in the general framework of $f(R)$ gravity. In Sec. 3.1 we analyse the various energy conditions, the stability in terms of the TOV equation, and the amount of exotic matter required to sustain traversable wormholes in the framework of $f(R)$ gravity with a background of string cloud. Next, in Sec. 3.2 we estimate the shape function in the considered form of $f(R) = \alpha R^m - \beta R^n$ gravity model [45] with a string cloud background and analyse the properties of the wormhole space-time. For a comparative analysis, in Sec. 3.3 we present wormhole solutions supported by ordinary matter for the $f(R)$ model [45] considered in Sec. 3.2 using our proposed shape function obtained by employing Padé approximation in Sec. 2.1. Finally, we conclude the work with remarks in Sec. 4. We adhere to the natural system of units ($G = c = 1$) throughout the work.

2. TRAVERSABLE WORMHOLES

Morris & Thorne [8] used the following metric ansatz to describe a static, spherically symmetric space-time

$$ds^2 = -e^{2\Phi(r)}dt^2 + \frac{dr^2}{1 - \frac{b(r)}{r}} + r^2d\theta^2 + r^2sin^2\theta d\phi^2 \tag{1}$$

Eq. (1) is the line element of a traversable wormhole. The proper radial coordinate $l(r) = \int_{r_0}^r \frac{dr}{\sqrt{1-\frac{b}{r}}}$ should be well-behaved throughout the space-time in order to avoid singularities. It imposes the constraint $\frac{b}{r} \leq 1$ at the throat. The metric function $\Phi(r)$ in Eq. (1) is known as the red-shift function, and the first co-efficient of the line element in Eq. (1) provides a measure of the gravitational red-shift. The topological configuration of the space-time is determined by the second coefficient of the line element in Eq. (1) and the metric function $b(r)$ is known as the shape function. At some minimum value of the radial coordinate r, the throat of the wormhole is located at some arbitrary value r_0. A significant aspect of traversable wormholes is that the throat should not be surrounded by an event horizon. Horizons in spherically symmetric space-times are described by physically non-singular surfaces at $g_{00} = -e^{2\Phi} \to 0$, and this results in the constraint that throughout the space-time $\Phi(r)$ should be well defined. Moreover, the geometric constraints on the shape function $b(r)$ demanded by traversability are: (i) $b(r_o) = r_o$, (ii) $\frac{b(r)-b'(r)r}{b^2} > 0$, (iii) $b'(r_o) - 1 \leq 0$, (iv) $\frac{b(r)}{r} < 1, \forall r > r_o$, (v) $\frac{b(r)}{r} \to 0$ as $r \to \infty$, where prime denotes a derivative with respect to the radial coordinate r. The energy density ρ, radial pressure p_r, and transverse pressure p_t of the matter sources are constrained by these conditions on the metric functions through the EFEs. Therefore, while constructing traversable wormhole configurations violations of the energy conditions appear owing to these constraints. Next, we propose a novel form of the shape function and check the viability of the shape function by analysing the various constraints. In addition, in this work, we consider tideless traversable wormhole solutions described by a constant red-shift function $\Phi'(r) = 0$.

2.1. A novel shape function
We examine the following functional form as a probable shape function

$$b(r) = r_0 \left[\log\left(\frac{r}{r_0}\right) + \coth(r_0)\tanh(r)\right]^a \tag{2}$$

where, r_0 is the location of the throat, and a is a free parameter. The viability of the shape function $b(r)$ depends on several constraints as discussed in Sec 2. Analysing these constraints for the functional form of Eq. (2), insights can be obtained about the throat radius r_0, and the parameter a. However, it can be observed Eq. (2), does not satisfy the condition of $b(r_0) = r_0$, which is an important consequence of traversable wormholes, the other required conditions for the viability of the shape function, such as the asymptotic flatness, and the flaring out condition are also not satisfied. Thus, to have a plausible form of $b(r)$, the next step involves adopting the Padé approximation for the functional form in Eq. (2), and to check if a viable form of $b(r)$ can be obtained that satisfies all the required constraints on a shape function. Use of rational expansions made by Padé functions is common in existing literature [46, 47, 48, 49]. The Padé approximation is built on the Taylor series expansion. For a given function such as $f(z) = \sum_{i=1}^{\infty} c_i z^i$, expanding the series with the coefficients c_i, the (n, m) Padé approximant ratio is given as [50],

$$P_{n,m}(z) = \frac{\sum_{k=0}^{n} a_k z^k}{1 + \sum_{\sigma=0}^{m} b_\sigma z^\sigma} \qquad (3)$$

The most simple forms of Padé approximant are of the orders $(1,0)$ & $(0,1)$. Thus, considering the $(1,0)$ approximation and expanding Eq. (2) about the throat radius r_0, the shape function is

$$b(r) = r_0 - a(r_0 - r)\left[1 + r_0 \ \text{cosech}(r_0)\text{sech}(r_0)\right] \qquad (4)$$

With the form as described in Eq. (4), the various conditions required for the viability are analyzed and it becomes evident that the function in Eq. (4) satisfies all the necessary conditions to be a shape function for $r_0 = 3$ and $0 < a < 1$. Moreover, the function satisfies the condition $b(r_0) = r_0$. We therefore propose $b(r) = r_0 - a(r_0 - r)\left[1 + r_0 \ \text{cosech}(r_0)\text{sech}(r_0)\right]$ as a new viable shape function.

The plots of the asymptotic flatness $b(r)/r \to 0$ as $r \to \infty$, and flaring out condition $\frac{b(r) - b'(r)r}{b^2} > 0$ are shown in Figure 1.

(a)   (b)
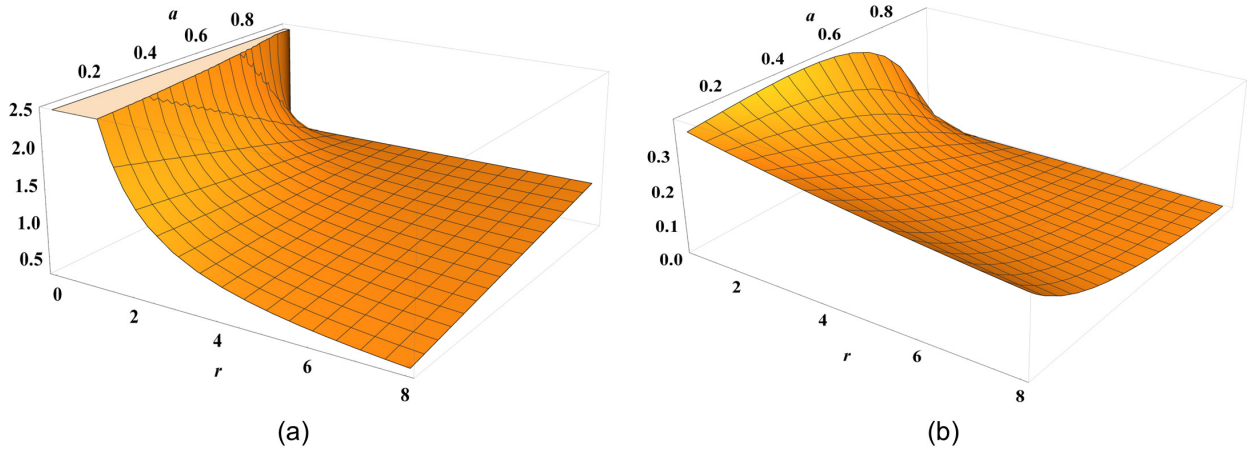
Figure 1. Profile of the (a) Asymptotic flatness $\frac{b(r)}{r} \to 0$ as $r \to \infty$, and (b) Flaring out condition $\frac{b(r) - b'(r)r}{b^2} > 0$ respectively vs. r for $0 < a < 1$

With the obtained viable shape function, next the traversable wormhole solutions are analyzed in the framework of $f(R)$ gravity with a background of string cloud.

3. TRVERSABLE WORMHOLES IN $f(R)$ GRAVITY

A general form of the action in $f(R)$ modified theories is [22]

$$S = \int d^4x \sqrt{-g}\left[f(R) + \mathcal{L}_m\right] \qquad (5)$$

Using the metric formalism of $f(R)$ gravity, the modified EFEs are obtained as

$$FR_{\mu\nu} - \frac{1}{2}f(R)\,g_{\mu\nu} - \nabla_\mu\nabla_\nu F + g_{\mu\nu}\Box F = T_{\mu\nu}^m, \qquad (6)$$

where $F \equiv df/dR$, and $T^m_{\mu\nu} = \frac{-2}{\sqrt{-g}}\frac{\delta \mathcal{L}_m}{\delta g^{\mu\nu}}$ is the stress-energy tensor of background matter. We consider that the spherically symmetric space-time is represented by the line-element in Eq. (1). Taking the trace of Eq. (6) yields:

$$FR - 2f(R) + 3\Box F = T \tag{7}$$

Here, T is the trace of the stress-energy tensor of matter and $\Box F$ is:

$$\Box F = \frac{1}{\sqrt{-g}}\partial_\mu(\sqrt{-g}g^{\mu\nu}\partial_\nu F) = \left(1 - \frac{b}{r}\right)\left[F'' - \frac{b'r - b}{2r^2(1 - b/r)}F' + \frac{2F'}{r}\right] \tag{8}$$

with $F' = df(R)/dR$ and $b' = d\,b(r)/dr$. Substituting Eq. (7) in Eq. (6) yields the modified EFEs as:

$$G_{\mu\nu} \equiv R_{\mu\nu} - \frac{1}{2}g_{\mu\nu}R = T^{\text{eff}}_{\mu\nu} \tag{9}$$

Here, $T^{\text{eff}}_{\mu\nu}$ is the effective stress-energy tensor, responsible for the energy condition violations and is generally interpreted as a gravitational fluid. $T^{\text{eff}}_{\mu\nu}$ comprises of the matter stress energy tensor $T^m_{\mu\nu}$ and the curvature stress-energy tensor $T^c_{\mu\nu}$ given by

$$T^c_{\mu\nu} = \frac{1}{F}\left[\nabla_\mu\nabla_\nu F - \frac{1}{4}g_{\mu\nu}\left(RF + \Box F + T\right)\right] \tag{10}$$

Assuming that the geometry of the wormhole is threaded by an anisotropic distribution of matter

$$T_{\mu\nu} = (\rho + p_t)U_\mu U_\nu + p_t\,g_{\mu\nu} + (p_r - p_t)\chi_\mu\chi_\nu\,, \tag{11}$$

where U^μ is the four-velocity, and χ^μ represents a unit space-like vector.

With the line element in Eq. (1), the modified EFEs can be expressed as the following [22]

$$\rho = \frac{Fb'}{r^2} \tag{12}$$

$$p_r = -\frac{bF}{r^3} + \frac{F'}{2r^2}(b'r - b) - F''\left(1 - \frac{b}{r}\right) \tag{13}$$

$$p_t = -\frac{F'}{r}\left(1 - \frac{b}{r}\right) + \frac{F}{2r^3}(b - b'r) \tag{14}$$

The Ricci scalar is given as $R = \frac{2b'}{r^2}$. With the explicit forms of energy density ρ, radial pressure p_r, and transverse pressure p_t in Eqs. (12)-(14), the various energy conditions, stability, and the amount of exotic matter required for the wormhole configuration can be analyzed.

3.1. Cloud of Strings as a source

A cloud of strings is analogous to the perfect fluid models of gas and dust. However, the difference is that it comprises one-dimensional objects extended along some specific direction. The string cloud can exist in different geometrical configurations such as planar, axisymmetric, or spherical [51]. A general solution for the spherical distribution of the cloud of strings was reported in [51]. In addition, thermodynamic properties of string gas have been reported in [52]. For a spherically symmetric string cloud in four dimensions, the energy momentum tensor has the following non-null components [51]

$$T^t{}_t = T^r{}_r = -\frac{\eta^2}{r^2} \tag{15}$$

where η is a constant related to the total energy of the string cloud. With the form of the shape function as described in Eq. (4), and using Eq. (12), we get

$$F(r) = -\frac{\eta^2}{a\left(r_0\,\text{cosech}(r_0)\,\text{sech}\,(r_0) + 1\right)} \tag{16}$$

With the obtained $F(r)$ and the field equations Eqs. (12)-(14), the numerical analyses are conducted to obtain the energy conditions, check the stability, and estimate the amount of exotic matter.

For any observer traversing a time-like curve to detect the energy density of the matter field to be positive, the stress-energy tensor of matter must adhere to some sets of inequalities known as the energy conditions in GR [53, 21]. The weak energy condition (WEC) implies $\rho \geq 0$, the NEC implies $\rho + p_r \geq 0$, and $\rho + p_t \geq 0$, whereas the strong energy condition (SEC) implies $\rho + p_r + 2p_t \geq 0$. The profile of energy conditions with a background of string cloud is presented with the throat radius fixed at $r_0 = 3$. Emphasis is made on the effect of the string cloud constant η on the energy conditions. Results are discussed by fixing the parameter $a = 0.5$. For the whole range of a, $0 < a < 1$, the energy conditions show similar behavior. Previous studies indicate that the constant associated with the total energy of the string cloud should be small [38, 43].

Figure 2 shows the profile of the NEC terms $\rho + p_r$ and $\rho + p_t$. It can be observed that the first NEC term is satisfied at the throat $r_0 = 3$ for the considered values of the η as $\eta = 0.1$, 0.3, and 0.5. However, the second NEC term $\rho + p_t$ is violated for all the values of η. Owing to the violation of the second NEC term, as a whole the NEC is inferred to be violated.
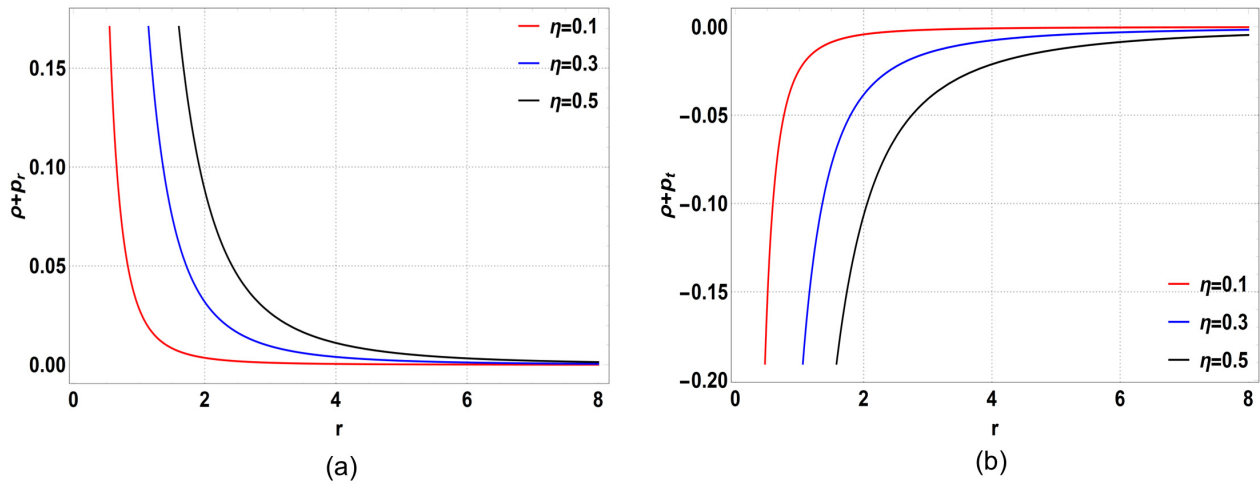
Figure 2. Profile of the NEC terms (a) $\rho + p_r$, and (b) $\rho + p_t$ respectively vs. r with $b(r)$ as in Eq. 4

From Figure 3, it can be observed that the WEC is violated at the wormhole throat for all the values of η. It is also evident from the fact that the non-null components of the stress-energy tensor of the string cloud come with a minus sign as shown in Eq. (15). Moreover, it is seen that the SEC exhibits an oscillatory (indeterminate) behavior along the radial coordinate r. With increasing r, the oscillation between positive and negative values decreases; however, the behavior extends asymptotically.
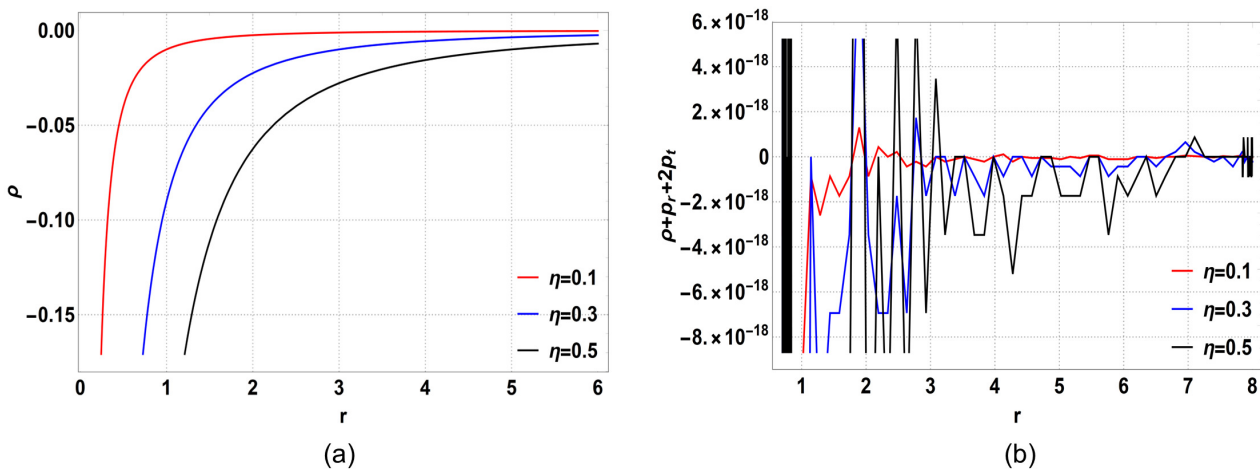
Figure 3. Profile of the (a) WEC ρ, and (b) SEC $\rho + p_r + 2p_t$ vs. r respectively with $b(r)$ as in Eq. 4

In addition to the energy conditions, analysing two other parameters, viz. the equation of state (EoS) parameter $\omega = p_r/\rho$, and anisotropy parameter $\Delta = p_t - p_r$ turns out to be useful. Information about the nature of the matter source threading the wormhole geometry can be obtained from the EoS parameter, and

the attractive or repulsive nature of the space-time geometry (geometrical viability) can be understood by the anisotropy parameter.
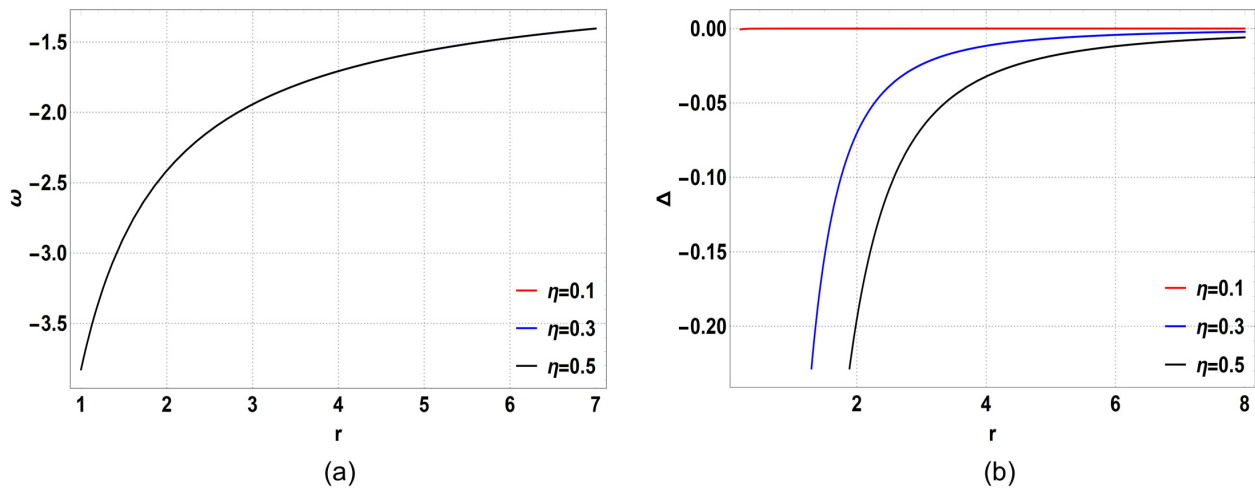
Figure 4. Profile of the (a) EoS parameter ω, and (b) anisotropy parameter Δ vs. r respectively with $b(r)$ as in Eq. 4

Figure 4 shows the behavior of the EoS and anisotropy parameters. Near the wormhole throat, the EoS parameter is $\omega < -1$, signifying a phantom-like behavior of the string cloud for all values of η. The anisotropy parameter $\Delta < 0$ near the wormhole throat, signifies an attractive nature of the space-time geometry. The summary of the energy conditions is presented in Table 1.

Table 1. Summary of the energy conditions discussed in Sec. 3.1

Terms	Result	Interpretation
ρ	< 0 near throat, for $\eta = 0.1, 0.3, 0.5$	WEC violated at throat
$\rho + p_r$	> 0 near throat, for $\eta = 0.1, 0.3, 0.5$	NEC satisfied at throat
$\rho + p_t$	< 0 near throat, for $\eta = 0.1, 0.3, 0.5$	NEC violated at throat
$\rho + p_r + 2p_t$	oscillates, for $\eta = 0.1, 0.3, 0.5$	SEC indeterminate
ω	< -1 near throat, for $\eta = 0.1, 0.3, 0.5$	phantom-like source at throat
Δ	< 0 near throat, for $\eta = 0.1, 0.3, 0.5$	attractive geometry at throat

First reported in the context of neutron stars [54, 55], the Tolman-Oppenheimer-Volkov (TOV) equation provides information regarding the stability of stellar structures. To probe the stability of wormholes in terms of the hydrostatic, gravitational, and anisotropic forces in the space-time, a more generalized version of the formalism was developed in [56]. The generalized TOV equation [56, 57] is given as

$$-\frac{dp_r}{dr} - \frac{\epsilon'(r)}{2}(\rho + p_r) + \frac{2}{r}(p_t - p_r) = 0, \tag{17}$$

where $\epsilon(r) = 2\Phi(r)$. F_{h} represents the hydrostatic force, F_{g} the gravitational force, and F_{a}, the anisotropic force. These three terms of the TOV equation can determine the equilibrium anisotropic mass distribution [57] in that stable stellar structures satisfy Eq. (17).

$$F_{\text{h}} = -\frac{dp_r}{dr}, \qquad F_{\text{a}} = \frac{2}{r}(p_t - p_r), \qquad F_{\text{g}} = -\frac{\epsilon'}{2}(\rho + p_r) \tag{18}$$

Owing to the constant red-shift function $\Phi'(r) = 0$, the gravitational force is $F_{\text{g}} = 0$ in the analysis.

Using the averaged null energy condition, $\int_{\lambda_1}^{\lambda_2} T_{ij}k^i k^j d\lambda \geq 0$, evaluated along the radial coordinate r, the amount of exotic matter in wormhole space-times can be estimated. However, the amount of energy condition

violating matter can be estimated in a more generalized manner by using a volume integral instead of the line integral, namely the volume integral quantifier (VIQ) [58, 59, 60], which is defined as

$$I_v = \oint [\rho + p_r] dV = 8\pi \int_{r_0}^{s} (\rho + p_r) r^2 dr \tag{19}$$

After matching the wormhole space-time with an exterior metric and cutting off the stress-energy tensor at some $r = s$ away from the throat, an estimate of the amount of NEC violating matter can be obtained by using the VIQ. For arbitrarily small quantities of NEC violating matter, the requirement is $I_v \to 0$ as $s \to r_0$ [58, 59].
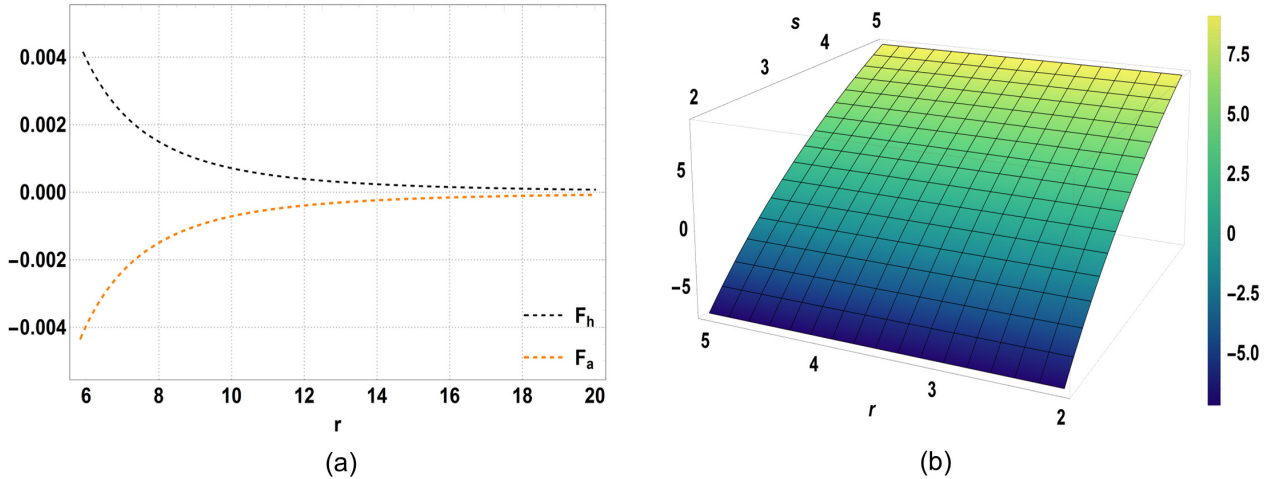
Figure 5. Profile of the (a) F_{h}, and F_{a} vs. r (b) VIQ with $b(r)$ as in Eq. 4

Figure 5 shows the terms of the TOV equation and the profile of the VIQ. It is seen that that the hydrostatic force F_{h}, and the anisotropic force F_{a} cancel each other asymptotically, signifying a stable configuration. In addition, it can be observed that the VIQ, $I_v \to 0$ as $s \to r_0$, indicates that the wormhole solution is feasible with arbitrarily small amounts of exotic matter. The terms of the TOV and VIQ equations are shown with $\eta = 0.5$. For $\eta = 0.1$, and 0.3 the corresponding terms of the TOV and VIQ equations depict a similar behavior.

Thus, wormhole solutions can be formulated in a model-independent manner using the novel shape function, Eq. (4), in the framework of $f(R)$ gravity with a string cloud background. The next motive remains to check whether a feasible form of the shape function can be obtained in a particular form of the $f(R)$ gravity model with the string cloud cloud background.

3.2. Traversable wormholes in $f(R) = \alpha R^m - \beta R^n$ gravity with a string cloud background

In this section, we obtain a form of the shape function $b(r)$ by fixing $f(R)$ and analyze its viability. For the analysis, we consider a simple form of $f(R)$ gravity model as [45]

$$f(R) = \alpha R^m - \beta R^n \tag{20}$$

where α and β are positive constants and m and n are positive integers satisfying the condition $m > n$ [45]. Using Eq. (15) in Eq. (12), we obtain

$$-\frac{\eta^2}{r^2} = \frac{Fb'}{r^2} \tag{21}$$

Considering the $f(R)$ model as described in Eq. (20), and obtaining F, the shape function can be found from Eq. (21). To simplify the calculations, the integers m and n are set as $m = 2$ and $n = 1$ satisfying the condition $m > n$. Again, using the expression for the Ricci scalar $R = \frac{2b'}{r^2}$, F is found in terms of r. Eq. (21) reduces to a quadratic equation in b' of the form

$$4\alpha b'^2 - b'\beta r^2 + \eta^2 r^2 = 0 \tag{22}$$

Solving Eq. (22) and considering only the positive root for mathematical feasibility, we get

$$b' = \frac{\beta r^2 + \sqrt{\beta^2 r^4 - 16\alpha \eta^2 r^2}}{8\alpha} \tag{23}$$

Integrating Eq. (23), we get

$$b = \frac{1}{8\alpha}\left[\frac{\beta r^3}{3} + \frac{\left(\beta^2 r^2 - 16\alpha\eta^2\right)\sqrt{\beta^2 r^4 - 16\alpha\eta^2 r^2}}{3\beta^2 r}\right] + c \tag{24}$$

where c is a constant of integration. In order to evaluate the constant c, we use the condition at the wormhole throat, $b(r_0) = r_0$. This leads to the following form of the shape function

$$b = r_0 + \frac{1}{24\alpha\beta^2}\left[\frac{\beta^3 r^4 + \left(\beta^2 r^2 - 16\alpha\eta^2\right)\sqrt{\beta^2 r^4 - 16\alpha\eta^2 r^2}}{r}\right.$$
$$\left. - \frac{\beta^3 r_0^4 + \left(\beta^2 r_0^2 - 16\alpha\eta^2\right)\sqrt{\beta^2 r_0^4 - 16\alpha\eta^2 r_0^2}}{r_0}\right] \tag{25}$$

With the shape function in Eq. (25), the various conditions required for the viability of the shape function as described in Sec 2 are analyzed. It is interesting to note that the asymptotic flatness $\frac{b}{r} \to 0$ as $r \to \infty$, and the flaring out condition $\frac{b-b'r}{b^2} > 0$ are satisfied only for negative values of the constants α and β ($\alpha = -0.5$ and $\beta = -0.8$). The profile of the asymptotic flatness and flaring out condition are shown in Figure 6 with different values of η.
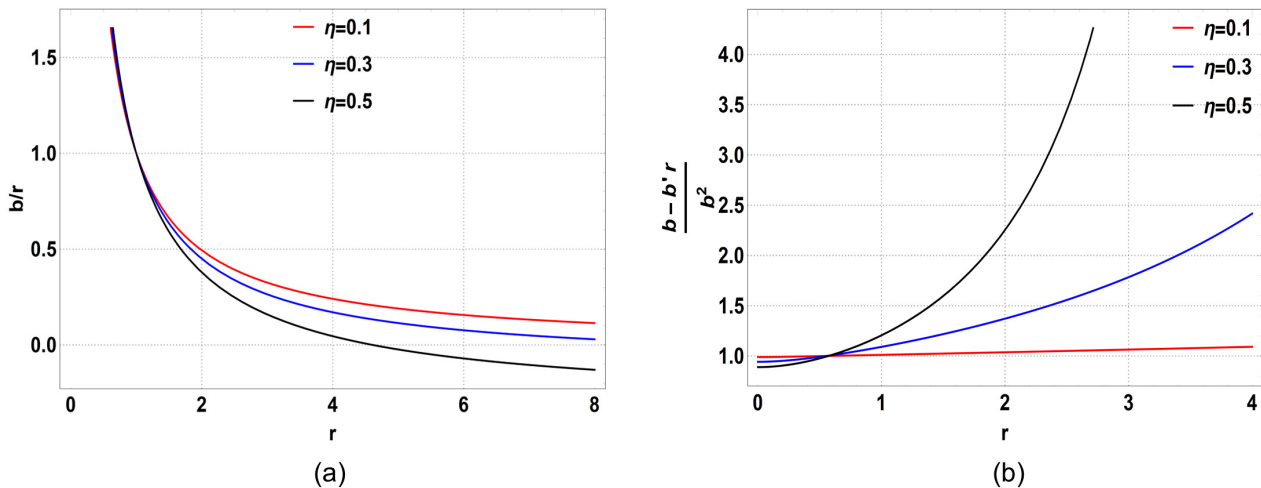
Figure 6. Profile of the (a) asymptotic flatness $\frac{b}{r}$ and (b) flaring out condition $\frac{b-b'r}{b^2}$ vs. r with $r_0 = 1$, $\alpha = -0.5$ and $\beta = -0.8$, for $b(r)$ in Eq. 25

With the shape function in Eq. (25), and the $f(R)$ model described by Eq. (20), the energy conditions, stability and the amount of exotic matter required for the wormhole configuration are analyzed next.

Using Eqs. (12)-(14), the various energy conditions are analyzed with the throat at $r_0 = 1$, and by fixing the model parameters of the $f(R)$ gravity model (Eq. (20)) as, $m = 2$, $n = 1$, $\alpha = -0.5$ and $\beta = -0.8$.

Figure 7 shows the NEC terms $\rho + p_r$, and $\rho + p_t$. It can be observed that the first NEC term $\rho + p_r$ is violated at the wormhole throat. The second NEC term $\rho + p_t$ is satisfied at the wormhole throat. However, owing to violation to the first NEC term, as a whole the NEC is inferred to be violated.

Figure 8 shows the WEC and the SEC. It can be seen that the WEC is violated at the wormhole throat, and this violation can again be attributed to the negative sign associated with the non-null components of the stress-energy tensor of the string cloud as in Eq. (15). The SEC is satisfied at the throat and also asymptotically, which is again an interesting point to note as in $f(R)$ gravity, the SEC should be asymptotically violated to account for the late-time accelerated expansion of the universe.

Figure 9 shows the variation of the EoS parameter ω and the anisotropy parameter Δ. It can be seen that the EoS parameter ω is $\omega > 0$ near the wormhole throat for all values of η, signifying that the string cloud as the source behaves like ordinary matter without any phantom-like behavior. The anisotropy parameter Δ is positive near the wormhole throat for all the values of η, signifying a repulsive geometry at the throat. The summary of the energy conditions is presented in Table 2.

Figure 10 shows the terms of the TOV equation and the VIQ. It is seen that the hydrostatic force F_h, and anisotropic force F_a do not cancel each other out, signifying that the wormhole configuration is unstable. From
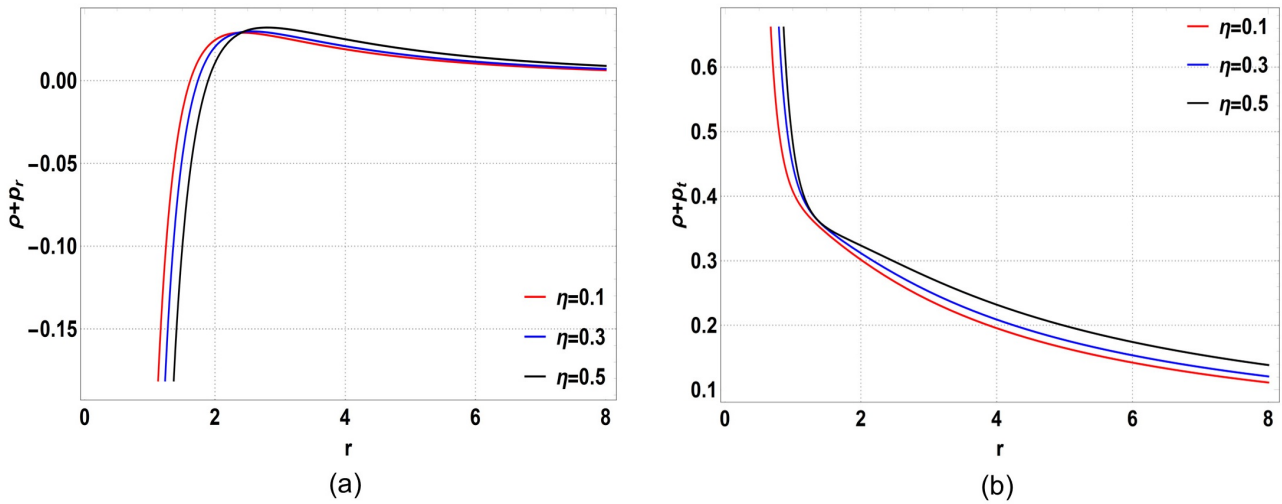
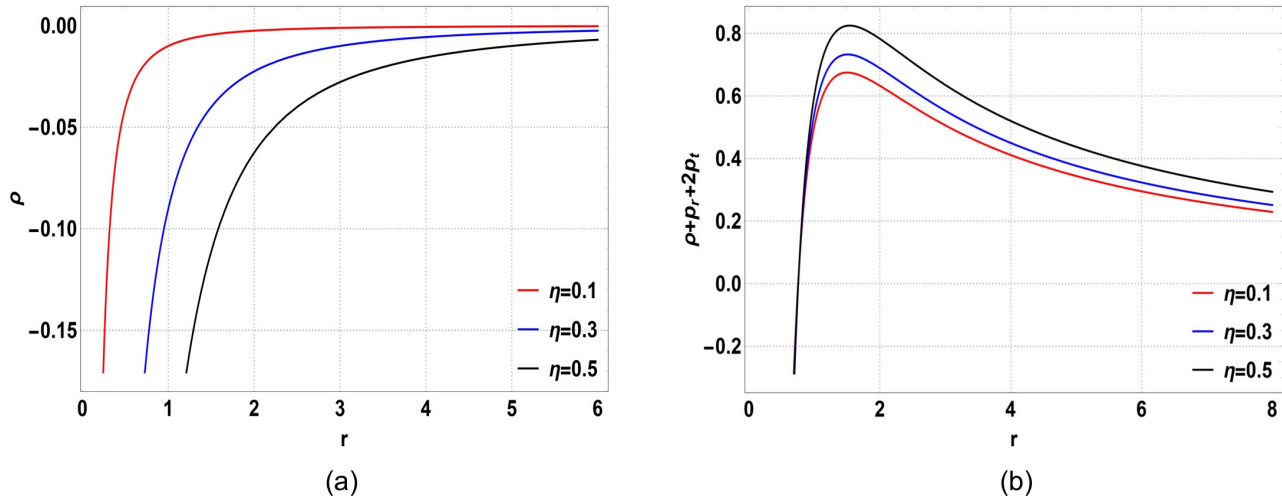**Figure 7.** Profile of the NEC terms (a) $\rho + p_r$ and (b) $\rho + p_t$ vs. r with $b(r)$ as in Eq. 25

Figure 8. Profile of the (a) WEC ρ and (b) SEC $\rho + p_r + 2p_t$ vs. r with $b(r)$ as in Eq. 25

Table 2. Summary of the energy conditions discussed in Sec. 3.2

Terms	Result	Interpretation
ρ	< 0 near throat, for $\eta = 0.1, 0.3, 0.5$	WEC violated at throat
$\rho + p_r$	< 0 near throat, for $\eta = 0.1, 0.3, 0.5$	NEC violated at throat
$\rho + p_t$	> 0 near throat, for $\eta = 0.1, 0.3, 0.5$	NEC satisfied at throat
$\rho + p_r + 2p_t$	> 0 near throat, for $\eta = 0.1, 0.3, 0.5$	SEC satisfied at throat
ω	> 0 near throat, for $\eta = 0.1, 0.3, 0.5$	normal matter like source at throat
Δ	> 0 near throat, for $\eta = 0.1, 0.3, 0.5$	repulsive geometry at throat

the VIQ, it is evident that $I_v \rightarrow 0$ as $s \rightarrow r_0$, indicating that the wormhole configuration can be obtained with arbitrarily small amounts of exotic matter.

With the results presented in Sec 3.1 and Sec 3.2, it is clear that wormhole solutions in $f(R)$ gravity with
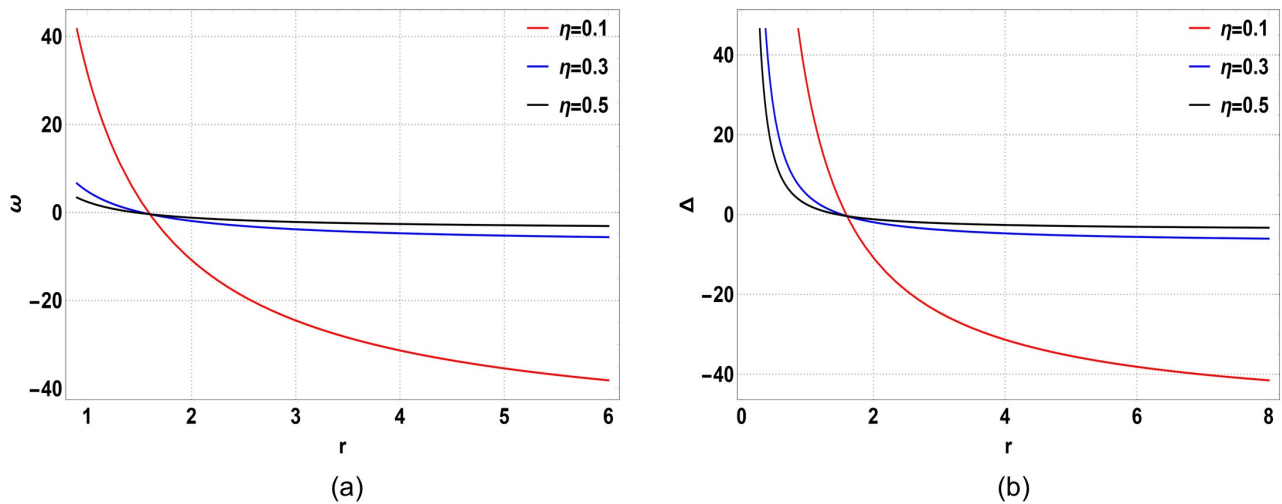
Figure 9. Profile of the (a) EoS parameter ω and (b) anisotropy parameter Δ vs. r with $b(r)$ as in Eq. 25
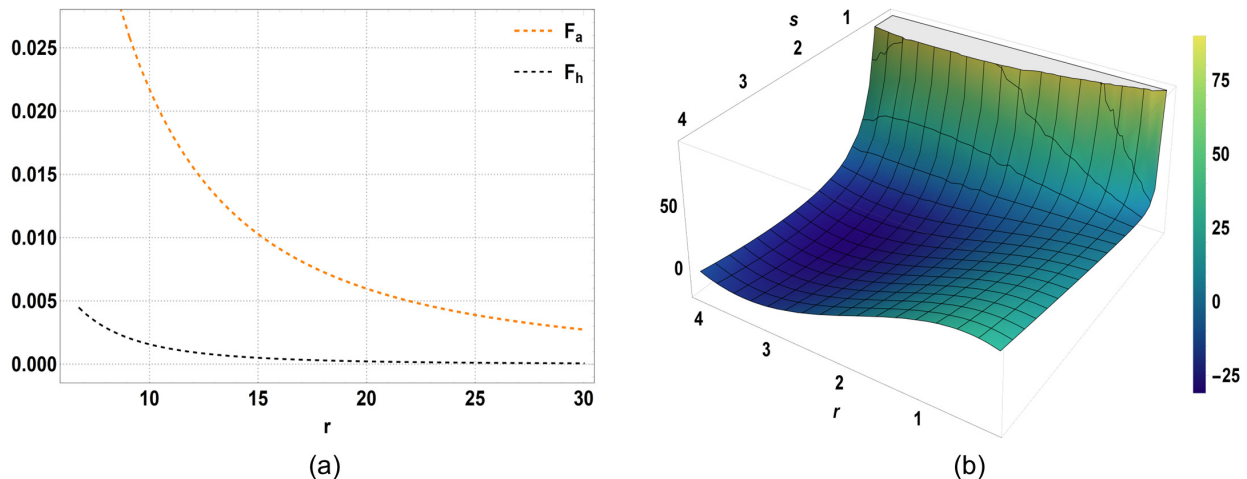

Figure 10. Profile of the (a) F_h, and F_a vs. r and (b) VIQ with $b(r)$ as in Eq. 25

background a string cloud are feasible with characteristic violation of the NEC. However, with $f(R) = \alpha R^m - \beta R^n$ gravity, the wormhole configuration is not stable. To have a better understanding, the next section presents the results of wormhole solution in $f(R) = \alpha R^m - \beta R^n$ gravity supported by ordinary matter and with the form of the shape function as in Eq. (4).

3.3. Traversable wormholes in $f(R) = \alpha R^m - \beta R^n$ gravity with ordinary matter

With the shape function in Eq. (4), the field equations Eqs. (12)-(14) are analyzed with the form of the $f(R)$ model as in Eq. (20). We assume that the wormhole geometry is threaded by ordinary matter with the stress-energy tensor $T_\nu^\mu = \text{diag}[-\rho(r), p_r(r), p_\theta(r), p_\phi(r)]$. Owing to the properties of the shape function, the throat radius is fixed at $r_0 = 3$, and the free parameter a is considered for the whole range $0 < a < 1$. The model parameters of the $f(R) = \alpha R^m - \beta R^n$ gravity are fixed as, $\alpha = 0.8$, $\beta = 0.5$, and $m = 2$, $n = 1$. The values of α and β should be smaller than unity, and we consider up to one decimal point to avoid errors in the numerical calculation. The various energy conditions, stability of the wormhole space-time, and the VIQ are presented below.

Figure 11 shows the profile of the NEC terms $\rho + p_r$ and $\rho + p_t$. It is evident that that the first NEC term $\rho + p_r$ is violated at the wormhole throat. However, the second NEC term $\rho + p_t$ is satisfied at the throat. Owing to the violation of the first NEC term, as a whole the NEC is considered to be violated.

Figure 12 depicts the WEC and the SEC. It is seen that the WEC is violated near the wormhole throat. The SEC is satisfied at the wormhole throat and asymptotically for the whole range of a, $0 < a < 1$. It is

interesting to note that even with ordinary matter as the source, the SEC is satisfied asymptotically for $f(R) = \alpha R^m - \beta R^n$ gravity.
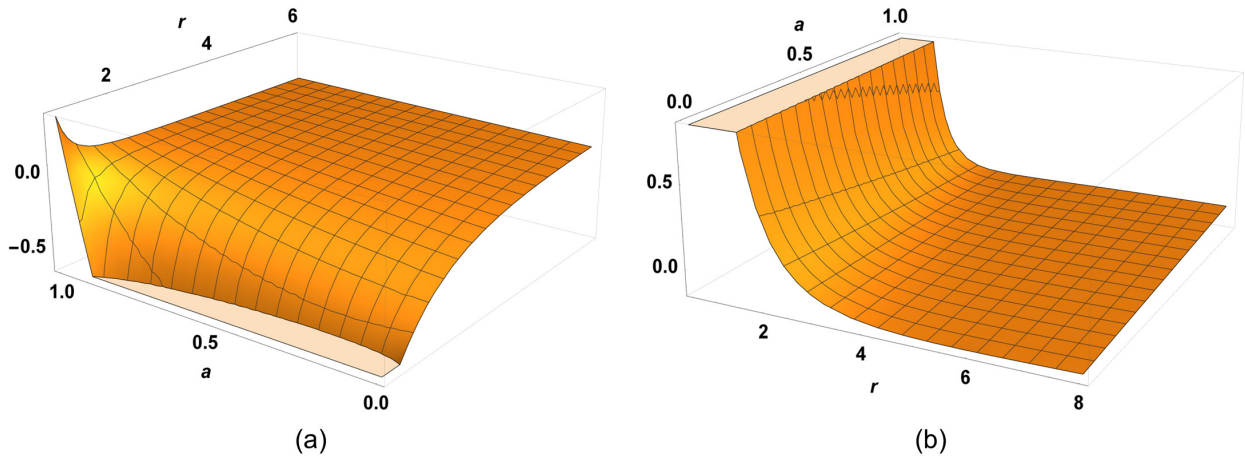

Figure 11. Profile of the NEC terms (a) $\rho + p_r$ and (b) $\rho + p_t$ vs. r with $b(r)$ as in Eq. 4
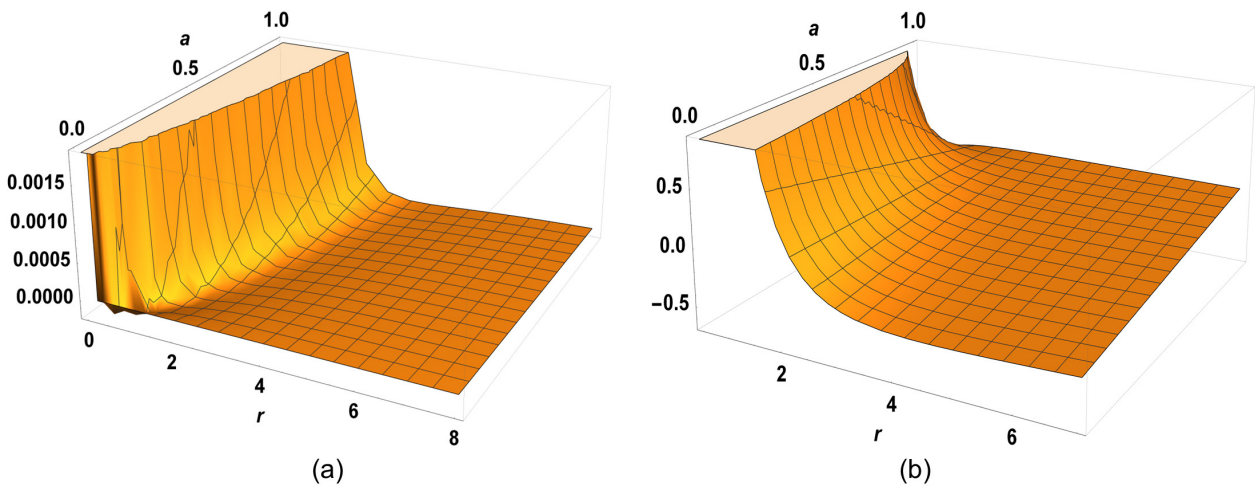

Figure 12. Profile of the (a) WEC ρ and (b) SEC $\rho + p_r + 2p_t$ vs. r with $b(r)$ as in Eq. 4

Figure 13 shows the variation of the EoS parameter and the anisotropy parameter. As expected, the EoS parameter is $\omega > 0$ near the wormhole throat, signifying that the source threading the wormhole geometry has no phantom-like behavior. The anisotropy parameter $\Delta > 0$ near the throat signifies a repulsive geometry at the throat. The energy conditions are summarized in Table 3.

Figure 14 shows the corresponding terms of the TOV equation and the VIQ. It is seen that both the hydrostatic force F_h, and the anisotropic force F_a do not cancel each other out asymptotically for the whole range of $0 < a < 1$, signifying that the wormhole configuration is not stable. From the VIQ it is evident that $I_v \to 0$ as $s \to r_0$, indicating that the wormhole solution can be obtained with arbitrarily small amount of exotic matter. However, the VIQ is only shown for $a = 0.5$, and for the whole range of $0 < a < 1$, the VIQ has a similar profile.

4. DISCUSSION AND CONCLUSION

In this study, we investigated the traversable wormholes in the framework of $f(R)$ gravity with a background of string clouds. A novel form of the shape function using Padé approximation was proposed for the analysis. Using this shape function a specific form of $F(r)$ was obtained in Eq. (16) to analyse the EFEs. However, it is observed that the $F(r)$ depends on the parameters of the metric functions and on the string cloud parameter η. Eliminating this dependence and obtaining a cosmologically viable form of $f(R)$ remains an
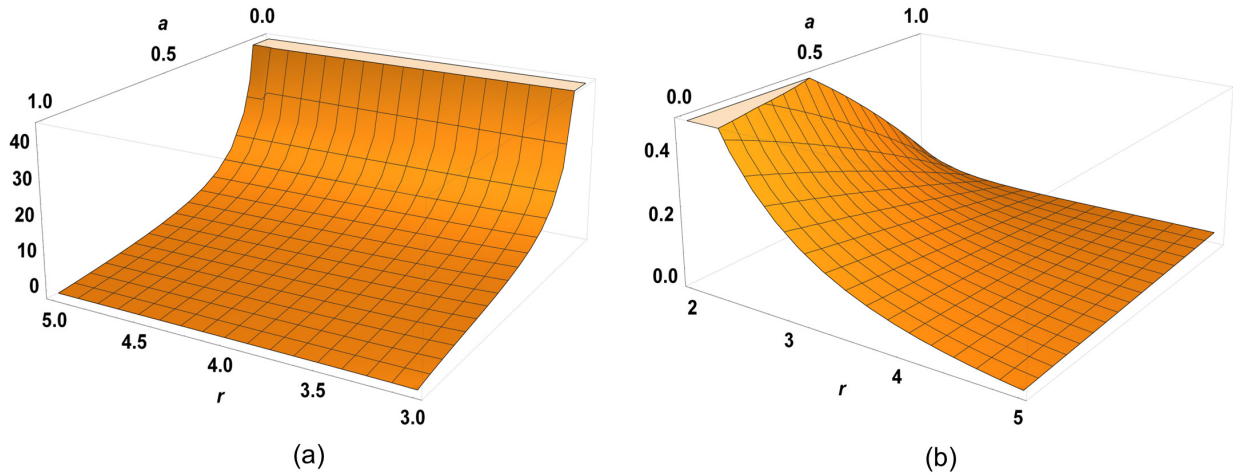
Figure 13. Profile of the (a) EoS parameter ω and (b) anisotropy parameter Δ vs. r with $b(r)$ as in Eq. 4

Table 3. Summary of the energy conditions discussed in Sec. 3.3

Terms	Result	Interpretation
ρ	< 0 near throat, for $0 < a < 1$	WEC violated at throat
$\rho + p_r$	< 0 near throat, for $0 < a < 1$	NEC violated at throat
$\rho + p_t$	> 0 near throat, for $0 < a < 1$	NEC satisfied at throat
$\rho + p_r + 2p_t$	> 0 near throat, for $0 < a < 1$	SEC satisfied at throat
ω	> 0 near throat, for $0 < a < 1$	normal matter like source at throat
Δ	> 0 near throat, for $0 < a < 1$	repulsive geometry at throat
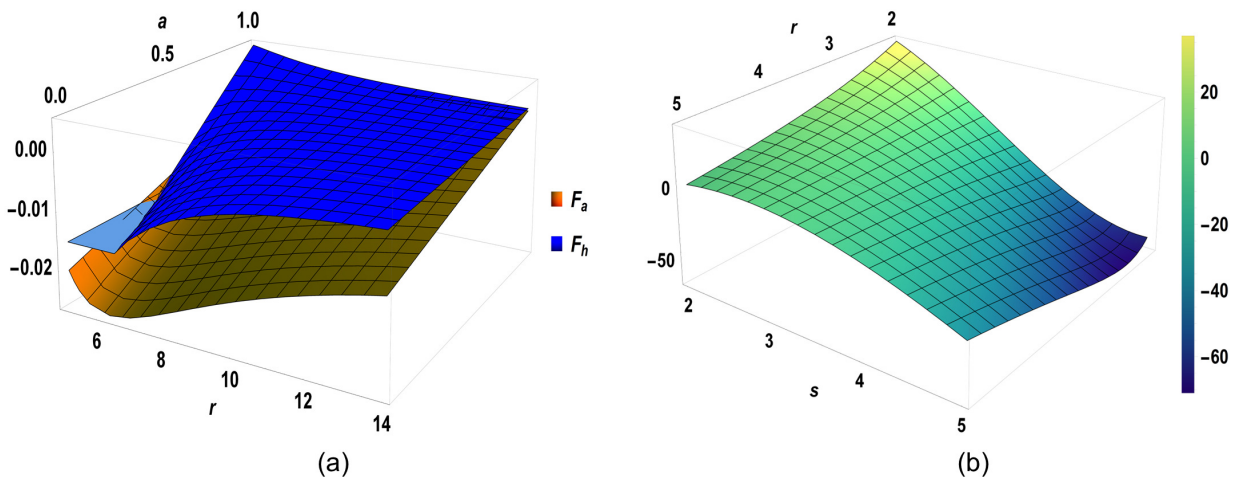
Figure 14. Profile of the (a) F_{h}, and F_{a} vs. r and (b) VIQ with $b(r)$ as in Eq. 4

open issue. The results demonstrate that stable wormhole solutions with characteristic violation of the energy conditions (especially the NEC) are feasible in the framework of $f(R)$ gravity with the new shape function in the background of a string cloud. In addition, the EoS parameter near the wormhole throat indicates that the string cloud has phantom-like properties. The anisotropy parameter $\Delta < 0$ near the throat signifies an attractive geometry. In addition, the SEC shows an indeterminate behavior as it oscillates between positive and negative values. Therefore, to have a better understanding of the wormhole solutions, traversable wormholes

are considered in a string cloud background with a simple form of $f(R)$ gravity model, $f(R) = \alpha R^m - \beta R^n$. It is interesting to note that the shape function in this case can yield viable wormhole geometries for negative values of α and β. The results demonstrate characteristic violations of the NEC. Interestingly, the SEC is satisfied both at the throat and asymptotically. The EoS parameter $\omega > 0$ at the throat indicates that that the string cloud behaves as normal matter. The anisotropy parameter $\Delta > 0$ near the wormhole throat signifies a repulsive geometry at the throat. However, the TOV equation shows that the wormhole space-time is unstable. For a comparative analysis, wormholes threaded by normal matter are analyzed in $f(R) = \alpha R^m - \beta R^n$ gravity, using the Padé approximate shape function given in Eq. (4). The constants α and β are considered with positive values. The results demonstrate a characteristic violation of the NEC and show that the wormhole space-time is unstable. The SEC is satisfied at the wormhole throat and asymptotically.

Although wormholes have not been detected yet, studying these exact solutions of the EFEs provides with far reaching insight into the nature of space-time and fundamental building blocks of the universe. Wormholes also play a crucial role in several important issues such as the cosmic censorship conjecture [61]. Studies have reported strong indications for their presence in the form of black hole mimickers [62, 63, 4]. Further studies regarding the observational constraints of these wormhole solutions remain an open issue to be addressed in the near future.

ORCID

🄳 **Parangam Goswami**, https://orcid.org/0000-0002-8666-2544; 🄳 **Anshuman Baruah**, https://orcid.org/0000-0001-6420-7666; 🄳 **Atri Deshamukhya**, https://orcid.org/0000-0003-4350-6645

REFERENCES

[1] K. Schwarzschild, "On the gravitational field of a mass point according to Einstein's theory," Preuss. Akad. Wiss. Berlin, (Math. Phys.) **1916**, 189 (1916). https://arxiv.org/abs/physics/9905030.

[2] L. Flamm, "Contributions to Einstein's theory of gravitation," Phys. Z. **17**, 448 (1916). https://doi.org/10.1007/s10714-015-1908-2

[3] A. Einstein, and N. Rosen, Phys. Rev. **48**(1), 73 (1935). https://doi.org/10.1103/PhysRev.48.73

[4] V. De Falco, E. Battista, S. Capozziello, and M. De Laurentis, "Reconstructing wormhole solutions in curvature based Extended Theories of Gravity," Eur. Phys. J. C, **81**(2), 157 (2021). https://doi.org/10.1140/epjc/s10052-021-08958-4

[5] V. De Falco, E. Battista, S. Capozziello, and M. De Laurentis, "Testing wormhole solutions in extended gravity through the Poynting-Robertson effect," Phys. Rev. D, **103**(4), 044007 (2021). https://doi.org/10.1103/PhysRevD.103.044007

[6] H.G. Ellis, "Ether flow through a drainhole: A particle model in general relativity," J. Math. Phys. **14**(1), 104–118 (1973). https://doi.org/10.1063/1.1666161

[7] K.A. Bronnikov, "Scalar-tenzor theory and scalarcharge," Acta Phys. Pol. **B4**, 251-266 (1973). https://inspirehep.net/files/1a28c080a733a1b776867157a30efd12

[8] M.S. Morris, and K.S. Thorne, "Wormholes in spacetime and their use for interstellar travel: A tool for teaching general relativity," Am. J. Phys. **56**, 395–412 (1988). https://doi.org/10.1119/1.15620

[9] M. Visser, *Lorentzian wormholes: From Einstein to Hawking*, (American Institute of Physics Melville, NY, USA, 1996)

[10] L. Susskind, Fortschritte der Phys. "ER=EPR, GHZ, and the consistency of quantum measurements," **64**(1), 72–83 (2016). https://doi.org/10.1002/prop.201500094

[11] S. Perlmutter, M.S. Turner, and M. White, "Constraining Dark Energy with Type Ia Supernovae and Large-Scale Structure," Phys. Rev. Lett. **83**(4), 670 (1999). https://doi.org/10.1103/PhysRevLett.83.670

[12] Calzà M., Rinaldi M. and Sebastiani L., "A Special Class of Solutions in $f(R)$ Gravity," Eur. Phys. J. C, **78**, 178 (2018). https://doi.org/10.1140/epjc/s10052-018-5681-8

[13] A.G. Riess, P.E. Nugent, R.L. Gilliland, B.P. Schmidt, J. Tonry, M. Dickinson, R.I. Thompson, et al., "The Farthest Known Supernova: Support for an Accelerating Universe and a Glimpse of the Epoch of Deceleration," Astrophys. J. **560**(1), 49 (2001). https://doi.org/10.1086/322348

[14] A. Linde, *Particle physics and inflationary cosmology*, vol. 5 (CRC press, London, 1990)

[15] A.A. Starobinsky, "A new type of isotropic cosmological models without singularity," Phys. Lett. B **91**(1), 99–102 (1980). https://doi.org/10.1016/0370-2693(80)90670-X

[16] E.J. Copeland, M. Sami, and S. Tsujikawa, "Dynamics of dark energy," Int. J. Mod. Phys. D, **15**(11), 1753–1935 (2006). https://doi.org/10.1142/S021827180600942X

[17] S. Capozziello, and M. De Laurentis, "Extended Theories of Gravity," Phys. Rep. **509**(4-5), 167–321 (2011). https://doi.org/10.1016/j.physrep.2011.09.003

[18] T.P. Sotiriou, and V. Faraoni, "$f(R)$ theories of gravity," Rev. Mod. Phys. **82**(1), 451 (2010). https://doi.org/10.1103/RevModPhys.82.451

[19] J.Q. Guo, "Solar system tests of $f(R)$ gravity," Int. J. Mod. Phys. D, **23**(04), 1450036 (2014). https://doi.org/10.1142/S0218271814500369

[20] S. Capozziello, F.S. Lobo, and J.P. Mimoso, "Generalized energy conditions in extended theories of gravity," Phys. Rev. D, **91**(12), 124 (2015). https://doi.org/10.1103/PhysRevD.91.124019

[21] A. Baruah, and A.Deshamukhya, "Traversable Lorentzian wormholes in higher dimensional theories of gravity," J. Phys. Conf. Ser. **1330**(1), 012001 (2019). https://doi.org/10.1088/1742-6596/1330/1/012001

[22] F.S. Lobo, and M.A. Oliveira, "Wormhole geometries in $f(R)$ modified theories of gravity," Phys. Rev. D, **80**(10), 104012 (2009). https://doi.org/10.1103/PhysRevD.80.104012

[23] N. Furey, and A. DeBenedictis, "Wormhole throats in R^m gravity," Class. Quantum Gravity, **22**(2), 313 (2004). https://doi.org/10.1088/0264-9381/22/2/005

[24] N. Godani, and G.C. Samanta, "Wormhole modeling supported by non-exotic matter," Mod. Phys. Lett. A, **34**(28), 1950226 (2019). https://doi.org/10.1142/S0217732319502249

[25] N. Godani, and G.C. Samanta, "Traversable wormholes and energy conditions with two different shape functions in $f(R)$ gravity," Int. J. Mod. Phys. D, **28**(02), 1950039 (2019). https://doi.org/10.1142/S0218271819500391

[26] T. Azizi, "Wormhole Geometries in $f(R,T)$ Gravity," Int. J. Theor. Phys. **52**, 3486–3493 (2013). https://doi.org/10.1007/s10773-013-1650-z

[27] A.K. Mishra, U.K. Sharma, V.C. Dubey, and A. Pradhan, "Traversable wormholes in $f(R,T)$ gravity," Astrophys. Space Sci. **365**(2), 34 (2020). https://doi.org/10.1007/s10509-020-3743-5

[28] S. Nojiri, and S.D. Odintsov, "Unified Cosmic History in Modified Gravity: From $f(R)$ Theory to Lorentz Non-invariant Models," Phys. Rept. **505**, 59-144 (2011). https://doi.org/10.1016/j.physrep.2011.04.001

[29] S. Nojiri, and S.D. Odintsov, and V.K. Oikonomou, "Modified Gravity Theories on a Nutshell: Inflation, Bounce and Late-time Evolution," Phys. Rept. **692**, 1-104 (2017). https://doi.org/10.1016/j.physrep.2017.06.001

[30] C.G. Böehmer, T. Harko, and F.S. Lobo, ",Wormhole geometries in modified teleparallel gravity and the energy conditions," Phys. Rev. D, **85**(4), 044033 (2012). https://doi.org/10.1103/PhysRevD.85.044033

[31] G. Mustafa, Z. Hassan, and P. Sahoo, "Traversable wormhole inspired by non-commutative geometries in $f(Q)$ gravity with conformal symmetry," Ann. Phys. **437**, 168751 (2022). https://doi.org/10.1016/j.aop.2021.168751

[32] A. Baruah, P. Goswami, and A. Deshamukhya, "New wormhole solutions in a viable $f(R)$ gravity model," Int. J. Mod. Phys. D, **31**(16), 2250119 (2022). https://doi.org/10.1142/S021827182250119X

[33] A. Baruah, P. Goswami, and A. Deshamukhya, "Non-commutative wormholes in $f(R)$ gravity satisfying the energy conditions," New Astron. **99**, 101956 (2023). https://doi.org/10.1016/j.newast.2022.101956

[34] S. Mukhi, "String theory: a perspective over the last 25 years," Class. Quantum Gravity, **28**(15), 153001 (2011). https://doi.org/10.1088/0264-9381/28/15/153001

[35] M. Kalb, and P. Ramond, "Classical direct interstring action," Phys. Rev. D, **9**(8), 2273 (1974). https://doi.org/10.1103/PhysRevD.9.2273

[36] P.S. Letelier, "Gauge-invariant theory of direct interaction between strings," Phys. Rev. D, **15**(4), 1055 (1977). https://doi.org/10.1103/PhysRevD.15.1055

[37] F. Lund, and T. Regge, "Unified approach to strings and vortices with soliton solutions," Phys. Rev. D, **14**(6), 1524 (1976). https://doi.org/10.1103/PhysRevD.14.1524

[38] P.S. Letelier, "Clouds of strings in general relativity," Phys. Rev. D, **20**(6), 1294 (1979). https://doi.org/10.1103/PhysRevD.20.1294

[39] E. Herscovich, and M.G. Richarte, "Black holes in Einstein–Gauss–Bonnet gravity with a string cloud background," Phys. Lett. B, **689**(4-5), 192-200 (2010). https://doi.org/10.1016/j.physletb.2010.04.065

[40] S.G. Ghosh, and S.D. Maharaj, "Cloud of strings for radiating black holes in Lovelock gravity," Phys. Rev. D, **89**(8), 084027 (2014). https://doi.org/10.1103/PhysRevD.89.084027

[41] A. Belhaj, and Y. Sekhmani, "Shadows of rotating quintessential black holes in Einstein–Gauss–Bonnet gravity with a cloud of strings," Gen. Relativ. Gravit. **54**(2), 17 (2022). https://doi.org/10.1007/s10714-022-02902-x

[42] D.V. Singh, S.G. Ghosh, and S.D. Maharaj, "Clouds of strings in $4D$ Einstein–Gauss–Bonnet black holes," Phys. Dark Universe, **30**, 100730 (2020). https://doi.org/10.1016/j.dark.2020.100730

[43] M.G. Richarte, and C. Simeone, "Traversable wormholes in a string cloud," Int. J. Mod. Phys. D, **17**(08), 1179–1196 (2008). https://doi.org/10.1142/S0218271808012759

[44] D.J. Gogoi, and U.D. Goswami, "Tideless traversable wormholes surrounded by cloud of strings in $f(R)$ gravity," J. Cosmol. Astropart. Phys. **2023**(02), 027 (2023). https://doi.org/10.1088/1475-7516/2023/02/027

[45] S. Nojiri, and S.D. Odintsov, "Modified $f(R)$ gravity unifying R^m inflation with the Λ**CDM** epoch," Phys. Rev. D, **77**(2), 026007 (2008). https://doi.org/10.1103/PhysRevD.77.026007

[46] S. Capozziello, and R. D'Agostino, O. Luongo, "Extended gravity cosmography," Int. J. Mod. Phys. D, **28**(10), 1930016 (2019). https://doi.org/10.1142/S0218271819300167

[47] C. Gruber, and O. Luongo, "Cosmographic analysis of the equation of state of the universe through Padé approximations," Phys. Rev. D, **89**(10), 103506 (2014). https://doi.org/10.1103/PhysRevD.89.103506

[48] Y.N. Zhou, D.Z. Liu, X.B. Zou, and H. Wei, "New generalizations of cosmography inspired by the Padé approximant," Eur. Phys. J. C, **76**, 281 (2016). https://doi.org/10.1140/epjc/s10052-016-4091-z

[49] S. Capozziello, O. Luongo, and L. Mauro, "Traversable wormholes with vanishing sound speed in $f(R)$ gravity," Eur. Phys. J. Plus, **136**, 1–14 (2021). https://doi.org/10.1140/epjp/s13360-021-01104-9

[50] H. Padé, "Sur la représentation approchée d'une fonction par des fractions rationnelles," in: *Ann. Sci. de l'Ecole Norm. Superieure*, vol. 9 (1892), pp. 3–93. http://www.numdam.org/item/10.24033/asens.378.pdf

[51] J.M. Graça, I.P. Lobo, and I.G. Salako, "Cloud of strings in $f(R)$ gravity," Chin. Phys. C, **42**(6), 063105 (2018). https://doi.org/10.1088/1674-1137/42/6/063105

[52] T.G. Mertens, H. Verschelde, and V.I. Zakharov, "Near-Hagedorn thermodynamics and random walks: a general formalism in curved backgrounds," J. High Energy Phys. **2014**(11), 127 (2014). https://doi.org/10.1007/JHEP02(2014)127

[53] E. Curiel, in: *Towards a theory of spacetime theories*, (Springer, New York, 2017), pp. 43–104.

[54] R.C. Tolman, *Relativity, thermodynamics, and cosmology*, (The Clarendon Press, Oxford, London, 1934).

[55] R.J. Oppenheimer, and G.M. Volkoff, "On Massive Neutron Cores," Phys. Rev. **55**(4), 374 (1939). https://doi.org/10.1103/PhysRev.55.374

[56] V. Gorini, U. Moschella, A.Y. Kamenshchik, V. Pasquier, and A.A. Starobinsky, "Tolman-Oppenheimer-Volkoff equations in the presence of the Chaplygin gas: Stars and wormholelike solutions," Phys. Rev. D, **78**(6), 064064 (2008). https://doi.org/10.1103/PhysRevD.78.064064

[57] J.P. de Leon, "Limiting configurations allowed by the energy conditions," Gen. Relat. Gravit. **25**(11), 1123–1137 (1993). https://doi.org/10.1007/BF00763756

[58] M. Visser, S. Kar, and N. Dadhich, "Traversable Wormholes with Arbitrarily Small Energy Condition Violations," Phys. Rev. Lett. **90**(20), 201102 (2003). https://doi.org/10.1103/PhysRevLett.90.201102

[59] S. Kar, N. Dadhich, and M. Visser, "Quantifying energy condition violations in traversable wormholes," Pramana - J. Phys. **63**(4), 859–864 (2004). https://doi.org/10.1007/BF02705207

[60] F.S.N. Lobo, F. Parsaei, and N. Riazi, "New asymptotically flat phantom wormhole solutions," Phys. Rev. D, **87**(8), 084030 (2013). https://doi.org/10.1103/PhysRevD.87.084030

[61] R. Penrose, ""Golden Oldie": Gravitational Collapse: The Role of General Relativity," Gen. Relativ. Gravit. **34**(7), 1141–1165 (2002). https://doi.org/10.1023/A:1016578408204

[62] R.N. Izmailov, A. Bhattacharya, E.R. Zhdanov, A.A. Potapov, and K.K. Nandi, "Can massless wormholes mimic a Schwarzschild black hole in the strong field lensing?," Eur. Phys. J. Plus, **134**(8), 384 (2019). https://doi.org/10.1140/epjp/i2019-12914-5

[63] K.K. Nandi, R.N. Izmailov, A.A. Yanbekov, and A.A. Shayakhmetov, "Ring-down gravitational waves and lensing observables: How far can a wormhole mimic those of a black hole?," Phys. Rev. D, **95**(10), 104011 (2017). https://doi.org/10.1103/PhysRevD.95.104011

[64] F. Duplessis, and D.A. Easson, "Traversable wormholes and non-singular black holes from the vacuum of quadratic gravity," Phys. Rev. D **92**(4) 043516 (2015). https://doi.org/10.1103/PhysRevD.92.043516

ПРОХІДНІ ЧЕРВОТОЧИНИ В $f(R)$ ГРАВІТАЦІЇ, СТВОРЕНІ ХМАРОЮ СТРУН

Парангам Ґосвамі, Аншуман Баруах, Атрі Дешамух'я
Факультет фізики, Ассамський університет, Сілчар, 788011, Ассам, Індія

Розв'язання червоточин у загальній теорії відносності (ОТО) потребує *екзотичних* джерел матерії, які порушують умову нульової енергії (NEC), і добре відомо, що модифікації ОТО вищого порядку та деякі альтернативні джерела матерії можуть підтримувати червоточини. У цьому дослідженні ми досліджуємо можливість формулювання прохідних червоточин у $f(R)$ модифікованій гравітації, яка є, мабуть, найбільш обговорюваною модифікацією ОТО, за допомогою двох підходів. По-перше, щоб дослідити вплив геометричних обмежень на глобальні характеристики, ми вимірюємо rr–компонент метричного тензора та використовуємо наближення Падè, щоб перевірити, чи добре обмежена *функція форми* можна сформулювати таким чином. Потім ми виводимо рівняння поля на тлі струнної хмари та чисельно аналізуємо енергетичні умови, стабільність і кількість екзотичної матерії в цьому просторі-часі. Далі, як альтернативне джерело в простій гравітаційній моделі $f(R)$, ми використовуємо фонову хмару струн для оцінки функції форми червоточини та аналізу відповідних властивостей простору-часу. Потім ці результати порівнюються з даними про червоточини, пронизані нормальною матерією, у простій розглянутій моделі гравітації $f(R)$. Результати демонструють, що струнна хмара є життєздатним джерелом червоточин із порушеннями NEC; однак простір-час червоточини в простій гравітаційній моделі $f(R)$, розглянутій у цьому дослідженні, нестабільний.
Ключові слова: *рівняння Ейнштейна; рішення червоточини; хмара струн*

BIANCHI TYPE-III VISCOUS HOLOGRAPHIC RICCI DARK ENERGY COSMOLOGICAL MODEL IN BRANS-DICKE THEORY OF GRAVITATION

P.E. Satyanarayana, ⬤K.V.S. Sireesha*

Department of Mathematics, GIS, GITAM Deemed to be University, Visakhapatnam, India
Corresponding Author e-mail: skuppili2@gitam.edu

This paper investigates and examines a wide range of findings related to the description of holographic Ricci dark energy (HRDE) with the bulk viscosity within Universe's late-time accelerated expansion in the framework of an anisotropic Bianchi type-III cosmological model with pressure less matter content in the Brans-Dicke theory of gravity. We are using the relationship between the metric potentials to obtain a precise conclusion to the field equations, resulting in a rapid expansion. To investigate the physical behaviour of our dark energy model, several major cosmological parameters, including Hubble, deceleration, matter energy density, Ricci dark energy density (RDE), and Equation of state (EoS), are used. We examined some of the viscosity of the holographic Ricci dark energy model using current cosmological observations. We describe how the models' physical and geometric properties are compatible with recent compilations.

Keywords: *Bianchi type- III metric; Holographic Ricci dark energy (HRDE); Bulk Viscosity; Brans-Dicke theory*
PACS: 95.10.-a, 95.35. + d, 95.36. + x, 98.80. ES, 98.80. JK, 98.80. QC

1. INTRODUCTION

Recent experimental cosmology substantiates the idea that the Universe's expansion is accelerating [1-3]. The interaction between two galaxies caused by an unknown, dark element, that produces considerable negative pressure, is generally dark energy (DE). It is compatible with all cosmological substances inside the simplest model, that is, within a ΛCDM model. Still, it has problems similar to fine-tuning and thus, the cosmic coincidence problem, which has led to some indispensable styles to its description. Researchers have hypothecated that radiation and ordinary matter (baryons) account for 5% of the Universe's present energy, with the remaining 95% dominated by this dark component, to explain the Universe's ultimate-rapid growth.

Interestingly, dark energy explores as a possible explanation for the physical Universe's late-time rapid expansion [5]. Dark energy (DE) is considered to regard for 73% of the energy in our Universe, with Dark Matter (DM) accounting for 23% and baryonic matter accounting for the remaining 6% [6,7]. Two main approaches were proposed to explain this late time acceleration, the first is to investigate better DE possibilities, and the second is to investigate modified Einstein's theory of gravity. To characterize the behavior of DE events, the equation of state (EoS) parameter w ($= p/\rho$), where p represents pressure and ρ denotes energy density, is generally employed. The EoS parameter w with the range (-1, -1/3) describes the substance DE model, whereas $w = -1$ explains the vacuum DE, also known as the cosmological constant or ΛCDM model, and $w < -1$ defines the phantom DE model. This phantom DE model will nearly clearly affect an ineluctable space-time singularity.

As a possible result of these difficulties, physicists worldwide have presented good dynamic DE models. These models classify into two categories: scalar-field models, which represent quintessence, phantom, k-essence, tachyon, and quintom [8-13], and interactions between the models, similar as the Chaplygin gas family, the brane-world Holographic DE (HDE), the age-graphic DE models [14-16], and so on. Changes in the quality of the Einstein-Hilbert reaction, for illustration, led to several modified gravity theories. Some modified gravity theories include the Brans-Dicke scalar-tensor theory [17], the f(R) and f(R, T) theories [18–22], (where R is the curvature scalar and T is the trace of the energy momentum tensor), and so on. Among the options, as preliminarily indicated, it is a good conception for a model to attract further, and further attention to the so-called "Holographic dark energy (HDE)". According to the holographic principle, the number of degrees of freedom of a physical system, the scope of the surrounding area L_2, rather than its volume, [23], will not be confined to an infrared (IR) cut-off point. Cohen et al. [24], confirm that the vacuum energy density is commensurable to the Hubble scale $L \approx H^{-1}$. The energy density of holographic dark energy is described by Li [25] as $\rho_\Lambda = 3c^2 M_{pl}^2 L^{-2}$, where L is the IR cut-off radius, C is constant, and $M_{pl}^2 = 1/_{8\pi G}$ is the Planck mass. This HDE model can explain the Universe's rapid expansion, and it is consistent with the data set available. Numerous investigations on the HDE models have been conducted to understand the Universe's accelerating nature. Later, Gao et al. [26] investigated the longer-term event horizon, which is supposed to be changed by inversion of the Ricci scalar curvature, i.e., $L \approx R^{-1/_2}$. In this case, the model is called the Ricci Dark Energy Model. Granda and Oliveros [27, 28] proposed a new holographic Ricci Dark Energy Model with the energy density supplied by $\rho_\Lambda = \frac{3}{8\pi G}(\xi H^2 + \eta \dot{H})$, which was further meliorated by Chen and Jing [29] and termed modified holographic Ricci dark energy (MHRDE) with the energy density provided by

$$\rho_h = \frac{3}{8\pi G}\left(\varepsilon_0 H^2 + \eta\dot{H} + \zeta\ddot{H}H^{-1}\right). \tag{1}$$

Sireesha et al. [30] examined modified holographic Ricci dark energy (MHRDE) cosmological models in $f(R, T)$ gravity. In papers [31–34], the RDE is suitable for expressing the current acceleration of the Universe. During neutrino emulsion in the early cosmos, matter behaves like a viscous fluid. The coefficient of viscosity decreases as the Universe expands. The influence of viscosity on the expansion of the Universe, and Thus, the radiation anisotropy from a black body regenerated by Misner [35, 36] is greatly decreased by the extreme scattering produced on by viscosity. Rao et al. [37] investigated bulk viscous string cosmological models in the Saez – Ballester theory. Chakraborty et al. [38] derived the cosmology of an expanded form of HDE in the presence of bulk viscosity and the inflation dynamics using slow-roll parameters.

Anisotropic and spatially homogenous Universes have drawn a lot of attention in theoretical cosmology over the past few decades. Since the main observational data from CMBR (Bennett et al. [39]) has been thought to suggest the presence of an evolution from the anisotropic to the isotropic phase of the cosmos (Akarsu and Kilinc [40]). Additionally, it has been suggested that the isotropic FRW model might not provide an accurate and comprehensive description of matter in the early epochs of the universe. For a realistic analysis of cosmological models, it is necessary to assume spatially homogeneous and anisotropic space-times in order to examine whether they may evolve to the known level of homogeneity and isotropy. Many scientists have been interested in Bianchi type (BT) cosmological models, which are homogenous but not necessarily isotropic among different anisotropic space-times. Many scientists have developed innovative cosmological models in recent years that use DE against the context of anisotropic Bianchi space-times. Koussour et al., [41, 42] explored Anisotropic nature of space-time in **f(Q)** gravity and Late-time acceleration in **f(Q)** gravity: Analysis and constraints in an anisotropic background.

Modified theories of gravitation are generalized models that lead to the rise of changes in the force of gravity as a result of the Einstein-Hilbert action. Most importantly, in scalar-tensor gravity, Brans-Dick (BD) theory provides a practical approach to explore cosmic events in later ages of the Universe. This theory's significant features include variable gravitational constants, a scalar field and geometry combination, compliant with numerous physical laws, and solar launch restrictions. Variable-G theories developed from the Brans-Dicke (BD) scalar-tensor theory [17] and its generalization to other types of scalar-tensor theories, similar to the overall scalar-tensor theory with particular terms presented by Wagoner [43]. During this theory, the inverse of the gravitational constant G is substituted by a scalar field $'\varphi'$, which is the gravitational force coupling according to a new parameter. Within the Brans-Dicke field equations, the combined scalar and tensor fields are given by

$$G_{ij} = -8\pi\varphi^{-1}T_{ij} - \omega\varphi^{-2}\left(\varphi_{,i}\varphi_{,j} - \frac{1}{2}g_{ij}\varphi_{,k}\varphi^{,k}\right) - \varphi^{-1}\left(\varphi_{i;j} - g_{ij}\varphi_{;k}^{;k}\right), \tag{2}$$

and

$$\varphi_{;k}^{,k} = 8\pi(3 + 2\omega)^{-1}\mathrm{T} \tag{3}$$

We have also constructed an equation for energy conservation.

$$T_{;j}^{ij} = 0 \tag{4}$$

This equation results from the field equations (2) and (3).

Several authors have examined the different features of Brans-Dicke cosmology thoroughly. Rao and Sireesha [44, 45] studied several string cosmological models within the Brans-Dicke theory of gravity, while Rao et al. [46] anatomized the FRW holographic dark energy as a cosmological model. Dasu Naidu et al. [47] developed a new holographic DE cosmological model within the SB theory of gravity with an anisotropic background. Sandhya Rani et al. [48] investigated Bianchi type-III, V, and VI0 generalized ghost dark energy models with polytropic gas using the Brans-Dicke (BD) theory of gravity. Sireesha & Rao [49] examined Bianchi type II, VIII, and IX Holographic dark energy cosmological models within the Brans-Dicke theory of gravity.

According to the earlier, we should take into account the spatially homogenous anisotropic Bianchi type-III cosmological model with pressure less matter and holographic Ricci dark energy with bulk viscosity in the Brans – Dicke theory of gravity. We structured our efforts for this paper as follows: In section 2, we derived the Brans-Dicke theory field equations in the presence of pressure less matter and holographic Ricci dark energy with bulk viscosity within the Bianchi type-III cosmological model. In Section 3, we solved the field equations. In Section 4, we developed and examined numerous essential physical properties of the model. In section 5, we concluded our compliances.

2. METRIC AND FIELD EQUATIONS:
We consider a spatially homogeneous Bianchi type-III metric form

$$ds^2 = dt^2 - A^2x^2 - B^2e^{-2x}y^2 - C^2z^2 \tag{5}$$

where A, B and C are functions of 't' only.

The holographic Ricci dark energy (HRDE) energy momentum tensor with bulk viscosity is $T_{ij} = T_{ij}^m + T_{ij}^h$, T_{ij}^m is that the energy-momentum tensor for matter and T_{ij}^h is that the energy momentum tensor for holographic Ricci dark energy. They are

$$T_{ij}^h = (\rho_h + \overline{p_h})u_i u_j - \overline{p_h} g_{ij} \tag{6}$$

and

$$T_{ij} = \rho_m u_i u_j \tag{7}$$

Where ρ_m denotes the matter energy density, ρ_h indicates the holographic Ricci dark energy density, and $\overline{p_h}$ means the viscous holographic dark energy's pressure.

In the co-moving frame of reference, and that we will get

$$T_1^{m\,1} + T_1^{h\,1} = T_2^{m\,2} + T_2^{h\,2} = T_3^{m\,3} + T_3^{h\,3} = -\overline{p_h} \,\&\, T_4^{m\,4} + T_4^{h\,4} = \rho_m + \rho_h \tag{8}$$

where ρ_m, ρ_h and $\overline{p_h}$ are all functions of time 't' only.

The viscous holographic Ricci dark energy pressure satisfies the relation $\overline{p_h} = p_h - 3\varepsilon H$. In the late time evolution of the universe, dark energy with bulk viscosity generates phantom type rapid expansion. We have assumed that dark matter has no pressure, which the effective pressure of viscous holographic Ricci dark energy is suitable to the sum of HRDE pressure and bulk viscosity.

The field equations of Brans-Dicke theory (2), for the metric (5) with the backing of equations (6) - (8) are

$$\frac{\ddot{B}}{B} + \frac{\ddot{C}}{C} + \frac{\dot{B}\dot{C}}{BC} + \frac{\omega\dot{\varphi}^2}{2\varphi^2} + \frac{\ddot{\varphi}}{\varphi} + \frac{\dot{B}\dot{\varphi}}{B\varphi} + \frac{\dot{C}\dot{\varphi}}{C\varphi} = -8\pi\varphi^{-1}\overline{p_h}, \tag{9}$$

$$\frac{\ddot{A}}{A} + \frac{\ddot{C}}{C} + \frac{\dot{A}\dot{C}}{AC} + \frac{\omega\dot{\varphi}^2}{2\varphi^2} + \frac{\ddot{\varphi}}{\varphi} + \frac{\dot{A}\dot{\varphi}}{A\varphi} + \frac{\dot{C}\dot{\varphi}}{C\varphi} = -8\pi\varphi^{-1}\overline{p_h} \tag{10}$$

$$\frac{\ddot{A}}{A} + \frac{\ddot{B}}{B} + \frac{\dot{A}\dot{B}}{AB} + \frac{\omega\dot{\varphi}^2}{2\varphi^2} + \frac{\ddot{\varphi}}{\varphi} + \frac{\dot{A}\dot{\varphi}}{A\varphi} + \frac{\dot{B}\dot{\varphi}}{B\varphi} - \frac{1}{A^2} = -8\pi\varphi^{-1}\overline{p_h} \tag{11}$$

$$\frac{\dot{A}\dot{B}}{AB} + \frac{\dot{B}\dot{C}}{BC} + \frac{\dot{C}\dot{A}}{CA} - \frac{\omega\dot{\varphi}^2}{2\varphi^2} + \frac{\dot{A}\dot{\varphi}}{A\varphi} + \frac{\dot{B}\dot{\varphi}}{B\varphi} + \frac{\dot{C}\dot{\varphi}}{C\varphi} - \frac{1}{A^2} = 8\pi\varphi^{-1}(\rho_m + \rho_h) \tag{12}$$

$$\frac{1}{A^2}\left(\frac{\dot{B}}{B} - \frac{\dot{A}}{A}\right) = 0 \tag{13}$$

$$\ddot{\varphi} + \dot{\varphi}\left(\frac{\dot{A}}{A} + \frac{\dot{B}}{B} + \frac{\dot{C}}{C}\right) = 8\pi(3 + 2\omega)^{-1}(\rho_m + \rho_h - 3\overline{p_h}) \tag{14}$$

$$\dot{\rho}_m + \dot{\rho}_h + 3H(\rho_m + \rho_h + \overline{p_h}) = 0 \tag{15}$$

3. HOLOGRAPHIC RICCI DARK ENERGY COSMOLOGICAL MODELS

From equation (13), we get $B = c_1 A$ without loss of generality, by taking $c_1 = 1$, we get

$$B = A. \tag{16}$$

The field equations (9) to (12) are four independent equations with six unknowns that are functions of 't': $B, C, \rho_m, \rho_h, \overline{P}_h \,\&\, \varphi$. Because these equations are very nonlinear, we use the following reasonable physical condition to obtain a deterministic result:

1. The connection between the scalar field φ and thus the average scale factor, a(t), is given by (Johri and Kalyani [50])

$$\varphi = a^m \tag{17}$$

where m is a constant.

2. The shear scalar is proportional to the expansion scalar, leading to the metric potentials relation (Collins et al. [51])

$$C = B^n \tag{18}$$

where *n* is an arbitrary constant.

3. We assume that the parameterized kind of Bulk viscosity is (Reng and Meng [52])

$$\varepsilon = \left(\varepsilon_1 + \varepsilon_2\left(\frac{\dot{a}}{a}\right) + \varepsilon_3\left(\frac{\ddot{a}}{\dot{a}}\right)\right), \tag{19}$$

where $\varepsilon_0, \varepsilon_1 \,\&\, \varepsilon_2$ are constants.

From equations (9) - (11), (17) and (18), we get

$$\frac{\ddot{B}}{B} - \frac{\ddot{C}}{C} + \frac{\dot{B}}{B}\left(\frac{\dot{B}}{B} - \frac{\dot{C}}{C}\right) + \frac{\dot{\varphi}}{\varphi}\left(\frac{\dot{B}}{B} - \frac{\dot{C}}{C}\right) - \frac{1}{B^2} = 0. \tag{20}$$

Using equations (17 & 18), From equation (20), we get

$$A = B = K\,Sinh(k_2 t + k_3), \tag{21}$$

$$C = [K\,Sinh(k_2 t + k_3)]^n. \tag{22}$$

From equations (17), (21) and (22), we get

$$\varphi = [K\,Sinh(k_2 t + k_3)]^{-(n+2)}. \tag{23}$$

where $K = \frac{1}{k_2\sqrt{n-1}}$, k_2 & k_3 are integrating constants
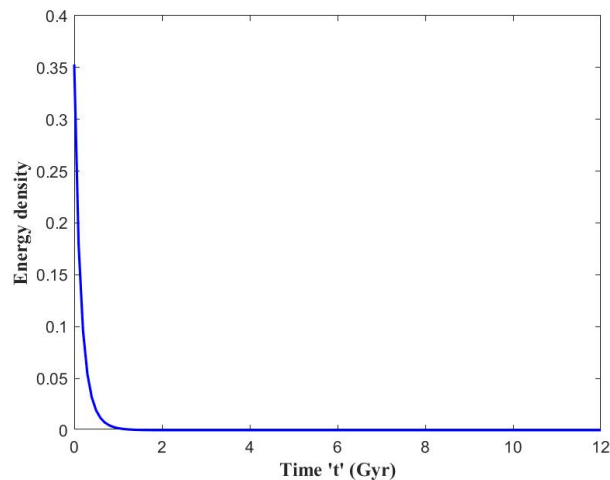
The Hubble parameter H is

$$H = \frac{1}{3}\left(\frac{2\dot{B}}{B} + \frac{\dot{C}}{C}\right) = \frac{(n+2)K_2}{3}\,Coth(k_2 t + k_3) \tag{24}$$

Now metric (5), with the assistance of metric potentials (21 & 22), are frequently written as

$$ds^2 = dt^2 - [K\,Sinh(k_2 t + k_3)]^2(dx^2 + e^{-2x}dy^2) - [K Sinh(k_2 t + k_3)]^{2n}dz^2 \tag{25}$$

The energy density of holographic Ricci dark energy within the universe could also be calculated using the equations (1) and (24) as

$$\rho_h = \frac{3k_2^2\varphi}{8\pi}\left[Coth^2(k_2 t + k_3)\left\{\frac{\varepsilon_0(n+2)^2}{9} - \frac{\eta(n+2)}{3} + 2\zeta\right\} + \frac{\eta(n+2)}{3} - 2\zeta\right] \tag{26}$$

Figure 1. Plot of energy density versus time for $k_2 = 1, k_3 = 0.85, n = 1.81, \varepsilon_0 = 1.015, \eta = 0.025$ *and* $\zeta = 0.15$

In terms of cosmic time 't', Fig. 1 describes the energy density of HRDE with bulk viscosity of our model. Throughout the development of the model, the energy density is positive. We also see that as cosmic time increases, the energy density ρ_h declines. As a result, we may infer that our model achieves the realistic energy requirements, $\rho_h \geq 0$.

We suppose that matter and viscous holographic dark energy factors interact minimally. Hence, they're conserved independently (Sarkar [53]). Therefore, as result of the conservation equation

$$\dot{\rho}_m + \left(\frac{\dot{A}}{A} + \frac{\dot{B}}{B} + \frac{\dot{C}}{C}\right)\rho_m = 0, \tag{27}$$

$$\dot{\rho}_m + \left(\frac{\dot{A}}{A} + \frac{\dot{B}}{B} + \frac{\dot{C}}{C}\right)(\rho_h + \overline{p_h}) = 0. \tag{28}$$

From eqs. (21), (22) and (27), we get the energy density of the matter is

$$\rho_m = k_1[K\,Sinh(k_2 t + k_3)]^{-(n+2)}, \tag{29}$$
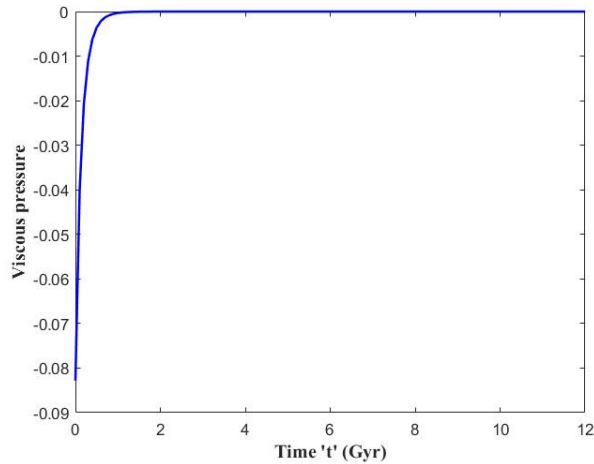
where k_1 is an integrating constant.

The coefficient of bulk viscosity is given by

$$\varepsilon = \varepsilon_1 + \varepsilon_2 \left[\left(\frac{k_2(n+2)}{3} \right) Coth(k_2 t + k_3) \right] + \varepsilon_3 \left[k_2 \left(\frac{(n-1)}{3} \right) Coth(k_2 t + k_3) + k_2 Tanh(k_2 t + k_3) \right]. \quad (30)$$

Using equations (21) – (23), we obtain the viscous pressure of the holographic Ricci dark energy as

$$\bar{P}_h = \frac{\varphi}{16\pi} [k_4 Coth^2(k_2 t + k_3) + k_5] \ , \quad (31)$$

where $k_4 = \left\{ \frac{1}{K^2} - (n+3)k_2 - k_2^2 [\omega(n+2)^2 - 2(3n+4) + 2(n+3)(n+2)] \right\}$
and $k_5 = \left\{ 2(n+2)k_2^2 - (n+3)k_2 - \frac{1}{K^2} \right\}$

Figure 2. Plot of viscous pressure versus time for $k_2 = 1, k_3 = 0.85, n = 1.81, \varepsilon_0 = 1.015, \eta = 0.025, w = -1.25 \ and \ \zeta = 0.15$

According to the graph of Fig. 2, the viscous pressure of the HRDE is constantly negative throughout the elaboration and rises with time. Based on the substantiation of the Universe's rapid expansion, it is generally allowed that some energy-matter causes this cosmic acceleration with negative pressure known as DE.

The pressure of the holographic Ricci dark energy as

$$P_h = \frac{\varphi}{16\pi} [k_4 Coth^2(k_2 t + k_3) + k_5] + k_2(n+2) \left\{ \varepsilon_1 Coth(k_2 t + k_3) + \frac{k_2}{3} Coth^2(k_2 t + k_3) [\varepsilon_2(n+2) + \varepsilon_3(n-1)] + \varepsilon_3 k_2 \right\} (32)$$

From equations (26) and (32), we obtain
The EoS parameter of the Ricci dark energy as

$$W_h = \frac{P_h}{\rho_h} = \frac{\frac{\varphi}{16\pi}[k_4 Coth^2(k_2 t + k_3) + k_5] + k_2(n+2)\{\varepsilon_0 Coth(k_2 t + k_3) + \frac{k_2}{3}Coth^2(k_2 t + k_3)[\varepsilon_1(n+2) + \varepsilon_2(n-1)] + \varepsilon_2 k_2\}}{\frac{3\varphi k_2^2}{8\pi}\left[Coth^2(k_2 t + k_3)\left\{\frac{\varepsilon_0(n+2)^2}{9} - \frac{\eta(n+2)}{3} + 2\zeta\right\} + \frac{\eta(n+2)}{3} - 2\zeta\right]}. \quad (32)$$
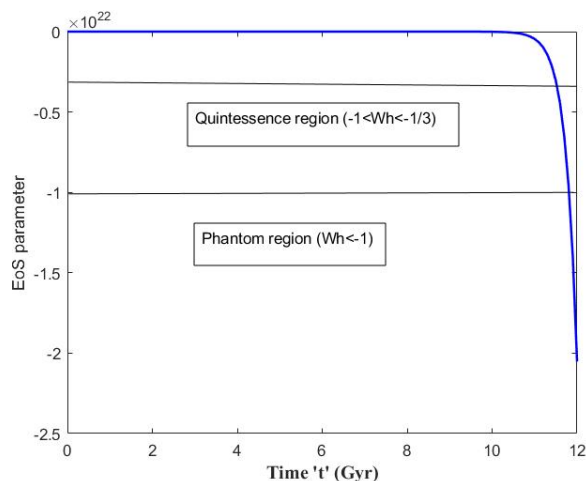
Figure 3. Plot of EoS parameter versus time for $k_2 = 1, k_3 = 0.85, n = 1.81, \varepsilon_0 = 1.015, \eta = 0.025, w = -1.25 \ and \ \zeta = 0.15$

The EoS parameter is defined as $w = p/\rho$, where p stands for pressure and ρ stands for energy density. Various EoS parameter values correlate to various epochs of the Universe's early decelerating and current accelerating expansion. The decelerating phase consists of stiff fluid ($w = 1$), radiation ($w = 1/3$), and matter-dominated (dust) ($w = 0$). The accelerating phase is made up of quintessence $-1 < w < -1/3$, the cosmological constant $w = -1$, and the phantom case, $w < -1$.

The above Fig.-3 illustrates the EoS parameter as a function of cosmic time (t). We see that at the very beginning of the cosmos, the EoS parameter $w_h > 0$. As a result, at early epochs of the Universe, the EoS parameter of HRDE with bulk viscosity may play a significant role in representing the initial stage matter-dominated era of the universe. It is discovered that the EoS parameter reaches zero at some point, implying that our model reflects a dusty universe. Meanwhile, the EoS parameter of HRDE with bulk viscosity acts like quintessence ($-1 < w_h < -1/3$) and phantom ($w_h < -1$), resulting in an accelerated expansion phase of the cosmos.

The coincident parameter is

$$r = \frac{\rho_h}{\rho_m} = \frac{\frac{3k_2^2\varphi}{8\pi}\left[Coth^2(k_2t+k_3)\left\{\frac{\varepsilon_0(n+2)^2}{9} - \frac{\eta(n+2)}{3} + 2\zeta\right\} + \frac{\eta(n+2)}{3} - 2\zeta\right]}{K_1[K\,inh(k_2t+k_3)]^{-(n+2)}} \tag{33}$$

4. SOME ESSENTIAL PROPERTIES OF THE MODEL

The spatial volume is

$$V = ABC = [K\,Sinh(k_2t + k_3)]^{(n+2)} \tag{34}$$
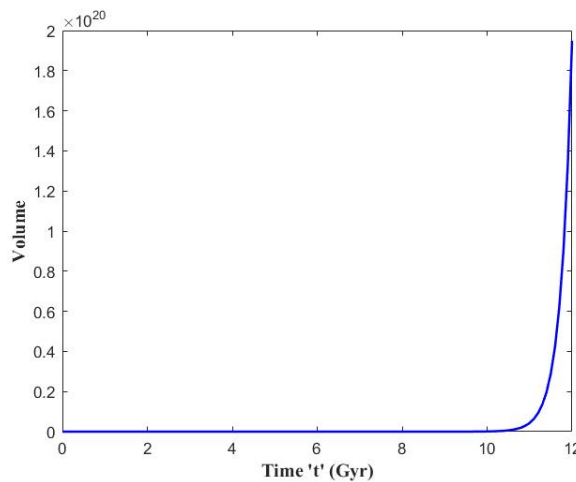
Figure 4. Plot of Volume versus time for $k_2 = 1, k_3 = 0.85\ \&\ n = 1.81$

Fig. 4 illustrates the volume concerning cosmic time. We can see that as the time 't' rises, the spatial volume 'V' increases and eventually becomes infinitely large, as displayed in the graph. It demonstrates that the cosmos expands as time goes.

The average scale factor is

$$a(t) = V^{1/3} = [K\,Sinh(k_2t + k_3)]^{(n+2)/3}. \tag{35}$$

For the flow vector u^i, the expansion and shear scalar expressions are calculated as

$$\theta = 3H = k_2(n + 2)Coth(k_2t + k_3). \tag{36}$$

$$\sigma^2 = \frac{7}{18}\theta^2 = \frac{7}{18}k_2^2(n + 2)^2Coth^2(k_2t + k_3) \tag{37}$$

Along the axes x,y, and z, the directional Hubble parameters H_1, H_2, and H_3 are given by

$$H_1 = H_2 = \frac{\dot{A}}{A} = \frac{\dot{B}}{B} = k_2Coth(k_2t + k_3), \tag{38}$$

$$H_3 = \frac{n\dot{B}}{B} = nk_2Coth(k_2t + k_3), \tag{39}$$

whereas the generalized Hubble parameter is given by

$$H = \frac{1}{3}\left(\frac{2\dot{A}}{A} + \frac{\dot{B}}{B}\right) = \frac{k_2(n+2)}{3}Coth(k_2t + k_3) \tag{40}$$
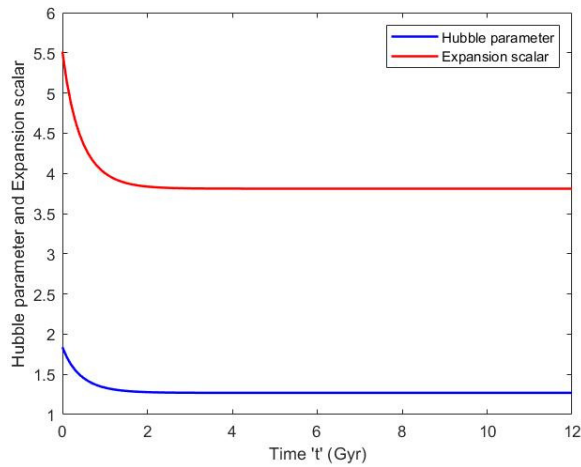
Figure 5. Plot of Hubble parameter & Expansion scalar versus time for $k_2 = 1, k_3 = 0.85$ & $n = 1.81$

The graph of Fig. 5 above depicts the variability of the Hubble parameter and the expansion scalar concerning cosmic time. These are two significant observable factors in cosmology that play an essential part in the Universe's expansion path. Both the expansion scalar graph and the Hubble parameter demonstrate that they are positive-valued, decreasing functions of cosmic time that approach zero over very long time periods. The Hubble parameter is generally known to be the rate of expansion of the Universe, and a measure of the fractional increase in the scale in unit time of the Universe. It is discovered that the expansion rate is quicker in the beginning and slower later on.

The average anisotropy parameter is defined by

$$A_m = \frac{1}{3}\sum_{i=1}^{3}\left(\frac{H_i - H}{H}\right)^2 = \frac{2(n-1)^2}{(2n+1)^2} \tag{41}$$

The deceleration parameter (DP) q is given by

$$q = -\frac{3\dot{\theta}}{\theta^2} - 1 = \frac{3}{(n+2)}Sech^2(k_2 t + k_3) - 1 \tag{42}$$
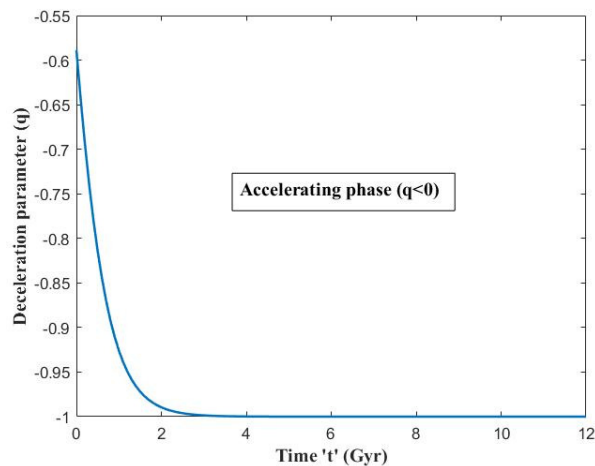
Figure 6. Plot of deceleration parameter versus time for $k_2 = 1, k_3 = 0.85, n = 1.81$

The model's acceleration or deceleration is determined by the sign of the deceleration parameter (DP) 'q'. A positive deceleration parameter (DP) 'q' value implies model slowdown, whereas a negative sign suggests model acceleration. Fig. 6, depicts the elaboration of the deceleration parameter following cosmic time. We discover that our model displays a Universe expansion phase. It can also be shown that the current value (i.e., at $t_o = 13.8\ Gyr$) of the deceleration parameter is $q_o = -1$, which is consistent with recent observations.

5. CONCLUSIONS

This study investigates the spatially homogeneous anisotropic Bianchi type-III cosmological model with bulk viscosity in the presence of pressure less matter and holographic Ricci dark energy in the Brans – Dicke theory of gravity.

It is essential to remember that physical volume increases with time. Fig. 4 illustrates the volume concerning cosmic time. We can see that as the time 't' increases, the spatial volume V increases and ultimately becomes infinitely large, as displayed in the graph. It demonstrates that the Universe expands as time goes. It is frequently seen that the above-mentioned physical parameters, such as θ, σ^2 and H of the model, acquire a constant value at late intervals. This indicates that the cosmos expands consistently. Fig.5 depicts the variability of the Hubble parameter and the expansion scalar concerning cosmic time. These are two significant observable factors in cosmology that play an essential part in the Universe's expansion path. The Hubble parameter and the expansion scalar graphs show that both are positive-valued decreasing functions of cosmic time that tend to zero over long time scales. The Hubble parameter is generally acknowledged as the rate of expansion of the Universe, and a measure of the fractional increase in the scale in unit time of the Universe. It is discovered that the expansion rate is faster in the beginning and slower later on. We can also see that as time increases, the energy density ρ_m of matter increases, and therefore the Ricci dark energy (RDE) density ρ_h decreases. In terms of cosmic time 't', fig. 1 describes the energy density of HRDE with the bulk viscosity of our model. Throughout the development of the model, the energy density is positive. We also see that as cosmic time increases, the energy density ρ_h decreases. As a result, we may infer that our model achieves the actual energy needs, $\rho_h \geq 0$. Figure-2 shows the viscous pressure of the HRDE is constantly negative throughout the elaboration and increases with time. Based on the substantiation of the Universe's rapid expansion, it is generally allowed that some energy-matter causes this cosmic acceleration with negative pressure known as DE. We will see that Ricci Dark Energy has a negative pressure during the Universe's development, suggesting that the Universe is expanding faster. In our model, the EoS parameter starts within the phantom area ($W_h << -1$) and crosses the phantom dividing line ($W_h = -1$). Within the region of quintessence, the model progressively approaches the constant value ($-1 < W_h < -1/3$). Fig.3 illustrates the EoS parameter as a function of cosmic time (t). We see that at the very beginning of the cosmos, the EoS parameter $w_h > 0$. As a result, at early epochs of the Universe, the EoS parameter of HRDE with bulk viscosity may play a significant role in representing the initial stage matter-dominated era of the Universe. It is discovered that the EoS parameter reaches zero at some point, implying that our model reflects a dusty Universe. Meanwhile, the EoS parameter of HRDE with bulk viscosity acts like quintessence ($-1 < w_h < -1/3$) and phantom ($w_h < -1$), resulting in an accelerated expansion phase of the cosmos. The model's acceleration or deceleration is determined by the sign of the deceleration parameter (DP) 'q'. A positive deceleration parameter (DP) 'q' value implies model slowdown, whereas a negative sign suggests model acceleration. Fig. 6, depicts the evolution of the deceleration parameter in accordance to cosmic time. We discovered that our model displays a Universe expansion phase. It can also be shown that the current value (i.e., at $t_o = 13.8\ Gyr$) of the deceleration parameter is $q_o = -1$, which is consistent with recent observations.

ORCID

K.V.S. Sireesha, https://orcid.org/0000-0002-9751-2787

REFERENCES
[1] S. Perlmutter, et al., Astrophys. J. **517,** 565 (1999). https://doi.org/10.1086/307221
[2] A.G. Riess, et al., Astrophys. J. **659,** 98 (2007). https://doi.org/10.1086/510378
[3] R. Amanullah, et al., Astrophys. J. **716,** 712 (2010). https://doi.org/10.1088/0004-637X/716/1/712
[4] A.G. Riess, et al., The Astronomical Journal, **116,** 1009 (1998). https://doi.org/10.1086/300499
[5] R. von Marttens et al., Physics of the Dark Universe, **28,** 100490 (2020). https://doi.org/10.1016/j.dark.2020.100490
[6] S.M. Carroll, et al., Living Rev. Relativ. **4,** 1 (2001). https://doi.org/10.12942/lrr-2001-1
[7] T. Padmanabhan, Phys. Rep. **380,** 235 (2003). https://doi.org/10.1016/S0370-1573(03)00120-0
[8] T. Padmanabhan, Phys. Rev. D, **66,** 02131 (2002). https://doi.org/10.1103/PhysRevD.66.021301
[9] T. Padmanabhan, Gen. Relativ. Gravit. **40,** 529 (2008). https://doi.org/10.1007/s10714-007-0555-7
[10] M. Bento, O. Bertolami, and A.A. Sen, Phys. Rev. D, **66,** 043507 (2002). https://doi.org/10.1103/PhysRevD.66.043507
[11] R.R. Caldwell, Phys. Lett. B, **545,** 23 (2002). https://doi.org/10.1016/S0370-2693(02)02589-3
[12] S. Nojiri, and S.D. Odintsov, Phys. Rev. D, **562,** 147 (2003). https://doi.org/10.1016/S0370-2693(03)00594-X
[13] B. Feng, et al., Phys. Lett. B, **607,** 35 (2005). https://doi.org/10.1016/j.physletb.2004.12.071
[14] A.Y. Kamenshchik et al., Phys. Lett. B, **511,** 265 (2001). https://doi.org/10.1016/S0370-2693(01)00571-8
[15] M.C. Bento et al., Phys. Rev. D, **66,** 043507 (2002). https://doi.org/10.1103/PhysRevD.66.043507
[16] V. Sahni, and Y. Shtanov, J. Cosmol, Astropart. Phys. **11,** 014 (2003). https://doi.org/10.15407/ujpe57.12.1257
[17] C. Brans, and R.H. Dicke, Phys. Rev. **124,** 925 (1961). https://doi.org/10.1103/PhysRev.124.925
[18] S.D.H. Hsu, Phys. Lett. B, **594,** 13 (2004). https://doi.org/10.1016/j.physletb.2004.05.020
[19] R.G. Cai, Phys. Lett. B, **657,** 228 (2007). https://doi.org/10.1016/j.physletb.2007.09.061
[20] S. Nojiri, and S.D. Odintsov, Phys. Rev. D, **68,** 123512 (2003). https://doi.org/10.1103/PhysRevD.68.123512
[21] S. Capozziello, and M. De Laurentis, Physics Reports, **509**(4-5), 167 (2011). https://doi.org/10.1016/j.physrep.2011.09.003
[22] T. Harko, et al., Phys. Rev. D, **84,** 024020 (2011). https://doi.org/10.1103/PhysRevD.84.024020
[23] G. Hoof't, https://doi.org/10.48550/arXiv.gr-qc/9310026
[24] A. Cohen, et al., Phys. Rev. Lett. **82,** 4971 (1999). https://doi.org/10.1103/PhysRevLett.82.4971

[25] M. Li, Phys. Lett. B, **603**, 1 (2004). https://doi.org/10.1016/j.physletb.2004.10.014
[26] C. Gao et al., Phys. Rev. D, **79**, 043511 (2009). https://doi.org/10.1103/PhysRevD.79.043511
[27] L.N. Granda, and A. Oliveros, Phys. Lett. B, **669**, 275 (2008). https://doi.org/10.1016/j.physletb.2008.10.017
[28] L.N. Granda, and A. Oliveros, Phys. Lett. B, **671**, 199 (2009). https://doi.org/10.1016/j.physletb.2008.12.025
[29] S. Chen, and J. Jing, Phys. Lett. B, **679**, 144 (2009). https://doi.org/10.1016/j.physletb.2009.07.018
[30] K.V.S. Sireesha, and V.U.M. Rao, Journal of Physics: Conf. Series, **1344,** 012028 (2019). https://doi.org/10.1088/1742-6596/1344/1/012028
[31] C.J. Feng, Phys. Lett. B, **670,** 231 (2008). https://doi.org/10.1016/j.physletb.2008.11.005
[32] M. Bouhmadi-Lo´pez, and Y. Tavakoli, Phys. Rev. D, **87,** 023515 (2013). https://doi.org/10.1103/PhysRevD.87.023515
[33] M. Suwa, et al., J. Mod. Phys., **6,** 327 (2015). http://dx.doi.org/10.4236/jmp.2015.63035
[34] S. Ghaffari, et al., Phys. Rev. D, **91,** 023007 (2015). https://doi.org/10.1103/PhysRevD.91.023007
[35] C.W. Misner, Nature, **214,** 40 (1967). https://doi.org/10.1038/214040a0
[36] C.W. Misner, Astrophys. J., **151**, 431 (1968). https://doi.org/10.1086/149448
[37] V.U.M. Rao, et al., Iran. J. Phys. Res. **18**, 3 (2018). https://doi.org/10.29252/ijpr.18.3.497
[38] Chakraborty, et al., https://arxiv.org/abs/2006.07142v1
[39] C.L. Bennett, C.L. Astron, et al., The Astrophysical Journal Supplement Series, **148**, 97 (2003). https://doi.org/10.1086/377253
[40] O. Akarsu, and C.B. Kilinc, Astrophys. Space Sci. **326**, 315 (2010). https://doi.org/10.1007/s10509-009-0254-9
[41] M. Koussour, S.H. Shekh, and M. Bennai, https://doi.org/10.1016/j.dark.2022.101051(2022).
[42] M. Koussour, K.E. Bourakadi, S.H. Shekh, S.K. Pacif, and M. Bennai, https://doi.org/10.1016/j.aop.2022.169092
[43] R.V. Wagoner, Phys. Rev. D, **1**, 3209 (1970). https://doi.org/10.1103/PhysRevD.1.3209
[44] V.U.M. Rao, and K.V.S. Sireesha, Eur. Phys. J. Plus, **127,** 33 (2012). https://doi.org/10.1140/epjp/i2012-12033-y
[45] V.U.M. Rao, and K.V.S. Sireesha, Int. J. Theor. Phys. **51,** 3013 (2012). https://doi.org/10.1007/s10773-012-1183-x
[46] V.U.M. Rao, et al., Prespacetime Journal, **7,** 520 (2016).
[47] K.D. Naidu, et al., Eur. Phys. J. Plus, **133,** 303 (2018). https://doi.org/10.1140/epjp/i2018-12139-2
[48] N.S. Rani, et al., Journal of Physics : Conf. Series, **1344,** 012045 (2019). https://doi.org/10.1088/1742-6596/1344/1/012045
[49] K.V.S. Sireesha, and V.U.M. Rao, The African Review of Physics, **14,** 0010 (2019). http://lamp.ictp.it/index.php/aphysrev/article/viewFile/1692/605
[50] V.B. Johri, and K. Desikan, Gen. Relat. Gravit. **26,** 1217 (1994). https://doi.org/10.1007/BF02106714
[51] C.B. Collins, et al., Gen. Relativ. Gravit. **12,** 805 (1980). https://doi.org/10.1007/BF00763057
[52] J. Ren, and X.H. Meng, Int. J. Mod. Phys. D, **16,** 1341 (2007). https://doi.org/10.1142/S0218271807010821
[53] S. Sarkar, Astrophys. Space. Sci. **349,** 985 (2014). https://doi.org/10.1007/s10509-013-1684-y

В'ЯЗКА ГОЛОГРАФІЧНА КОСМОЛОГІЧНА МОДЕЛЬ ТЕМНОЇ ЕНЕРГІЇ РІЧІ ТИПУ Б'ЯНКІ III В ТЕОРІЇ ГРАВІТАЦІЇ БРЕНСА-ДІКЕ

П.Е. Сатьянараяна, К.В.С. Сіріша
Департамент математики, ГІС, GITAM вважається університетом, Вісакхапатнам, Індія

У цій роботі досліджується та розглядається широкий спектр знахідок, пов'язаних з описом голографічної темної енергії Річчі (HRDE) з об'ємною в'язкістю в рамках прискореного розширення Всесвіту в пізній час у рамках анізотропної космологічної моделі Б'янкі типу III із вмістом матерії без тиску. в теорії гравітації Бренса-Дікке. Ми використовуємо співвідношення між метричними потенціалами, щоб отримати точний висновок рівнянь поля, що призводить до швидкого розширення. Щоб дослідити фізичну поведінку нашої моделі темної енергії, використовуються кілька основних космологічних параметрів, включаючи Хаббла, уповільнення, щільність енергії матерії, щільність темної енергії Річчі (RDE) і рівняння стану (EoS). Використовуючи поточні космологічні спостереження, ми виявили деяку в'язкість голографічної моделі темної енергії Річчі. Ми описуємо, як фізичні та геометричні властивості моделей сумісні з останніми компіляціями.

Ключові слова: *метрика Б'янкі III типу; голографічна темна енергія Річчі (HRDE); об'ємна в'язкість; теорія Бренса-Дікке*

EFFECTIVE SEMICLASSICAL EVOLUTION OF BOSE EINSTEIN CONDENSATES

 Hector Hernandez-Hernandez

Facultad de Ingenieria, Universidad Autonoma de Chihuahua, Mexico
*Corresponding Author e-mail: hhernandez@uach.mx

In this work we analyze the effective evolution of a one dimensional Bose-Einstein Condensate (BEC) within a semiclassical description of quantum systems based on expectation values of quantum dispersions and physical observables, known as momentous quantum mechanics. We show that the most prominent features and physical parameters of the system can be determined from the dynamics of the corresponding semiclassical system, consisting of an extended phase space including original classical observables and quantum dispersions, and we also show that particle trajectories for expectation values of observables are a particular characteristic in this framework. We also demonstrate that interactions with several potentials can be implemented in an intuitive way.

Keywords: *Effective quantum mechanics; Bose-Einstein condensate; Semiclassical evolution*

PACS: 03.75.Kk, 03.75.Lm

1. INTRODUCTION

Around 100 years ago, Einstein and Bose made a groundbreaking prediction that a system of noninteracting bosons, under certain conditions, would undergo a phase transition to a state with a macroscopic population in the ground state, even at finite (low) temperatures [1]. This remarkable phenomenon, known as Bose-Einstein condensation (BEC), has since captured the attention of the physics community, and has laid the foundation for exploring the quantum world on a macroscopic scale. However, it was only in recent years that experimental techniques, such as laser and evaporative cooling [2], and the development of novel traps [3], have allowed for the unambiguous observation of BEC in weakly interacting atomic Bose gases within laboratory settings [4].

On the theoretical front, the dynamics of dilute trapped Bose-Einstein gases have been effectively described by mean-field theories, with the Gross-Pitaevskii equation (GPE), a nonlinear Schrödinger equation (NLSE), proving to be a highly accurate representation of the BEC ground state and its excitation spectrum at or near absolute zero temperature [5]. Most theoretical work has primarily focused on the Thomas-Fermi limit, where the nonlinearity of the GPE dominates the bare trap excitation energies, corresponding to situations with a large number of particles [6]. Yet, the NLSE and GPE have also found applications beyond the realm of BEC, with the NLSE appearing in various fields such as optics, acoustics, and materials science [5]. In particular, the NLSE serves as a universal equation in three-dimensional problems, where analytical solutions are challenging, and numerical simulations typically demand substantial computational resources. An effective approach to the study of such systems could offer a powerful method for gaining valuable insights into the behavior of BEC models.

Effective techniques in quantum mechanics enable us to approximate solutions for complex systems. Notably, the momentous quantum mechanics formulation transforms a quantum system into a semiclassical counterpart, where the system's dynamics are determined via an effective-semiclassical Hamiltonian [7]. This method reintroduces the concept of particle trajectories, which is absent in traditional quantum mechanics. These trajectories depict the evolution of expectation values of position and momentum operators, and of quantum dispersions as well, obtained as an average of these values across an infinite number of quantum ensembles. This interpretation is akin to the evolution obtained in the Bohm description of quantum mechanics [9]. The versatility of this approach has made it applicable to the study of a wide range of quantum systems, spanning from relatively simple models such as quantum tunneling [10] to more intricate models within the domain of quantum cosmology.

In this work we explore a semiclassical analysis of a Bose-Einstein condensate in one dimension, attempting to bridge the gap between the theoretical foundations of BEC, the NLSE, and the practical applications of these principles in quantum physics and beyond.

As experimental advances continue to unlock new possibilities for the study of BEC, it is crucial to investigate the collective dynamics of these macroscopic ensembles, particularly in the context of one-dimensional systems. Our analysis aims to provide valuable insights and analytical solutions that complement numerical

studies, further enhancing our understanding of BEC and its broader implications in various domains of physics and engineering.

2. THE GROSS-PITAEVSKII EQUATION AS A NLSE

In this first approach we analyze a one dimensional BEC as a semiclassical system, for which we obtain its dynamical evolution, displaying the effectiveness of the method, and discuss the broad spectrum of generalizations to more complex systems, including higher dimensional ones. This section follows closely [11].

We start considering a gas of bosons with a fixed average number of particles, N, confined by a potential well trap. The ground state of N noninteracting bosons confined by the potential is obtained by putting all the particles in their lowest energy state, its normalized single-particle wave function is

$$\psi_0 = \left(\frac{m\omega}{\pi\hbar}\right)^{1/4} e^{\frac{-m\omega}{2\hbar}x^2}. \tag{1}$$

The density distribution is $n(x) = N|\psi_o|^2$. At finite temperatures, there are particles occupying the lowest energy level (condensate), for which we require their occupation number to be large and close to the total number N, and others occupying higher levels (thermal component) N_T, so the condition for BEC occurrence is then $N_T < N$, satisfied for T sufficiently small. The critical temperature at which this happens is

$$k_B T_c = 0.94\hbar\omega n^{1/3}. \tag{2}$$

Typical values of these parameters in available experiments are $N \sim 10^4 - 10^7$, and $T_c \sim (10^2 - 10^3)$nK, values very well in agreement with experimental results.

Non-interacting boson particles are well described by the expressions above, and have also been corroborated by experiments [12]. However, this non-interacting picture is simplistic: the gas in this case has infinite compressibility, and one would expect interaction between the particles to drastically change its behavior, even for very dilute samples. Therefore, and interacting system should be considered, and the conditions under which Bose-Einstein condensation is attained further studied.

The dynamic of a gas of interacting boson particles is well described by the NLSE, the Gross-Pitaevskii equation or GPE [11]

$$i\hbar\frac{\partial\psi}{\partial t} = \left[-\frac{\hbar^2}{2m}\nabla^2 + V_{\text{ext}}(\mathbf{r}) + g|\psi|^2\right]\psi \tag{3}$$

where

$$g = \frac{4\pi\hbar^2 a}{m} \tag{4}$$

modulates the interaction and is defined in terms of the ground-state scattering length a. N is fixed from the normalization condition for its macroscopic wave function $N = \int \psi^2 d^3\mathbf{r}$. We will consider a harmonic trapping potential V_{ext}.

We will analyze the evolution of this macroscopic system under an effective description, under the physical conditions discussed above, and the average distance between particles much larger than the scattering length a.

For a one dimensional BEC, in eq. (3) we take $\nabla \to \frac{\partial}{\partial x}$. Several methods and analysis were implemented over the past years attempting to solve, analytically, approximately and numerically the GP equation, in 1, 2 and 3 dimensions, for harmonic and more general potentials (Thomas-Fermi limit [6], numerical [13], variational analytical [14]). We describe now the momentous quantum mechanics method.

3. EFFECTIVE DESCRIPTION OF BOSE-EINSTEIN CONDENSATES
3.1. Momentous quantum mechanics

Momentous quantum mechanics is an effective formulation describing the semiclassical evolution of quantum systems provided by a Hamiltonian defined in an extended phase space, with expectation values of observables and quantum dispersions as classical variables [7]. The dynamical system so obtained has (in general) an infinite number of degrees of freedom. Expectation values of quantum dispersion (termed "quantum variables"), for one degree of freedom, are defined as follows

$$\Delta(x^a p^b) = \langle(\hat{x} - x)^a(\hat{p} - p)^b\rangle_{\text{Weyl}}. \tag{5}$$

where $p = \langle\hat{p}\rangle, q = \langle\hat{q}\rangle$, and Weyl refers to a totally symmetrical ordering. Similar expressions apply for more than one degree of freedom.

The quantum effective Hamiltonian, defined as $H_Q = \langle \hat{H} \rangle$, is given explicitly as

$$H_Q = H(x,p) + \sum_{n=2}^{\infty} \sum_{a=0}^{n} \frac{1}{n!} \binom{n}{a} \frac{\partial^n H(x,p)}{\partial x^a \partial p^{n-a}} \Delta(x^a p^{n-a}). \tag{6}$$

$H(q,p)$ is the corresponding classical Hamiltonian of the system. The semiclassical dynamics can be obtained from the Hamiltonian (6) in the usual way, that is, $\dot{f} = \{q, H\}$, and for quantum variables we use $i\hbar \{q, H\} = \left\langle \left[\hat{q}, \hat{H} \right] \right\rangle$.

This formulation for the effective dynamics is valid for general quantum systems, even for those that cannot be expressed with the usual kinetic and potential terms for the Hamiltonian, that is, $H = K + U$, although one may need to implement consistent truncations to the series for complex systems, as we show below. There is an alternate description in terms of canonical Casimir-Darboux variables [8].

The variables defined in (5) are not canonical order by order in the Hamiltonian (6). It is possible to get a canonical pair of variables, and a Darboux Casimir, for one degree of freedom, by means of the following transformation

$$s = \sqrt{\Delta(x^2)}, \quad p_s = \frac{\Delta(xp)}{\sqrt{\Delta(p^2)}}, \quad U = \Delta(x^2)\Delta(p^2) - \Delta(xp)^2, \tag{7}$$

for which we get $\{s, p_s\} = 1$, and $\{s, U\} = \{p_s, U\} = 0$.

Even more, under general arguments it can be shown that all the relevant qantum information in the system can be obtained from the canonical variable s, and the effective Hamiltonian can be written in the following way

$$H_Q(x,s) = \frac{p^2 + p_s^2}{2m} + V_{\text{eff}}(x,s), \tag{8}$$

where the effective, all-order potential is

$$V_{\text{eff}} = \frac{U}{2ms^2} + \frac{1}{2}[V(x+s) + V(x-s)], \tag{9}$$

where $V(x)$ is the classical interaction potential.

In this way we can generate the dynamics from this canonical effective Hamiltonian and its correspondent all-order potential in the usual way. We will analyze the effective quantum evolution for the BEC under both schemes described above.

3.2. Effective GPE

The prescription to obtain the quantum Hamiltonian described above can be implemented for the one-dimensional GPE (3). Particularly, since this is a non-linear Schrödinger equation, we can deduce the corresponding classical Hamiltonian in the following way

$$\begin{aligned} \hat{H} &\equiv -\frac{\hbar^2}{2m}\nabla^2 + V_{ext}(x) + g|\psi|^2 \rightarrow \\ H_{\text{class}} &\equiv \frac{p^2}{2m} + V_{ext}(x) + g|\psi|^2, \end{aligned} \tag{10}$$

considering the term $g|\psi|^2$ in H_Q as part of the effective interacting potential, as we will describe below.

By far, the most interesting trapping potential V_{ext} is harmonic, since it represents the most common experimental implementation for BEC's, and we will use this in the following.

As for the interpretation of the interacting, non-linear potential $\psi(x,t)$ at the classical level, we point out that the *classical* system is a starting reference upon which the effective analysis will be built, although its energy may be taken from experimental settings. The bridge between these two regimes, the quantum and the classical, is the wave function for the non interacting boson gas discussed in section 2, so we propose considering a generic squeezed coherent state of the form

$$\psi(x,t) = \frac{1}{(2\pi\rho^2)^{1/4}} \exp\left[-\frac{\alpha}{4\rho^2}(x - \langle x \rangle)^2 + ip(x - \langle x \rangle)\right]. \tag{11}$$

with $\alpha = 1 - i\langle \Delta x \Delta p + \Delta p \Delta x \rangle$. From this the interacting potential reads (taking $\langle x \rangle = 0$)

$$g|\psi|^2 = \frac{g}{(2\pi\rho^2)^{1/2}} \exp\left[-\frac{(x - \langle x \rangle)^2}{2\rho^2}\right] = \frac{g}{(2\pi\rho^2)^{1/2}} \exp\left[-\frac{x^2}{2\rho^2}\right]. \tag{12}$$

One can see this already at second order because there are three quantum variables, and they cannot conform a canonical system.

The classical Hamiltonian (10) then reads

$$H(x,p) = \frac{p^2}{2m} + \frac{1}{2}m\omega^2 x^2 + \frac{ge^{-\frac{x^2}{2\rho^2}}}{(2\pi\rho^2)^{1/2}}. \tag{13}$$

We can determine the behavior of the 1 dimensional BEC as if it were a classical particle, driven by (13). In fig. (1) we show the "classical potential", and in fig. (2) the corresponding semiclassical trajectories, a particularly interesting feature of our effective treatment. The classical BEC particle is trapped inside the potential, and is confined in the right (left) valley, or the harmonic trap, depending on whether its energy E is greater or less than the local potential maximum $\frac{a\hbar^2}{m\rho}$.

(a) Classical potential for a=10

(b) Classical potential as a function of x and a.
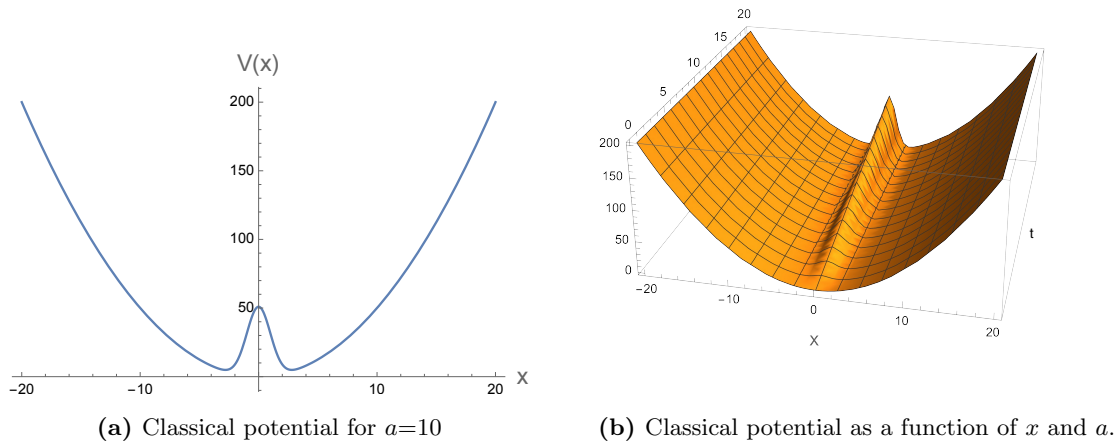
Figure 1. Classical potential for the 1 dimensional BEC in a harmonic trap

(a) Classical trajectory for $E \geq \frac{a\hbar^2}{m\rho}$

(b) Classical trajectory for $E \leq \frac{a\hbar^2}{m\rho}$
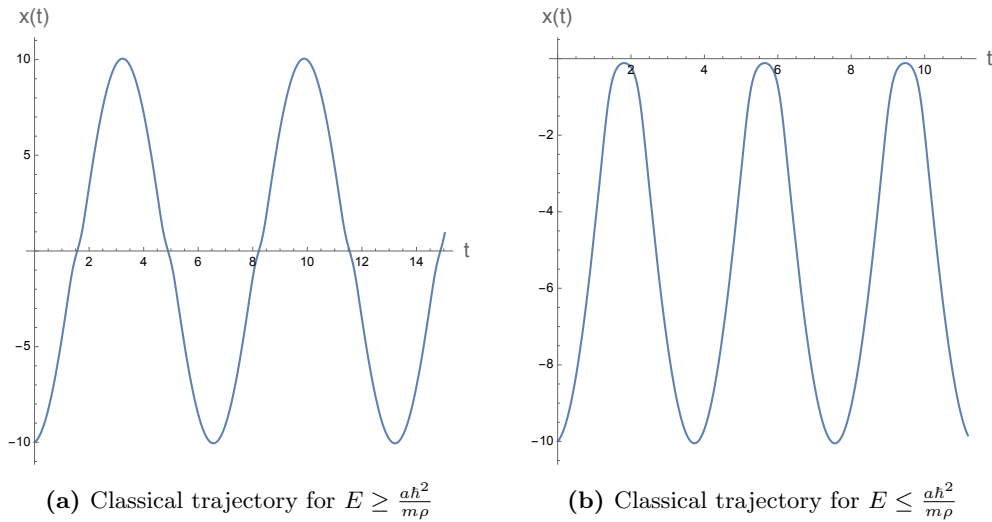
Figure 2. Classical trajectories for the 1 dimensional BEC in a harmonic trap.

The classical Hamiltonian (13) shows the kinetic and potential terms, a form suited for the momentous effective treatment. We discuss the evolution in two parts: one where ρ varies slowly and can be treated as a constant, and the general case.

4. EFFECTIVE EVOLUTION

We proceed to analyze the effective evolution for the BEC system, both in the order by order and the canonical descriptions.

As was discussed in the previous sections, the macroscopic quantum evolution of the condensate for non interacting particles ($g = 0$) can be determined from its wave function, which has an analytic expression given in (1); values of physical observables can be readily obtained. On the other hand, momentous quantum mechanics determines the dynamical evolution of expectation values of observables as a function of time: the macroscopic evolution of the BEC can be interpreted as an effective particle governed, at the quantum level, by the GPE (3).

For the effective quantum description of the general interacting picture we make use of the non interacting behavior, by choosing initial values of classical and quantum (dispersions) variables from their corresponding values of the later. That is, we use the expectation values obtained from the ideal BEC, and experimental parameters employed in the obtention of the condensate, as initial values for the evolution of the full quantum effective system. That is, we take $f(0) = <\hat{f}>_0$, for classical and quantum variables.

The total energy, described by the three terms in the Hamiltonian (10), $E = E_{\text{kin}} + E_{\text{ho}} + E_{\text{int}}$ (kinetic, harmonic and interacting components), is restricted by the virial relation [11]

$$0 = 2E_{\text{kin}} - 2E_{\text{ho}} + 3E_{\text{int}}. \tag{14}$$

Again, the initial values for each one of the components are obtained from the non interacting system. In this way, we can determine the effective dynamical evolution of the interacting BEC, as we show below.

4.1. Constant variance ρ

4.1.1. Second order system. As we mentioned above, we analyze first the case where ρ is slowly varying, for which it can be considered constant. ρ is the width of the distribution, so slow variation would represent the period of time during which stable evolution is attained, before the colapse and revival of the matter wave [15]. Its value can be controlled in experimental settings.

The effective Hamiltonian (6), together with (13) reads in this case

$$H_Q = \quad \frac{p^2}{2m} + \frac{1}{2}m\omega^2 x^2 + \frac{ge^{-\frac{x^2}{2\rho^2}}}{(2\pi\rho^2)^{1/2}} + \frac{\Delta(p^2)}{2m} + \frac{1}{2}m\omega^2\Delta(x^2) +$$
$$+ \quad \frac{ge^{-\frac{x^2}{2\rho^2}}}{(2\pi\rho^2)^{1/2}} \sum_{n=2}^{\infty} \frac{1}{n!}\left(-\frac{1}{\sqrt{2}\rho}\right)^n H_n\left(\frac{x}{\sqrt{2}\rho}\right)\Delta(x^n), \tag{15}$$

where $H_n(z)$ is the Hermite polynomial of degree n. As can be seen in this expression, the total Hamiltonian has an infinite number of terms, rendering an impossible system to treat in full, so we truncate the series to lowest orders in dispersions.

The Hamiltonian H_Q up to second order in momenta is

$$H_Q = \quad \frac{p^2}{2m} + \frac{1}{2}m\omega^2 x^2 + \frac{ge^{-\frac{x^2}{2\rho^2}}}{(2\pi\rho^2)^{1/2}}$$
$$+ \quad \frac{\Delta(p^2)}{2m} + \frac{\Delta(x^2)}{2}\left\{m\omega^2 + \frac{ge^{-\frac{x^2}{2\rho^2}}}{(2\pi\rho^2)^{1/2}}\left(\frac{x^2}{\rho^4} - \frac{1}{\rho^2}\right)\right\}. \tag{16}$$

Equations of motion for classical variables follow

$$\dot{x} = \frac{p}{m},$$
$$\dot{p} = -m\omega^2 x + \frac{ge^{-\frac{x^2}{2\rho^2}}}{(2\pi\rho^2)^{1/2}}\left\{\frac{x}{\rho^2} + \frac{\Delta(x^2)}{2}\left(\frac{x^3}{\rho^6} - \frac{3x}{\rho^4}\right)\right\}, \tag{17}$$

whereas for quantum variables [16]) we get

$$\frac{\mathrm{d}\Delta(x^2)}{\mathrm{d}t} = 2\frac{\Delta(xp)}{m},$$

$$\frac{\mathrm{d}\Delta(xp)}{\mathrm{d}t} = \frac{\Delta(p^2)}{m} - \Delta(x^2)\left\{m\omega^2 + \frac{ge^{-\frac{x^2}{2\rho^2}}}{(2\pi\rho^2)^{1/2}}\left(\frac{x^2}{\rho^4} - \frac{1}{\rho^2}\right)\right\},$$

$$\frac{\mathrm{d}\Delta(p^2)}{\mathrm{d}t} = -2\Delta(xp)\left\{m\omega^2 + \frac{ge^{-\frac{x^2}{2\rho^2}}}{(2\pi\rho^2)^{1/2}}\left(\frac{x^2}{\rho^4} - \frac{1}{\rho^2}\right)\right\}. \tag{18}$$

4.1.2. Canonical system. Now, for the canonical formulation (8) the effective Hamiltonian (13) reads

$$H_Q(x,s) = \frac{p^2 + p_s^2}{2m} + \frac{U}{2ms^2} + \frac{1}{2}m\omega^2(x^2 + s^2) + \frac{ge^{-\frac{(x^2+s^2)}{2\rho^2}}}{(2\pi\rho^2)^{1/2}}\cosh\left(\frac{xs}{\rho^2}\right). \tag{19}$$

The corresponding equations of motion are as follows

$$
\begin{aligned}
\dot{x} &= \frac{p}{m}, \\
\dot{s} &= \frac{p_s}{m}, \\
\dot{p} &= -m\omega^2 x - \frac{ge^{-\frac{x^2+s^2}{2\rho^2}}}{\rho^2(2\pi\rho^2)^{1/2}}\left[s\sinh\left(\frac{xs}{\rho^2}\right) - x\cosh\left(\frac{xs}{\rho^2}\right)\right], \\
\dot{p_s} &= \frac{U}{ms^3} - m\omega^2 s - \frac{ge^{-\frac{x^2+s^2}{2\rho^2}}}{\rho^2(2\pi\rho^2)^{1/2}}\left[x\sinh\left(\frac{xs}{\rho^2}\right) - s\cosh\left(\frac{xs}{\rho^2}\right)\right].
\end{aligned}
\tag{20}
$$

4.2. General variance $\rho^2 = \Delta(x^2)$

For the general case for which ρ is dynamical we need to modify the dynamics obtained in the previous section. Though more general, it is interesting to contrast this evolution with the one in the previous subsection, to determine under which regimes, or parameter values, the constant variance analysis is sufficient.

4.2.1. Second order system In this case, where $\rho^2 = \Delta(x^2)$, the Hamiltonian (13) gives the effective Hamiltonian, up to second order in momenta

$$
\begin{aligned}
H_Q = \quad & \frac{p^2}{2m} + \frac{1}{2}m\omega^2 x^2 + \frac{ge^{-\frac{x^2}{2\Delta(x^2)}}}{[2\pi\Delta(x^2)]^{1/2}} \\
+ \quad & \frac{\Delta(p^2)}{2m} + \frac{\Delta(x^2)}{2}\left\{m\omega^2 + \frac{ge^{-\frac{x^2}{2\Delta(x^2)}}}{[2\pi\Delta(x^2)]^{1/2}}\left(\frac{x^2}{\Delta(x^2)^2} - \frac{1}{\Delta(x^2)}\right)\right\},
\end{aligned}
\tag{21}
$$

or

$$H_Q = \frac{p^2 + \Delta(p^2)}{2m} + \frac{m\omega^2}{2}\left[x^2 + \Delta(x^2)\right] + \frac{ge^{-\frac{x^2}{2\Delta(x^2)}}}{2[2\pi\Delta(x^2)]^{1/2}}\left(1 + \frac{x^2}{\Delta(x^2)}\right). \tag{22}$$

Equations of motion for classical variables are

$$
\begin{aligned}
\dot{x} &= \frac{p}{m}, \\
\dot{p} &= -m\omega^2 x + \frac{ge^{-\frac{x^2}{2\Delta(x^2)}}}{2[2\pi\Delta(x^2)]^{1/2}}\left(\frac{x^3}{\Delta(x^2)^2} - \frac{x}{\Delta(x^2)}\right),
\end{aligned}
\tag{23}
$$

while for quantum variables read

$$\frac{d\Delta(x^2)}{dt} = 2\frac{\Delta(xp)}{m},$$

$$\frac{d\Delta(xp)}{dt} = \frac{\Delta(p^2)}{m} - m\omega^2\Delta(x^2) + \frac{ge^{-\frac{x^2}{2\Delta(x^2)}}}{2[2\pi\Delta(x^2)]^{1/2}}\left\{1 - \frac{x^2}{\Delta(x^2)^{1/2}} + x^2\left(\frac{3}{\Delta(x^2)} - \frac{x^2}{\Delta(x^2)^2}\right)\right\},$$

$$\frac{d\Delta(p^2)}{dt} = -2m\omega^2\Delta(xp) + \frac{ge^{-\frac{x^2}{2\Delta(x^2)}}}{[2\pi\Delta(x^2)]^{1/2}}\left\{\frac{\Delta(xp)}{\Delta(x^2)} + 2x^2\frac{\Delta(xp)}{\Delta(x^2)^2} - x^4\frac{\Delta(xp)}{\Delta(x^2)^3}\right\}. \tag{24}$$

Equations of motion for higher order truncations can be readily obtained. In the appendix we show the third order system for general ρ.

4.2.2. Canonical system for general variance Since, from (7) we have $\rho^2 = \Delta(x^2) = s^2$, the canonical all-order Hamiltonian (19) is now

$$H_Q(x,s) = \frac{p^2 + p_s^2}{2m} + \frac{U}{2ms^2} + \frac{1}{2}m\omega^2(x^2 + s^2) + \frac{ge^{-\frac{(x^2+s^2)}{2s^2}}}{(2\pi s^2)^{1/2}} \cosh\left(\frac{x}{s}\right). \quad (25)$$

It is evident that the equations of motion for this case will be modified. We get

$$\begin{aligned}
\dot{x} &= \frac{p}{m}, \\
\dot{s} &= \frac{p_s}{m}, \\
\dot{p} &= -m\omega^2 x - \frac{ge^{-\frac{(x^2+s^2)}{2s^2}}}{(2\pi)^{1/2}s^3}\left[s\sinh\left(\frac{x}{s}\right) - x\cosh\left(\frac{x}{s}\right)\right], \\
\dot{p_s} &= \frac{U}{ms^3} - m\omega^2 s - \frac{ge^{-\frac{(x^2+s^2)}{2s^2}}}{(2\pi)^{1/2}s^4}\left[(x^2 - s^2)\cosh\left(\frac{x}{s}\right) - xs\sinh\left(\frac{x}{s}\right)\right]. \quad (26)
\end{aligned}$$

5. NUMERICAL EVOLUTION

We present the evolution for each one of the cases discussed in section 4. Being the dynamics governed by a system of nonlinear coupled differential equations we analyzed their solution numerically.

5.1. Constant variance ρ, second order in momenta

In this case we obtained the following initial conditions for momenta from (5) and (11): $\Delta(x^2) = \frac{1}{2\rho^2}, \Delta(p^2) = \frac{\rho^2}{2}, \Delta(xp) = 0$, and parameters: $\hbar = m = \omega = 1, a = 3$.

In Figure 3 we show the effective potential, displaying its dramatic departure from the classical one (Figure 1) due to quantum back reaction. We may also show its evolution as a function of a, although it is not so critical as ρ. The semiclassical particle evolves according to the effective potentials depicted, and we display some interesting trajectories in Figure 4: the behavior is affected by the value of ρ, which is the variance of the state considered.
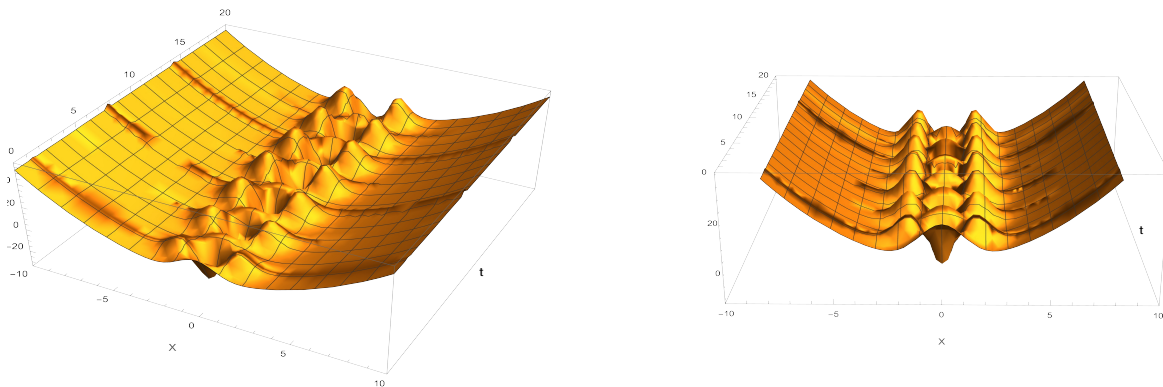
Figure 3. Effective potential for the BEC with constant variance $\rho = 2.5$, $a = 3$.

This system was obtained by truncating the Hamiltonian (6) up to second order in momenta, $\Delta(x^2), \Delta(xp), \Delta(p^2)$, and this could be extended to higher orders to take into account higher order dispersions, as shown in Appendix (B) for example. There is a generalization, though, where we do not need to make such truncations, which we analyze next.

5.2. Constant variance ρ, all-order potential

We analyze now the system for ρ constant, employing the canonical formulation of the effective formulation described in subsection 4.1.2. We expect this description to be more general than the one in the previous subsection, particularly because now we have no truncations in the potential. Employing the same initial conditions and parameters as before, with the obvious modifications for variables (7) we obtain the potential shown in fig. 5

(a) Trajectory for $\rho = 1$

(b) Trajectory for $\rho = 7.5$

(c) Trajectory for $\rho = 15$

(d) Trajectory for $\rho = 30$
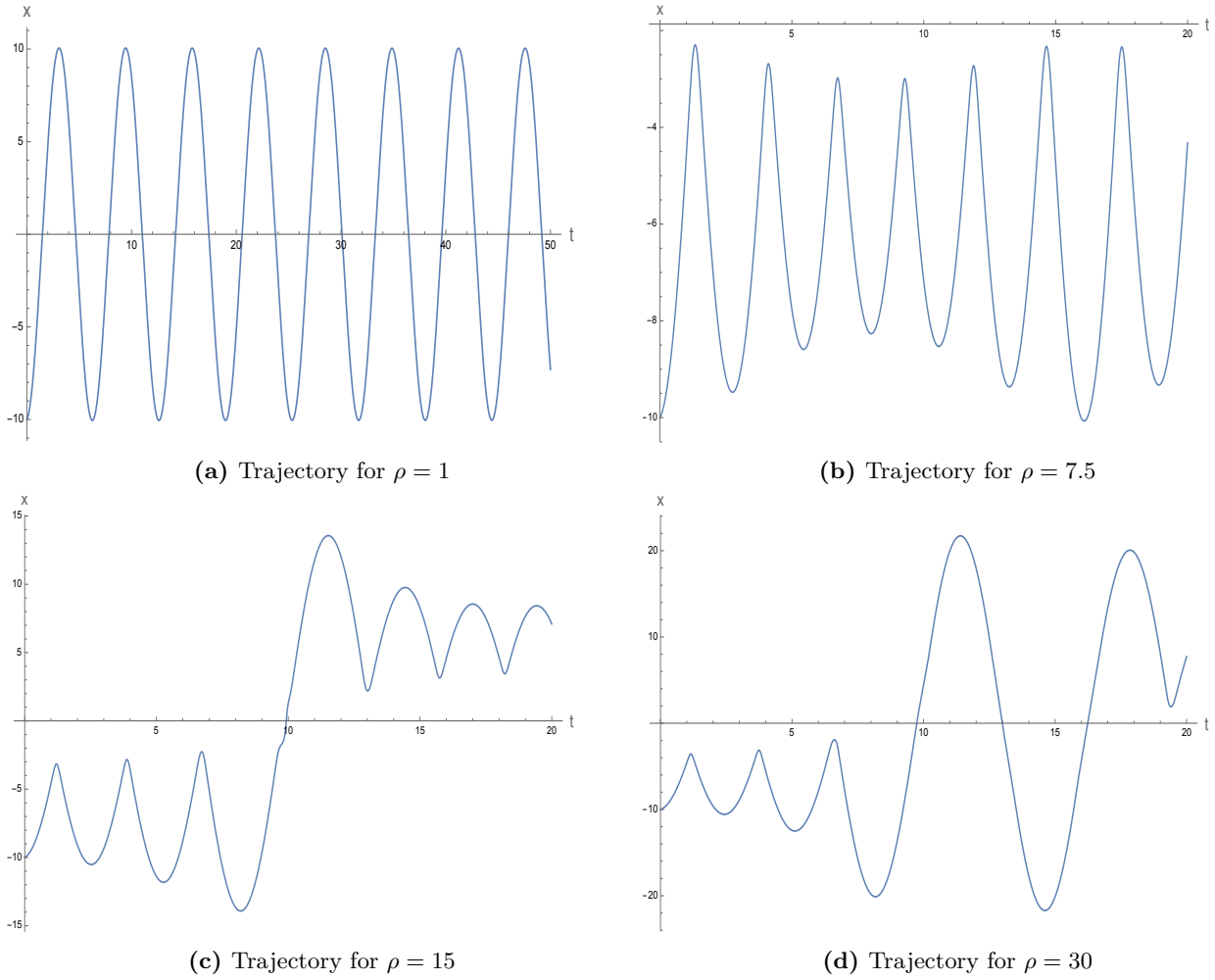
Figure 4. Effective trajectories with constant variance ρ , $a = 3$.

(a) Potential for $\rho = 2.5$
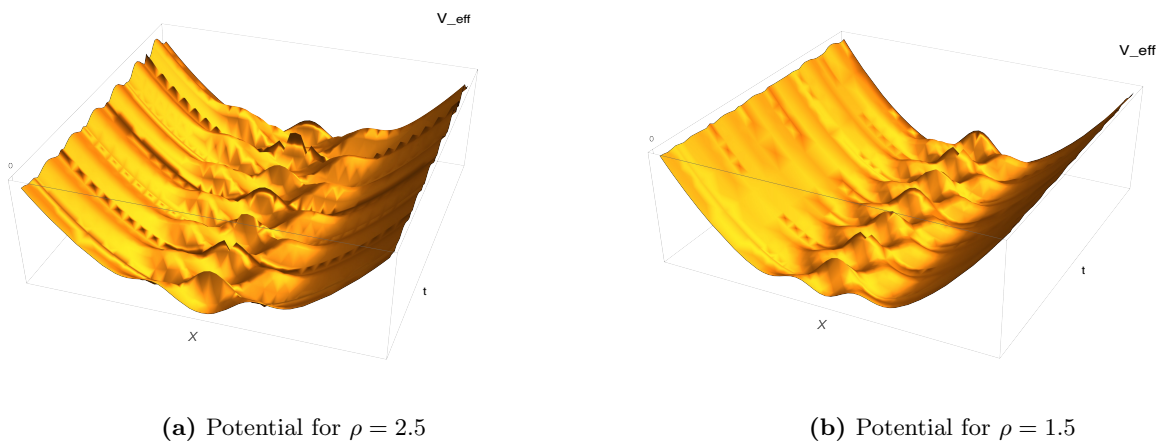
(b) Potential for $\rho = 1.5$

Figure 5. Effective potential for the BEC with constant variance $\rho = 2.5$, canonical variable s.

This is the *all-orders effective potential* in (19). It is important to note that determining an effective potential, for which no truncations are needed, is the most interesting feature of our treatment, for one can analyze the entire quantum-effective evolution of the system from it. Effective trajectories are shown in fig. 6.

The behavior of the system can be analyzed from these trajectories, where one can modify the parameters and conditions according to experimental settings or phenomenological guidelines.

(a) Trajectory for $\rho = 1$

(b) Trajectory for $\rho = 7.5$

(c) Trajectory for $\rho = 15$

(d) Trajectory for $\rho = 30$
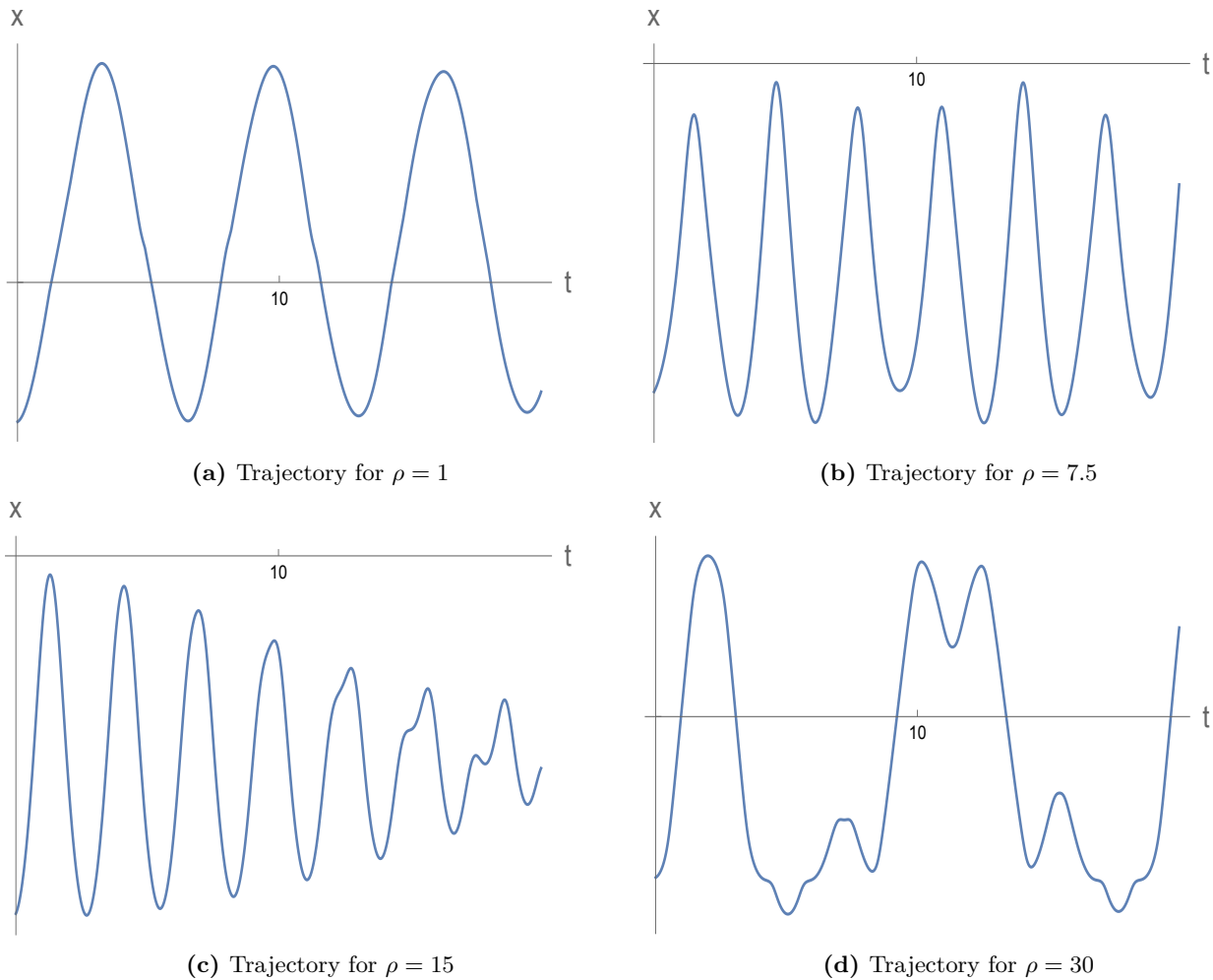
Figure 6. Effective trajectories with constant variance ρ , $a = 3$, canonical variable s

5.3. General variance ρ, effective potential

We now study the evolution for the general variance ρ as a dynamical variable. One can analyze several regions of interest in the physics of BEC, including interactions between two or more BEC's, evolution in the presence of external fields, among many other possibilities.

The dynamics is governed by the Hamiltonian (25). The last three terms in the r.h.s. of this expression is the effective potential for the system, for general variance. Its behavior is displayed in fig. 7, where the values for ρ are the initial ones.

We can obtain the evolution of classical observables, and also determine the spreading $\Delta(x^2), \Delta(p^2)$ of the initial wave function (11), just as in [17]. Actually, this can be extended to more general interactions driven by different trapping potentials. We show trajectories in fig. 8.

Interpretation of the dynamical evolution of the interacting BEC can be obtained from this effective treatment, particularly from the semiclassical potential and trajectories. For instance, while the "classical" particle, corresponding to the non interacting system, has a well defined behavior given the potential in fig. 1, in the interacting case, figures 5 and 7, depending on initial conditions and time of evolution, the BEC can *tunnel* from different regions in the trap. This corresponds to the collapse and revival of the matter wave discussed in [15]. By considering different trapping potentials, and even interacting BEC's, one can describe very interesting phenomena by applying this effective setting.

It is important to remember that the effective BEC is quantum in nature, so it should display its probabilistic nature. It is indeed the case, and the trajectories (and the whole evolution for that matter) should actually be displayed as $< \hat{x} > \pm \Delta x$, which is shown in fig. 9.

It is interesting to note that the trajectories evolve within a bounded dispersion.

(a) Effective potential for $\rho_0 = 1$

(b) Potential for $\rho_0 = 1.8$

(c) Potential for $\rho_0 = 2$

(d) Potential for $\rho_0 = 2.5$
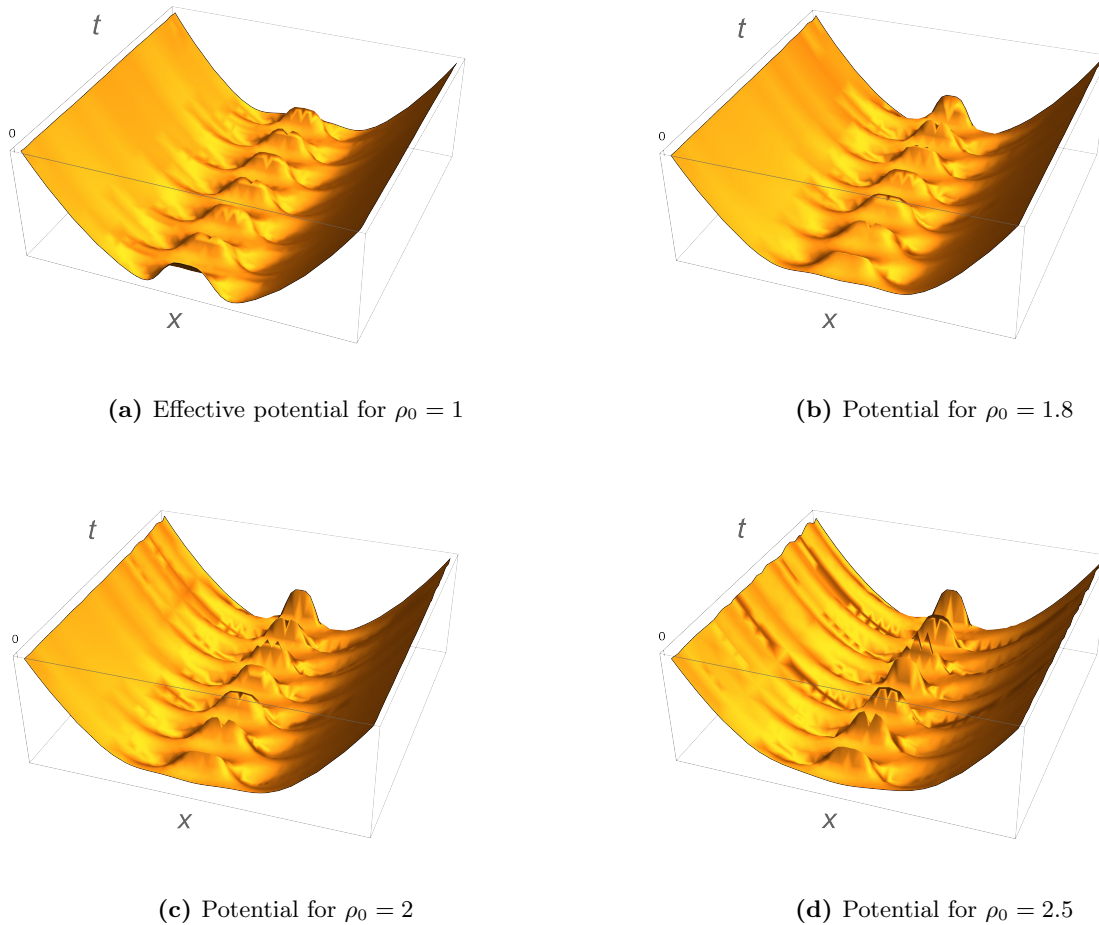
Figure 7. Effective potential with time-dependant variance ρ, in terms of the canonical variable s.
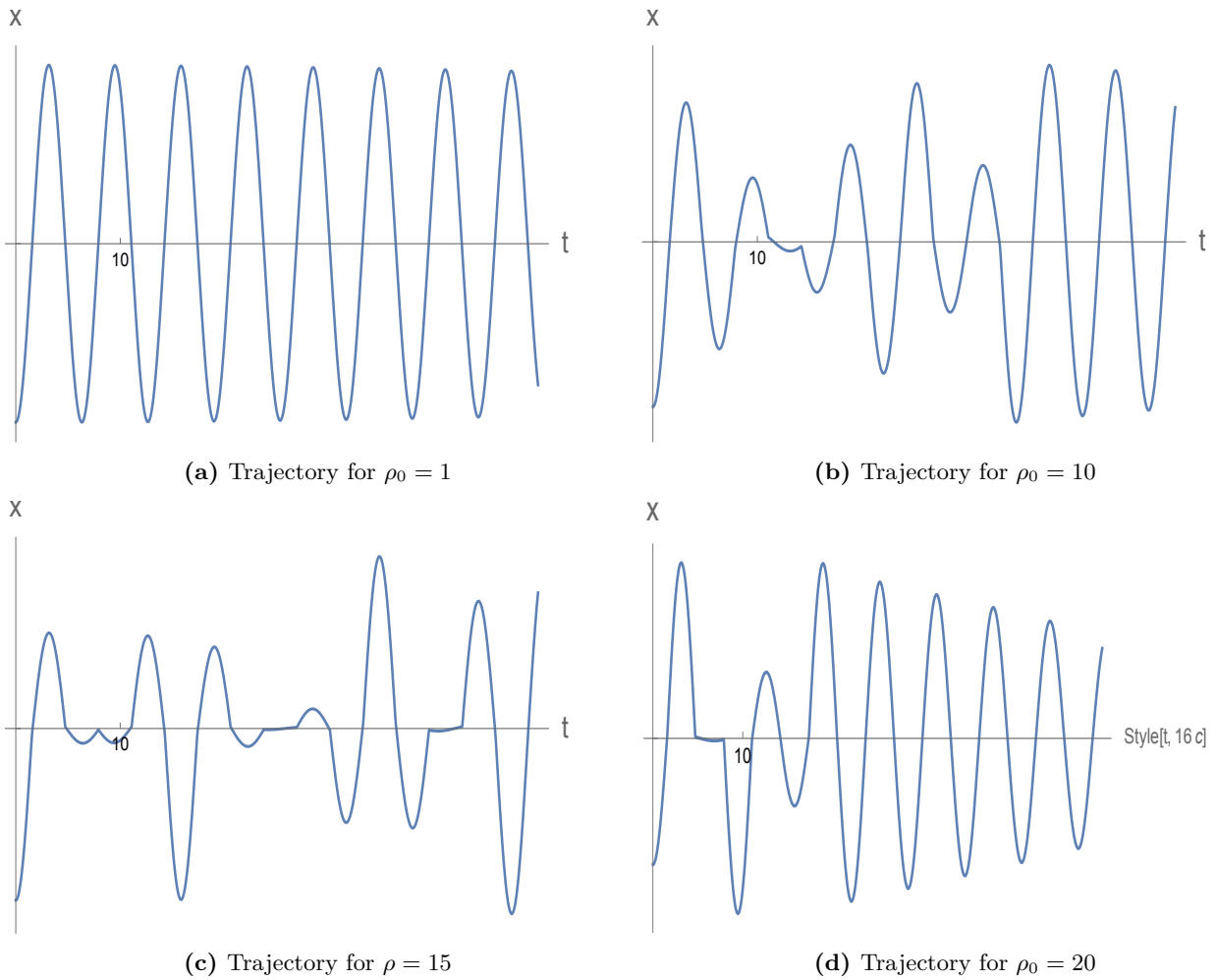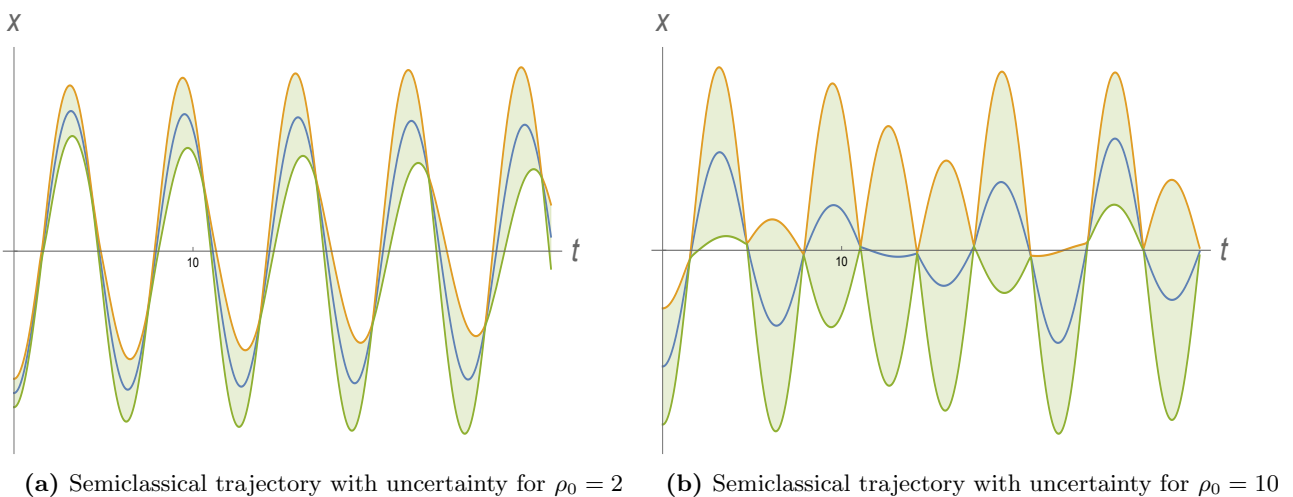
6. DISCUSSION

In this work we have presented a semiclassical effective treatment for a one dimensional Bose Einstein condensate in a harmonic trap with the typical interacting potential depending on the macroscopic wave function $\psi(x, t)$, whose dynamic is dictated by the Gross–Pitaevskii equation, a particular form of a non linear Schrödinger equation. We have shown that the physical information of the system is encoded in the expectation values of observables and quantum dispersions, acting as classical variables in an extended phase-space, with an effective Hamiltonian; their quantum evolution can be followed with one-particle trajectories, a very useful feature in the dynamical analysis of the system.

Our results match those obtained in different approaches of the GPE, particularly those in variational descriptions where the center and the width of the BEC cloud evolve as particles subjected to classical potentials (see [14]). Those results have been extended to the explanation of experimental results [18]. Since the setting for the momentous quantum mechanics is semiclassical, many generalizations to this one-dimensional system can be studied: two and three dimensional systems can be readily implemented, and the behavior nicely depicted as a one-particle one. Different interactions with, for example, traps or external fields can also be discussed, and the evolution can be interpreted from the effective quantum potential that we obtained, as mentioned in section 3. Moreover, the values taken for the parameters in the model come from phenomenological descriptions: experimental settings and constraints dictate the physically interesting values for quantum and effective variables.

The most remarkable feature of our analysis is the semiclassical characteristic of the condensate, allowing to treat it as a single particle (the most classical form of a matter wave) that inherently has a trajectory, something not present in usual quantum mechanics. We obtain an effective potential that controls the dynamics and evolution of the system and, from this, general features of the evolution can be obtained. As such, the question of quantum tunneling can be treated in a direct way [10], a very interesting phenomena currently under investigation. As discussed above, our results show a tunneling between regions in the trap, corresponding to

(a) Trajectory for $\rho_0 = 1$

(b) Trajectory for $\rho_0 = 10$

(c) Trajectory for $\rho = 15$

(d) Trajectory for $\rho_0 = 20$

Figure 8. Effective trajectories with time dependant variance ρ , $a = 3$.

(a) Semiclassical trajectory with uncertainty for $\rho_0 = 2$ **(b)** Semiclassical trajectory with uncertainty for $\rho_0 = 10$

Figure 9. Effective trajectories with with quantum uncertainty, shaded region.

the collapse and revival of the matter wave described in [15]. Actual time of flight for condensates can also be estimated under our description.

Finally we presented two derivations for the evolution of the system, one in terms of (infinite) quantum momenta -hence the name-, and the other in terms of a all-order potential, mentioned above. We mentioned that the effective potential includes all the information that the moments do; however, the momenta expression

is important in its own right because it is the one suited for systems whose Hamiltonian is not expressed in the usual kinetic and potential term.

Our methodology may serve as a valuable instrument for studying the dynamics of Bose-Einstein condensates. It offers a systematic approach to predicting and analyzing an several experimental scenarios, encompassing the influence of core-core interactions. Future applications to the investigation of interactions with radiation, expansions in BEC's and many other phenomena.

A. GENERAL POISSON ALGEBRA FOR EXPONENTIAL TERMS

The interaction potential for the Bose-Einstein condensate includes the momenta inside an exponential function. To obtain the corresponding equations of motion we need to expand in a Taylor series, once in this polynomial form one computes the Poisson brackets among variables, and then switch back to the original expression. We perform this procedure explicitly.

First the Taylor series for the exponential

$$e^{-\frac{x^2}{2\Delta(x^2)}} = \sum_{n=0}^{\infty} \frac{(-1)^n}{n!2^n} \frac{x^{2n}}{\Delta(x^2)^n}. \tag{27}$$

Poisson brackets have the following generic form

$$\left\{ \Delta(x^a p^b), \frac{e^{-\frac{x^2}{2\Delta(x^2)}}}{[\Delta(x^2)]^{1/2}} \right\} = e^{-\frac{x^2}{2\Delta(x^2)}} \left\{ \Delta(x^a p^b), \Delta(x^2)^{-1/2} \right\} + \left\{ \Delta(x^a p^b), e^{-\frac{x^2}{2\Delta(x^2)}} \right\} \Delta(x^2)^{-1/2}. \tag{28}$$

The second term in the r.h.s. of this expression gives

$$\left\{ \Delta(x^a p^b), \frac{e^{-\frac{x^2}{2\Delta(x^2)}}}{[\Delta(x^2)]^{1/2}} \right\} = e^{-\frac{x^2}{2\Delta(x^2)}} \left\{ \Delta(x^a p^b), \Delta(x^2)^{-1/2} \right\}$$
$$+ \sum_{n=0}^{\infty} \frac{(-1)^n}{n!2^n} x^{2n} \left\{ \Delta(x^a p^b), \Delta(x^2)^{-n} \right\} \Delta(x^2)^{-1/2}. \tag{29}$$

One can obtain generic formulae for any order momenta, however we obtain those for second and third order, that is, for momenta $\Delta(xp)$, $\Delta(p^2)$, $\Delta(x^2 p)$, $\Delta(xp^2)$ y $\Delta(p^3)$.

For instance

$$\left\{ \Delta(xp), \Delta(x^2) \right\} = \left\{ \Delta(xp), \Delta(x^2)^{1/2}\Delta(x^2)^{1/2} \right\}$$
$$= \Delta(x^2)^{1/2} \left\{ \Delta(xp), \Delta(x^2)^{1/2} \right\} + \left\{ \Delta(xp), \Delta(x^2)^{1/2} \right\} \Delta(x^2)^{1/2}$$
$$= 2\Delta(x^2)^{1/2} \left\{ \Delta(xp), \Delta(x^2)^{1/2} \right\}$$
$$= -2\Delta(x^2), \tag{30}$$

or

$$\left\{ \Delta(xp), \sqrt{\Delta(x^2)} \right\} = -\sqrt{\Delta(x^2)}, \tag{31}$$

which agrees with [16]. Repeating n times we obtain

$$\left\{ \Delta(xp), \frac{1}{\Delta(x^2)^n} \right\} = \frac{2n}{\Delta(x^2)^n}. \tag{32}$$

Similar expression can be obtained for other momenta

$$\left\{ \Delta(p^2), \frac{1}{\Delta(x^2)^n} \right\} = 4n \frac{\Delta(xp)}{\Delta(x^2)^{n+1}}, \tag{33}$$

$$\left\{\Delta(x^2p), \frac{1}{\Delta(x^2)^n}\right\} = 2n\frac{\Delta(x^3)}{\Delta(x^2)^{n+1}}, \tag{34}$$

$$\left\{\Delta(xp^2), \frac{1}{\Delta(x^2)^n}\right\} = 4n\frac{\Delta(x^2p)}{\Delta(x^2)^{n+1}}, \tag{35}$$

$$\left\{\Delta(p^3), \frac{1}{\Delta(x^2)^n}\right\} = 6n\frac{\Delta(xp^2)}{\Delta(x^2)^{n+1}}. \tag{36}$$

Writing back in (29) we get the final result

$$\left\{\Delta(xp), e^{-\frac{x^2}{2\Delta(x^2)}}\right\} = -\frac{x^2}{\Delta(x^2)}e^{-\frac{x^2}{2\Delta(x^2)}}, \tag{37}$$

$$\left\{\Delta(p^2), e^{-\frac{x^2}{2\Delta(x^2)}}\right\} = -2x^2\frac{\Delta(xp)}{\Delta(x^2)^2}e^{-\frac{x^2}{2\Delta(x^2)}}, \tag{38}$$

$$\left\{\Delta(x^2p), e^{-\frac{x^2}{2\Delta(x^2)}}\right\} = -x^2\frac{\Delta(x^3)}{\Delta(x^2)^2}e^{-\frac{x^2}{2\Delta(x^2)}}, \tag{39}$$

$$\left\{\Delta(xp^2), e^{-\frac{x^2}{2\Delta(x^2)}}\right\} = -2x^2\frac{\Delta(x^2p)}{\Delta(x^2)^2}e^{-\frac{x^2}{2\Delta(x^2)}}, \tag{40}$$

$$\left\{\Delta(p^3), e^{-\frac{x^2}{2\Delta(x^2)}}\right\} = -3x^2\frac{\Delta(xp^2)}{\Delta(x^2)^2}e^{-\frac{x^2}{2\Delta(x^2)}}. \tag{41}$$

B. THIRD ORDER DYNAMICAL SYSTEM

The effective Hamiltonian (6) up to third order in momenta reads

$$H_Q = \frac{p^2 + \Delta(p^2)}{2m} + \frac{m\omega^2}{2}\left[x^2 + \Delta(x^2)\right] + \frac{ge^{-\frac{x^2}{2\Delta(x^2)}}}{2[2\pi\Delta(x^2)]^{1/2}}\left\{1 + \frac{x^2}{\Delta(x^2)}\right.$$
$$\left. - \frac{\Delta(x^3)}{3}\left(\frac{x^3}{\Delta(x^2)^3} - \frac{3}{\Delta(x^2)^2}\right)\right\} \tag{42}$$

Equations of motion for classical variables are

$$\dot{x} = \frac{p}{m}, \tag{43}$$

$$\dot{p} = -m\omega^2x + \frac{ge^{-\frac{x^2}{2\Delta(x^2)}}}{2[2\pi\Delta(x^2)]^{1/2}}\left\{\frac{x^3}{\Delta(x^2)^2} - \frac{x}{\Delta(x^2)}\right.$$
$$\left. - \Delta(x^3)\left(\frac{x^4}{3\Delta(x^2)^4} - \frac{x^2}{\Delta(x^2)^3} - \frac{x}{\Delta(x^2)^3}\right)\right\} \tag{44}$$

As before, we compute the equations of motion for momenta using $i\hbar\{q, H\} = \left\langle\left[\hat{q}, \hat{H}\right]\right\rangle$. The equations of motion for third order momenta are

$$\frac{\mathrm{d}\Delta(x^2)}{\mathrm{d}t} = 2\frac{\Delta(xp)}{m}, \tag{45}$$

$$\frac{\mathrm{d}\Delta(xp)}{\mathrm{d}t} = \frac{\Delta(p^2)}{m} - m\omega^2\Delta(x^2) + \frac{ge^{-\frac{x^2}{2\Delta(x^2)}}}{2[2\pi\Delta(x^2)]^{1/2}}\left\{1 - \frac{x^4}{\Delta(x^2)^2} + \frac{3x^2}{\Delta(x^2)} - \frac{x^2}{\Delta(x^2)^{1/2}}\right.$$
$$\left. + \frac{\Delta(x^3)}{3}\left(\frac{x^5}{\Delta(x^2)^4} - \frac{4x^3}{\Delta(x^2)^3} - \frac{3x^2}{\Delta(x^2)^3} + \frac{6}{\Delta(x^2)^2}\right)\right\}, \tag{46}$$

$$\frac{\mathrm{d}\Delta(p^2)}{\mathrm{d}t} = -2m\omega^2\Delta(xp) \quad + \quad \frac{ge^{-\frac{x^2}{2\Delta(x^2)}}}{[2\pi\Delta(x^2)]^{1/2}}\left\{\frac{\Delta(xp)}{\Delta(x^2)} + x^2\left(2\frac{\Delta(xp)}{\Delta(x^2)^2} - x^2\frac{\Delta(xp)}{\Delta(x^2)^3}\right)\right.$$

$$+ \quad \frac{x^3}{3}\left(x^2\frac{\Delta(x^3)\Delta(xp)}{\Delta(x^2)^5} + 3\frac{\Delta(x^2p)}{\Delta(x^2)^3} - 7\frac{\Delta(x^3)\Delta(xp)}{\Delta(x^2)^4}\right)$$

$$+ \quad \left.5\frac{\Delta(x^3)\Delta(xp)}{\Delta(x^2)^3} - 3\frac{\Delta(x^2p)}{\Delta(x^2)^2} - x^2\frac{\Delta(x^3)\Delta(xp)}{\Delta(x^2)^4}\right\}, \tag{47}$$

$$\frac{\mathrm{d}\Delta(x^3)}{\mathrm{d}t} = 3\frac{\Delta(x^2p)}{m}, \tag{48}$$

$$\frac{\mathrm{d}\Delta(x^2p)}{\mathrm{d}t} = 2\frac{\Delta(xp^2)}{m} - m\omega^2\Delta(x^3) \quad + \quad \frac{ge^{-\frac{x^2}{2\Delta(x^2)}}}{2[2\pi\Delta(x^2)]^{1/2}}\left\{3 + \frac{\Delta(x^3)}{\Delta(x^2)} + 5\frac{\Delta(x^3)^2}{\Delta(x^2)^3} - 3\frac{\Delta(x^4)}{\Delta(x^2)^2}\right.$$

$$+ \quad x^2\left(2\frac{\Delta(x^3)}{\Delta(x^2)^2} - x^2\frac{\Delta(x^3)}{\Delta(x^2)^3} - \frac{\Delta(x^3)^2}{\Delta(x^2)^4}\right)$$

$$+ \quad \left.\frac{x^3}{3}\left(3\frac{\Delta(x^4)}{\Delta(x^2)^3} + x^2\frac{\Delta(x^3)^2}{\Delta(x^2)^5} - 7\frac{\Delta(x^3)^2}{\Delta(x^2)^4} - \frac{3}{\Delta(x^2)}\right)\right\}, \tag{49}$$

$$\frac{\mathrm{d}\Delta(xp^2)}{\mathrm{d}t} = \frac{\Delta(p^3)}{m} \quad - \quad 2m\omega^2\Delta(x^2p) + \frac{ge^{-\frac{x^2}{2\Delta(x^2)}}}{[2\pi\Delta(x^2)]^{1/2}}\left\{\frac{\Delta(x^2p)}{\Delta(x^2)} + 5\frac{\Delta(x^2p)\Delta(x^3)}{\Delta(x^2)^3} + 3\frac{\Delta(xp)}{\Delta(x^2)} - 3\frac{\Delta(x^3p)}{\Delta(x^2)^2}\right.$$

$$+ \quad x^2\left(2\frac{\Delta(x^2p)}{\Delta(x^2)^2} - x^2\frac{\Delta(x^2p)}{\Delta(x^2)^3} - \frac{\Delta(x^2p)\Delta(x^3)}{\Delta(x^2)^4}\right)$$

$$+ \quad \left.\frac{x^3}{3}\left(3\frac{\Delta(x^3p)}{\Delta(x^2)^3} + x^2\frac{\Delta(x^2p)\Delta(x^3)}{\Delta(x^2)^5} - 7\frac{\Delta(x^2p)\Delta(x^3)}{\Delta(x^2)^4} - 3\frac{\Delta(xp)}{\Delta(x^2)^2}\right)\right\}, \tag{50}$$

$$\frac{\mathrm{d}\Delta(p^3)}{\mathrm{d}t} = \quad - \quad 3m\omega^2\Delta(xp^2) + \frac{ge^{-\frac{x^2}{2\Delta(x^2)}}}{[2\pi\Delta(x^2)]^{1/2}}\left\{3\frac{\Delta(xp^2)}{\Delta(x^2)} + 15\frac{\Delta(xp^2)\Delta(x^3)}{\Delta(x^2)^3} + 9\frac{\Delta(p^2)}{\Delta(x^2)}\right.$$

$$- \quad 9\frac{\Delta(x^2p^2)}{\Delta(x^2)^2} + \frac{3\hbar^2}{2\Delta(x^2)^2}$$

$$+ \quad x^2\left(6\frac{\Delta(xp^2)}{\Delta(x^2)^2} - 3x^2\frac{\Delta(xp^2)}{\Delta(x^2)^3} - 3\frac{\Delta(xp^2)\Delta(x^3)}{\Delta(x^2)^4}\right)$$

$$+ \quad \left.x^3\left(x^2\frac{\Delta(xp^2)\Delta(x^3)}{\Delta(x^2)^5} - 7\frac{\Delta(xp^2)\Delta(x^3)}{\Delta(x^2)^4} + 3\frac{\Delta(x^2p^2)}{\Delta(x^2)^3} - 3\frac{\Delta(p^2)}{\Delta(x^2)^2} - \frac{\hbar^2}{2\Delta(x^2)^3}\right)\right\} \tag{51}$$

ORCID

 Hector Hernandez-Hernandez, https://orcid.org/0000-0001-6041-7471

REFERENCES

[1] S.N. Bose. "Plancks gesetz und lichtquantenhypothese." Zeitschrift für Physik **26**, 178-181 (1924).
Einstein. "Quantentheorie des einatomigen idealen gases, sitzungsberichte kgl." Preuss. Akad. Wiss **261** (1924).
http://dx.doi.org/10.1007/BF01327326

[2] F. Schreck, and K. van Druten, "Laser cooling for quantum gases," Nature Phys. **17**(12), 1296-1304 (2021). https://doi.org/10.1038/s41567-021-01379-w

[3] B. Rhyno, N. Lundblad, D.C. Aveline, C. Lannert, S. Vishveshwara, "Thermodynamics in expanding shell-shaped Bose-Einstein condensates," Physical Review A, **104**6, 063310 (2021). https://doi.org/10.1103/PhysRevA.104.063310

[4] R.A. Dunlap, *Lasers and Their Application to the Observation of Bose-Einstein Condensates*, (Morgan and Claypool Publishers, 2019). https://doi.org/10.1088/2053-2571/ab2f2f

[5] J. Tempere, *Bose-Einstein Condensation, Superfluidity and Superconductivity*, (Universiteit Antwerpen, 2019).

[6] S. Stringari, "Collective excitations of a trapped Bose-condensed gas," Physical Review Letters, **77**, 2360 (1996). https://doi.org/10.1103/PhysRevLett.77.2360
F. Dalfovo, S. Giorgini, L. Pitaevskii, and S. Stringari," Rev. Mod. Phys. **71**, 463 (1999). https://doi.org/10.1103/RevModPhys.71.463

[7] M. Bojowald, and A. Skirzewski, "Effective equations of motion for quantum systems," Rev. Mathematical Phys. **18**(07), 713-745 (2006). https://doi.org/10.1142/S0129055X06002772

[8] B. Baytaş, M. Bojowald, and S. Crowe, "Effective potentials from semiclassical truncations," Physical Review A, **99**(4), 042114 (2019). https://doi.org/10.1103/PhysRevA.99.042114

[9] J.T. Cushing, A. Fine, and S. Goldstein, editors *Bohmian mechanics and quantum theory: an appraisal*. Vol. **184**, (Springer Science Business Media, 2013).

[10] L. Aragon-Muñoz, G. Chacón-Acosta, and H. Hernandez-Hernandez, "Effective quantum tunneling from a semiclassical momentous approach," International Journal of Modern Physics B, **34**(29), 2050271 (2020). https://doi.org/10.1142/S0217979220502719

[11] L. Pitaevskii, and S. Stringari, *Bose-Einstein condensation and superfluidity*, Vol. 164. (Oxford University Press, 2016).

[12] J.R. Ensher, et al., "Bose-Einstein condensation in a dilute gas: Measurement of energy and ground-state occupation," Physical Review Letters **77**, 4984 (1996). https://doi.org/10.1103/PhysRevLett.77.4984

[13] X. Antoine, W. Bao, and C. Besse, "Computational methods for the dynamics of the nonlinear Schrödinger/Gross–Pitaevskii equations," Computer Physics Communications, **184**(12), 2621-2633 (2013). https://doi.org/10.1016/j.cpc.2013.07.012

[14] V.M. Pérez-García, H. Michinel, J.I. Cirac, M. Lewenstein, and P. Zoller, "Dynamics of Bose-Einstein condensates: Variational solutions of the Gross-Pitaevskii equations," Physical Review A, **56**(2), 1424 (1997). https://doi.org/10.1103/PhysRevA.56.1424

[15] M. Greiner, O. Mandel, T.W. Hänsch, and I. Bloch, "Collapse and revival of the matter wave field of a Bose–Einstein condensate." Nature 419, **6902**, 51-54 (2002). https://doi.org/10.1038/nature00968

[16] B. Baytaş, M. Bojowald, and S. Crowe, "Faithful realizations of semiclassical truncations," Annals of Physics, **420**, 168247 (2020). https://doi.org/10.1016/j.aop.2020.168247

[17] L.C. Pereira, and V.A. do Nascimento. "Dynamics of Bose–Einstein Condensates Subject to the Pöschl–Teller Potential through Numerical and Variational Solutions of the Gross–Pitaevskii Equation," Materials, **13**(10), 2236 (2020). https://doi.org/10.3390/ma13102236

[18] V.M. Pérez-García, H. Michinel, J.I. Cirac, M. Lewenstein, and P. Zoller, "Low energy excitations of a Bose-Einstein condensate: A time-dependent variational analysis," Physical review letters, **77**(27), 5320 (1996). https://doi.org/10.1103/PhysRevLett.77.5320

ЕФЕКТИВНА НАПІВКЛАСИЧНА ЕВОЛЮЦІЯ КОНДЕНСАТІВ БОЗЕ-ЕЙНШТЕЙНА
Гектор Ернандес-Ернандес

Факультет інженерії, Автономний університет Чіуауа, Мексика

У цій роботі ми аналізуємо ефективну еволюцію одновимірного конденсату Бозе-Ейнштейна (BEC) у напівкласичному описі квантових систем на основі очікуваних значень квантових дисперсій і фізичних спостережуваних, відомих як важлива квантова механіка. Ми показуємо, що найвидатніші особливості та фізичні параметри системи можна визначити з динаміки відповідної напівкласичної системи, що складається з розширеного фазового простору, включаючи оригінальні класичні спостережувані та квантові дисперсії, і ми також показуємо, що траєкторії частинок для очікуваних значень спостережувані є особливою характеристикою в цій структурі. Ми також демонструємо, що взаємодія з декількома потенціалами може бути реалізована інтуїтивно зрозумілим способом.
Ключові слова: *ефективна квантова механіка; конденсат Бозе-Ейнштейна; напівкласична еволюція*

NONCLASSICALITIES OF THE SUPERPOSITION STATE OF COHERENT AND PHOTON-ADDED-COHERENT STATE

Sandip Kumar Giri

Department of Physics, Panskura Banamali College, Panskura-721152, India
Corresponding Author e-mail: sandipgiri26@gmail.com

The nonclassical properties of the hybrid coherent state (HCS), which is the superposition state of the coherent state and photon-added coherent (PAC) state, is investigated analytically. We evaluated the photon number statistics, the Wigner-Yanase skew information, the Mandel Q factor and the quadrature squeezing of the HCS to quantify its nonclassicality. This superposition state exhibits more nonclassical properties than the PAC state and even the superposition state of coherent state and single-photon-added coherent (SPAC) state. We reported that the addition of more photons to the PAC state part of the HCS generally quantifies more nonclassicalities. The nonclassical properties of the HCS also depend on the amplitudes of coherent state and the PAC state in the HCS.

Keywords: *Coherent state; Photon-added coherent state; Hybrid coherent state; Wigner-Yanase skew information; Mandel Q factor; Quadrature squeezing; Nonclassical effect*
PACS: 42.50.-p; 42.50.Dv; 42.50.Ar

1. INTRODUCTION

The coherent state $|\alpha\rangle$ of light is the classical like state which exhibits the Poissonian photon number distribution with $|\alpha|^2$ average number of photons. On the contrary, the Fock state $|m\rangle$ is completely quantum mechanical and contains precisely m photons. The PAC state of order m and amplitude α is defined as $|\alpha, m\rangle = a^{\dagger m}|\alpha\rangle$ ($a^\dagger$ is the photon creation operator and the m times application of $a^\dagger$ on the coherent state $|\alpha\rangle$ results $|\alpha, m\rangle$) which has intermediate properties between the coherent state and Fock state. The state $|\alpha, m\rangle$ reduces to coherent state or Fock state for $m \to 0$ or $\alpha \to 0$, respectively. The nonclassical properties such as squeezing and sub-Poissonian photon statistics of PAC state were first described by Agarwal and Tara [1]. They also described theoretically how the PAC can be prepared. The experimental realization of SPAC state via parametric down-conversion in nonlinear crystals has been reported by Zavatta *et al.* [2]. Mattos and Vidiella-Barranco investigated the photon-added and photon-subtracted state using the optical amplifier and beam splitter [3-4]. Hu *et al.* proposed a scheme to prepare the SPAC state via three-wave mixing [5]. The SPAC state has large single photon probability as it has no vacuum part and also shows nonclassicalities. The nonclassical states have tremendous applications in various fields. Several applications of the nonclassical effects of the Bose-Einstein condensates system and Raman processes have been reported [6-8]. The nonclassical photon-added coherent states also have applications in various fields, such as it is essential in quantum communication [9], quantum key distribution [10], quantum state engineering [11], quantum metrology [12], quantum dense coding protocol [13], and to improve the perfection in quantum digital signature protocols [14]. The more nonclassicalities the quantum states have, the more effective it will be in practical applications. To improve the depth of nonclassicalities, scientists also prepare and study the superposition state of SPAC state and coherent state and in some cases, they achieved this [15-17]. But there is no such work on the HCS which is the superposition state of coherent state and PAC state $|\alpha, m\rangle$ with $m > 1$. In this paper we have investigated the nonclassical properties of such HCS in details. Turek *et al.* have theoretically shown that such hybrid coherent state can be prepared through the cross-Kerr interaction of coherent state with the single-photon state [17].

The HCS we have investigated is the superposition state of coherent state $|\alpha\rangle$ and PAC state $a^{\dagger m}|\alpha\rangle$. Such state can be written as

$$|\psi\rangle = \mathcal{N}\left[\sqrt{\varepsilon}\, e^{i\theta}|\alpha\rangle + \sqrt{1-\varepsilon}\, a^{\dagger m}|\alpha\rangle\right] \tag{1}$$

where ε is the superposition parameter that lies between $0 \leq \varepsilon \leq 1$ and θ is the phase difference between the coherent state and PAC state. Shringarpure and Franson showed that such a state can be generated from the output of an optical parametric amplifier by introducing the coherent state and the photon number state in the input signal mode and idler mode of the amplifier, respectively [15]. The superposition parameter can be controlled by varying the gain of the optical parametric amplifier. For $\varepsilon = 0$ or $\varepsilon = 1$ the HCS $|\psi\rangle$ will reduce to a PAC state or coherent state, respectively. Here, $\mathcal{N}$ is the normalization constant which is given by

$$\mathcal{N} = \left[\varepsilon + 2\sqrt{\varepsilon(1-\varepsilon)}\, Re\left[e^{i\theta}\alpha^m\right] + (1-\varepsilon)L_m(-|\alpha|^2)\, m!\right]^{-\frac{1}{2}} \tag{2}$$

where $L_m(x)$ is the Laguerre polynomial of order m and $\alpha = |\alpha|e^{i\omega}$. We study various nonclassical properties of the state as described in Eq. (1) by varying $|\alpha|$, and the superposition parameter ε. We also investigate the nonclassical properties of the HCS by varying the photon number m.

To study the photon number distribution of the HCS, we derive the probability of finding n photons in ψ, i.e. $P_n = |\langle n|\psi\rangle|^2$, which is given by

$$P_n = \left| \mathcal{N} e^{-\frac{|\alpha|^2}{2}} \left(\sqrt{\varepsilon}\, e^{i\theta} \frac{\alpha^n}{\sqrt{n!}} + \sqrt{1-\varepsilon}\, \frac{\sqrt{n!}}{(n-m)!} \alpha^{n-m} \right) \right|^2 \qquad (3)$$

We plot the Eq. (3) with n for different values of m (Figure 1(a)) and ε (Figure 1(b)). Here we have taken $\theta = \pi$, $\omega = 0$, and $|\alpha| = 2$. For $\varepsilon = 1$, the state is a coherent state and it shows the Poisson distribution (Black line in Fig. 1). For $\varepsilon = 0$, the state is a photon-added coherent and for $0 \leq \varepsilon \leq 1$ the state is a HCS. For $\varepsilon = 0.5$ the HCS is the 50:50 superposition of the coherent state and PAC state. The different m values in Figure 1(a) correspond to the numbers of photons added with the coherent state to prepare the PAC state part of the HCS. For nonclassicalities, the width of the distribution curve requires to be narrower than that of the coherent state [18]. But it is difficult to quantifying the nonclassicality from the number distribution plot. To view this we derive the Mandel Q-factor and the Wigner-Yanase skew information [18-20].
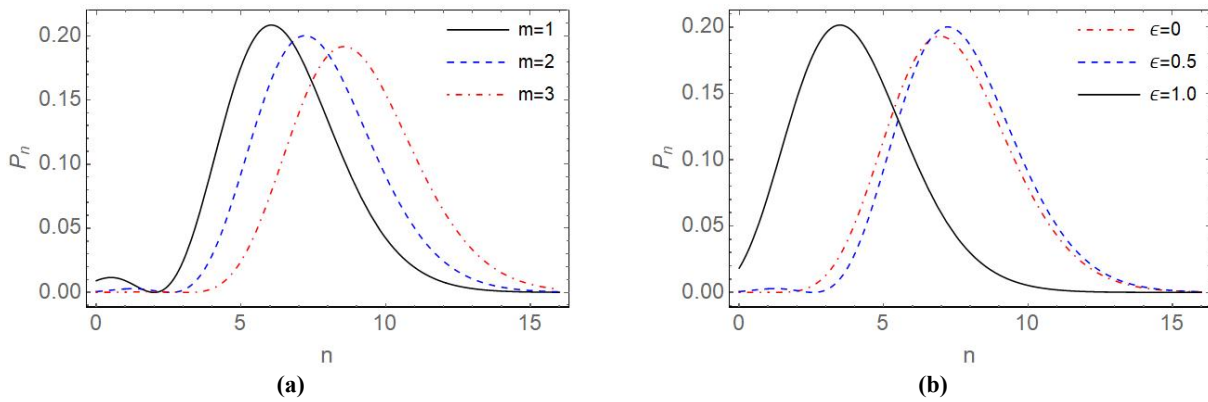
Figure 1. Variation of P_n with n: (a) for different m with $\varepsilon = 0.5$; (b) for different ε with $m = 2$

This paper is organized as follows. We study the Mandel Q factor in Section 2. We study the Wigner-Yanase skew information in Section 3 and quantum squeezing in section 4. Finally, we concluded in Section 5.

2. MANDEL Q FACTOR

The sub-Poissonian statistical property of a quantum system is a nonclassical effect. Mandel Q factor (Q_m) efficiently quantifying the sub-Poissonian distribution of photons. The Q_m factor is defined as

$$Q_m = \frac{\langle a^{\dagger 2} a^2 \rangle - \langle a^\dagger a \rangle^2}{\langle a^\dagger a \rangle}. \qquad (4)$$

For coherent state, $Q_m = 0$; for Fock state, $Q_m = -1$. If $Q_m > 0$, the photon statistics is super-Poissonian. If $0 > Q_m \geq -1$, the number statistics of the state is sub-Poissonian and this is the sufficient condition of a quantum state to be nonclassical. For the state defined in Eq. (1), we evaluate

$$\langle a^{\dagger 2} a^2 \rangle = |\mathcal{N}|^2 \left[\varepsilon |\alpha|^4 + 2\sqrt{\varepsilon(1-\varepsilon)}\, Re[e^{i\theta}\alpha^m \{m(m-1) + 2m|\alpha|^2 + |\alpha|^4\}] \right.$$
$$\left. + (1-\varepsilon)\{(m+2)!\, L_{m+2}(-|\alpha|^2) - 4(m+1)!\, L_{m+1}(-|\alpha|^2) + 2m!\, L_m(-|\alpha|^2)\} \right]. \qquad (5)$$

The average photon number $\langle n \rangle$ is

$$\langle a^\dagger a \rangle = |\mathcal{N}|^2 \left[\varepsilon |\alpha|^2 + 2\sqrt{\varepsilon(1-\varepsilon)}\, Re[e^{i\theta}\alpha^m(m + |\alpha|^2)] \right.$$
$$\left. + (1-\varepsilon)\{(m+1)!\, L_{m+1}(-|\alpha|^2) - m!\, L_m(-|\alpha|^2)\} \right]. \qquad (6)$$

Using Eq. (4)-(6) we plot Q_m with $|\alpha|$ for different values of m (Figure 2(a)) and ε (Figure 2(b)). Figure 2(a) shows that for $m = 1$, i.e., when a single photon is added to the PAC state part, the photon distribution of HCS is sub-Poissonian only for $0.3 > |\alpha| > 1.4$. But for $m > 1$, the distribution is sub-Poissonian for all values of $|\alpha|$ (Dashed blue line is for $m = 2$, and red dotdashed line for $m = 3$). More the negativity of Q_m indicates more nonclassicality. The higher the nonclassicality, it will be more useful in practical applications. The Q_m factor of the superposition state of coherent state and SPAC state was investigated by Turek *et al*. [17]. It is interesting to note that the HCS may have better useful applications as a nonclassical state when its PAC state part is prepared with the addition of more photons than the addition of a single photon. The depth of nonclassicality decreases with higher values of $|\alpha|$ because higher the values of $|\alpha|$, the

PAC state part will go toward the coherent state. Figure 2(b) shows that for $\varepsilon = 1$, i.e., when the HCS reduces to a coherent state, $Q_m = 0$ as usual (solid black line). For $|\alpha| > 1.7$, the HCS (blue dashed line) shows more nonclassicalities than the PAC state (dotdashed red line). This is a very important result because it reveals the necessity and importance of introduction of HCS over the PAC state.
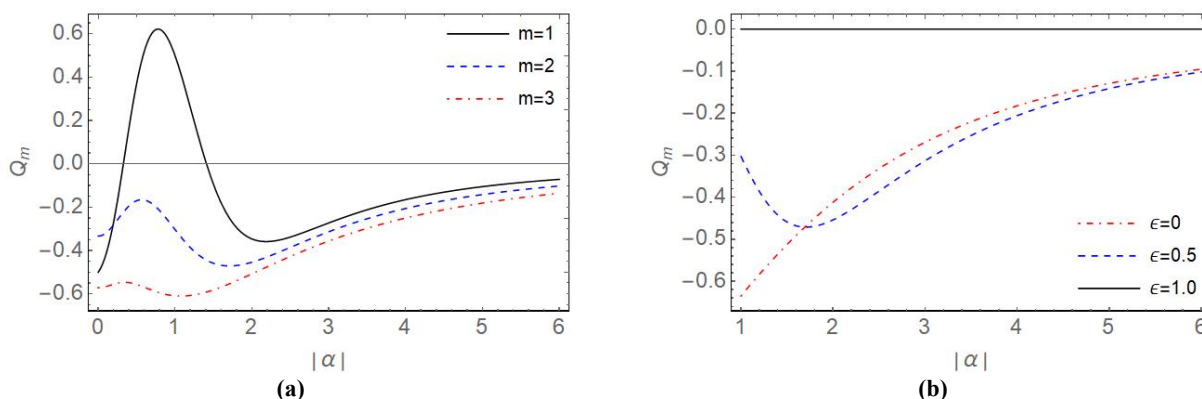
Figure 2. Variation of Q_m with $|\alpha|$: (a) for different m with $\varepsilon = 0.5$; (b) for different ε with $m = 2$. We take $\theta = \pi, \omega = 0$
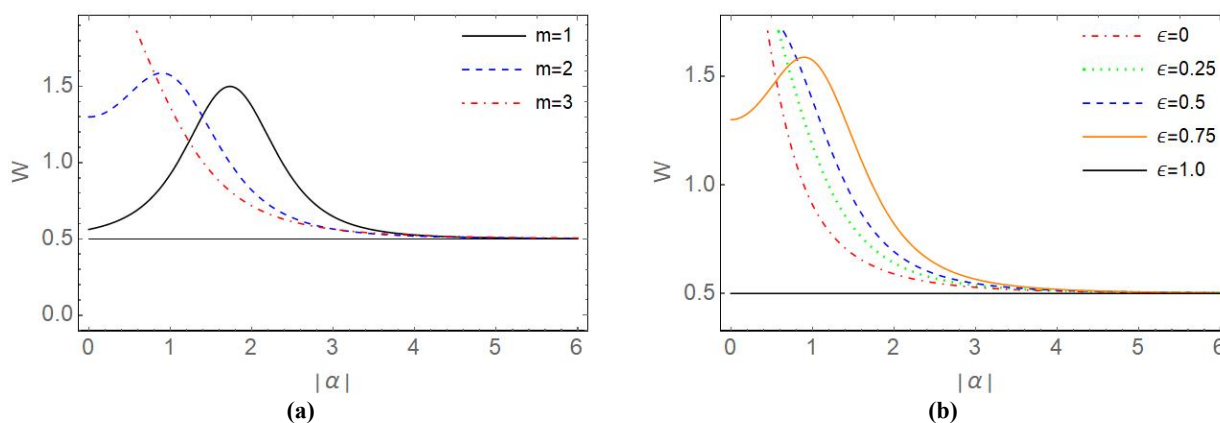
3. Wigner-Yanase skew information

The Wigner-Yanase skew information is also a measure of the quantumness of a state and it is a special version of quantum Fisher information [21]. The skew information quantifies the nonclassicality present in a quantum state in terms of the ladder operators of the states involved. It contains the noticeable properties which have been found remarkable applications in quantum information theory [22, 23]. For single-mode radiation field the skew information (W) is defined as

$$W = 0.5 + \langle a^\dagger a \rangle - \langle a^\dagger \rangle \langle a \rangle. \tag{7}$$

The average of the field annihilation operator for the HCS defined in Eq. (1) is

$$\langle a \rangle = |\mathcal{N}|^2 \Big[\varepsilon \alpha + \sqrt{\varepsilon(1-\varepsilon)} \left\{ e^{-i\theta} \alpha^{*(m-1)}(m + |\alpha|^2) + e^{i\theta} \alpha^{(m+1)} \right\}$$

$$+ (1-\varepsilon) e^{-|\alpha|^2} \sum_{p=0}^{\infty} \frac{|\alpha|^{2p} \alpha (m+1+p)!}{p! \, (p+1)!} \Big]. \tag{8}$$

Figure 3. Variation of W with $|\alpha|$: (a) for different m with $\varepsilon = 0.75$; (b) for different ε with $m = 2$. We take $\theta = \pi, \omega = 0$

Using Eq. (6)-(8), we plot the skew information W with $|\alpha|$ for different values of m (Figure 3(a)) and ε (Fig. 3(b)). For coherent state, $W = 0.5$ (black line in Figure 3(b)). For nonclassical states, $W > 0.5$. The higher the values of W, the higher the nonclassicality. Figure 3(a) shows that for smaller values of $|\alpha|$, more photon addition in the PAC state part quantifies more nonclassicality. But for large $|\alpha|$ values, the quantumness of the HCS state is higher for smaller m values and finally the skew information W reduces to its coherent state value for more large values of $|\alpha|$. Figure 3(b) shows that the amount of nonclassicality of the HCS ($\varepsilon \neq 0, 1$) is more than that of the photon-added coherent state ($\varepsilon = 0$) (the only exception when $|\alpha| < 0.55$ for $\varepsilon = 0.75$). So, controlling the m-value and the superposition parameter in the HCS, we can magnify the depth of nonclassicality which is essential for practical applications of quantum state in quantum computation and quantum information. For large $|\alpha|$ the value skew information W reduces to its coherent state value irrespective of m and ε.

4. QUADRATURE SQUEEZING

Squeezed light has the fluctuation below the standard quantum limit and it is also a nonclassical quantum effect. It has various applications in sensitive measurements and quantum communications. The most nonclassical state is the single-photon state and the nonclassicality is also possible for photon number more than one [18]. The quadrature squeezing of PAC state is reported by Francis and Tame [16]. More the depth of squeezing below the minimum uncertainty has the better applications in quantum sensing. The quadrature operator X_φ and the squeezing parameter S_φ of a single mode field is defined as

$$X_\varphi = \frac{1}{\sqrt{2}}(ae^{-i\varphi} + a^\dagger e^{i\varphi}), \; S_\varphi = \left(\Delta X_\varphi\right)^2 - \frac{1}{2}, \tag{9}$$

where $\left(\Delta X_\varphi\right)^2 = \sqrt{\langle X_\varphi{}^2\rangle - \langle X_\varphi\rangle^2}$. Then, Eq. (9) can be written as

$$S_\varphi = \frac{1}{2}[e^{2i\varphi}(\langle a^{\dagger 2}\rangle - \langle a^\dagger\rangle^2) + e^{-2i\varphi}(\langle a^2\rangle - \langle a\rangle^2) + 2(\langle a^\dagger a\rangle - \langle a^\dagger\rangle\langle a\rangle)]. \tag{10}$$

The value of $\langle a^2\rangle$ for the HCS as defined in Eq. (1) is given by

$$\langle a^2\rangle = |\mathcal{N}|^2 \Big[\varepsilon\alpha^2 + \sqrt{\varepsilon(1-\varepsilon)}\left\{e^{-i\theta}\alpha^{*(m-2)}(m^2 - m + 2m|\alpha|^2 + |\alpha|^4) + e^{i\theta}\alpha^{(m+2)}\right\}$$
$$+ (1-\varepsilon)e^{-|\alpha|^2}\sum_{p=0}^{\infty}\frac{|\alpha|^{2p}\,\alpha^2\,(m+2+p)!}{p!\,(p+2)!}\Big] \tag{11}$$

For the coherent state, $S_\varphi = 0$. For quadrature squeezing in the X_φ quadrature, $-0.5 < S_\varphi < 0$. Using Eq. (6), (8)-(11), we plot the squeezing parameter S_φ with $|\alpha|$ in the $X_{\varphi=0}$ quadrature for different values of m (Figure 4(a)) and ε (Figure 4(b)). Interestingly, Figure 4(a) shows that the signature of squeezing appears at lower values of $|\alpha|$ for higher m values, i.e., when more photons are added to The PAC state part of the HCS. The amount of squeezing is also higher for higher m values indicating more reduction of quantum noise. Figure 4(b) shows that for $|\alpha| > 2.35$, the HCS with 50:50 superposition of coherent state and PAC state has higher squeezing than that of the PAC state part. So, the superposition of PAC state with coherent state will be more useful than the PAC state in practical applications.
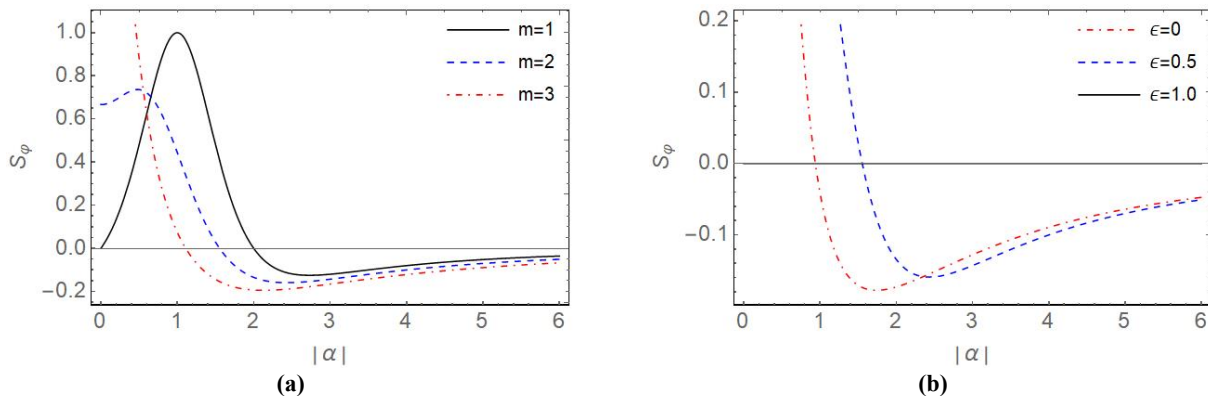
Figure 4. Variation of S_φ with $|\alpha|$: (a) for different m with $\varepsilon = 0.5$; (b) for different ε with $m = 2$. We take $\theta = \pi$, and $\omega = 0$

5. CONCLUSIONS

We have studied the photon number statistics, the Mandel Q factor, Wigner-Yanase skew information and the quadrature squeezing of the hybrid coherent state which is the superposition state of coherent state and photon-added-coherent state. Mandel Q factor indicates that for $|\alpha| > 0.2$, addition of more photons to the PAC state part of the HCS improved the depth of nonclassicality. Also, for $|\alpha| > 1.7$, the HCS manifested more nonclassicalities than what would have been achieved with PAC state alone. The Wigner-Yanase skew information reveals that the for $|\alpha| < 0.8$, the quantumness of the HCS increases with m values and the depth of nonclassicality of the HCS is more than that of the PAC state with the only exception for $|\alpha| < 0.55$ with $m = 2, \varepsilon = 0.75$. The quadrature squeezing is reported in the $X_{\varphi=0}$ quadrature for $|\alpha| > |\alpha|_{min}$. For $\varepsilon = 0.5$, the minimum values of $|\alpha|$ to appear squeezing are 1.1, 1.5, and 2 for $m = 3$, $m = 2$, and $m = 1$, respectively. The amount of squeezing is also higher for larger m. For $|\alpha| > 2.35$, the HCS with $m = 2$ and $\varepsilon = 0.5$ shows more squeezing than the PAC state in the $X_{\varphi=0}$ quadrature. All the nonclassicalities disappear for higher $|\alpha|$ values because for large $|\alpha|$ the PAC state reduces to a coherent state. Generally, the HCS with $m > 1$ quantifies more nonclassicalities than the PAC state and even the HCS with $m = 1$ that reveal the importance and necessity of this work.

ORCID

Sandip Kumar Giri, https://orcid.org/0009-0002-6862-2773

REFERENCES

[1] G.S. Agarwal, and K. Tara, Phys. Rev. A, **43**, 492 (1991). https://doi.org/10.1103/PhysRevA.43.492
[2] A. Zavatta, S. Viciani, and M. Bellini, Science, **306**, 660 (2004). https://www.science.org/doi/10.1126/science.1103190
[3] E. P. Mattos, and A. Vidiella-Barranco, Phys. Rev. A, **104**, 033715 (2021). https://doi.org/10.1103/PhysRevA.104.033715
[4] E. P. Mattos, and A. Vidiella-Barranco, J. Opt. Soc. Am. B, **39**, 1885 (2022). https://doi.org/10.1364/JOSAB.450622
[5] Q. Hu, T. Yusufu, and Y. Turek, Phys. Rev. A, **105**, 022608 (2022). https://doi.org/10.1103/PhysRevA.105.022608
[6] S. K. Giri, B. Sen, C. H. Raymond Ooi, and A. Pathak, Phys. Rev. A, **89**, 033628 (2014). https://doi.org/10.1103/PhysRevA.89.033628
[7] S. K. Giri, B. Sen, A. Pathak, and P. C. Jana, Phys. Rev. A, **93**, 012340(2016). https://doi.org/10.1103/PhysRevA.93.012340
[8] S. K. Giri, K. Thapliyal, B. Sen, and A. Pathak, Physica A, 466, **140** (2017). https://doi.org/10.1016/j.physa.2016.09.004
[9] P. V. P. Pinheiro, and R. V. Ramos, Quant. Infor. Proc. **12**, 537 (2013). https://doi.org/10.1007/s11128-012-0400-0
[10] D. Wang, M. Li, F. Zhu, Z-Q. Yin, W. Chen, Z-F. Han, G-C. Guo, and Q. Wang, Phys. Rev. A, **90**, 062315 (2014). https://doi.org/10.1103/PhysRevA.90.062315
[11] Q. Dai, and H. Jing, Inter. J. Theor. Phys. **47**, 2716 (2008), https://doi.org/10.1007/s10773-008-9710-5
[12] D. Braun, P. Jian, O. Pinel, and N. Treps, Phys. Rev. A, **90**, 013821 (2014). https://doi.org/10.1103/PhysRevA.90.013821
[13] S. A. Podoshvedov, Phys. Rev. A, **79**, 012319 (2009), https://doi.org/10.1103/PhysRevA.79.012319
[14] J-J. Chen, C-H. Zhang, J-M. Chen, C-M. Zhang, and Q. Wang, Quant. Infor. Proc. **19**, 198 (2020). https://doi.org/10.1007/s11128-020-02695-5
[15] S. U. Shringarpure, and J. D. Franson, Phys. Rev. A, **100**, 043802 (2019). https://doi.org/10.1103/PhysRevA.100.043802
[16] J. T. Francis, and M. S. Tame, Phys. Rev. A, **102**, 043709 (2020). https://doi.org/10.1103/PhysRevA.102.043709
[17] Y. Turek, N. Aishan, and A. Islam, Phys. Scr. **98**, 075103 (2023). https://iopscience.iop.org/article/10.1088/1402-4896/acdcca
[18] C. C. Gerry, and P. L. Knight, *Introductory Quantum Optics*, (Cambridge, New York, 2005), pp. 150-165.
[19] L. Mandel, Opt. Lett. 4, **205** (1979). https://doi.org/10.1364/OL.4.000205
[20] S. Luo, and Y. Zhang, Phys. Rev. A, **100**, 032116 (2019). https://doi.org/10.1103/PhysRevA.100.032116
[21] S. Luo, Phys. Rev. Lett. **91**, 180403 (2003), https://doi.org/10.1103/PhysRevLett.91.180403
[22] S. Luo, and Y. Sun, Phys. Rev. A, **98**, 012113 (2018). https://doi.org/10.1103/PhysRevA.98.012113
[23] S. Luo, and Y. Sun, Phys. Rev. A, **96**, 022130 (2017). https://doi.org/10.1103/PhysRevA.96.022130

НЕКЛАСИЧНІСТЬ СУПЕРПОЗИЦІЙНОГО СТАНУ КОГЕРЕНТНОГО І ФОТОННО-ДОДАНОГО КОГЕРЕНТНОГО СТАНУ

Сандіп Кумар Гірі
Факультет фізики, Коледж Панскура Банамалі, Панскура-721152, Індія

Аналітично досліджено некласичні властивості гібридного когерентного стану (HCS), який є станом суперпозиції когерентного стану та фотонно-доданого когерентного стану (PAC). Ми оцінили статистику кількості фотонів, інформацію про викривлення Вігнера-Янасе, Q-фактор Манделя та квадратурне стиснення HCS, щоб кількісно визначити його некласичність. Цей стан суперпозиції демонструє більше некласичних властивостей, ніж стан PAC і навіть стан суперпозиції когерентного стану та однофотонно-доданого когерентного стану (SPAC). Ми повідомляємо, що додавання більшої кількості фотонів до частини стану PAC HCS загалом кількісно визначає більше некласичностей. Некласичні властивості HCS також залежать від амплітуд когерентного стану та стану PAC у HCS.

Ключові слова: *когерентний стан; фотонно-доданий когерентний стан; гібридний когерентний стан; спотворена інформація Вігнера-Янасе; Q фактор Манделя; квадратурне видавлювання; некласичний ефект*

THERMAL PROPERTIES AND MASS SPECTRA OF HEAVY MESONS IN THE PRESENCE OF A POINT-LIKE DEFECT

⬤Etido P. Inyang[a,c*], ⬤N. Ali[c,e], ⬤R. Endut[c,e], ⬤N. Rusli[b], ⬤S.A. Aljunid[c,e], ⬤N.R. Ali[f], ⬤M. Asjad[d]

[a]*Department of Physics, National Open University of Nigeria, Jabi-Abuja, Nigeria*
[b]*Institute of Engineering Mathematics, Universiti Malaysia Perlis, 02600 Arau, Perlis, Malaysia*
[c]*Faculty of Electronic Engineering & Technology, Universiti Malaysia Perlis, 02600 Arau, Perlis, Malaysia*
[d]*Department of Mathematics, Khalifa University, Abu Dhabi 127788, United Arab Emirates*
[e]*Centre of Excellence Advanced Communication Engineering (ACE), Universiti Malaysia Perlis, 02600 Arau, Perlis, Malaysia*
[f]*School of Electrical and Electronic Engineering, Universiti Sains Malaysia, Engineering Campus, Nibong Tebal, Penang, Malaysia*
Corresponding Author e-mail: einyang@noun.edu.ng

In this research, the radial Schrödinger equation is solved analytically using the Nikiforov-Uvarov method with the Cornell potential. The energy spectrum and the corresponding wave function are obtained in close form. The effect of Topological Defect on the thermal properties and mass spectra of heavy mesons such as charmonium and bottomonium are studied with the obtained energy spectrum. It is found that the presence of the Topological Defect increases the mass spectra and moves the values close to the experimental data. Our results agreed with the experimental data and are seen to be improved when compared with other works.
Keywords: *Schrödinger equation; Nikiforov-Uvarov method; Cornell Potential; Mass Spectra; Topological Defect*
PACS: 12.39.Jh

I.   INTRODUCTION

Recent years have seen an increase in interest among academics in the study of mass spectra, thermal properties, energy spectra, information theory, and expectation values of a quantum system [1-5]. This is achieved by solving the Schrodinger equation (SE) or the Klein- Gordon equation. In order to determine a system's eigenvalues and eigenfunctions, potential models like the Yukawa potential [6], Eckart potential [7], Hellmann potential [8], Kratzer potential [9], and so on are utilized. Analytical techniques are used to solve these equations with the potential of choice. The majority of analytical techniques used include the Nikiforov-Uvarov (NU) method [10-20], the Nikiforov-Uvarov Functional Analysis (NUFA) method [21-26], the series expansion method (SEM) [27-29], Laplace transformation method (LTM) [30], the Exact Quantization Rule [31,32], WKB approximation method [33-36] and others [37-41]. The Schrodinger equation can be used to study the interactions of the heavy quarkonium system (HQS) [42]. In defining the mass spectra (MS) of the heavy quarkonium system, such as bottomonium and charmonium, the solutions of the Schrodinger equation with spherically symmetric potentials are of great importance [43,44]. Confining-type potentials, such as the Cornell potential (CP) with two terms, a confining and a Coulomb interaction term, are typically utilized to analyze this system [45]. Several authors have been interested in the investigation of the heavy quarkonium system with the Cornell potential [46-49]. For instance, Kumar et al.,[50] solved the Schrodinger equation with the generalized Cornell potential and the result was used to calculate the mass spectra of the heavy mesons (HMs). Vega and Flores, [51] studied the mass spectra of the heavy mesons using the Cornell potential. Also, Mutuk [52] solved the Schrodinger equation with the Cornell potential using a neural network approach. The bottomonium, charmonium, and bottom-charmed spectra were calculated. Additionally, Hassanabadi et al. [53], used the variational method to solve the Schrodinger equation with the Cornell potential. The eigenvalues were used to calculate the mesonic wave function. Furthermore, the thermal properties (TPs) of the heavy mesons have been studied recently with extended Cornell potential and exponential-type potentials [54-58]. Researchers have been interested in the study of quantum systems interacting with a single particle in a specific potential with a topological defect (TD). It is believed that the early universe phase transition occurs when topological defect was formed [59,60]. Researchers have recently become interested on how topological defect affects the dynamics of both relativistic and non-relativistic systems, including screw dislocation [61], bound electron eigenstates, and holes to a declination. Furtado et al., [62] examined the Landau levels in the presence of a topological defect. Moreover, Hassanabadi and Hosseinpour [63] examined how topological defect affected the hydrogen atom's position in curve-space time. The topological defect plays a vital role in altering the physical properties of many quantum systems, such as condensed matter physics, which it appears as monopoles and strings [64-66]. A linear defect in an elastic medium, such as a dislocation or crack, causes a change in the topology of the medium, which has an effect on the medium's physical characteristics [67]. In light of these observations, no researcher is yet to document how topological defect affects the thermal and mass spectra of the heavy mesons to the best of our knowledge. So, the purpose of this work is to examine how topological defect affects the mass spectra and

thermal properties of the heavy mesons by employing the Nikiforov-Uvarov approach to solve the Schrodinger equation with the Cornell potential. For convenience, we have assumed that our heavy mesons are spinless particles [42,57, 68-70]. This is because most potentials with spin addition cannot be solved analytically, necessitating the employment of numerical methods like the Runge-Kutte approximation [71], Numerov matrix approach [72], Fourier grid Hamiltonian method [73], and so on [74].

II.   THE MODEL

For space time with a point-like global monopole (PGM), the line element that explains it, takes the form [75]

$$ds^2 = -c^2 dt^2 + \frac{dr^2}{\alpha^2} + r^2 d\theta^2 + r^2 \sin^2\theta d\varphi^2 \tag{1}$$

Where α is the parameter related to the PGM which depends on the energy scale $0 \prec \alpha = 1 - 8\pi G\eta_0^2 \prec 1$. Furthermore, Eq. (1) portrays a space time with scalar curvature. On inserting the potential under consideration, we have

$$R = R_\mu^\mu = \frac{2\left(1-\alpha^2\right)}{r^2} \tag{2}$$

In this way, the Schrodinger equation takes the form

$$-\frac{\hbar^2}{2\mu}\nabla^2_{LB}\psi(\vec{r},t) + V(r,t)\psi(\vec{r},t) = i\hbar\frac{\partial\psi(\vec{r},t)}{\partial t} \tag{3}$$

where μ is the particle's mass, $\nabla^2_{LB} = \frac{1}{\sqrt{g}}\partial_i\left(\sqrt{g}g^{ij}\partial_j\right)$ with $g = \det(g_{ij})$, is the Laplace-Beltrami operator and $V(r,t) = V(r)$ is GMP(1). Thereby, the Schrodinger equation for the GMP in a medium with the presence of the PGM(1) is

$$-\frac{\hbar^2}{2\mu r^2}\left[\begin{array}{l}\alpha^2\frac{\partial}{\partial r}\left(r^2\frac{\partial}{\partial r}\right) + \frac{1}{\sin\theta}\frac{\partial}{\partial\theta}\left(\sin\theta\frac{\partial}{\partial\theta}\right) \\ +\frac{1}{\sin^2\theta}\frac{\partial^2}{\partial\varphi^2}\end{array}\right]\psi(r,\theta,\varphi,t) + V\psi(r,\theta,\varphi,t) = i\hbar\frac{\partial\psi(r,\theta,\varphi,t)}{\partial t} \tag{4}$$

Where the $V(r) = w_1 r - w_2/r$ is the Cornell potential employed for modeling the quarkonium interaction [70]. This model has been greatly utilized for this purpose in recent past by numerous researchers.

Here, let us consider a particular solution to Eq. (5) given in terms of the eigenvalues of the angular momentum operator $\hat{L}^2$ as

$$\psi(r,\theta,\varphi,t) = e^{-\frac{E_{nl}t}{\hbar}}\frac{U(r)}{r}Y_{l,m}(\theta,\varphi) \tag{5}$$

where $Y_{l,m}(\theta,\varphi)$ are spherical harmonics and $R(r)$ is the radial wave function.

On substitution of Eq. (6) into Eq. (4), the radial part of the Schrodinger equation for the Cornell potential in the presence of TD is obtained as follows

$$\frac{d^2 R_{nl}(r)}{dr^2} + \left[\frac{2\mu E_{nl}}{\alpha^2\hbar^2} - \frac{2\mu w_1 r}{\alpha^2\hbar^2} + \frac{2\mu w_2}{\alpha^2\hbar^2 r} - \frac{l(l+1)}{\alpha^2 r^2}\right]R_{nl}(r) = 0 \tag{6}$$

Eq. (6) is not solvable in its present form, Eq. (6) needs to be transformed from $r \to x$ coordinate using the following $x = 1/r$, on application, Eq. (6) is rewritten as follows:

$$\frac{d^2 R_{nl}(x)}{dx^2} + \frac{2}{x}\frac{dR_{nl}(x)}{dx} + \frac{1}{x^4}\left[\frac{2\mu E_{nl}}{\alpha^2\hbar^2} - \frac{2\mu w_1}{\alpha^2\hbar^2 x} + \frac{2\mu w_2 x}{\alpha^2\hbar^2} - \frac{l(l+1)x^2}{\alpha^2}\right]R_{nl}(x) = 0 \tag{7}$$

The approximation scheme on the term w_1/x is introduced by assuming that there is a characteristic radius r_0 of the meson. The approximation scheme is achieved by the expansion of w_1/x in a power series around r_0; i.e. around $\delta \equiv \sim 1/r_0$, up to the second order [56]. By setting $y = x - \delta$ and around $y = 0$ we have;

$$\frac{d^2 R_{nl}(x)}{dx^2} + \frac{2x}{x^2}\frac{dR_{nl}(x)}{dx} + \frac{1}{x^4}\left[-\tilde{\varepsilon} + \tilde{\beta}_1 x - \tilde{\beta}_2 x^2 \right] R_{nl}(x) = 0 \tag{8}$$

where

$$-\tilde{\varepsilon} = \frac{2\mu E_{nl}}{\alpha^2 \hbar^2} - \frac{6\mu w_1}{\alpha^2 \hbar^2 \delta}, \tilde{\beta}_1 = \frac{2\mu w_2}{\alpha^2 \hbar^2} + \frac{6\mu w_1}{\alpha^2 \hbar^2 \delta^2}, and\ \tilde{\beta}_2 = \frac{2\mu w_1}{\alpha^2 \hbar^2 \delta^3} + \frac{l(l+1)}{\alpha^2} \ .$$

The equation above is expressed in the form solvable by the Nikiforov-Uvarov formalism. The major equation closely related with this method is given in the following form;

$$P''(x) + \frac{\tilde{\tau}(x)}{\sigma(x)} P'(x) + \frac{\sigma(x)}{\sigma^2(x)} P(x) = 0 \ . \tag{9}$$

The following is obtained; $\tilde{\tau}(x) = 2x, \sigma(x) = x^2, and\ \tilde{\sigma}(x) = -\tilde{\varepsilon} + \tilde{\beta}_1 x - \tilde{\beta}_2 x^2,$ which shows explicitly that our Eq. (8) satisfies the requirement of the Nikiforov-Uvarov approach. It is worthy to point out also that $\tilde{\sigma}(x), and\ \sigma(x)$ are polynomials of at most second degree, and $\tilde{\tau}(x),$ is at most a polynomial of first degree. The Nikiforov-Uvarov method is a really popular method amongst mathematical scientist and related discipline. Several authors have used this method to solve similar problems of interest [10-20]. Even through the method is quite popular, it will be useful to highlight some details, so as to make our paper self-contained. For this reason, this will be detailed in the appendix. Following the steps outlined in the appendix (Eqs. (A1-A7), the energy equation and radial wave function are obtained as follows

$$E_{nl} = \frac{3w_1}{\delta} - \frac{\alpha^2 \hbar^2}{8\mu}\left[\frac{\frac{6\mu w_1}{\alpha^2 \delta^2 \hbar^2} + \frac{2w_2}{\alpha^2 \hbar^2}}{n + \frac{1}{2} + \sqrt{\frac{1}{4} + \frac{2\mu w_1}{\alpha^2 \delta^3 \hbar^2} + \frac{l(l+1)}{\alpha^2}}} \right]^2 \tag{10}$$

and

$$R_{nl} = N_{nl} x^{-\frac{\tilde{\beta}_1}{2\sqrt{\tilde{\varepsilon}}}} e^{-\frac{\tilde{\varepsilon}}{x\tilde{\varepsilon}}} L_n^{\frac{\tilde{\beta}_1}{\sqrt{\tilde{\varepsilon}}}}\left(\frac{2\tilde{\varepsilon}}{x\sqrt{\tilde{\varepsilon}}} \right) \tag{11}$$

THERMAL PROPERTIES OF THE CORNELL POTENTIAL IN THE PRESENCE OF DEFECT

We introduce the partition function $Z(\beta)$, which provides a measure of thermally accessible states, to explore the thermal properties of the heavy mesons. It can be determined by adding together all possible energy states. Following the Boltzmann-Gibbs distribution, $Z(\beta)$ is given by the relation [76];

$$Z(\beta) = \sum_{n=0}^{n_{max}} e^{-\beta E_{nl}} \ . \tag{12}$$

Where $\beta = 1/kT$ and with k is the Boltzmann constant. Substituting Eq. (10) in Eq. (12), summing over all accessible energy levels, we obtain the partition function as follows:

$$Z(\beta, \alpha, n_{max}) = \left(x_1 e^{\frac{A_4 \beta}{x_1^2}} - e^{\frac{A_4 \beta}{x_2^2}} x_2 - \sqrt{A_4}\sqrt{\pi}\sqrt{\beta}erf\left(\frac{\sqrt{A_4}\sqrt{\beta}}{x_1} \right) + \sqrt{A_4}\sqrt{\pi}\sqrt{\beta}erf\left(\frac{\sqrt{A_4}\sqrt{\beta}}{x_2} \right) \right) . \tag{13}$$

Where the following non-dimensional parameters have been defined for simplicity;

$$x_1 = A_3, x_2 = A_3 + n_{max}, A_1 = \frac{3w_1}{\delta^2}, A_2 = \frac{6w_1\mu}{\alpha^2\delta} + \frac{2w_2\mu}{\alpha^2\delta}. A_3 = \frac{1}{2} + \sqrt{\frac{2w_1\mu}{\hbar^2\alpha^2\delta^3} + \frac{l(l+1)}{\alpha^2\delta} + \frac{1}{4}}, and\ A_4 = \frac{A_2^2\hbar}{8\mu}A_3 .$$

On successful evaluation of the partition function, several other thermodynamic variables can be obtained by using the following;

Internal Energy: $U(\beta) = -\frac{d\ln Z(\beta)}{d\beta}$ [76], The Helmholtz free energy: $F(\beta) = -\frac{1}{\beta}\ln Z(\beta)$ [76], heat capacity;

$C(\beta) = \beta^2 \frac{d^2 \ln Z(\beta)}{d\beta^2}$ [76] and entropy; $S(\beta) = \ln Z(\beta) - \beta \frac{d\ln Z(\beta)}{d\beta}$ [76].

DISCUSSION AND RESULTS

The prediction the mass spectra (MS) of HQS such as charmonium and bottomonium is carried out using the following relation [77,78].

$$M = 2\mu + E_{nl} \tag{14}$$

where μ is quarkonium mass and $E_{n\ell}$ is energy eigenvalues. Substituting Eq. (10) into Eq. (14) gives,

$$M = 2\mu + \frac{3w_1}{\delta} - \frac{\alpha^2\hbar^2}{8\mu}\left[\frac{\frac{6\mu w_1}{\alpha^2\delta^2\hbar^2} + \frac{2w_2}{\alpha^2\hbar^2}}{n + \frac{1}{2} + \sqrt{\frac{1}{4} + \frac{2\mu w_1}{\alpha^2\delta^3\hbar^2} + \frac{l(l+1)}{\alpha^2}}}\right]^2 \tag{15}$$

The numerical values of bottomonium and charmonium masses are $\mu_b = 4.823 GeV$ and $\mu_c = 1.209 GeV$, and the corresponding reduced mass are $\tilde{\mu}_b = 2.4115 GeV$ and $\tilde{\mu}_c = 0.6045 GeV$ respectively [79]. The potential parameters were fitted with experimental data (ED) [80]. This was achieved by solving a simultaneous equation for α equals to 0.1,0.2 and 1 respectively. The mass spectra of the heavy mesons were predicted in the absent and present of the topological defect for different quantum states. In the case of charmonium predictions for 1S and 2S states we noticed that the prediction were accurate with the experimental data in the present and absent of the topological defect. In 3S and 4S, it was noticed that as the topological defect increased to 0.2 the value of the mass spectra was very close to the experimental data. A similar trend was noticed in 1P,2P,1D and 2D states when the topological defect was introduced and the predicted values were close to the experimental data and was seen to be improved from works reported by [27, 30,42] as shown in Table 1.

Table I. Mass spectra of Charmonium in (GeV). The following fitting parameters has been employed; $m_C = 1.209 GeV$, $\mu = 0.6045 GeV$, $W_1 = 0.20 GeV$, $W_2 = 1.244 GeV$, $\delta = 0.231 GeV$, and $\hbar = 1$.

State	α	Our result	AIM [42]	LTM [30]	SEM[27]	Experiment [80]
1S	0.1	3.096	3.096	3.0963	3.095922	3.096
	0.2	3.096	3.096	3.0963	3.095922	3.096
	1.0	3.096	3.096	3.0963	3.095922	3.096
2S	0.1	3.686	3.686	3.5681	3.685893	3.686
	0.2	3.686	3.686	3.5681	3.685893	3.686
	1.0	3.686	3.686	3.5681	3.685893	3.686
3S	0.1	4.040	4.275	4.0400	4.322881	4.040
	0.2	4.040	4.275	4.0400	4.322881	4.040
	1.0	4.040	4.275	4.0400	4.322881	4.040
4S	0.1	4.261	4.865	4.5119	4.989406	4.263
	0.2	4.262	4.865	4.5119	4.989406	4.263
	1.0	4.269	4.865	4.5119	4.989406	4.263
1P	0.1	3.515	3.214	3.5687	-	3.525
	0.2	3.524	3.214	3.5687	-	3.525
	1.0	3.255	3.214	3.5687	-	3.525
2P	0.1	3.771	3.773	3.5687	3.756506	3.773
	0.2	3.772	3.773	3.5687	3.756506	3.773
	1.0	3.779	3.773	3.5687	3.756506	3.773
1D	0.1	3.734	3.412	4.0407	-	3.770
	0.2	3.769	3.412	4.0407	-	3.770
	1.0	3.504	3.412	4.0407	-	3.770
2D	0.1	4.149	-	-	-	4.159
	0.2	4.158	-	-	-	4.159
	1.0	4.146	-	-	-	4.159

In the case of bottomonium, it was observed that for 1S, and 2S quantum states the mass spectra were all equal to the experimental data and works reported by [27, 30,42] as shown in Table 2. It was noticed that for 3S and 4S states, a significant change in the mass spectra was observed when the topological defect was set to 0.1 and 0.2. A similar trend was observed with other predicted states when the topological defect was increased as shown in Table 2.

Table II. Mass spectra of Bottomonium in (GeV). The following fitting parameters has been employed; $m_b = 4.823\ GeV$, $\mu = 2.4115\ GeV$, $W_1 = 0.20 GeV$, $W_2 = 1.569\ GeV$, $\delta = 0.378\ GeV$, and $\hbar = 1$.

State	α	Our result	AIM [42]	LTM [30]	SEM[27]	Experiment [80]
1S	0.1	9.460	9.460	9.745	9.515194	9.460
	0.2	9.460	9.460	9.745	9.515194	9.460
	1.0	9.460	9.460	9.745	9.515194	9.460

State	α	Our result	AIM [42]	LTM [30]	SEM[27]	Experiment [80]
2S	0.1	10.023	10.023	10.023	10.01801	10.023
	0.2	10.023	10.023	10.023	10.01801	10.023
	1.0	10.023	10.023	10.023	10.01801	10.023
3S	0.1	10.355	10.585	10.302	10.44142	10.355
	0.2	10.355	10.585	10.302	10.44142	10.355
	1.0	10.355	10.585	10.302	10.44142	10.355
4S	0.1	10.570	11.148	10.580	10.85777	10.580
	0.2	10.577	11.148	10.580	10.85777	10.580
	1.0	10.567	11.148	10.580	10.85777	10.580
1P	0.1	9.879	9.492	10.025	-	9.899
	0.2	9.789	9.492	10.025	-	9.899
	1.0	9.619	9.492	10.025	-	9.899
2P	0.1	10.230	10.038	10.303	10.09446	10.260
	0.2	10.124	10.038	10.303	10.09446	10.260
	1.0	10.114	10.038	10.303	10.09446	10.260
1D	0.1	9.994	9.551	10.303	-	10.164
	0.2	9.999	9.551	10.303	-	10.164
	1.0	9.864	9.551	10.303	-	10.164

We observed that the results obtained from the prediction of the mass spectra of charmonium and bottomonium for different quantum states are in agreement with the experimental data and are improved with the reports of [27, 30,42]. The thermal properties for charmonium are plotted as shown in Fig. 1(a-e).
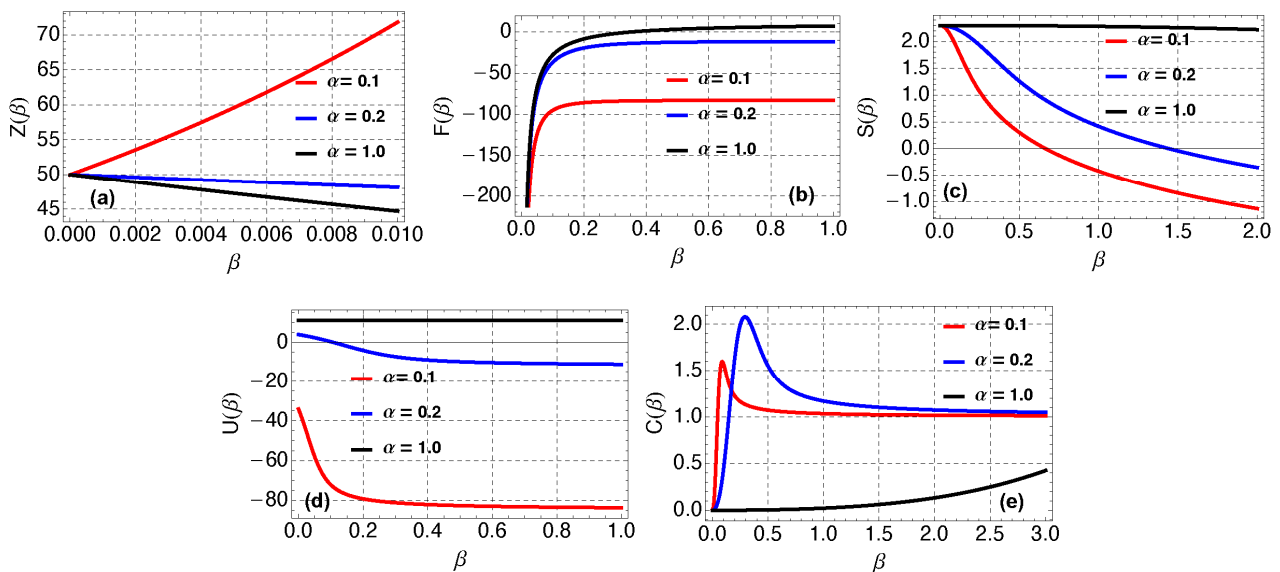

Figure 1. (a) Partition of Charmonium versus β. (b) Free Energy of Charmonium versus β. (c) Entropy of Charmonium versus β.(d) Mean Energy of Charmonium versus β. (e) Specific Heat Capacity of Charmonium versus β. For all five plots, α = 0.1 (red curve), α = 0.2 (blue curve) and α = 1.0 (red curve); all other parameters are the same as in Table (I).

In Fig. 1 (a), the partition function for topological defect = 0.1 shows a linear increase when the temperature is increased. When topological defect is equal to 0.2 and 1.0, the partition function is seen to decrease with an increase in temperature; same behavior is reported by Abu Shady et al., [55] and Kumar et al., [58]. In Fig. 1 (b), the free energy (FE) is plotted against temperature, we noticed that as the topological defect increases from 0.1 to 1.0, the free energy increases, which is in agreement with the experimental data. In Fig. 1 (c), the entropy of the system for charmonium is plotted. It is observed that when topological defect is equal to 0.1 and 0.2, the entropy is seen to decrease as the temperature increases, but when topological defect = 1.0, we noticed a steady entropy as the temperature is increased. In Fig.1 (d), the internal energy (IE) is plotted as a function of temperature. When topological defect = 1.0, a steady internal energy is noticed, but for topological defect = 0.1 and 0.2 an exponential decrease is observed followed by the internal energy of the system being steady when the temperature increases. Abu-Shady et al., [55] reported a decrease with increasing of temperature and maximum quantum number, our trend is on the expected line.

In Fig. 2 (a-e), the thermal properties of bottomonium is plotted as shown. In Fig.2 (a), the partition function is plotted as a function of temperature. When the topological defect = 0.1 a linear increase is noticed. For topological defect = 0.2 and 1.0, a slight increase and no increase on the partition function is seen respectively. In Fig. 2 (b), the free energy of the bottomonium is plotted against the temperature. We observed as the topological

defect increases, the free energy is seen to increase. A similar observation was reported by Abu-Shady et al [55] and Kumar et al [58]. In Fig. 2 (c), the entropy is plotted against temperature for different values of topological defect, it was noticed that the entropy decreases with an increase in temperature. In [55,58] the authors found the entropy decreases with increasing temperature. In Fig. 2 (d), the inter energy plots shows that when topological defect = 1.0, no increase in the internal energy is noticed, but for topological defect = 0.1 and 0.2 a slight decrease is seen at the beginning then followed a constant value in the internal energy. In Fig.2 (e), the specific heat capacity is plotted against temperature. A sharp increase in specific heat capacity is noticed for topological defect = 0.1 and 0.2 and later converges at a point when the m specific heat capacity = 1. An exponential increase is noticed when topological defect = 1.
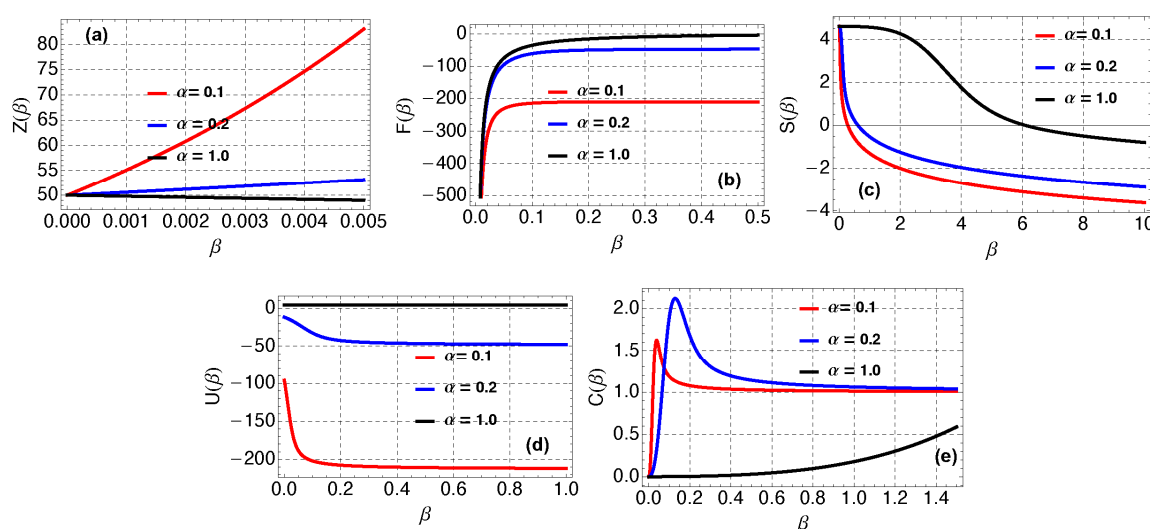
Figure 2. (a) Partition of Bottomonium versus β. (b) Free Energy of Bottomonium versus β. (c) Entropy of Bottomonium versus β.(d) Mean Energy of Bottomonium versus β. (e) Specific Heat Capacity of Bottomonium versus β. For all five plots, α = 0.1 (red curve), α = 0.2 (blue curve) and α = 1.0 (red curve); all other parameters are the same as in Table (II)

CONCLUSION

In this study, the effect of the topological defect on the mass spectra of heavy mesons is studied with the Cornell potential. The Schrodinger equation was solved analytically using the Nikiforov-Uvarov method. The approximate solutions of the energy spectrum and wave function in terms of Laguerre polynomials were obtained. We apply the present results to predict the mass spectra of heavy mesons such as charmonium and bottomonium in the present and absent of the topological defect for different quantum states and its thermal properties. We noticed that when the topological defect increases the mass spectra and moves closer to the experimental data. However, the results obtained showed an improvement when compared with the work of other researchers.

Authors Declaration

Conflicts of interest/Competing interest
All the authors declared that there is no conflict of interest in this manuscript

ORCID
 Etido P. Inyang, https://orcid.org/0000-0002-5031-3297; **Norshamsuri Ali,** https://orcid.org/0000-0002-9348-0714
 Rosdisham Endut, https://orcid.org/0000-0003-3659-9740; **Nursalasawati Rusli,** https://orcid.org/0009-0006-0153-8461
 Muhammad Asjad, https://orcid.org/0000-0001-6895-3332; **Syed Alwee Aljunid,** https://orcid.org/0000-0003-2739-6220
 Norshah Rizal Ali, https://orcid.org/0000-0002-6031-666x

REFERENCES
[1] E.P. Inyang, E.S. William, J.O. Obu, B.I. Ita, E.P. Inyang, and I.O. Akpan, "Energy spectra and expectation values of selected diatomic molecules through the solutions of Klein-Gordon equation with Eckart-Hellmann potential model," Molecular Physics. **119**(23), e1956615 (2021). https://doi.org/10.1080/00268976.2021.1956615
[2] E. Omugbe, O.E. Osafile, I.B. Okon, E.P. Inyang, E.S. William, and A. Jahanshir, "Any L-state energy of the spinless Salpeter equation under the Cornell potential by the WKB Approximation method: An Application to mass spectra of mesons," Few-Body Systems, **63**, 7 (2022). https://doi.org/10.1007/s00601-021-01705-1

[3] E.P. Inyang, E. Omugbe, M. Abu-shady and E.S. William, "Investigation of Quantum Information Theory with the screened modified Kratzer and a class of Yukawa potential model," The European Physical Journal Plus, **138**, 969 (2023). https://doi.org/10.1140/epjp/s13360-023-04617-7

[4] J.A. Obu, E.P. Inyang, J.E. Ntibi, I.O. Akpan, E.S. William, and E.P. Inyang, "The Effect of Debye Mass on the Mass Spectra of Heavy Quarkonium System and Its Thermal Properties with Class of Yukawa Potential," Jordan Journal of Physics, **16**(3), 329-339 (2023). https://doi.org/10.47011/16.3.8

[5] F.O. Faithpraise, and E.P. Inyang, "Bound State and Ro-Vibrational Energies Eigenvalues Of Selected Diatomic Molecules With A Class Of Inversely Quadratic Yukawa Plus Hulthén Potential Model," East European Journal of Physics, 3, 158-166 (2023). https://doi.org/10.26565/2312-4334-2023-3-12

[6] E.P. Inyang, E.P. Inyang, J.E. Ntibi, E.E. Ibekwe, and E.S. William, **"**Approximate solutions of D-dimensional Klein-Gordon equation with Yukawa potential via Nikiforov-Uvarov method**"**, Indian Journal of Physics, **95**, 2733–2739 (2021). https://doi.org/10.1007/s12648-020-01933-x

[7] C. Eckart, "The Penetration of a potential Barrier by Electrons," Phys. Rev. **35**, 1303 (1930). https://doi.org/10.1103/PhysRev.35.1303

[8] H. Hellmann, "A New Approximation Method in the Problem of Many Electrons," J. Chem. Phys. **3**, 61 (1935). https://doi.org/10.1063/1.1749559

[9] S. Hassanabadi, A.A. Rajabi, and S. Zarrinkamar, "Cornell and Kratzer potentials within the semi-relativistic treatment," Mod. Phys. Lett. A. **27**, 1250057 (2012). https://doi.org/10.1142/S0217732312500575

[10] E.S. William, E.P. Inyang, I.O. Akpan, J.A. Obu, A.N. Nwachukwu, and E.P. Inyang, "Ro-vibrational energies and expectation values of selected diatomic molecules via Varshni plus modified Kratzer potential model," Indian Journal of Physics, **96**, 3461-3476 (2022). https://doi.org/10.1007/s12648-022-02308-0

[11] E.P. Inyang, E.P. Inyang, E.S. William, and E.E. Ibekwe, "Study on the applicability of Varshni potential to predict the mass-spectra of the Quark-antiquark systems in a non-relativistic framework," Jordan Journal of Physics, **14**(4), 339-347 (2021). https://doi.org/10.47011/14.4.8

[12] I.O. Akpan, E.P. Inyang, E.P. Inyang, and E.S. William, "Approximate solutions of the Schrödinger equation with Hulthen-Hellmann Potentials for a Quarkonium system," Revista Mexica De Fisica, **67**(3), 482-490 (2021). https://doi.org/10.31349/RevMexFis.67.482

[13] J.A. Obu, E.P. Inyang, E.S. William, D.E. Bassey, and E.P. Inyang, "Comparative Study of The Mass Spectra of Heavy Quarkonium System with an Interacting Potential Mode," East Eur. J. Phys. 3, 146-157 (2023). https://doi.org/10.26565/2312-4334-2023-3-11

[14] E.P. Inyang, J. Ntibi, E.A. Ibanga, F. Ayedun, E.P. Inyang, and E. William, "Thermal Properties, Mass Spectra and Root Mean Square Radii of Heavy Quarkonium System with Class of Inversely Quadratic Yukawa Potential," AIP Conference Proceedings **2679**, 030003 (2023). https://doi.org/10.1063/5.0112829

[15] E.S. William, S.C. Onye, A.N. Ikot, A.N. Nwachukwu, E.P. Inyang, I.B. Okon, I.O. Akpan, and B.I. Ita, "Magnetic susceptibility and Magnetocaloric effect of Frost-Musulin potential subjected to Magnetic and Aharonov-Bohm (Flux) for CO and NO diatomic molecules," Journal of Theoretical and Applied Physics, **17**(12), 172318 (2023). https://doi.org/10.30495/JTAP.172318

[16] F. Ayedun, E.P. Inyang, E.A. Ibanga, and K.M. Lawal, "Analytical Solutions to The Schrödinger Equation with Collective Potential Models: Application to Quantum Information Theory," East Eur. J. Phys. 4, 87-98 (2022). https://doi.org/10.26565/2312-4334-2022-4-06

[17] E.S. William, E.P. Inyang and E.A. Thompson, "Arbitrary l -solutions of the Schrödinger equation interacting with Hulthen-Hellmann potential model," Revista Mexicana de Fisica, **66**(6), 730-741 (2020). https://doi.org/10.31349/RevMexFis.66.730

[18] E.P. Inyang, E.O. Obisung, J. Amajama, D.E Bassey, E.S William, and I.B. Okon, "The Effect of Topological Defect on the Mass Spectra of Heavy and Heavy-Light Quarkonia," Eurasian Physical Technical Journal, **19**(4), 78-87 (2022). https://doi.org/10.31489/2022No4/78-87

[19] E.P. Inyang, E.O. Obisung, P.C. Iwuji, J.E. Ntibi, J. Amajama, and E.S. William, "Masses and thermal properties of a Charmonium and Bottomonium Mesons," Journal of the Nigerian Society of Physical Sciences, **4**, 875-884 (2022). https://doi.org/10.46481/jnsps.2022.884

[20] E.P. Inyang, and E.O. Obisung, "The study of electronic states of NI and ScI molecules with screened Kratzer potential," East European Journal of Physics, 3, 32-38 (2022). https://doi.org/10.26565/2312-4334-2022-3-04

[21] A.N. Ikot, U.S. Okorie, P.O. Amadi, C.O. Edet, G.J. Rampho, and R. Sever, "The Nikiforov-Uvarov –Functional Analysis (NUFA) Method: A new approach for solving exponential – Type potentials," Few-Body System, **62,** 9 (2021). https://doi.org/10.1007/s00601-021-021-01593-5

[22] E.P. Inyang, P.C. Iwuji, J.E. Ntibi, E. Omugbe, E.A. Ibanga, and E.S. William, "Quark-antiquark study with inversely quadratic Yukawa potential using Nikiforov-Uvarov-Functional analysis method," East European Journal of Physics**, 2,** 43-51 (2022). https://doi.org/10.26565/2312-4334-2022-2-05

[23] E.P. Inyang, E.P. Inyang, E.S. William**,** J.E. Ntibi**,** and E.A. Ibanga, "Bound State Solutions of the Schrödinger equation with Frost-Musulin potential using the Nikiforov-Uvarov-Functional Analysis (NUFA) method," Bulgarian Journal of Physics, **49**(4), 329-339 (2022). https://doi.org/10.55318/bgjp.2022.49.4.329

[24] I.B. Okon, C.A. Onate, R. Horchani, O.O. Popoola, E. Omugbe, E.S. William, U.S. Okorie, et al., "Thermomagnetic properties and its efects on Fisher entropy with Schioberg plus Manning-Rosen potential (SPMRP) using Nikiforov-Uvarov functional analysis (NUFA) and supersymmetric quantum mechanics (SUSYQM) methods," Scientifc Reports, **13**, 8193 (2023). https://doi.org/10.1038/s41598-023-34521-0

[25] E.P. Inyang, E.S. William, E. Omugbe, E.P. Inyang, E.A. Ibanga, F. Ayedun, I.O. Akpan, and J.E. Ntibi, "Application of Eckart-Hellmann potential to study selected diatomic molecules using Nikiforov-Uvarov-Functional analysis method," Revista Mexicana de Fisica, **68**, 020401 (2022). https://doi.org/10.31349/RevMexFis.68.020401

[26] E.P. Inyang, E.S. William, J.E. Ntibi, J.A. Obu, P.C. Iwuji, and E.P. Inyang, "Approximate solutions of the Schrodinger equation with Hulthen plus screened Kratzer potential using the Nikiforov-Uvarov-Functional analysis method: An Application to diatomic molecules," Canadian Journal of Physics, **100**(10), (2022). https://doi.org/10.1139/cjp-2022-0030

[27] E.E. Ibekwe, U.S. Okorie, J.B. Emah, E.P. Inyang, and S.A. Ekong, "Mass spectrum of heavy quarkonium for screened Kratzer potential (SKP) using series expansion method," Eur. Phys. J. Plus, **87,** 136 (2021). https://doi.org/10.1140/epjp/s13360-021-01090-y

[28] E.P. Inyang, P.C. Iwuji, J.E. Ntibi, E.S. William, and E.A. Ibanga, "Solutions of the Schrodinger equation with Hulthen – screened Kratzer potential: Application to diatomic molecules," East European Journal of Physics, 1, 12-22 (2022). https://doi.org/10.26565/2312-4334-2022-2-02

[29] E.P. Inyang, E.P. Inyang, J.E. Ntibi, and E.S. William, "Analytical solutions of the Schrödinger equation with Kratzer-screened Coulomb potential for a Quarkonium system," Bulletin of Pure and applied Sciences - Physics, **40**(1), 12-24 (2020). https://acspublisher.com/journals/index.php/bpasphy/article/view/8660

[30] M. Abu-Shady, T.A. Abdel-Karim, and E.M. Khokha, "Exact solution of the N-dimensional Radial Schrödinger Equation via Laplace Transformation method with the Generalized Cornell potential," Journal of theoretical Physics, **45**, 567-587 (2018). https://doi.org/10.48550/arXiv.1802.02092

[31] E.P. Inyang, I.B. Okon, F.O. Faithpraise, E.S. William, P.O. Okoi, and E.A. Ibanga, "Quantum mechanical treatment of Shannon entropy measure and energy spectra of selected diatomic molecules with the modified Kratzer plus generalized inverse quadratic Yukawa potential model," Journal of Theoretical and Applied Physics, **17**(4), 1-13 (2023). https://dx.doi.org/10.57647/j.jtap.2023.1704.40

[32] E.P. Inyang, F.O. Faithpraise, J. Amajama, E.S. William, E.O. Obisung, and J.E. Ntibi, "Theoretical Investigation of Meson Spectrum using Exact Quantization Rule Technique," East European Journal of Physics, 1, 53-62 (2023). https://doi.org/10.26565/2312-4334-2023-1-05

[33] E. Omugbe, O.E. Osafile, and M.C. Onyeajh, "Mass spectrum of mesons via WKB Approximation method," Advances in High Energy Physics, **10**, 1143 (2020). https://doi.org/10.1155/2020/5901464

[34] E. Omugbe, O.E. Osafile, E.P. Inyang, and A. Jahanshir, "Bound state solutions of the hyper-radial Klein-Gordon equation under the Deng-Fan potential by WKB and SWKB methods," Physica Scripta, **96**(12), 125408 (2021). https://doi.org/10.1088/1402-4896/ac38d4

[35] E. Omugbe, E.P. Inyang, I.J. Njoku, C. Martínez-Flores, A. Jahanshir, I.B. Okon, E.S. Eyube, et al., "Approximate mass spectra and root mean square radii of quarkonia using Cornell potential plus spin-spin interactions," Nuclear Physics A, **1034**, 122653 (2023). https://doi.org/10.1016/j.nuclphysa.2023.122653

[36] E. Omugbe, J.N. Aniezi, E.P. Inyang, I.J. Njoku, C.A. Onate, E.S. Eyube, S.O. Ogundeji, et al., "Non-relativistic Mass Spectra Splitting of Heavy Mesons Under the Cornell Potential Perturbed by Spin–Spin, Spin–Orbit and Tensor Components," Few-Body System, **64**, 66 (2023). https://doi.org/10.1007/s00601-023-01848-3

[37] C.O. Edet, S. Mahmoud, E.P. Inyang, N. Ali, S.A. Aljunid, R. Endut, A.N. Ikot, and M. Asjad, "Non-Relativistic Treatment of the 2D Electron System Interacting via Varshni-Shukla Potential Using the Asymptoptic Iteration Method," Mathematics, **10**, 2824 (2022). https://doi.org/10.3390/math10152824

[38] C.O. Edet, E.B. Al, F. Ungan, E.P. Inyang, N. Ali, M.M. Ramli, R. Endut, and S.A. Aljunid, "Influence of perturbations on linear and nonlinear optical properties of quantum dot," The European Physical Journal Plus, **138**, 904 (2023). https://doi.org/10.1140/epjp/s13360-023-04519-8

[39] M. Abu-Shady, and E.P. Inyang, "The Fractional Schrödinger Equation With The Generalized Woods-Saxon Potential," East European Journal of Physics, 1, 63-68 (2023). https://doi.org/10.26565/2312-4334-2023-1-06

[40] A.N. Ikot, L.F. Obagboye, U.S. Okorie, E.P. Inyang, P.O. Amadi, and A. Abdel-Aty, "Solutions of Schrodinger equation with generalized Cornell potential (GCP) and its applications to diatomic molecular systems in D-dimensions using Extended Nikiforov–Uvarov (ENU) formalism," The European Physical Journal Plus, **137**, 1370 (2022). https://doi.org/10.1140/epjp/s13360-022-03590-x

[41] M. Abu-Shady, and E.P. Inyang, "Heavy-Light Meson masses in the Framework of Trigonometric Rosen-Morse Potential using the Generalized Fractional Derivative," East European Journal of Physics, 4, 80-87 (2022). https://doi.org/10.26565/2312-4334-2022-4-06

[42] H. Ciftci, and H.F. Kisoglu, "Nonrelativistic-Arbitrary l-states of quarkonium through Asymptotic Iteration method," Advances in High Energy Physics, **2018**, 4549705 (2018). https://doi.org/10.1155/2018/4549705

[43] H. Mutuk, "Mass Spectra and Decay constants of Heavy-light Mesons: A case study of QCD sum Rules and Quark model," Advan. in High Energy Phys. 8095653 (2018). https://doi.org/10.1155/2018/8095653

[44] M. Allosh, Y. Mustafa, N.K. Ahmed, and A.S. Mustafa, "Ground and Excited state mass spectra and properties of heavy-light mesons," Few-Body Syst. **62**, 26 (2021). https://doi.org/10.1007/s00601-021-01608-1

[45] M.S. Ali, G.S. Hassan, A.M. Abdelmonem, S.K. Elshamndy, F. Elmasry, and A.M. Yasser, "The spectrum of charmed quarkonium in non-relativistic quark model using matrix Numerov's method," J. Rad. Research and Applied Sciences, **13**, 233 (2020). https://doi.org/10.1080/16878507.2020.1723949

[46] H. Mansour, and A. Gamal, "Bound state of Heavy Quarks using a General polynomial potential," Adv. in High Ener. Phys. 7269657 (2018). https://doi.org/10.1155/2018/7269657

[47] A. Al-Oun, A. Al-Jamel, and H. Widyan, "Various properties of Heavy Quakonium from Flavor-independent Coulomb plus Quadratic potential," Jord. J. Phys. **40**, 453-464 (2015).

[48] M. Abu-Shady, "N-dimensional Schrödinger equation at finite temperature using the Nikiforov-Uvarov method," J. Egypt. Math. Soc. **25**, 86-89 (2017). https://doi.org/10.1016/j.joems.2016.06.006

[49] R. Rani, S.B. Bhardwaj and F. Chand, "Mass spectra of heavy and light mesons using asymptotic iteration method," Commun. Theor. Phys. **70**, 179 (2018). https://doi.org/10.1088/0253-6102/70/2/179

[50] R. Kumar, R.M. Singh, S.B. Bhahardivaj, R. Rani and F. Chand, "Analytical solutions to the Schrodinger equation for generalized Cornell potential and its application to diatomic molecules and heavy mesons," Mod. Phys. Lett. A, **37**, 2250010 (2022). https://doi.org/10.1142/S0217732322500109

[51] A. Vega and J. Flores, "Heavy quarkonium properties from Cornell potential using variational method and supersymmetric quantum mechanics," Pramana-J. Phys. **87**, 73 (2016). https://doi.org/10.1007/s12043-016-1278-7

[52] H. Mutuk, "Cornell Potential: A Neural Network Approach," Advan. in High Energy Phys. **2019**, 3105373 (2019). https://doi.org/10.1155/2019/3105373

[53] H. Hassanabadi, M. Ghafourian and S. Rahmani, "Study of the Heavy-Light mesons properties via the Variational method for Cornell interaction," Few-Body Syst. **57**, 249–254 (2016). https://doi.org/10.1007/s00601-015-1040-6

[54] E.P. Inyang, A.N. Ikot, E.P. Inyang, I.O. Akpan, J.E. Ntibi, E. Omugbe, and E.S. William, "Analytic study of thermal properties and masses of heavy mesons with quarkonium potential," Results in Physics. **39**, 105754 (2022). https://doi.org/10.1016/j.rinp.2022.105754

[55] M. Abu-Shady, T.A. Abdel-Karim, and Y. Ezz-Alarab, "Masses and thermodynamic properties of heavy mesons in the non-relativistic quark model using the Nikiforov-Uvarov method", Journal of Egyptian Mathematical Society, **23**, 155 (2019). https://doi.org/10.1186/s42787-019-0014-0

[56] E.P. Inyang, E.P. Inyang, I.O. Akpan, J.E. Ntibi, and E.S. William, "Masses and thermodynamic properties of a Quarkonium system," Canadian Journal Physics, **99**, 990 (2021). https://doi.org/10.1139/cjp-2020-0578

[57] M. Abu-Shady, and S.Y. Ezz-Alarab, "Trigonometric Rosen–Morse Potential as a Quark–Antiquark Interaction Potential for Meson Properties in the Non-relativistic Quark Model Using EAIM," Few-Body Systems, **60** 66 (2019). https://doi.org/10.1007/s00601-019-1531-y

[58] V. Kumar, S.B. Bhardwaj, R.M. Singh and F. Chand, "Mass spectra and thermodynamic properties of some heavy and light mesons," Pramana J. Phys. **96**, 125 (2022). https://doi.org/10.1007/s12043-022-02377-0

[59] C.O. Edet, and A.N. Ikot, "Effect of Topological Defect on the Energy spectra and Thermo-magnetic properties of CO diatomic molecule," J. Low Temp. Phys. **203**, 84-111 (2021). https://doi.org/10.1007/s10909-021-02577-9

[60] A. Vilenkin, and E.P.S. Shellard, *Cosmic Strings and other Topological Defects*, (Cambridge University Press, Cambridge, UK, 1994).

[61] C. Furtado, and F. Morades, "Landau levels in the presence of a screw dislocation," Europhys. Lett. **45**, 279-282 (1999). https://doi.org/10.1209/epl/i1999-00159-8

[62] C. Furtado, and F. Morades, "On the binding of electrons and holes to disclinations," Phys. Lett. A, **188**, 394-396 (1994). https://doi.org/10.1016/0375-9601(94)90482-0

[63] H. Hassanabadi, and M. Hosseinpour, "Thermodynamic properties of neutral particle in the presence of topological defects in magnetic cosmic string background," Eur. Phys. J. C, **76**, 553 (2016). https://doi.org/10.1140/epjc/s10052-016-4392-2

[64] P. Nwabuzor, C. Edet, A.N. Ikot, U. Okorie, M. Ramantswana, R. Horchani, A. Abdel-Aty, and G. Rampho, "Analyzing the effects of Topological Defect (TD) on the Energy spectra and Thermal Properties of LiH, TiC and I_2 diatomic molecules," Entropy, **23**(8), 1060 (2021). https://doi.org/10.3390/e23081060

[65] A. Vilenkin, "Cosmic Strings and domain walls," Phys. Rep. **121**, 263-315 (1985). https://doi.org/10.1016/0370-1573(85)90033-X

[66] M. Barriola, and A. Vilenkin, "Gravitational field of a global monopole," Phys. Rev. Lett. **63**, 341 (1989). https://doi.org/10.1103/PhysRevLett.63.341

[67] G. De A. Marques, C. Furtado, V.B. Bezerra, and F. Moraes, "Landau levels in the presence of topological defects," J. Phys. A, Math. Gen. **34**, 5945 (2001). https://doi.org/10.1088/0305-4470/34/30/306

[68] S. Jacobs, M.G. Olsson, and C. Suchyta, "Comparing the Schrodinger and Spinless Salpeter equations for heavy-quark bound states," Physical Review D, **33**, 3338 (1986). https://doi.org/10.1103/PhysRevD.33.3338

[69] B. Grinstein, "A modern introduction to quarkonium theory," Int. J. Mod. Phys. **15**, 461-495 (2000). https://doi.org/10.1142/S0217751X00000227

[70] W. Lucha, F. Schoberl, and D. Gromes, "Bound states of quarks," Phys. Reports. **200**, 127-240 (1991). https://doi.org/10.1016/0370-1573(91)90001-3

[71] S. Patel, P.C. Vinodkumar, and S. Bhatnagar, "Decay rates of charmonia within a quark-antiquark confining potential," Chinese Physics C, **40**, 053102 (2016). https://doi.org/10.1088/1674-1137/40/5/053102

[72] V. Mateu, P.G. Ortega, D.R. Entem, and F. Fernadez, "Calibrating the nave Cornell model with NRQCD," The European Physical Journal C, **79**, 323 (2019). https://doi.org/10.1140/epjc/s10052-019-6808-2

[73] F. Brau, and C. Sernay, "The three-dimensional Fourier grid Hamiltonian method," Journal of computational physics, **139**, 127-136 (1998). https://doi.org/10.1006/jcph.1997.5866

[74] A. Bhaghyesh, "Charmonium properties using the Discrete variable representation (DVR)method," Advances in High Energy Physics, **2021**, 9991152 (2021). https://doi.org/10.1155/2021/9991152

[75] C.O. Edet, and P.O. Okoi, "Any l-state solutions of the Schrodinger equation for q-deformed Hulthen plus generalized inverse quadratic Yukawa potential in arbitrary dimensions," Revista Mexicana De Fisica, **65**, 333-344 (2019). https://doi.org/10.31349/RevMexFis.65.333

[76] E.P. Inyang, F. Ayedun, E.A. Ibanga, K.M. Lawal, I.B. Okon, E.S. William, O. Ekwevugbe, et al., "Analytical Solutions of the N-Dimensional Schrödinger equation with modified screened Kratzer plus Inversely Quadratic Yukawa potential and Thermodynamic Properties of selected Diatomic Molecules," Results in Physics, 43, 106075 (2022). https://doi.org/10.1016/j.rinp.2022.106075

[77] K.R. Purohit, P. Jakhad, and A.K. Rai, "Quarkonium spectroscopy of the linear plus modified Yukawa potential," Phys. Scripta, **97**, 044002 (2022). https://doi.org/10.1088/1402-4896/ac5bc2

[78] M. Abu-shady, C.O. Edet, and A.N. Ikot, "Non-relativistic Quark model under external magnetic and Aharanov-Bohm (AB) fields in the presence of Temperature-Dependent confined Cornell potential," Canadian J. Phys. **99**(11), (2021). https://doi.org/10.1139/cjp-2020-0101

[79] R. Olive, D.E. Groom, and T.G. Trippe, Particle Data Group, Chin. Phys. C, **38**, 60 (2014). https://doi.org/10.1088/1674-1137/38/9/090001

[80] M. Tanabashi, C.D. Carone, T.G. Trippe, and C.G. Wohl, Particle Data Group, Phys. Rev. D, **98**, 546 (2018). https://doi.org/10.1103/PhysRevD.98.030001

[81] S.K. Nikiforov, and V.B. Uvarov, *Special functions of Mathematical Physics*, (Birkhauser, Basel, 1988).

[82] E.P. Inyang, E.O. Obisung, E.S. William, and I.B. Okon, "Non-Relativistic study of mass spectra and thermal properties of a quarkonium system with Eckart-Hellmann potential," East European Journal of Physics, 3, 104-114 (2022). https://doi.org/10.26565/2312-4334-2022-3-14

[83] E.S. William, E.P. Inyang, J.E. Ntibi, J.A. Obu, and E.P. Inyang, "Solutions of the Non-relativistic Equation Interacting with the Varshni-Hellmann potential model with some selected Diatomic molecules," Jordan Journal of Physics, **15**(2), 179-193 (2022). https://doi.org/10.47011/15.2.8

[84] E.S. William, I.B. Okon, O.O. Ekerenam, I.O. Akpan, B.I. Ita, E.P. Inyang, I.P. Etim, and I.F. Umoh, "Analyzing the effects of magnetic and Aharonov-Bohm (AB) flux fields on the energy spectra and thermal properties of N_2, NO, CO, and H_2 diatomic molecules," International Journal of Quantum Chemistry, **122**(16), e26925 (2022). https://doi.org/10.1002/qua.26925

[85] J.E. Ntibi, E.P. Inyang, E.P. Inyang, E.S. William, and E.E. Ibekwe, "Solutions of the N-dimensional Klein-Gordon Equation with Ultra Generalized Exponential–Hyperbolic Potential to Predict the Mass Spectra of Heavy Mesons," Jordan Journal of Physics, **15**(4), 393-402 (2022). https://doi.org/10.47011/15.4.8

[86] E.S. William, E.P. Inyang, I.B. Okon, O.O. Ekerenam, C.A. Onate, I.O. Akpan, A.N. Nwachukwu, et al., "Thermo-magnetic properties of Manning-Rosen plus inversely quadratic Yukawa potential under the influence of magnetic and Aharonov-Bohm (AB) flux fields," Indian Journal of Physics, **97**, 1359–1379 (2023). https://doi.org/10.1007/s12648-022-02510-0

[87] E.P. Inyang, J.E. Ntibi, E.O. Obisung, E.S. William, E.E. Ibekwe, I.O. Akpan, and E.P. Inyang, "Expectation Values and Energy Spectra of the Varshni Potential in Arbitrary Dimensions," Jordan Journal of Physics, **5**, 495-509 (2022). https://doi.org/10.47011/15.5.7

[88] E.P. Inyang, E.S. William, and J.A. Obu, "Eigensolutions of the N-dimensional Schrödinger equation interacting with Varshni-Hulthen potential model," Revista Mexicana de Fisica, **67**(2), 193-205 (2021). https://doi.org/10.31349/RevMexFis.67.193

APPENDIX A: Review of Nikiforov-Uvarov (NU) method

In this section, the basic formalism of the Nikiforov-Uvarov method is reviewed. The relevant steps needed to arrive at the eigenvalue and eigenfunction are highlighted. This method was proposed by Nikiforov and Uvarov [81] to solving Hypergeometric-type differential equations of the form in Eq. (9). The solutions of Eq. (9) can be obtained by employing the trial wave function

$$P(x) = \phi(x) y_n(x), \tag{A1}$$

Which reduces Eq.(9) to an hypergeometric-type differential equation of the form ;

$$\sigma(x) y_n''(x) + \tau(x) y_n'(x) + \lambda y_n(x) = 0, \tag{A2}$$

The function $\phi(x)$ is defined as the logarithmic derivative [82-88]

$$\frac{\phi'(x)}{\phi(x)} = \frac{\pi(x)}{\sigma(x)} \tag{A3}$$

Where $\pi(x)$ is a polynomial of first–degree. The second term in Eq.(A1) is the hypergeometric function with its polynomial solution given by Rodrigues relation as follows;

$$y_n(x) = \frac{B_n}{\rho(x)} \frac{d^n}{dx^n} \left[\sigma^n \rho(x) \right] \tag{A4}$$

The term B_n is the normalization constant and $\rho(x)$ is known as the weight function which in principle must satisfy the condition given:

$$\frac{d}{dx} \left[\sigma(x) \rho(x) \right] = \tau(x) \rho(x). \tag{A5}$$

Where $\tau(x) = \tilde{\tau}(x) + 2\pi(x)$.

It is imperative that we note here that the derivative of $\tau(x)$ should be $\tau(x) \prec 0$. The eigenfunctions and eigenvalues can be obtained using the expression defined by $\pi(x)$ and parameter λ, defined as follows

$$\pi(x) = \frac{\sigma'(x) - \tilde{\tau}(x)}{2} \pm \sqrt{\left(\frac{\sigma'(x) - \tilde{\tau}(x)}{2} \right)^2 - \tilde{\sigma}(x) + k\sigma(x)}, \, and \, \lambda = k_- + \pi'_-(x) \tag{A6}$$

The value of k can be obtained by setting the discriminant in the square root in Eq. (A6) equal to zero. As such, the new eigenvalues equation can be given as

$$\lambda + n\tau'(x) + \frac{n(n-1)}{2} \sigma''(x) = 0, (n = 0, 1, 2, ...) \tag{A7}$$

APPENDIX B: Solutions in Detail

Substituting $\tilde{\sigma}(x) = -\tilde{\varepsilon} + \tilde{\beta}_1 x - \tilde{\beta}_2 x^2$, into Eq. (A6) yields;

$$\pi(x) = \pm\sqrt{\tilde{\varepsilon} - \tilde{\beta}_1 x + (\tilde{\beta}_2 + k)x^2} \tag{B1}$$

The discriminant of the quadratic expression under the square root above is given as; $k = \dfrac{\tilde{\beta}_1^2 - 4\tilde{\beta}_2\tilde{\varepsilon}}{4\tilde{\varepsilon}}$, and substituting k into

eq.(B1) yields; $\pi(x) = \pm\left(\dfrac{\tilde{\beta}_1 x}{2\sqrt{\tilde{\varepsilon}}} - \dfrac{\tilde{\varepsilon}}{\sqrt{\tilde{\varepsilon}}}\right)$ with derivative given as; $\pi'(x) = -\dfrac{\tilde{\beta}_1}{2\sqrt{\tilde{\varepsilon}}}$.

Recalling the expression for $\tau(x)$, we obtain the expression for $\tau(x)$, and its derivative respectively as follows;

$$\tau(x) = 2x - \frac{\tilde{\beta}_1 x}{\sqrt{\tilde{\varepsilon}}} + \frac{\tilde{\varepsilon}}{\sqrt{\tilde{\varepsilon}}} \quad and \quad \tau'(x) = 2 - \frac{\tilde{\beta}_1}{\sqrt{\tilde{\varepsilon}}}. \tag{B2}$$

From Eq. (A7) and (A6), we have the following;

$$\frac{\tilde{\beta}_1^2 - 4\tilde{\beta}_2\tilde{\varepsilon}}{4\tilde{\varepsilon}} - \frac{\tilde{\beta}_1}{2\sqrt{\tilde{\varepsilon}}} = \frac{n\tilde{\beta}_1}{2\sqrt{\tilde{\varepsilon}}} - n^2 - n \tag{B3}$$

Eq.(B3) yields the energy equation of the Cornell potential presented in Eq. (10).

**ТЕПЛОВІ ВЛАСТИВОСТІ ТА СПЕКТРИ МАСИ ВАЖКИХ МЕЗОНІВ
ЗА ПРИСУТНОСТІ ТОЧКОВОГО ДЕФЕКТУ**
Е.П. Іньянг[a,c], Н. Алі[c,e], Р. Ендут[c,e], Н. Руслі[b], С.А. Алджунід[c,e], Н.Р. Алі[f], М. Асджад[d]
[a]Відділ фізики, Національний відкритий університет Нігерії, Джабі-Абуджа, Нігерія
[b]Інститут інженерної математики, Університет Малайзії в Перліс, 02600 Арау, Перліс, Малайзія
[c]Факультет технології електронної інженерії, Університет Малайзії в Перліс, 02600 Арау, Перліс, Малайзія
[d]Факультет математики, університет у Халіфі, Абу-Дабі, 127788, Об'єднані Арабські емірати
*[e]Центр передового досвіду в галузі передової комунікаційної інженерії (ACE), Університет Малайзії в Перліс,
02600 Арау, Перліс, Малайзія*
*[f]Школа електротехніки та електронної інженерії, Університет Сайнс Малайзії, Інженерний кампус,
Нібонг Тебал, Пенанг, Малайзія*

У цьому дослідженні радіальне рівняння Шредінгера розв'язується аналітично за допомогою методу Нікіфорова-Уварова з потенціалом Корнела. Отримано в близькому вигляді енергетичний спектр і відповідну хвильову функцію. Вплив топологічного дефекту на теплові властивості та мас-спектри важких мезонів, таких як чармоній і боттоніум, вивчається за допомогою отриманого енергетичного спектру. Встановлено, що наявність топологічного дефекту збільшує мас-спектри та зміщує значення, близькі до експериментальних даних. Наші результати узгоджуються з експериментальними даними та вважаються кращими порівняно з іншими роботами.
Ключові слова: *рівняння Шредінгера; метод Нікіфорова-Уварова; потенціал Корнела; мас-спектри; топологічний дефект*

EFFECTS OF TOPOLOGICAL DEFECTS AND MAGNETIC FLUX ON DISSOCIATION ENERGY OF QUARKONIUM IN AN ANISOTROPIC PLASMA

Mohamed Abu-Shady[a], **Etido P. Inyang[b]***

aDepartment of Mathematics and computer science, Faculty of Science, Menoufia University, Shbien El-Kom, Egypt
bDepartment of Physics, National Open University of Nigeria, Jabi, Abuja, Nigeria
*Corresponding Author e-mail: einyang@noun.edu.ng

In this paper, we investigate the effects of anisotropic parameters, topological defects, and magnetic flux on the dissociation energy of bottomonium in an anisotropic quark-gluon plasma. We use the three-dimensional Schrödinger equation and derive the energy eigenvalues. Our findings show that the dissociation energy decreases with increasing temperature, but there is a slight shift towards higher values when the magnetic flux is increased. Furthermore, the inclusion of topological defects causes further shifts in the dissociation energy at high temperatures. Additionally, we analyze the impact of anisotropic medium on dissociation energy, both with and without considering topological defects. We observe that including topological defects results in higher values for the dissociation energy across all temperatures, while ignoring them leads to lower values at all temperatures studied. Moreover, we consider the baryonic chemical potential and find that its effect on dissociation is negligible compared to temperature variations. These findings provide valuable insights into the behavior of heavy quarkonium systems under different physical conditions and contribute to our understanding of topological effects in anisotropic media.

Keywords: *Topological effects; Schrödinger equation; Nikiforov-Uvarov method; Finite temperature; Baryonic chemical potential*
PACS: 12.39.Jh

1. INTRODUCTION

The study contributes to the understanding of heavy quarkonium systems, specifically bottomonium mesons, in a hot and dense medium. It explores the effects of anisotropic parameters, topological defects, magnetic flux, and baryonic chemical potential on dissociation energy. By investigating these factors and their impact on quarkonium behavior, it adds valuable insights to this area of research. Dissociation of quarkonium in hot and dense media has been a topic of significant interest in the field of in the quark-gluon plasma. Quarkonium refers to a bound state of a heavy quark-antiquark pair, such as charm-anticharm (J/ψ) or bottom-antibottom (Y). In the non-relativistic quark model, quarkonium are considered to be akin to a heavy particle moving in a Coulomb potential. When exposed to extremely high temperatures and densities, as found in heavy-ion collision experiments, quarkonium states may undergo dissociation due to the effects of the surrounding anisotropic plasma [1-4]. Further studies are extended to relativistic quark models to study the properties of hadron in high temperature [5-10]

The presence of an anisotropic plasma plays a crucial role in the dissociation process. Anisotropy refers to a situation in which the thermal motion of particles is not uniformly distributed in all directions. In the context of quarkonium dissociation, the anisotropic plasma can affect the screening properties of the medium. The ability of the plasma to screen the quark-antiquark potential depends on the direction of the motion of the heavy quark. Consequently, the dissociation rates of quarkonium states can exhibit a dependence on the direction of their relative motion through the anisotropic plasma [11].

Studying the dissociation of quarkonium in an anisotropic plasma requires theoretical frameworks that incorporate both non-relativistic quark models and the effects of the plasma. This is known as the non-relativistic QCD (NRQCD) framework. NRQCD provides a valuable tool to analyze the behavior of quarkonium in different plasma environments. It allows for the calculation of dissociation rates and other properties relevant to the study of quarkonium suppression in heavy-ion collisions. Understanding the dissociation of quarkonium in hot and dense media is crucial for unraveling the nature of the quark-gluon plasma and the properties of QCD matter under extreme conditions [12-13].

The study of point-like global monopoles has attracted significant interest in various branches of theoretical physics. These defects have implications in cosmology and astrophysics, as their existence could have left observable imprints on the early universe. Furthermore, their properties and interactions are of utmost importance in understanding the dynamics of field theories and the fundamental nature of particle physics. Experimental searches and theoretical investigations continue to shed light on the intriguing properties and implications of point-like global monopoles. Point-like global monopoles are hypothetical topological defects that may have formed during phase transitions in the early universe such as [14-15].

One area where point-like global monopoles have important implications is in the study of cosmic strings. Cosmic strings are linear topological defects that can form during phase transitions, and their interaction with point-like global monopoles can lead to the creation of cosmic junctions. These junctions serve as sources of gravitational radiation and

can potentially leave imprints in the cosmic microwave background, providing valuable insights into the early universe's dynamics and supporting inflationary cosmology models [17].

Furthermore, the presence of point-like global monopoles can lead to the formation of cosmic texture. Cosmic textures are two-dimensional tangled structures that arise due to the evolution of coupled fields with non-trivial topology. The interaction between point-like global monopoles and cosmic textures can contribute to the generation of anisotropies in the cosmic microwave background, which can be probed through experiments such as the Planck satellite mission [18].

Beyond their impact on cosmic string evolution and cosmic texture formation, point-like global monopoles can also have implications on the large-scale structure of the universe. The presence of these topological defects can affect the distribution and clustering of matter over cosmological distances, potentially leaving detectable signatures in galaxy surveys and cosmological observables [19]. Their influence on structure formation is highly dependent on their initial conditions and properties, making their study crucial for understanding the dynamics of the universe at different scales.

The work explores the characteristics of heavy mesons in an anisotropic-plasma environment, paying attention to the impact of topological effects in space. Novelty: The incorporation of anisotropic parameters and topological defects in studying quarkonium dissociation energy sets this paper apart from previous works that primarily focus on classical cases or neglect these factors altogether. This novel approach provides a more comprehensive understanding of how different physical conditions affect heavy quarkonia.

The paper is structured as follows: Section 2 briefly describes the new method, Section 3 delves into the computation of energy eigenvalues and wave functions, Section 4 discusses the results obtained, and finally, Section 5 provides a summary and conclusion of the findings.

2. THE SCHRÖDINGER EQUATION IN POINT-LIKE GLOBAL MONOPOLEWITH POTENTIAL INTERACTION

In this section, we find the solution for the eigenvalues of non-relativistic particles in the presence of a quantum flux field, considering a point-like global monopole with potential.

For a detailed explanation of the two-particle system interacting through an electromagnetic spherically symmetric potential $V(r)$ in the framework of radial-Schrodinger equation, see Ref. [16].

$$\left[\frac{d^2}{dr^2} + \frac{1}{\alpha^2} \left(2\mu \left(E - V(r) \right) - \frac{L'(L'+1)}{r^2} \right) \right] \Psi(r) = 0 , \tag{1}$$

where $L' = L - \Phi$ and μ are the angular momentum quantum number and the reduced mass for the quarkonium particle (for charmonium $\mu = m_c/2$ and for bottomonium $\mu = m_b/2$), respectively, and $0 < \alpha \leq 1$ characterize the topological defect parameter of point-like global monopole and Φ is the amount of magnetic flux which is a positive integer.

Real Part of The Potential in An Anisotropic Medium

Here, we aim to find the potential due to the presence of a dissipative anisotropic hot QCD medium. The in-medium modification can be obtained in the Fourier space by dividing the heavy-quark potential by the medium dielectric permittivity, $\varepsilon(K)$ as follows

$$\tilde{V}(k) = \frac{V(k)}{\varepsilon(K)}, \tag{2}$$

by taking the inverse Fourier transform, the modified potential is obtained as follows

$$V(r) = \int \frac{d^3k}{(2\pi)^{\frac{3}{2}}} \left(e^{ik \cdot r} - 1 \right) \tilde{V}(k), \tag{3}$$

where $V(k)$ is the Fourier transform of Cornell potential $V(r) = -\frac{\alpha}{r} + \sigma r$ that gives as follows

$$V(k) = -\sqrt{\frac{2}{\pi}} \left(\frac{\alpha}{k^2} + \frac{2\sigma}{k^4} \right), \tag{4}$$

$\varepsilon(K)$ may be calculated which found from the self-energy using finite temperature QCD. By applying hard thermal loop resummation technique as in Refs. [20, 21], the static gluon propagator which represents the inelastic scattering of an off-shell gluon to a thermal gluon is defined as follows

$$\Delta^{\mu\nu}(w,k) = k^2 g^{\mu\nu} - k^\mu k^\nu + \Pi^{\mu\nu}(w,k), \tag{5}$$

the dielectric tensor can then be obtained in the static limit in Fourier space, from the temporal component of the propagator as

$$\varepsilon^{-1}(K) = -\lim_{w \to 0} k^2 \Delta^{00}(w, k), \tag{6}$$

to calculate the real part of the inter-quark potential in the static limit, one can obtain first the temporal component of real part of the retarded propagator in Fourier space at finite temperature and chemical potential as given in Ref. [20] as follows

$$\mathrm{Re}\left[\Delta_R^{00}\right](w=0, k) = -\frac{1}{k^2 + m_D^2(T, \mu)} - \xi\left(\frac{1}{3\left(k^2 + m_D^2(T, \mu)\right)}\right) - \frac{m_D^2(T, \mu)(3\cos 2\theta - 1)}{6\left(k^2 + m_D^2(T, \mu)\right)^2}, \tag{7}$$

the medium dielectric permittivity $\varepsilon(K)$ is then given

$$\varepsilon^{-1}(K) = \frac{k^2}{k^2 + m_D^2} + k^2 \xi\left(\frac{1}{3\left(k^2 + m_D^2\right)}\right) - \frac{m_D^2(3\cos 2\theta - 1)}{6\left(k^2 + m_D^2\right)^2}. \tag{8}$$

Substituting Eqs. (4) and (8) into Eqs. $(2,3)$ and then taking its inverse Fourier transform, we can write the real part of the potential for $rm_D \ll 1$ as follows

$$V(r, \xi, T, \mu_b) = \sigma r\left(1 + \frac{\xi}{3}\right) - \frac{\alpha}{r}\left(1 + \frac{(rm_D)^2}{2} + \xi\left(\frac{1}{3} + \frac{(rm_D)^2}{16}\left(\frac{1}{3} + \frac{(rm_D)^2}{16}\left(\frac{1}{3} + \cos(2\theta)\right)\right)\right)\right), \tag{9}$$

where ξ is the anisotropic parameter. T and μ_b are the temperature and the baryonic chemical potential, respectively. In Eq. (9), the potential depends on θ which is the angle between the particle momentum and the direction of anisotropy. We note that the potential in Eq. (9) reduces to the Cornell potential for $\xi = 0$ and $m_D = 0$ {For details, see Ref. [20]}. In the present work, the Debye mass $D(T, \mu_b)$ is given as in Refs. [22, 23] by

$$D(T, \mu_b) = gT\sqrt{\frac{N_c}{3} + \frac{N_f}{6} + \frac{N_f}{2\pi^2}\left(\frac{\mu_q}{T}\right)^2}, \tag{10}$$

where, g is the coupling constant and μ_q is the quark chemical potential $\left(\mu_q = \frac{\mu_b}{3}\right)$, N_f is number of flavors, and N_c is number of colors. The NU method [24] is briefly given here to solve the form of the following equation

$$\Psi''(s) + \frac{\overline{\tau}(s)}{\sigma(s)}\Psi'(s) + \frac{\tilde{\sigma}(s)}{\sigma^2(s)}\Psi(s) = 0, \tag{11}$$

where $\sigma(s)$ and $\tilde{\sigma}(s)$ are polynomials of maximum second degree and $\overline{\tau}(s)$ is a polynomial of maximum first degree with an appropriate $s = s(r)$ coordinate transformation. We try to find a particular solution by separation of variables, if one deals with the transformation

$$\Psi(s) = \Phi(s)\chi(s). \tag{12}$$

Eq. (11) is written as

$$\sigma(s)\chi''(s) + \tau(s)\chi'(s) + \lambda\chi(s) = 0, \tag{13}$$

where

$$\sigma(s) = \pi(s)\frac{\Phi(s)}{\Phi'(s)}, \tag{14}$$

and

$$\tau(s) = \overline{\tau}(s) + 2\pi(s); \quad \tau'(s) < 0, \tag{15}$$

$$\lambda = \lambda_n = -n\tau'(s) - \frac{n(n-1)}{2}\sigma''(s), n = 0, 1, 2, \ldots, \tag{16}$$

$\chi(s) = \chi_n(s)$ is a polynomial of degree n which satisfies the hypergeometric equation, taking the form

$$\chi_n(s) = \frac{B_n}{\rho_n} \frac{d^n}{ds^n}(\sigma''(s)\rho(s)), \tag{17}$$

where B_n is a normalization constant and $\rho(s)$ is a weight function which satisfies the following equation

$$\frac{d}{ds}\omega(s) = \frac{\tau(s)}{\sigma(s)}\omega(s); \quad \omega(s) = \sigma(s)\rho(s), \tag{18}$$

$$\pi(s) = \frac{\sigma'(s) - \overline{\tau}(s)}{2} \pm \sqrt{(\frac{\sigma'(s) - \overline{\tau}(s)}{2})^2 - \tilde{\sigma}(s) + K\sigma(s)}, \tag{19}$$

and

$$\lambda = K + \pi'(s), \tag{20}$$

$\pi(s)$ is a polynomial of the first degree. The values of K in the square root of Eq. (19) is possible to calculate if the function under the square is a square of a function. This is possible if its discriminant is zero. For r parallel to the direction of n of anisotropy at $\theta = 0$, the potential is given by

$$V(r) = a_1 r - \frac{b_1}{r}, \tag{21}$$

where

$$a_1 = \sigma + \frac{1}{3}\sigma\xi - \frac{1}{2}\alpha m_D^2 - \frac{1}{2}\alpha\xi m_D^2, \tag{22}$$

$$b_1 = \alpha + \frac{\alpha\xi}{3}. \tag{23}$$

By applying the above method to the potential given in Eq. (21), we obtain the energy eigenvalues as follows

$$E_{nl}^{\parallel} = \frac{3a_1}{\delta} - \frac{2\mu_1(\frac{3a_1}{\delta^2} + b_1)^2}{[(2n+1) + \sqrt{1 + \frac{8\mu_1 a_1}{\delta^3} + \frac{4}{\alpha}L'(L'+1)}]^2}, \tag{23}$$

Similarly, for r perpendicular to the direction of n anisotropy at $\theta = \pi/2$, the potential is given by

$$V(r) = a_2 r - \frac{b_2}{r}, \tag{24}$$

where

$$a_2 = \sigma + \frac{1}{3}\sigma\xi - \frac{1}{2}\alpha m_D^2 + \frac{1}{24}\alpha\xi m_D^2, \tag{25}$$

$$b_2 = \alpha + \frac{\alpha\xi}{3}. \tag{26}$$

and the energy eigenvalues are given as follows

$$E_{nl}^{\perp} = \frac{3a_2}{\delta} - \frac{2\mu_1(\frac{3a_2}{\delta^2} + b_2)^2}{[(2n+1) + \sqrt{1 + \frac{8\mu_1 a_1}{\delta^3} + \frac{4}{\alpha}L'(L'+1)}]^2}, \tag{27}$$

where δ is a parameter will be determined as in Ref. [2].

DISCUSSION OF RESULTS

In this section, we calculate spectra of the heavy quarkonium system such as bottomonium mesons in the hot and dense medium. The mass of quarkonium is calculated in the 3-dimensional space. We apply the following relation as in Ref. [2].

$$M = 2m + E_{nL}, \tag{28}$$

where m is quarkonium bare mass for the charmonium or bottomonium mesons. By using Eq. (23), we write Eq. (28) as follows:

$$M = 2m + \frac{2\mu_1(\frac{3a_1}{\delta^2} + b_1)^2}{[(2n+1) + \sqrt{1 + \frac{8\mu_1 a_1}{\delta^3} + \frac{4}{\alpha} L'(L'+1)}]^2} \; . \tag{29}$$

Eq. (29) represents the quarkonium masses in hot and dense medium with topological effects and magnetic flux in an anisotropic plasma. By taking $\alpha = 1$ and $\Phi = 0$, we obtain

$$M = 2m + \frac{2\mu(\frac{3a_1}{\delta^2} + b_1)^2}{[(2n+1) + \sqrt{1 + \frac{8\mu a_1}{\delta^3} + \frac{4}{\alpha} L(L+1)}]^2} \; . \tag{30}$$

Eq. (30) coincides with Ref. [2]. We discuss the effect of the anisotropic parameter on the quarkonium dissociation energy, specifically focusing on the bottomonium meson. The parameters used in this calculation are based on Ref. [2] which sets the mass of the bottom quark to be 4.686 GeV. Furthermore, we are specifically considering the 1S state of the bottomonium meson. The Eq. (23) is employed to calculate the dissociation energy, in which r parallel to the direction of n of anisotropy at $\theta = 0$. In Fig. (1), the dissociation energy is plotted against the temperature, ranging from 0.17 to 0.35 GeV, which corresponds to the quark-gluon plasma phase. In this figure, the effect of topological defect is ignored, and we observe that the dissociation energy decreases as the temperature increases. When we increase the magnetic flux, the curves representing the dissociation energy slightly shift towards higher values at the starting temperature. However, the effect of the temperature becomes more apparent at higher temperatures, indicating that the magnetic flux has a stronger impact in very hot mediums. It is important to note that the medium in this context is anisotropic, with a parameter value of $\zeta = 0.3$. Moving on to Fig. (2), we consider the incorporation of topological defect in the anisotropic medium.
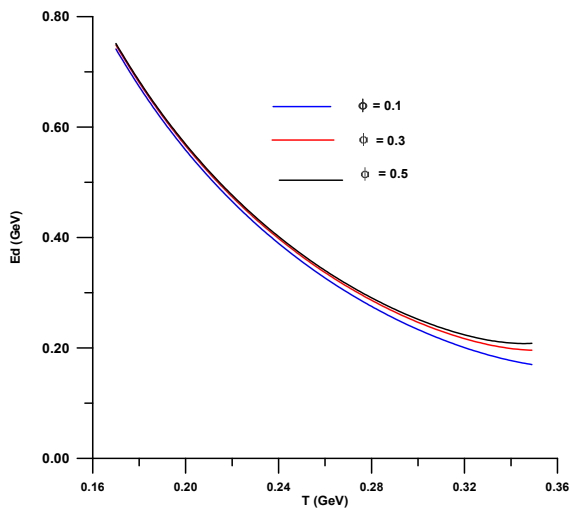
Figure 1. The dissociation energy is plotted with temperature for different values of magnetic flux at ζ=0.3, $\propto$= 1.0 and u_b=0
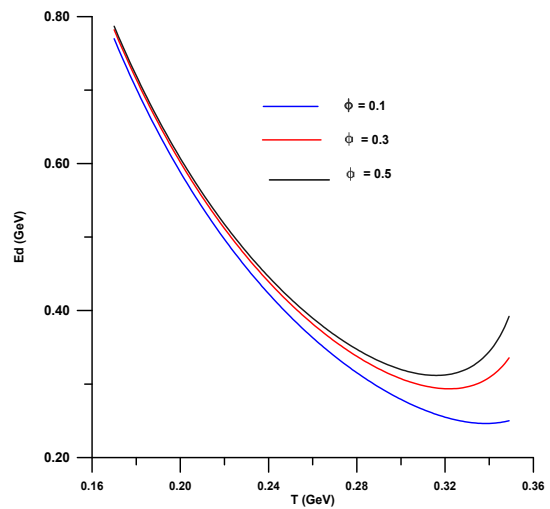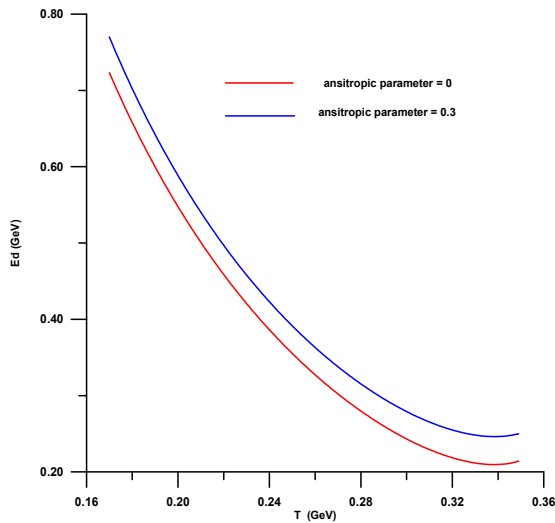
Figure 2. The dissociation energy is plotted with temperature for different values of magnetic flux at ζ=0.3, $\propto$= 0.5 and u_b= 0

Here, we observe that the dissociation energy is shifted to larger values for all different magnetic flux values. This effect becomes more prominent at very high temperatures, indicating that topological defect plays a crucial role in hot anisotropic mediums. Now, if we turn our attention to Figures (3,4), we concentrate on the effect of anisotropic medium on dissociation energy. In Fig. (3), with the inclusion of topological defect, the dissociation energy is shifted to higher values in the anisotropic medium at every temperature. On the other hand, in Fig. (4), when the topological defect is ignored, we observe that the dissociation energy decreases to lower values at all temperatures. It is worth noting that recent works have not considered topological defect, as most of them focus on the study of quarkonium in the classical case, which refers to zero temperature and chemical baryonic potential. In Ref. [16], a similar effect of the magnetic flux on the eigenvalue of energy is observed, where the energy is shifted to higher values with increasing magnetic flux. The authors of the work also investigated the potential interaction under different values of topological parameter and magnetic flux.

Also, in the present work, we considered the effect of a dense medium by including the baryonic chemical potential in our study. In Figure 5 and Figure 6, we examined two cases: one where we ignored the topological defect (as shown in Figure 5), and another where we considered it (as shown in Figure 6). We observed that without the topological defect, the dissociation occurs more rapidly with increasing temperature and gradually very slightly decreases with the baryonic chemical potential. However, when we include the topological defect, we see the same behavior but with a shift towards higher energy values. Furthermore, in contour 7, we note that higher values of dissociation are observed at lower temperature and lower chemical potential, and these values gradually decrease as the

temperature increases. We also observe that the effect of the baryonic chemical potential is negligible at every temperature point. A similar behavior is seen in contour 8 when the effect of the topological defect is considered.
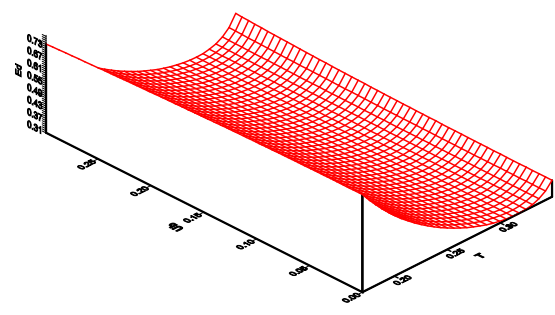

Figure 3. The dissociation energy is plotted with temperature for different values of ansitropic parameter at $\alpha = 0.5$ and $\Phi = 0.1$ and $u_b = 0$
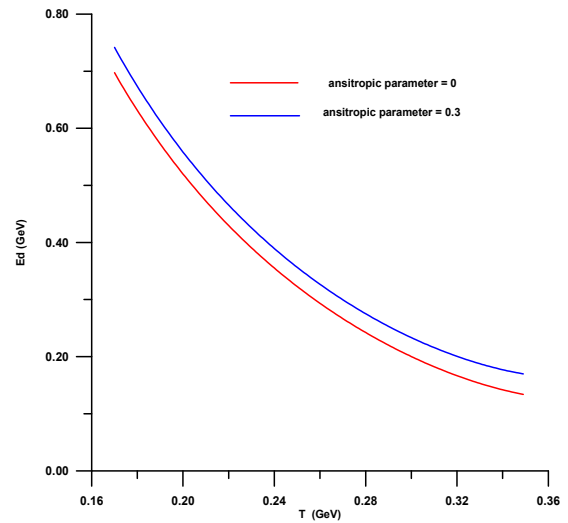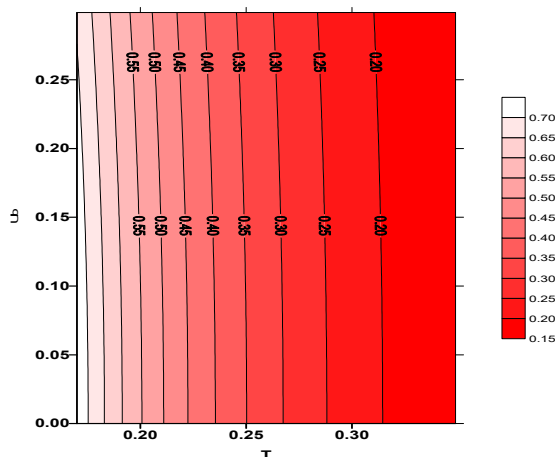

Figure 4. The dissociation energy is plotted with temperature for different values of ansitropic parameter at $\alpha = 1.0$ and $\Phi = 0.1$ and $u_b = 0$
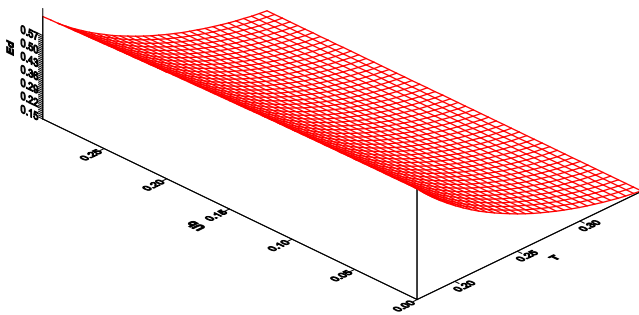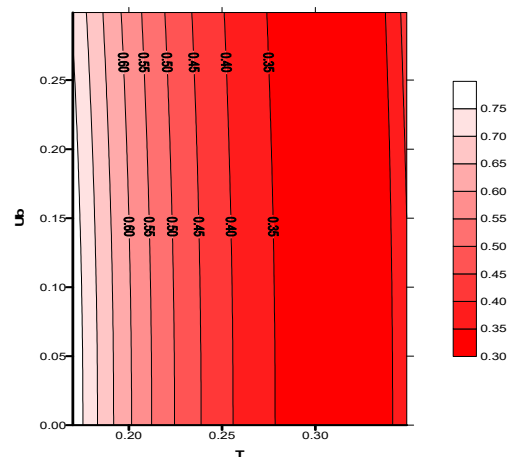

Figure 5. The dissociation energy is plotted as a function of temperature and baryonic chemical potential at $\alpha = 1.0$ and $\Phi = 0$

Figure 6. The dissociation energy is plotted as a function of temperature and baryonic chemical potential at $\alpha = 0.5$ and $\Phi = 0.5$

Figure 7. The dissociation energy is plotted as a countur of temperature and baryonic chemical potential at $\alpha = 1.0$ and $\Phi = 0$

Figure 8. The dissociation energy is plotted as a countur of temperature and baryonic chemical potential at $\alpha = 0.5$ and $\Phi = 0.5$

CONCLUSION

This study explores the effects of anisotropic parameters, topological defects, magnetic flux, and baryonic chemical potential on the dissociation energy of bottomonium mesons in a hot and dense medium. The results demonstrate that temperature plays a significant role in decreasing dissociation energy while magnetic flux slightly

shifts it towards higher values. Incorporating topological defects further increases dissociation energy at high temperatures. Additionally, considering anisotropic medium leads to higher dissociation energies compared to isotropic conditions. The inclusion of baryonic chemical potential has negligible impact on dissociation compared to temperature variations. These findings provide valuable insights into the behavior of heavy quarkonium systems under different physical conditions and contribute to our understanding of topological effects in anisotropic mediums. We hope to extend this work as future works relativistic quark model as in Ref. [25] with fractional derivative as in Ref. [26] or extend to molecular structure as in Ref. [27].

ORCID

Mohamed Abu-Shady, https://orcid.org/0000-0001-7077-7884; **Etido P. Inyang,** https://orcid.org/0000-0002-5031-3297

REFERENCES

[1]   M. Abu-Shady, and A.N. Ikot, "Analytic solution of multi-dimensional Schrodinger equation in hot and dense QCD media using the SUSYQM method," The European Physical Journal Plus, **134**(7), 321 (2019). https://doi.org/10.1140/epjp/i2019-12685-y

[2]   M. Abu-Shady, and H.M. Fath-Allah, "Melting of quarkonium in an anisotropic hot QCD medium in the presence of a generalized Debye screening mass and Nikiforov-Uvarov's method," International Journal of Modern Physics A, **35**(21), 2050110 (2020). https://doi.org/10.1142/S0217751X20501109

[3]   M. Abu-Shady, T.A. Abdel-Karim, and E.M. Khokha, "Binding energies and dissociation temperatures of heavy quarkonia at finite temperature and chemical potential in the N-dimensional space," Advances in High Energy Physics, **2018**, 1-12 (2018). http://dx.doi.org/10.1155/2018/7356843

[4]   M. Abu-Shady, "Quarkonium masses in a hot QCD medium using conformable fractional of the Nikiforov-Uvarov method," International Journal of Modern Physics A, **34**(31), 1950201 (2019). https://doi.org/10.1142/S0217751X19502014

[5]   M. Abu-Shady, "The effect of finite temperature on the nucleon properties in the extended linear sigma model," International Journal of Modern Physics E, **21**(06), 1250061 (2012). https://doi.org/10.1142/S0218301312500619

[6]   M. Abu-Shady, "Meson properties at finite temperature in the linear sigma model," International Journal of Theoretical Physics **49**, 2425-2436 (2010). https://doi.org/10.1007/s10773-010-0428-9

[7]   M. Abu-Shady, "Nucleon Properties Below the Critical Point Temperature," International Journal of Theoretical Physics, **50**, 1372-1381 (2011). https://doi.org/10.1007/s10773-010-0646-1

[8]   M. Abu-Shady, and M. Soleiman, "The extended quark sigma model at finite temperature and baryonic chemical potential," Physics of Particles and Nuclei Letters, **10**, 683-692 (2013). https://doi.org/10.1134/S1547477114010026

[9]   M. Abu-Shady, "Chiral logarithmic sigma model at finite temperature and baryonic chemical potential," Modern Physics Letters A, **29**(34), 1450176 (2014). https://doi.org/10.1142/S0217732314501764

[10] M. Abu-Shady, and H.M. Mansour, "Nucleon properties in the quantized linear sigma model at finite temperature and chemical potential," Journal of Physics G: Nuclear and Particle Physics, **43**(2), 025001 (2015). https://doi.org/10.1088/0954-3899/43/2/025001

[11] M. Abu-Shady, H.M. Mansour, and A.I. Ahmadov, "Dissociation of quarkonium in hot and dense media in an anisotropic plasma in the nonrelativistic quark model," Advances in High Energy Physics, **2019**, 4785615 (2019). https://doi.org/10.1155/2019/4785615

[12] M. Abu-Shady, A. N. Ikot, Dissociation of nucleon and heavy baryon in an anisotropic hot and dense QCD medium using Nikiforov–Uvarov method. Eur. Phys. J. Plus **135**, 406 (2020). https://doi.org/10.1140/epjp/s13360-020-00436-2

[13] M. Abu-Shady, "Studying quarkonium in the anisotropic hot-dense quark-gluon plasma medium in the framework of generalized fractional derivative," Revista Mexicana de Fisica, **69**(4), 040801-1 (2023). https://doi.org/10.31349/RevMexFis.69.040801

[14] A.L.C. de Oliverira, and E.R.B. de Mello, "Nonrelativistic Charged Particle-Magnetic Monopole Scattering in the Global Monopole Background," Int. J. Mod. Phys. A, **18**, 3175-3187 (2003). https://doi.org/10.1142/S0217751X03015829

[15] E.R.B. de Mello, and C. Furtado, "Nonrelativistic scattering problem by a global monopole," Phys. Rev. D, **56**, 1345 (1997). https://doi.org/10.1103/PhysRevD.56.1345

[16] F. Ahmed, "Topological Effects with Inverse Quadratic Yukawa Plus Inverse Square Potential on Eigenvalue Solutions," Grav. Cosmol. **29**, 232–239 (2023). https://doi.org/10.1134/S0202289323030039

[17] A. Vilenkin, "Cosmic strings and domain walls," Physics Reports, **121**(5-6), 263-315 (2000). https://doi.org/10.1016/s0370-1573(99)00103-4

[18] P.A.R. Ade, et al., (Planck Collaboration), "Planck 2015 results - XXIV. Cosmology from Sunyaev-Zeldovich cluster counts," Astronomy & Astrophysics, **594**, A24 (2016). https://doi.org/10.1051/0004-6361/201525833

[19] T. Matsuda, K. Tomita, and H. Sato, "Large-scale structure formation by global defects of the A2 type," Astrophysical Journal, **686**(1), 1-20 (2008). https://doi.org/10.1086/590073

[20] L. Thakur, N. Haque, U. Kakade, and B.K. Patra, "Dissociation of quarkonium in an anisotropic hot QCD medium," Physical Review D, **88**(5), 054022 (2013). https://doi.org/10.1103/PhysRevD.88.054022

[21] O. Kaczmarek, "Screening at finite temperature and density," hep-let/07100498 (2007). https://arxiv.org/abs/0710.0498v1

[22] M. Moring, S. Ejir, O. Kaczmarek, F. Karsch, and E. Laermann, PoSLAT, **2005**, 193 (2006).

[23] B. Liu, P.N. Shen, and H.C. Chiang, "Heavy quarkonium spectra and s dissociation in hot and dense matter," Physical Review C, **55**(6), 3021 (1997). https://doi.org/10.1103/PhysRevC.55.3021

[24] A.F. Nikiforov, and V.B. Uvarov, *Special Functions of Mathematical Physics*, (Birkhauser, Basel, 1988).

[25] M. Abu-Shady, and E.M. Khokha, "Bound state solutions of the Dirac equation for the generalized Cornell potential model," International Journal of Modern Physics A, **36**(29), 2150195 (2021). https://doi.org/10.1142/S0217751X21501955

[26] M. Abu-Shady, and Sh.Y. Ezz-Alarab, "Conformable fractional of the analytical exact iteration method for heavy quarkonium masses spectra," Few-Body Systems, 62, 1-8 (2021). https://doi.org/10.1007/s00601-021-01591-7

[27] S. B. Doma, M. Abu-Shady, F. N. El-Gammal & A. A. Amer, Ground states of the hydrogen molecule and its molecular ion in the presence of a magnetic field using the variational Monte Carlo method, Molecular Physics, 114:11, 1787-1793 (2016), https://doi.org/10.1080/00268976.2016.1154198

ВПЛИВ ТОПОЛОГІЧНИХ ДЕФЕКТІВ ТА МАГНІТНОГО ПОТОКУ НА ЕНЕРГІЮ ДИСОЦІАЦІЇ КВАРКОНІЮ В АНІЗОТРОПНІЙ ПЛАЗМІ

Мохамед Абу-Шаді[a], Етідо П. Іньянг[b]

[a]Кафедра математики та інформатики, факультет природничих наук, Університет Менуфія, Шбіен Ель-Ком, Єгипет
[b]Кафедра фізики, Національний відкритий університет Нігерії, Джабі, Абуджа, Нігерія

У цій статті ми досліджуємо вплив анізотропних параметрів, топологічних дефектів і магнітного потоку на енергію дисоціації боттомонію в анізотропній кварк-глюонній плазмі. Ми використовуємо тривимірне рівняння Шредінгера та отримуємо власні значення енергії. Наші результати показують, що енергія дисоціації зменшується зі збільшенням температури, але є невеликий зсув у бік вищих значень, коли збільшується магнітний потік. Крім того, включення топологічних дефектів викликає подальші зрушення в енергії дисоціації при високих температурах. Крім того, ми аналізуємо вплив анізотропного середовища на енергію дисоціації, як з урахуванням, так і без урахування топологічних дефектів. Ми спостерігаємо, що включення топологічних дефектів призводить до більш високих значень енергії дисоціації при всіх температурах, тоді як їх ігнорування призводить до нижчих значень при всіх досліджуваних температурах. Крім того, ми розглядаємо баріонний хімічний потенціал і знаходимо, що його вплив на дисоціацію є незначним у порівнянні зі змінами температури. Ці висновки дають цінну інформацію про поведінку важких кварконієвих систем за різних фізичних умов і сприяють нашому розумінню топологічних ефектів в анізотропних середовищах.

Ключові слова: *топологічні ефекти; рівняння Шредінгера; метод Нікіфорова-Уварова; кінцева температура; баріонний хімічний потенціал*

WEAKLY NONLINEAR BIOTHERMAL CONVECTION IN A POROUS MEDIA LAYER UNDER ROTATION, GRAVITY MODULATION, AND HEAT SOURCE

Michael I. Kopp[a]*, Volodymyr V. Yanovsky[a,b]

[a]Institute for Single Cristals, Nat. Academy of Science Ukraine, Nauky Ave. 60, Kharkiv 61072,Ukraine
[b]V.N. Karazin Kharkiv National University, 4, Svoboda Sq., Kharkiv, 61022, Ukraine
*Corresponding Author e-mail: michaelkopp0165@gmail.com

In this paper, the influence of gravitational modulation on weakly nonlinear biothermal convection in a porous rotating layer is investigated. We consider a layer of porous medium saturated with Newtonian fluid, containing gyrotactic microorganisms, and subject to gravitational modulation, rotation, and internal heating. To analyze linear stability, it is sufficient to represent disturbances in the form of normal modes, while nonlinear analysis includes a truncated Fourier series containing a harmonic of the nonlinear interaction. A six-dimensional nonlinear Lorentz-type model is constructed, exhibiting both reflection symmetry and dissipation. We determined heat and mass transfer using a weakly nonlinear theory based on the representation of a truncated Fourier series. Additionally, the behavior of nonstationary Nusselt and Sherwood numbers was investigated by numerically solving finite amplitude equations. Applying the expansion of regular perturbations in a small parameter to a six-dimensional model of Lorentz equations with periodic coefficients, we obtained the Ginzburg-Landau (GL) equation. This equation describes the evolution of the finite amplitude of the onset of convection. The amplitude of convection in the unmodulated case is determined analytically and serves as a standard for comparison. The study examines the effect of various parameters on the system, including the Vadasz number, modified Rayleigh-Darcy number, Taylor number, cell eccentricity, and modulation parameters such as amplitude and frequency. By varying these parameters, in different cases, we analyzed heat and mass transfer, quantitatively expressed by the Nusselt and Sherwood numbers. It has been established that the modulation amplitude has a significant effect on the enhancement of heat and mass transfer, while the modulation frequency has a decreasing effect.

Keywords: *Darcy-Brinkman model; Bio-thermal convection; Gravity modulation; Porous rotating medium; Gyrotactic microorganism*
PACS: 44.30.+v, 87.10.+e

1. INTRODUCTION

The study of fluid flow through porous media is of paramount importance in diverse practical applications such as soil mechanics, groundwater hydrology, oil production, and industrial filtration. In recent years, a novel research area called bioconvection in porous media has gained prominence. This field centers on investigating bacterial movement and biofilm growth, particularly in the context of microbiological oil production technologies. As a result, there is a compelling need for theoretical investigations to delve into the interactions between bioconvection and natural convection.

Ingham and Pop's monograph [1] and Nield and Bejan's work [2] serve as notable references extensively delving into the realm of thermal instability in fluid layers within porous media. Furthermore, Vadasz's comprehensive review [3] specifically focuses on fluid flow and heat transfer in rotating porous media. These monographs meticulously analyze and discuss various facets and challenges associated with thermal instability in these systems. Over time, the exploration of natural convection in fluid-saturated porous media has expanded to encompass additional factors, including rotation [3], magnetic fields [4]-[5], anisotropy [6], heterogeneity [7], gravity modulation [8], and other related effects. These investigations aim to unravel the influence and implications of these factors on the convective flow dynamics within porous media.

The classical Darcy's law, which describes flow in porous media, underwent modification by Brinkman to incorporate a Laplacian term in Stokes' equation. This modification accommodates the Darcy resistance within porous media and is commonly known as the Darcy-Brinkman equation. Widely employed for studying flow in porous media with high porosity [9], the Darcy-Brinkman model encounters several challenges and problems that demand careful consideration when applied to the investigation of bioconvection in highly porous media.

Several practical scenarios involve porous materials acting as their heat source. This presents an alternative approach to induce convective flow through localized heat generation within the porous material. This condition may arise from phenomena like radioactive decay or, in the present context, a relatively modest exothermic reaction occurring within the porous material. The internal heating of the Earth establishes a temperature gradient between the inner and outer layers of the Earth's crust, facilitating convective flow and transferring thermal energy to the planet's surface. Consequently, internal heat generation plays a crucial role in various applications, including geophysics, reactor safety assessments, the production of metal waste forms for used nuclear fuel, fire and combustion research, and the storage of radioactive materials. Despite its importance, the impact of internal heating on convective flow has only been explored in a limited number of investigations.

Yadav et al. [10] explored the impact of an internal heat source on the initiation of Darcy-Brinkman convection in a porous layer saturated with nanofluid under various boundary conditions, including free-free, rigid-rigid, lower-rigid, and upper-free. Analyzing the onset of convection induced by internal heating, such as that generated by microwave heating or chemical reactions, in a horizontal layer of nanofluid, Nield and Kuznetsov [11] conducted an analytical investigation, considering Brownian motion and thermophoresis. Khalid et al. [12] performed a linear stability analysis in the presence of feedback control to study the effect of an internal heat source on the initiation of Rayleigh-Benard convection in a rotating nanofluid layer with double-diffusive convection. Jain and Solomatov [13] delved into the onset of convection in internally heated fluids with strongly temperature-dependent viscosity. Devy et al. [14] investigated the Darcy-Brinkman convective instability of a non-Newtonian nanofluid layer saturated in a porous medium, considering the presence of an internal heat source.

The term "bioconvection" denotes the phenomenon wherein convective patterns emerge due to the presence of self-propelled microorganisms that are denser than the surrounding fluid medium [15]-[17]. These microorganisms exhibit responsive movement to various stimuli, such as gravity, light, chemicals, or the presence of food, a behavior known as taxis. Taxis can be categorized based on the type of stimulus and the direction of movement of the organisms. Positive taxis, or attraction, occur when organisms move toward the stimulus source, while negative taxis, or repulsion, describe movement away from the source. Gravitaxis refers to the directional movement of organisms in response to gravitational forces, while magnetotaxis involves their ability to detect and respond to magnetic fields. Chemotaxis is the response to a gradient in chemical concentration, and phototaxis is movement in response to light. In this context, our emphasis is on gravitactic microorganisms.

Pioneering work by Childress et al. [16] established a comprehensive theory and mathematical model for the bioconvection of gravitactic microorganisms. Hill et al. [17] further developed a theoretical model specifically for gravitactic microorganisms, focusing on their bioconvective behavior. Pedley et al. [18] contributed to the field by developing a linear stability theory to analyze the stability of bioconvection involving gyrotactic microorganisms in a shallow layer of fluid. These studies have identified the conditions required for the initiation of bioconvective flow, providing insights into the behavior of gravitactic microorganisms in convective systems.

Numerous publications have delved into the impact of gyrotactic microorganisms on fluid flows in confined porous media, with notable contributions from Nield, Kuznetsov, and Avramenko [19]-[23] that significantly advance the understanding of biological processes in porous environments. In their work [19], it was established that if the permeability remains below a critical value, the system remains stable, and bioconvection does not manifest. Conversely, surpassing the critical permeability threshold leads to the development of bioconvection. Their subsequent study explored the occurrence of bioconvection in a horizontal layer filled with a saturated porous medium [20], determining critical Rayleigh numbers for various values of the Peclet number, gyrotaxis number, and cell eccentricity. The impact of vertical flow on the onset of bioconvection in a suspension of gyrotactic microorganisms within a porous medium was investigated in [21]. A linear analysis was employed to derive an equation for the critical Rayleigh number, revealing that vertical throughflow stabilizes the system. [22] presented a continuum model of thermobioconvection, focusing on oxytactic bacteria in a porous medium. This study examined the effect of heating microorganisms from below on the stability of a horizontally layered fluid saturated with a porous medium. Utilizing the Galerkin method to solve the linear stability problem, the study established a relationship between the critical value of the Rayleigh number and the thermal Rayleigh number. Avramenko [23] developed a nonlinear theory of bioconvection for gyrotactic microorganisms in a layer of ordinary liquid based on the Lorenz approach [24]. This work [23] delineated the boundaries of various hydrodynamic regimes observed in two-dimensional bioconvection.

Hwang and Pedley [25] explored the impact of uniform shear on the instability of bioconvection in a shallow suspension containing swimming gyrotactic cells. They introduced shear by implementing a flat Couette flow, counteracting the influence of gravity on the cells. The study identified three distinct physical processes contributing to bioconvection instability: gravitational overturning, cell gyrotaxis, and negative cross-diffusion flow. High shear velocities acted as a stabilizing factor, akin to Rayleigh-Benard convection. However, at low shear rates, it destabilized perturbations through the overstability mechanism discussed by Hill, Pedley, and Kessler [16]. Dmitrenko [26] provided a comprehensive review of bioconvection in nanofluids and porous media, presenting a mathematical model based on Darcy's law for porous media. Sharma and Kumar [27] investigated the influence of high-frequency vertical vibration on the onset of bioconvection in a dilute solution of gyrotactic microorganisms using analytical and numerical methods. Their findings revealed that high-frequency, low-amplitude vertical vibration and the bioconvection Peclet number had a stabilizing effect on the system. Kushwaha et al. [28] conducted a more detailed analysis of the stability of vibrational systems consisting of shallow layers filled with randomly swimming gyrotactic microorganisms. In a recent study, Garg et al. [29] examined the stability of thermo-bioconvection flow in an anisotropic porous medium, considering a Jeffery fluid containing gravitactic microorganisms.

The Darcy-Brinkman model, widely employed in porous media research, found an extension in its application by Zhao et al. [30] to investigate biothermal convection within a highly porous medium. Their stability analysis delved into the dynamics of biothermal convection influenced by bottom heating. In another exploration utilizing the Darcy-Brinkman model, Kopp et al. [31] delved into biothermal instability within a porous medium saturated with a water-based nanofluid containing gyrotactic microorganisms in a vertical magnetic field. Their findings revealed that an

increase in the concentration of gyrotactic microorganisms amplifies the onset of magnetic convection. Additionally, the study highlighted the more significant role played by spherical gyrotactic microorganisms in developing biothermal instability. Moreover, Kopp and Yanovsky [32] investigated the impact of rotation, specifically the Coriolis force, on biothermal convection in a layer of porous medium saturated with a suspension containing gyrotactic microorganisms.

Controlling heat and mass transfer is paramount in engineering and technical applications, and one effective strategy involves manipulating convective processes through external perturbations or modulations. Understanding how these modulations influence the flow and transport phenomena within a system is crucial for optimizing performance. Common modulation techniques include temperature modulation, gravity modulation, rotation modulation, and magnetic field modulation. This study specifically focuses on a convection control method based on gravity modulation.

The use of gravity modulation to enhance the stability of a heated fluid layer from below was initially introduced by Gresho and Sani in their study [33]. Since then, numerous researchers have delved into the effects of gravity modulation on the onset of convection. Malashetty and Begum extended these investigations in their study [34], considering additional physical conditions and non-Newtonian fluids. They explored the impact of small-amplitude gravity modulation on the initiation of convection in both fluid layers and fluid-saturated porous layers. Kiran [35] conducted studies on the nonlinear thermal instability in a porous medium saturated with viscoelastic nanofluid under gravitational modulation. Over the years, Kiran et al. conducted several studies [36]-[38] to investigate the influence of gravity modulation on Rayleigh-Benard convection (RBC) and Darcy convection. Their focus was on the effect of g-jitter on RBC in nanofluids [39], using the Ginzburg-Landau (GL) model for nonlinear analysis. They calculated the thermal and concentration Nusselt numbers, considering various physical parameters. Additionally, Manjula et al. [40] studied the combined effects of gravity modulation and rotation on thermal instability in a horizontal layer of a nanofluid.

In the above literature review, there is a certain gap in studies of the effect of gravitational field modulation on biothermal convection in rotating porous media saturated with an aqueous solution containing gyrotactic microorganisms. Kopp and Yanovsky [41] were the first to explore the use of gravity modulation in controlling the development of bio-thermal convection in a layer of porous media that is saturated with Newtonian fluid and contains gyrotactic microorganisms. Their exploration focused on weakly nonlinear convective instability within a porous layer saturated with a Newtonian fluid containing gyrotactic microorganisms. The influence of gravitational modulation resulted in the gyrotaxis parameter becoming periodic over time. The study derived the non-autonomous Ginzburg-Landau equation to characterize heat transfer, quantified by the Nusselt number. Notably, the research extensively delved into the impact of various parameters on heat transfer, including Wadas numbers, the modified bioconvective Rayleigh-Darcy number, cell eccentricity, frequency modulation, and modulation amplitude. Their findings highlighted the remarkable efficiency enhancement of the heat transfer process due to the spherical shape of microorganisms, emphasizing the significant role of microorganism morphology in influencing convective heat transfer. In a related study, Kiran and Manjula [42] investigated the effects of thermal modulation and internal heating on Darcy-Brinkman bio-convection in a Newtonian porous medium containing gyrotactic microorganisms. In contrast to paper [41], the control of bio-thermal convection was specifically achieved through the modulation of the temperature gradient [42] without concurrent modulation of the gyrotaxis.

The motivation for this investigation stems from the significant roles of gravitaxis and gyrotaxis in bioconvection phenomena. Therefore, there is a need to deepen our understanding of the interplay between gravitaxis, gyrotaxis, and rotating thermal convection under gravity modulation to gain insights into the system's dynamics. The main objective of this article is to analyze the behavior of weakly nonlinear biothermal convection in a rotating porous medium with internal heating filled with a Newtonian fluid containing gyrotactic microorganisms.

2. DESCRIPTION OF THE PROBLEM AND MATHEMATICAL MODEL

We have an unbounded horizontal layer of a porous medium filled with a Newtonian fluid that contains gyrotactic microorganisms. This layer has a thickness of h and rotates steadily around a vertical axis with a constant angular velocity of Ω_0. The bottom boundary is where heating takes place, as shown in Fig. 1. The temperature at the lower boundary is T_d and at the upper boundary, it's T_u. To describe the problem's geometric configuration, we use a Cartesian coordinate system, denoted by (x, y, z), with the z-axis being vertically upward. Please refer to Fig. 1. To account for the influence of a time-periodic gravitational field, we introduce a vertically downward force given by $\vec{e} g_0 (1 + \varepsilon^2 \delta \cos(\omega_g t))$, where δ and ω_g denote the amplitude and frequency of the gravity modulation, respectively.

Our problem pertains to a physical model that is based on certain assumptions, which are as follows:

• We consider a Newtonian fluid containing a large number of gyrotactic microorganisms to be incompressible and a porous matrix incapable of absorbing microorganisms.
• We use the Darcy-Brinkman model for highly porous media.
• The heating from below and internal heating do not affect the cells' gyrotactic activity or viability.
• The pores of the material should be large enough to allow for the movement of biological organisms.
• The fluid phase and microorganisms are in a state of thermal equilibrium, so the heat flow may be described using a one-equation model.
• We assume that all thermophysical characteristics are constant, except for the density in the buoyancy force (Boussinesq approximation).
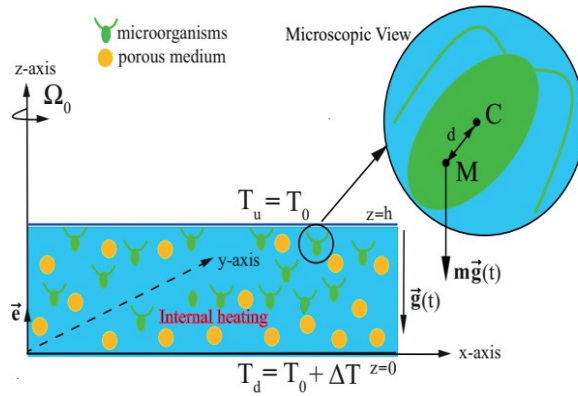
Figure 1. Scheme of swimming of gyrotaxic microorganisms (cells of green algae *Chlamydomonas Reinhardtii*) in a rotating layer of a porous medium. The center of buoyancy of the microorganism C is displaced by a distance d from the center of mass M

Under these assumptions, the mathematical model is based on the continuity, momentum, energy, and conservation equations for cells of the following form [2]-[3],[16],[19]:

$$\nabla \vec{V}_D = 0 , \tag{1}$$

$$\frac{\rho_0}{\varepsilon}\frac{\partial \vec{V}_D}{\partial t} = -\nabla P + \tilde{\mu}\nabla^2 \vec{V}_D - \frac{\mu}{K}\vec{V}_D + \frac{2\rho_0}{\varepsilon}[\vec{V}_D \times \vec{\Omega}] - \vec{e}g(t)\rho_0(1-\beta(T-T_0)) - \vec{e}g(t)(\delta\rho)\mathcal{V}n , \tag{2}$$

$$(\rho c)_m \frac{\partial T}{\partial t} + (\rho c)_f \vec{V}_D \cdot \nabla T = k_m \nabla^2 T + Q(T-T_0) , \tag{3}$$

$$\frac{\partial n}{\partial t} = -div\left(n\vec{V}_D + nW_c l - D_m \nabla n\right), \tag{4}$$

$$g(t) = g_0(1+\varepsilon^2\delta\cos(\omega_g t)) ,$$

where $\vec{V}_D = (u,v,w)$ is the Darcy velocity, which is related to the fluid velocity $\vec{V}$ as $\vec{V}_D = \varepsilon\vec{V}$, ε is the porosity of the porous medium, K is the permeability of the porous medium, ρ_0 is the fluid's density at the reference temperature, P is the pressure, β is the thermal expansion coefficient, $g(t)$ is the time-periodic gravitational acceleration, $\vec{e} = (0,0,1)$ is a unit vector in the direction of the axis z , $\tilde{\mu}$ is the Brinkman effective viscosity, μ is the viscosity of fluid, $(\rho c)_f$ is the heat capacity of fluid, $(\rho c)_m$ is the effective heat capacity, k_m is the effective thermal conductivity. Q is the internal heat source, n is the concentration of microorganisms, $\delta\rho$ is the density difference between microorganisms and a base fluid: $\rho_m - \rho_f$, $\mathcal{V}$ is the average volume of a microorganism, D_m is the diffusivity of microorganisms. We assumed that random motions of microorganisms are simulated by a diffusion process. $W_c \vec{\bar{l}}(0)$ is the average microorganism swimming velocity (W_c is constant). The unit vector $\vec{\bar{l}}(t)$ represents the direction of movement of the microorganisms, and it is a time-periodic quantity due to the modulation of the gravitational field.

At the boundaries, the temperature remains constant. Thus, the boundary conditions are: [20],[30]:

$$w = 0, \quad T = T_d, \quad \vec{J} \cdot \vec{e} = 0, \quad at \; z = 0, \tag{5}$$

$$w = 0, \quad T = T_u, \quad \vec{J} \cdot \vec{e} = 0, \quad at \; z = h, \tag{6}$$

where $\vec{J} = n\frac{\vec{V}_D}{\varepsilon} + nW_c\vec{\bar{l}} - D_m\nabla n$ is the flux of microorganisms. To aid problem analysis, we introduce non-dimensional parameters:

$$(x^*, y^*, z^*) = \frac{(x,y,z)}{h}, \vec{V}_D^* = \vec{V}_D \frac{h}{\alpha_m}, t^* = \frac{t\alpha_m}{h^2\tilde{\sigma}}, \quad T^* = \frac{T-T_u}{T_d-T_u},$$

$$P^* = \frac{PK}{\mu\alpha_m}, \quad \tilde{\sigma} = \frac{(\rho c)_m}{(\rho c)_f}, \quad n^* = n\mathcal{V}, \quad \omega_g^* = \omega_g \frac{h^2\tilde{\sigma}}{\alpha_m}, \tag{7}$$

where $\alpha_m = k_m / (\rho c)_f$ is the coefficient of thermal diffusivity.

Applying transformation (7) to Eqs. (1)-(4) and next omitting the asterisks, we derive the following system of dimensionless equations:

$$\nabla \vec{V}_D = 0 \,, \tag{8}$$

$$\frac{1}{\mathcal{V}_a}\frac{\partial \vec{V}_D}{\partial t} = -\nabla P + D_a \nabla^2 \vec{V}_D - \vec{V}_D - \vec{e}f_m \frac{R_b}{L_b}n + \vec{e}f_m Ra T + \sqrt{Ta}[\vec{V}_D \times \vec{e}] \,, \tag{9}$$

$$\frac{\partial T}{\partial t} + (\vec{V}_D \nabla)T = \nabla^2 T + R_i T \,, \tag{10}$$

$$\frac{1}{\widetilde{\sigma}}\frac{\partial n}{\partial t} = -\nabla\left(n\vec{V}_D + \frac{Pe}{L_b}n\widehat{\vec{l}}(t) - \frac{1}{L_b}\nabla n\right), \tag{11}$$

where $f_m = 1 + \varepsilon^2 \delta \cos(\omega_g t)$. We have introduced the following dimensionless parameters in Eqs. (8)-(11):

$\mathcal{V}_a = \dfrac{\varepsilon(\rho c)_m \widetilde{\mu}}{\rho_0 k_m D_a} = \dfrac{\varepsilon \widetilde{\sigma} \mathrm{Pr}}{D_a}$ is the modified Vadasz number, $\mathrm{Pr} = \dfrac{\widetilde{\mu}}{\alpha_m \rho_0}$ is the Prandtl number, $D_a = \dfrac{\widetilde{\mu}K}{\mu h^2}$ is the Darcy

number, $Ta = \dfrac{4\Omega_0^2 K^2}{\varepsilon^2 \mu^2}\rho_0^2$ is the Taylor-Darcy number, $R_b = \dfrac{g(\delta\rho)hK}{\mu D_m}$ is the bioconvection Rayleigh-Darcy number,

$L_b = \dfrac{\alpha_m}{D_m}$ is the bioconvection Lewis number, $Ra = \dfrac{\rho_0 ghK\beta\Delta T}{\mu\alpha_m}$ is the Rayleigh-Darcy number, $R_i = \dfrac{Qh^2}{\alpha_m}$ is the

internal Rayleigh number, $Pe = \dfrac{W_c h}{D_m}$ is the bioconvection Peclet number.

If we assume that in a stationary state the liquid is at rest, then the main physical quantities can be written as

$$\vec{V}_D = \vec{V}_b = 0, \quad P = P_b(z), \quad T = T_b(z), \quad n = n_b(z) \,. \tag{12}$$

The ground state temperature profile $T_b(z)$ and microorganism concentrations $n_b(z)$ are obtained by solving the following equations:

$$\frac{d^2 T_b}{dz^2} + R_i T_b(z) = 0 \,, \tag{13}$$

$$\frac{dn_b}{dz} = n_b(z)Pe \,. \tag{14}$$

Later on, we will come to realize that having knowledge of the pressure profile is not necessary. After solving equation (13) and imposing the boundary conditions (5)-(6), we can obtain the temperature distribution $T_b(z)$:

$$T_b(z) = \frac{\sin(\sqrt{R_i}(1-z))}{\sin(\sqrt{R_i})} \tag{15}$$

If there is no heat source $R_i \to 0$, then the base temperature profile has the form: $T_b(z) = 1 - z$. Next, we can obtain the solution for $n_b(z)$, which corresponds to the result presented in [20]:

$$n_b(z) = n_b(0)\exp(zPe) \,, \tag{16}$$

where $n_b(0)$ represents the value of the number density at the bottom of the layer. The constant $n_b(0)$ can be determined as follows:

$$n_b(0) = \frac{\langle n \rangle Pe}{\exp(Pe) - 1}, \quad \langle n \rangle = \int_0^1 n_b(z)dz \,. \tag{17}$$

Let the heating from below the mixed fluid layer cause small perturbations in the main flow as follows:

$$\vec{V}_D = \vec{V}(u', v', w'), \quad T = T_b + T', \quad n = n_b + n', \quad P = P_b + P', \quad \widehat{\vec{l}}(t) = \vec{e} + \widehat{\vec{m}}'(t) \,. \tag{18}$$

We can derive the following expressions by analyzing Eq. (9):

$$\left(\frac{1}{\mathcal{V}_a}\frac{\partial}{\partial t} + 1 - D_a\nabla_\perp^2\right)u' = -\frac{\partial P'}{\partial x} + \sqrt{Ta}v' \,, \tag{19}$$

$$\left(\frac{1}{\mathcal{V}_a}\frac{\partial}{\partial t} + 1 - D_a\nabla_\perp^2\right)v' = -\sqrt{Ta}u' \,, \tag{20}$$

$$\left(\frac{1}{\mathcal{V}_a}\frac{\partial}{\partial t}+1-D_a\nabla_\perp^2\right)w' = -\frac{\partial P'}{\partial z} - f_m\frac{\mathrm{R}_b}{\mathrm{L}_b}n' + f_m Ra T',\tag{21}$$

$$\nabla_\perp^2 = \frac{\partial^2}{\partial x^2} + \frac{\partial^2}{\partial z^2}.$$

Here, eliminating the pressure term results in an equation of the form:

$$\left(\frac{1}{\mathcal{V}_a}\frac{\partial}{\partial t}+1-D_a\nabla_\perp^2\right)\left(\frac{\partial u'}{\partial z}-\frac{\partial w'}{\partial x}\right) = \sqrt{Ta}\frac{\partial v'}{\partial z} + f_m\frac{\mathrm{R}_b}{\mathrm{L}_b}\frac{\partial n'}{\partial x} - f_m Ra\frac{\partial T'}{\partial x}\tag{22}$$

For convenience, we express the perturbations of velocities u' and w' in terms of the stream function:

$$u' = \frac{\partial \psi}{\partial z}, \quad w' = -\frac{\partial \psi}{\partial x}.\tag{23}$$

Equations (20) and (22) can be written in the following form:

$$\left(\frac{1}{\mathcal{V}_a}\frac{\partial}{\partial t}+1-D_a\nabla_\perp^2\right)\nabla_\perp^2\psi = \sqrt{Ta}\frac{\partial v'}{\partial z} + f_m\frac{\mathrm{R}_b}{\mathrm{L}_b}\frac{\partial n'}{\partial x} - f_m Ra\frac{\partial T'}{\partial x},\tag{24}$$

$$\left(\frac{1}{\mathcal{V}_a}\frac{\partial}{\partial t}+1-D_a\nabla_\perp^2\right)v' = -\sqrt{Ta}\frac{\partial \psi}{\partial z}\tag{25}$$

After reviewing previous research [19], [23] and considering gravity modulation, we formulate the equation of the unit vector perturbation that indicates the direction of microorganisms swimming in the form

$$\hat{m}'(t) = \mathcal{B}_0(1-\varepsilon^2\delta\cos(\widetilde{\omega}_g t))\zeta\vec{i} - \mathcal{B}_0(1-\varepsilon^2\delta\cos(\widetilde{\omega}_g t))\xi\vec{j} + 0\cdot\vec{e}.\tag{26}$$

Here, $\vec{i}$ and $\vec{j}$ are the unit vectors in the x- and y-directions, respectively. The parameter $\mathcal{B}_0$ represents the reorientation of microorganisms under the influence of a gravitational moment relative to viscous resistance in the absence of modulation, and it is defined as $\mathcal{B}_0 = (\mu\alpha_\perp/\rho_0 g_0 d)(\alpha_m/h^2)$. The displacement of the center of mass of the cell from the center of buoyancy is denoted as d.

In Eq. (26), the parameters ζ and ξ in the x- and y-components of the vector $\hat{m}'$ are given by:

$$\zeta = -(1-\alpha_0)\frac{\partial w'}{\partial x} + (1+\alpha_0)\frac{\partial u'}{\partial z}, \quad \xi = (1-\alpha_0)\frac{\partial w'}{\partial y} - (1+\alpha_0)\frac{\partial v'}{\partial z}.\tag{27}$$

The parameter α_0, representing the cell eccentricity, can be calculated using the following equation [15]-[19]:

$$\alpha_0 = \frac{r_{max}^2 - r_{min}^2}{r_{max}^2 + r_{min}^2},\tag{28}$$

where r_{max} and r_{min} are the semi-major and semi-minor axes of the spheroidal cell.

The perturbation equations, in their nonlinear form, can be written as follows (without the asterisks):

$$\left(\frac{1}{\mathcal{V}_a}\frac{\partial}{\partial t}+1-D_a\nabla_\perp^2\right)\nabla_\perp^2\psi = \sqrt{Ta}\frac{\partial v}{\partial z} + f_m\frac{\mathrm{R}_b}{\mathrm{L}_b}\frac{\partial n}{\partial x} - f_m Ra\frac{\partial T}{\partial x},\tag{29}$$

$$\left(\frac{1}{\mathcal{V}_a}\frac{\partial}{\partial t}+1-D_a\nabla_\perp^2\right)v = -\sqrt{Ta}\frac{\partial \psi}{\partial z},\tag{30}$$

$$-\frac{\partial \psi}{\partial x}\frac{dT_b}{dz} - \nabla_\perp^2 T - \mathrm{R}_i T = -\frac{\partial T}{\partial t} + \frac{\partial(\psi,T)}{\partial(x,z)},\tag{31}$$

$$PeG_0(2-f_m)n_0\hat{\alpha}\frac{\partial \psi}{\partial x} - \frac{\partial \psi}{\partial x}\frac{dn_b}{dz} + \frac{Pe}{L_b}\frac{\partial n}{\partial z} - \frac{1}{L_b}\nabla_\perp^2 n = -\frac{1}{\widetilde{\sigma}}\frac{\partial n}{\partial t} + \frac{\partial(\psi,n)}{\partial(x,z)},\tag{32}$$

$$\hat{\alpha} = \nabla_\perp^2 + \alpha_0\left(\frac{\partial^2}{\partial z^2} - \frac{\partial^2}{\partial x^2}\right),$$

where $G_0 = D_m \mathcal{B}_0 / h^2$ is a dimensionless orientation parameter in the absence of modulation [15]. We impose ideal boundary conditions for stream function, temperature, and concentration of microorganisms:

$$\psi = \nabla_\perp^2 \psi = \frac{dv}{dz} = T = n = 0 \quad at \quad z = 0 \quad and \quad z = 1. \tag{33}$$

3. WEAK NONLINEAR ANALYSIS

In the study of weakly nonlinear convective instability, it is common to use a truncated Fourier series representation for perturbed quantities because it provides a convenient and effective way to analyze and understand the system's behavior. In the linear stability analysis of convective systems, one typically starts with a base state (often a steady state) and perturbs it with small disturbances. These disturbances can be expanded in a Fourier series, and by analyzing the growth rates of different Fourier modes, you can determine whether the system is linearly stable or unstable. Truncating the series keeps the analysis tractable while capturing the essential behavior. For nonlinear system described by equations (29)-(32), we employ Fourier series representations for key physical variables, including the stream function ψ, velocity component v, temperature T, and concentration of microorganisms n:

$$\psi(x,z,t) = \sum_{n=1}^{\infty}\sum_{m=1}^{\infty} A_{mn}(t)\sin(mkx)\sin(n\pi z), \quad v(x,z,t) = \sum_{n=1}^{\infty}\sum_{m=1}^{\infty} V_{mn}(t)\sin(mkx)\cos(n\pi z),$$

$$T(x,z,t) = \sum_{n=1}^{\infty}\sum_{m=1}^{\infty} B_{mn}(t)\cos(mkx)\sin(n\pi z), \quad n(x,z,t) = \sum_{n=1}^{\infty}\sum_{m=1}^{\infty} C_{mn}(t)\cos(mkx)\sin(n\pi z). \tag{34}$$

We then conduct a local nonlinear stability analysis, focusing on specific modes, namely $(1,1)$ for the stream function and velocity component, and $(1,1) + (0,2)$ for temperature and microorganism concentration. Notably, we observe that nonlinearity introduces distortions in the temperature and concentration fields, resulting from the interactions among ψ, T, and n. Consequently, this interaction generates a sinusoidal component $\sin 2\pi z$, in the flow. Thus, we arrive at a simple expression that characterizes finite-amplitude convection in the form:

$$\psi = A_{11}(t)\sin(kx)\sin(\pi z), \quad v = V_{11}(t)\sin(kx)\cos(\pi z),$$

$$T = B_{11}(t)\cos(kx)\sin(\pi z) + B_{02}(t)\sin(2\pi z), \quad n = C_{11}(t)\cos(kx)\sin(\pi z) + C_{02}(t)\sin(2\pi z), \tag{35}$$

where the amplitudes $A_{11}(t), B_{11}(t), B_{02}(t), C_{11}(t), C_{02}(t), V_{11}(t)$ are functions of time. After substituting (35) into equations (29)-(32) and considering the orthogonality condition, the resulting evolution equations for amplitudes are obtained:

$$\frac{\partial A_{11}}{\partial \tilde{t}} = -\frac{1 + D_a a^2}{a^2} A_{11} + \frac{\pi\sqrt{Ta}}{a^4} V_{11} - f_m \frac{kRa}{a^2} B_{11} + f_m \frac{kR_b}{a^2 L_b} C_{11}, \tag{36}$$

$$\frac{\partial V_{11}}{\partial \tilde{t}} = -\frac{1 + D_a a^2}{a^2} V_{11} - \frac{\pi\sqrt{Ta}}{a^4} A_{11}, \tag{37}$$

$$\frac{\partial B_{11}}{\partial \tilde{t}} = -\frac{(1-b)}{\mathcal{V}_a} B_{11} - \frac{k\theta_0}{a^2 \mathcal{V}_a} A_{11} - \frac{\pi k}{a^2 \mathcal{V}_a} A_{11} B_{02}, \tag{38}$$

$$\frac{\partial B_{02}}{\partial \tilde{t}} = -\frac{\gamma - b}{\mathcal{V}_a} B_{02} + \frac{k\pi}{2a^2 \mathcal{V}_a} A_{11} B_{11}, \tag{39}$$

$$\frac{\partial C_{11}}{\partial \tilde{t}} = -\frac{\tilde{\sigma}}{L_b \mathcal{V}_a} C_{11} - \frac{k\pi\tilde{\sigma}}{a^2 \mathcal{V}_a} A_{11} C_{02} + \frac{\tilde{\sigma}}{a^2 \mathcal{V}_a}((2 - f_m)\gamma_1 + \gamma_2)kA_{11}, \tag{40}$$

$$\frac{\partial C_{02}}{\partial \tilde{t}} = -\frac{\gamma\tilde{\sigma}}{\mathcal{V}_a L_b} C_{02} + \frac{k\pi\tilde{\sigma}}{2a^2 \mathcal{V}_a} A_{11} C_{11}, \tag{41}$$

where $a = \sqrt{k^2 + \pi^2}$ is the total wave number, and $\tilde{t} = (a^2 \mathcal{V}_a)t$ is the reduced time, $\gamma = 4\pi^2 / a^2, b = \mathrm{R}_i / a^2$, $\omega_g t \to (\omega_g / a^2 \mathcal{V}_a)\tilde{t} = \tilde{\omega}_g \tilde{t}$.

The system of equations (36)-(41) is dissipative and its solutions are bounded in the phase space. The impact of many parameters $(Ta, Ra, Pe, D_a, R_b, L_b, \mathcal{V}_a)$ on trajectories is to attract them to a set of measures zero or fixed points.

The system of autonomous ordinary differential equations can be solved numerically, for example, in the Maple computer environment. However, in the steady state, Eqs. (36)-(41) have an exact solutions:

$$\frac{A_{11}^2}{8} = -\frac{w_1}{2} + \sqrt{\frac{w_1^2}{4} - w_2} \,, \tag{42}$$

$$V_{11} = -\frac{\pi\sqrt{Ta}}{1 + D_a a^2} A_{11}, \quad B_{11} = -\frac{2k\theta_0(4\pi^2 - R_i)A_{11}}{2(a^2 - R_i)(4\pi^2 - R_i) + k^2\pi^2 A_{11}^2} \,,$$

$$B_{02} = -\frac{\pi k^2 \theta_0 A_{11}^2}{2(a^2 - R_i)(4\pi^2 - R_i) + k^2\pi^2 A_{11}^2}, \quad C_{11} = \frac{8(\gamma_1 + \gamma_2)L_b k A_{11}}{8a^2 + k^2 L_b^2 A_{11}^2}, \quad C_{02} = \frac{(\gamma_1 + \gamma_2)L_b^2 k^2 A_{11}^2}{\pi(8a^2 + k^2 L_b^2 A_{11}^2)} \,,$$

where

$$w_1 = \frac{\xi_1 + \xi_2}{\xi_1 \xi_2} - \frac{1}{r\xi_1}\left(R_b(\gamma_1 + \gamma_2) + \frac{Ra\theta_0}{1 - \dfrac{R_i}{a^2}}\right), \quad \xi_1 = \frac{k^2 L_b^2}{a^2}, \quad \xi_2 = \frac{4\pi^2 k^2}{(a^2 - R_i)(4\pi^2 - R_i)} \,,$$

$$r = \frac{a^4(1 + D_a a^2)}{k^2} + \frac{\pi^2 a^2 Ta}{k^2(1 + D_a a^2)}, \quad \theta_0 = \frac{4\pi^2}{4\pi^2 - R_i} \,,$$

$$\gamma_1 = \frac{4\pi^2\langle n\rangle}{4\pi^2 + Pe^2}[PeG_0((1 - \alpha_0)k^2 + (1 + \alpha_0)\pi^2)], \quad \gamma_2 = \frac{4\pi^2\langle n\rangle Pe}{4\pi^2 + Pe^2}, \quad w_2 = -\frac{(Ra - Ra_c)\theta_0}{r\xi_1\xi_2\left(1 - \dfrac{R_i}{a^2}\right)} \,.$$

The expression for amplitude A_{11} (42) was obtained from solving a quadratic equation of the form:

$$\left(\frac{A_{11}^2}{8}\right)^2 + w_1\left(\frac{A_{11}^2}{8}\right) + w_2 = 0 \tag{43}$$

It is important to note that the stream function's amplitude must be real. Therefore, in solution (42), only the positive sign in front of the radical is taken into account. If we determine the value of A_{11}, we can calculate the heat and mass transfer in a steady state.

In the small amplitude limit $(A_{11} \to 0)$, equation (43), becomes a dispersion equation for linear stationary bio-thermal convection:

$$Ra_c = \left[\frac{a^4(1 + D_a a^2)}{k_c^2} + \frac{\pi^2 a^2 Ta}{k_c^2(1 + D_a a^2)} - R_b(\gamma_1 + \gamma_2)\right]\left[\frac{4\pi^2}{(4\pi^2 - R_i)\left(1 - \dfrac{R_i}{a^2}\right)}\right]^{-1} \tag{44}$$

In order to determine the wave number k_c that corresponds to the onset of convection, we need to minimize the critical Rayleigh number Ra_c with respect to k_c^2. We can achieve this by differentiating Ra_c with respect to k_c^2 and setting the derivative to zero. Once we solve this equation, we will have the value of k_c that is associated with the onset of convection. In the limit of small Peclet numbers, expression (43) coincides with the result first obtained by Kopp and Yanovsky [41] when there is no rotation $(Ta = 0)$ and internal heat source $(R_i = 0)$. When there are no microorganisms present ($n_0 = 0$), the critical Rayleigh number is the same as the results for the Darcy-Brinkman model of a rotating porous medium (without nanoparticles) that was derived by Chand and Rana [43]-[44]. However, if there is no heating or rotation within the system, ordinary bioconvection is observed, which is caused by the motion of microorganisms. In this case, the bioconvection Rayleigh number R_b serves as the governing parameter for bioconvection. The critical value of R_b, denoted as R_b^{cr}, for bioconvection in the Darcy model of a porous medium was initially determined by Nield et al. [20].

Additionally, the amplitudes can be rescaled using the following relations:

$$A_{11}(\tilde{t}) = -\frac{a^2\sqrt{2}}{k\pi}X(\tilde{t}), \quad B_{11}(\tilde{t}) = \frac{\sqrt{2}}{\pi}Y(\tilde{t}), \quad C_{11}(\tilde{t}) = \frac{\sqrt{2}}{\pi}\tilde{Y}(\tilde{t}), \quad B_{02}(\tilde{t}) = -\frac{Z(\tilde{t})}{\pi}, \quad C_{02}(\tilde{t}) = -\frac{\tilde{Z}(\tilde{t})}{\pi}, \quad V_{11}(\tilde{t}) = \frac{\sqrt{2}}{k}V(\tilde{t}) \,. \tag{45}$$

Applying rescaling the amplitudes (45) in Eqs. (36)-(41), we obtain the following set of equations:

$$\begin{cases} \dot{X} = -\mathcal{D}X - \mathrm{T}V + f_m(\mathrm{R}Y - \mathrm{R}b\tilde{Y}) \\ \dot{Y} = \mathcal{V}_a^{-1}(-(1-b)Y + X - XZ) \\ \dot{Z} = \mathcal{V}_a^{-1}(-(\gamma - b)Z + XY) \\ \dot{\tilde{Y}} = \tilde{\sigma}\mathcal{V}_a^{-1}(-\mathrm{L}_b^{-1}\tilde{Y} - ((2-f_m)\gamma_1 + \gamma_2)X - X\tilde{Z}) \\ \dot{\tilde{Z}} = \tilde{\sigma}\mathcal{V}_a^{-1}(-\gamma \mathrm{L}_b^{-1}\tilde{Z} + X\tilde{Y}) \\ \dot{V} = -\mathcal{D}V + \sqrt{\mathrm{Ta}}\,X \end{cases} \tag{46}$$

Here $(\cdot)$ represents the derivative with respect to time $\tilde{t}$; $\mathcal{D}, R, Rb, T$ are new dimensionless parameters of the following form:

$$\mathcal{D} = \frac{1 + D_a a^2}{a^2}, \quad \mathrm{R} = \frac{k^2 \mathrm{Ra}}{a^6}, \quad \mathrm{R}b = \frac{k^2 \mathrm{R}_b}{a^6 L_b}, \quad \mathrm{T} = \frac{\pi^2 \sqrt{\mathrm{Ta}}}{a^6}. \tag{47}$$

Equations (46) describe a model that can be simplified to the fundamental Lorenz model [24] for a regular fluid. The model is six-dimensional and uses variables X and V to represent the velocity field, while Y and Z represent the temperature changes, $\tilde{Y}$ and $\tilde{Z}$ are used to represent the changes in concentration of microorganisms. The Lorenz-like model in Eqs. (46) is invariant under the transformation $(X, Y, Z, \tilde{Y}, \tilde{Z}, V) \to (-X, -Y, Z, -\tilde{Y}, \tilde{Z}, -V)$.

Let's proceed to calculate the heat and mass transfer.

4. HEAT AND MASS TRANSPORTS

Determining the heat and mass transfer of microorganisms is important when studying the bio-thermal convection of liquids. This is due to the fact that the onset of convection with an increasing Rayleigh number is easier to observe because of its effect on heat and mass transfer. Therefore, thermal and mass flows of microorganisms are important for identifying thermo- and bioconvective movement in its early stages. Heat transfer can be calculated and described using the Nusselt number Nu:

$$Nu(\tilde{t}) = 1 + \left[\frac{\int_0^{2\pi/k_{cr}} \frac{\partial T}{\partial z}\, dx}{\int_0^{2\pi/k_{cr}} \frac{\partial T_b}{\partial z}\, dx} \right]_{z=0} \tag{48}$$

According to (15) and (35), we get from (48)

$$Nu(\tilde{t}) = 1 - 2\pi B_{02}(\tilde{t})\left(\sqrt{\mathrm{R}_i}\, ctg(\mathrm{R}_i)\right) \tag{49}$$

By analogy with (48), we find a quantitative characteristic of the mass transfer (Sherwood number Sh) of the concentration of microorganisms:

$$Sh(\tilde{t}) = 1 + \left[\frac{\int_0^{2\pi/k_{cr}} \frac{\partial n}{\partial z}\, dx}{\int_0^{2\pi/k_{cr}} \frac{\partial n_b}{\partial z}\, dx} \right]_{z=0} = 1 + 2\pi C_{02}(\tilde{t})\left(\frac{e^{\mathrm{Pe}} - 1}{\langle n \rangle \mathrm{Pe}^2}\right). \tag{50}$$

5. THE DERIVATION OF THE GINZBURG-LANDAU EQUATION FROM THE SIX-DIMENSIONAL LORENZ-LIKE MODEL

According to [46], we express all perturbed quantities in equations (46) in terms of a series expansion concerning the small supercritical parameter, ε:

$$\vec{X} = \varepsilon \vec{X}_1 + \varepsilon^2 \vec{X}_2 + \varepsilon^3 \vec{X}_3 + \ldots, \quad \vec{X} = [X, Y, Z, \tilde{Y}, \tilde{Z}, V]^{Tr}, \quad R = R_0 + \varepsilon^2 R_2 + \ldots. \tag{51}$$

Here, the amplitudes of perturbed quantities only depend on slow time $\tau = \varepsilon^2 \tilde{t}$. Upon substituting the expansion (51) into (46) for first-order ε, we obtain a linear system of equations:

$$\mathcal{L}\vec{X}_1 = 0, \quad \vec{X}_1 = [X_1, Y_1, Z_1, \tilde{Y}_1, \tilde{Z}_1, V_1]^{Tr}, \tag{52}$$

where the matrix $\mathcal{L}$ has the form

$$\mathcal{L} = \begin{bmatrix} -\mathcal{D} & R_0 & 0 & -Rb & 0 & -T \\ \mathcal{V}_a^{-1}\theta_0 & (b-1)\mathcal{V}_a^{-1} & 0 & 0 & 0 & 0 \\ 0 & 0 & (b-\gamma)\mathcal{V}_a^{-1} & 0 & 0 & 0 \\ -\widetilde{\sigma}\mathcal{V}_a^{-1}(\gamma_1+\gamma_2) & 0 & 0 & -L_b^{-1}\widetilde{\sigma}\mathcal{V}_a^{-1} & 0 & 0 \\ 0 & 0 & 0 & 0 & -\gamma L_b^{-1}\widetilde{\sigma}\mathcal{V}_a^{-1} & 0 \\ \sqrt{Ta} & 0 & 0 & 0 & 0 & -\mathcal{D} \end{bmatrix}.$$

For there to exist a nontrivial solution of the homogeneous linear system (52), a certain condition must be met:

$$R_0\left(\frac{\theta_0}{1-b}\right) = \mathcal{D} + \frac{T\sqrt{Ta}}{\mathcal{D}} - RbL_b(\gamma_1+\gamma_2) . \tag{53}$$

Expression (53) completely coincides with expression (44) for the critical Rayleigh number of stationary bio-thermal convection in the linear theory. The solutions to the system (52) are given by

$$Y_1 = \frac{\theta_0 X_1}{1-b}, Z_1 = 0, \widetilde{Y}_1 = -L_b(\gamma_1+\gamma_2)X_1, \widetilde{Z}_1 = 0, V_1 = \frac{\sqrt{Ta}}{\mathcal{D}}X_1 . \tag{54}$$

We can express the equations for the second order in ε as follows:

$$\mathcal{L}\vec{X}_2 = [\mathcal{R}_{21}, \mathcal{R}_{22}, \mathcal{R}_{23}, \mathcal{R}_{24}, \mathcal{R}_{25}, \mathcal{R}_{26}]^{Tr}, \quad \vec{X}_2 = [X_2, Y_2, Z_2, \widetilde{Y}_2, \widetilde{Z}_2, V_2]^{Tr} , \tag{55}$$

where the nonlinear terms $\mathcal{R}_{2j}$ $(j = 1,2,3,4,5,6)$ are

$$\mathcal{R}_{21} = 0, \mathcal{R}_{22} = \mathcal{V}_a^{-1}X_1 Z_1, \mathcal{R}_{23} = -\mathcal{V}_a^{-1}X_1 Y_1, \mathcal{R}_{24} = \widetilde{\sigma}\mathcal{V}_a^{-1}X_1\widetilde{Z}_1, \mathcal{R}_{25} = -\widetilde{\sigma}\mathcal{V}_a^{-1}X_1\widetilde{Y}_1, \mathcal{R}_{26} = 0 .$$

Solutions of the equations (55) have the form:

$$Y_2 = \frac{\theta_0 X_2}{1-b}, Z_2 = \frac{\theta_0 X_1^2}{(b-\gamma)(b-1)}, \widetilde{Y}_2 = -L_b(\gamma_1+\gamma_2)X_2, \widetilde{Z}_2 = -\frac{L_b^2}{\gamma}(\gamma_1+\gamma_2)X_1^2, V_2 = \frac{\sqrt{Ta}}{\mathcal{D}}X_2 . \tag{56}$$

We will now proceed to discuss third-order equations:

$$\mathcal{L}X_3 = [\mathcal{R}_{31}, \mathcal{R}_{32}, \mathcal{R}_{33}, \mathcal{R}_{34}, \mathcal{R}_{35}, \mathcal{R}_{36}]^{Tr}, \quad X_3 = [X_3, Y_3, Z_3, \widetilde{Y}_3, \widetilde{Z}_3, V_3]^{Tr} , \tag{57}$$

where

$$\mathcal{R}_{31} = \frac{\partial X_1}{\partial \tau} - R_2 Y_1 - R_0\delta\cos(\Omega\tau)Y_1 + Rb\delta\cos(\Omega\tau)\widetilde{Y}_1, \Omega = \frac{\widetilde{\omega}_g}{\varepsilon^2} ,$$

$$\mathcal{R}_{32} = \frac{\partial Y_1}{\partial \tau} + \mathcal{V}_a^{-1}(X_1 Z_2 + X_2 Z_1), \mathcal{R}_{33} = 0, \mathcal{R}_{34} = \frac{\partial \widetilde{Y}_1}{\partial \tau} - \widetilde{\sigma}\mathcal{V}_a^{-1}\gamma_1\delta\cos(\Omega\tau)X_1 + \widetilde{\sigma}\mathcal{V}_a^{-1}(X_1\widetilde{Z}_2 + X_2\widetilde{Z}_1) ,$$

$$\mathcal{R}_{35} = 0, \mathcal{R}_{36} = \frac{\sqrt{Ta}}{\mathcal{D}}\frac{\partial X_1}{\partial \tau} .$$

We utilized the Fredholm alternative condition [46] to obtain the Ginzburg-Landau amplitude equation in the following form:

$$\mathcal{A}_1\frac{\partial X_1}{\partial \tau} - \mathcal{A}_2 X_1 + \mathcal{A}_3 X_1^3 = 0 , \tag{58}$$

where the coefficients $\mathcal{A}_1, \mathcal{A}_2, \mathcal{A}_3$ are defined by:

$$\mathcal{A}_1 = 1 + \frac{R_0\theta_0\mathcal{V}_a}{(1-b)^2} + RbL_b^2\frac{(\gamma_1+\gamma_2)\mathcal{V}_a}{\widetilde{\sigma}} - \frac{T\sqrt{Ta}}{\mathcal{D}^2} , \quad \mathcal{A}_2 = \frac{R_2\theta_0}{1-b} + \frac{R_0\theta_0}{1-b}\delta\cos(\Omega\tau) + RbL_b\gamma_2\delta\cos(\Omega\tau) ,$$

$$\mathcal{A}_3 = \frac{R_0\theta_0}{(\gamma-b)(1-b)^2} + \frac{RbL_b^3}{\gamma}(\gamma_1+\gamma_2) . \tag{59}$$

Passing to the new rescaled derivative with respect to slow time $\dfrac{\partial}{\partial \tau_1} = (a^2 \mathcal{V}_a) \dfrac{\partial}{\partial \tau}$ and using relations (45), (47), we rewrite equation (58) in the following form:

$$A_1 \frac{\partial A}{\partial \tau_1} - A_2(\tau)A + A_3 A^3 = 0 , \tag{60}$$

where

$$A_1 = \frac{a^2}{\mathcal{V}_a} + \frac{4\pi^2 k_c^2 Ra_c}{(4\pi^2 - \mathrm{R}_i)(a^2 - \mathrm{R}_i)^2} + \frac{k_c^2}{a^4}\frac{R_b L_b}{\widetilde{\sigma}}\frac{4\pi^2 \langle n \rangle}{4\pi^2 + \mathrm{Pe}^2}\Big[PeG_0((1-\alpha_0)k^2 + (1+\alpha_0)\pi^2) + \mathrm{Pe}\Big] - \frac{\pi^2 \mathrm{Ta}}{\mathcal{V}_a(1 + D_a a^2)^2} ,$$

$$A_2 = \frac{4\pi^2 k_c^2}{(4\pi^2 - \mathrm{R}_i)(a^2 - \mathrm{R}_i)}\Big(Ra_2 + Ra_c \delta \cos(\Omega_1 \tau_1)\Big) + \frac{k_c^2 R_b}{a^2}\frac{4\pi^2 \langle n \rangle \mathrm{Pe}}{4\pi^2 + \mathrm{Pe}^2}\delta \cos(\Omega_1 \tau_1) ,$$

$$A_3 = \frac{k_c^4}{8a^4}\left(\frac{16\pi^4 a^4 Ra_c}{(16\pi^4 a^4 - \mathrm{R}_i^2)(a^2 - \mathrm{R}_i)^2} + R_b L_b^2(\gamma_1 + \gamma_2)\right), \quad \Omega_1 = \frac{\omega_g}{\varepsilon^2} . \tag{61}$$

In the case where there is no rotation and internal heating, the GL equation (60) for small Peclet numbers coincides with the result obtained by Kopp and Yanovsky [41]. They obtained the GL equation by applying perturbation theory for the small supercritical parameter of the Rayleigh number to the nonlinear system of equations (29)-(32). Because nonlinearity near the critical state of convection is considered in this approach, it is assumed that $Ra_2 \approx Ra_c$. Thus, a small expansion parameter ε^2 is introduced in the weakly nonlinear theory of convective instability, which is the relative deviation of the Rayleigh number Ra from its critical value Ra_c:

$$\varepsilon^2 = \frac{Ra - Ra_c}{Ra_c} \ll 1 .$$

For the unmodulated case, the analytical solution of the above equation (60) takes the following form:

$$\widetilde{A}(\tau_1) = \frac{A_0}{\sqrt{\dfrac{A_3}{A_2}A_0^2 + \left(1 - A_0^2 \dfrac{A_3}{A_2}\right)\exp\left(-\dfrac{2\tau_1 A_2}{A_1}\right)}} , \tag{62}$$

where $\widetilde{A}(\tau_1)$ represents the amplitude of convection for the unmodulated case, and A_1 and A_3 have the same expressions as given in (37), while $A_2 = k_c^2 Ra_2 / a^2$.

6. RESULTS AND DISCUSSION

In our study, we utilized a truncated Fourier series to analyze the phenomenon of weakly nonlinear biothermal convection. We focused on a rotating layer of a porous medium that is saturated with Newtonian fluid and contains gyrotactic microorganisms. The medium is subjected to gravitational modulation and internal heating. To solve the resulting nonlinear system of equations (36)-(41), we employed numerical methods to determine the heat and mass exchange coefficients, Nu and Sh. We chose a reasonable order of modulation amplitude, i.e., $\delta = 0.1$, and suitable initial conditions for the disturbance amplitudes, i.e., about 0.5. Let the value of the modified bioconvective Rayleigh-Darcy number $\mathrm{Ra}_B = \mathrm{R}_b \langle n \rangle$ change in the range $[0, 5000]$, and the values of the parameters Pe and G_0 change in the vicinity of $\mathrm{Pe} = 0.1$ and $G_0 = 0.01$ [34]. The cell eccentricity can vary in the range $\alpha_0 \in [0,1]$. Next, we started examining the impact of parameters $D_a, \mathrm{Ta}, \mathrm{Ra}_B, \mathrm{Pe}, \alpha_0$ and R_i on the development of in Fig. 2 illustrate the relationship between the stationary Rayleigh number (44) and the dimensionless wavenumber k_c in linear theory. From the graphs, it is clear that the stability curves divide the space into two regions: the region above the curve is unstable, and the region below the curve is stable. This provides a clear visual representation of the relationship between parameters and system stability.

Fig. 2a illustrates the relationship between the stationary Rayleigh-Darcy number Ra_c and k_c for different Darcy number values $D_a = (0.3, 0.5, 0.8)$. The plot has fixed parameters $\alpha_0 = 0.4$, $\mathrm{Ra}_B = 3000$, $\mathrm{Pe} = 0.1$, $\mathrm{R}_i = 0.5$ and $\mathrm{Ta} = 100$. The plot clearly shows that an increase in the Darcy number leads to a rise in the minimum Rayleigh-Darcy number, indicating that higher Darcy numbers stabilize the stationary convection and delay its onset.

Fig. 2b shows the relationship between the stationary Rayleigh-Darcy number Ra_c and the dimensionless wavenumber k_c for different values of the Taylor number: $\mathrm{Ta} = (100, 200, 300)$. The fixed parameters in this plot are

$D_a = 0.3$, $\mathrm{Ra}_B = 3000$, $Pe = 0.1$, $\mathrm{R}_i = 0.5$ and $\alpha_0 = 0.4$. The graph demonstrates that as the Taylor number increases, the minimum Rayleigh-Darcy number also increases. This means that higher Taylor numbers stabilize stationary convection and delay the onset of convection.
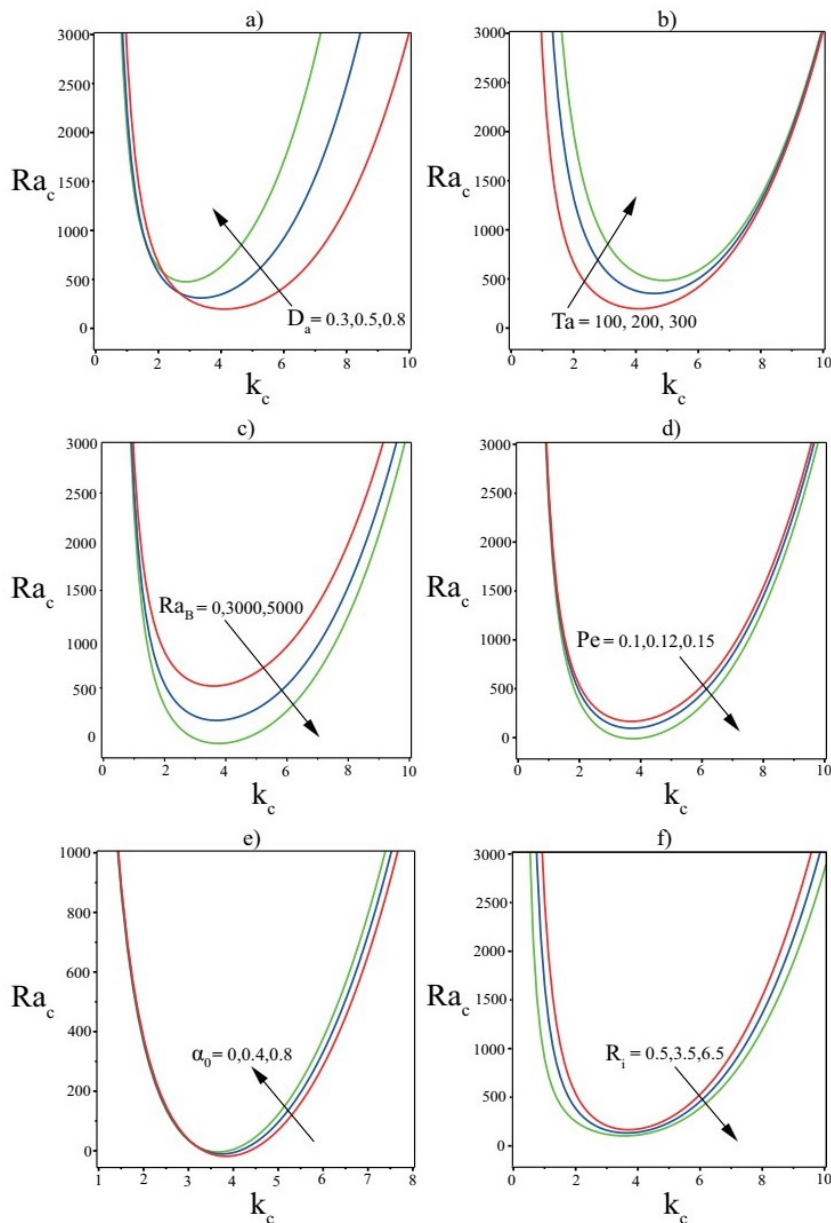
Figure 2. Plots of the stationary Rayleigh number Ra_c versus wave numbers k_c.

Fig. 2c shows the relationship between the stationary Rayleigh-Darcy number and the dimensionless wave number for various values of the modified bioconvection Rayleigh-Darcy number: $Ra_B = (0,3000,5000)$. The parameters $D_a = 0.3$, $Ta = 100$, $Pe = 0.1$, $\mathrm{R}_i = 0.5$ and $\alpha_0 = 0.4$ on this graph remain constant. The red curve represents the dependence of the stationary Rayleigh-Darcy number on the wave number in the absence of bioconvection of microorganisms ($Ra_B = 0$). Looking at Fig. 2c, it is clear that with increasing parameter Ra_B the threshold for the occurrence of biothermal convection decreases. This means that an increase in the concentration of microorganisms causes a redistribution of liquid density. Then, the swimming movement of microorganisms against gravity can destabilize the stationary process of biothermal convection.

Fig. 2d shows the relationship between the stationary Rayleigh-Darcy number and the dimensionless wave number for various values of the Peclet number: $Pe = (0.1,0.12,0.15)$. The parameters $D_a = 0.3$, $D_a = 0.3$, $Ra_B = 3000$, $\mathrm{R}_i = 0.5$ and $\alpha_0 = 0.4$ on this graph remain constant. From the graphs, it is evident that a decrease in the minimum Rayleigh numbers is correlated with an increase in the Peclet number or the swimming speed of cells. In other words, as Peclet numbers increase, the stability threshold of bio-thermal convection decreases.

Fig. 2e depicts the relationship between the stationary Rayleigh-Darcy number and the dimensionless wavenumber for different values of cell eccentricity: $\alpha_0 = (0, 0.4, 0.8)$. The parameters $D_a = 0.3$, $Ra_B = 3000$, $R_i = 0.5$ and $Pe = 0.15$ are fixed in this plot. By examining the graph, it becomes evident that as the cell eccentricity increases, the threshold for the onset of bio-thermal convection increases a bit. In simpler terms, microorganisms with a more elongated or non-spherical shape don't tend to facilitate the development of bio-thermal convection more than microorganisms with a spherical shape. This observation aligns with similar conclusions made in references [20],[23]. As a result, the shape of microorganisms influences the behavior and stability of the bio-thermal convection process within the studied system.

In Fig. 2f, the stationary Rayleigh-Darcy number Ra_c is plotted as a function of the dimensionless wave number k_c for different values of the internal heating parameter R_i. The fixed parameters in this graph are $D_a = 0.3$, $Ra_B = 3000$, $Ta = 100$, $Pe = 0.1$ and $\alpha_0 = 0.4$. The graph shows that as the internal Rayleigh number R_i increases, the minimum Rayleigh-Darcy numbers decrease. This indicates that higher R_i numbers have a destabilizing effect on stationary convection.

For numerical analysis of equations (36)-(41) and (49)-(50), we use the standard Maple computer environment programs. The Runge-Kutta-Felberg method (rfk45) was used to solve nonlinear equations (36)-(41) with the following initial conditions: $A_{11}(0) = B_{11}(0) = C_{11}(0) = B_{02}(0) = C_{02}(0) = V_{11}(0) = 0.5$.

In Figs. 3a and 4a, it is shown that an increase in the Vadas number $\mathcal{V}_a$ contributes to an increase in heat and mass transfer over a short time interval. This observation is consistent with investigations carried out by Kiran et al. [38]-[40], Bhadauria and Agarwal [47], and Kopp and Yanovsky [42] where a comparable phenomenon was observed. The Vadasz number, which is directly proportional to the Prandtl number, assumes a pivotal role in determining the convective heat transfer characteristics. As the Vadasz number surges, it signifies an increased ratio of kinematic viscosity to thermal diffusivity in the fluid. This, in turn, leads to heightened fluid mobility. Consequently, elevating the Vadasz number results in a heightened rate of heat and mass transfer within the system.
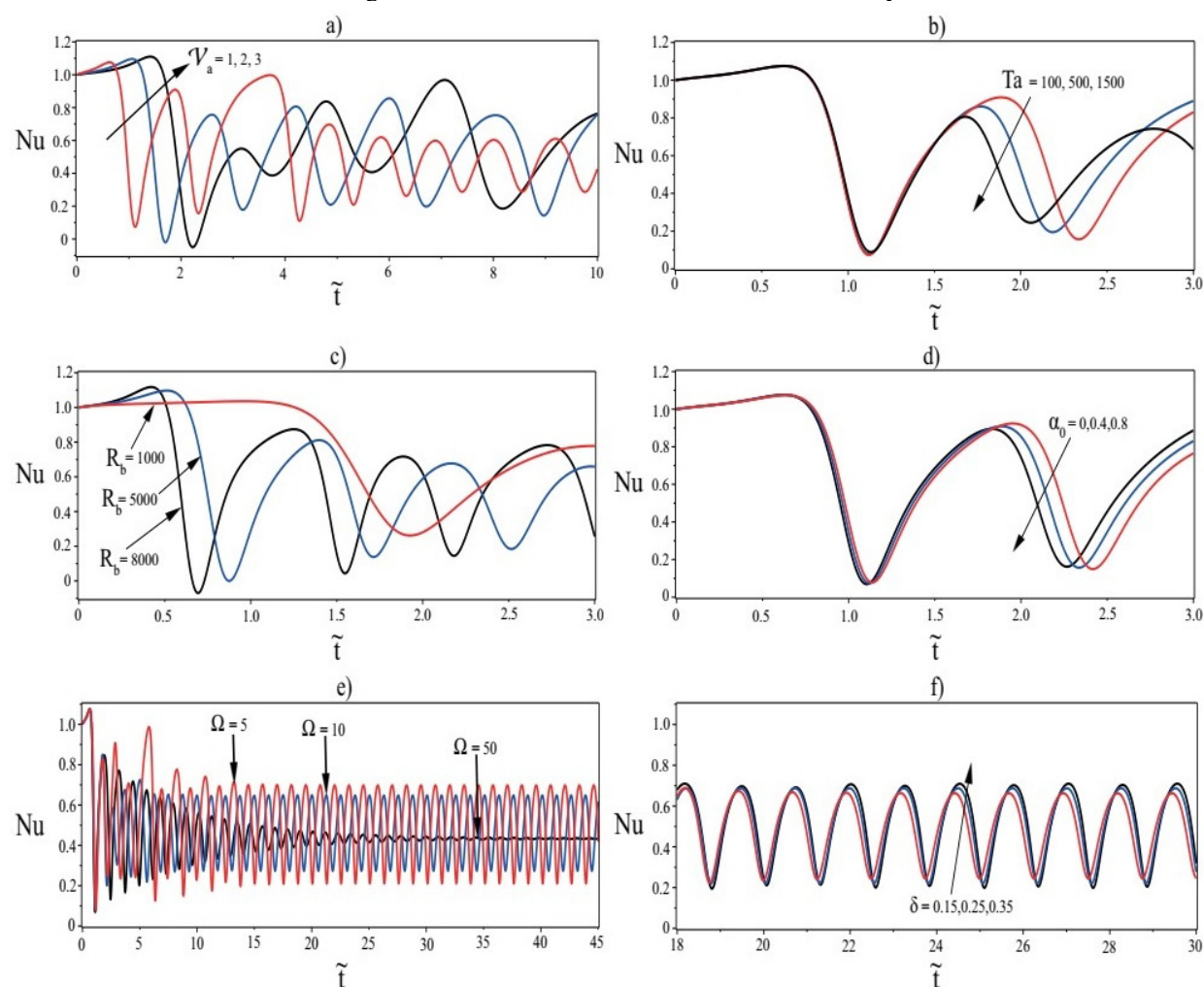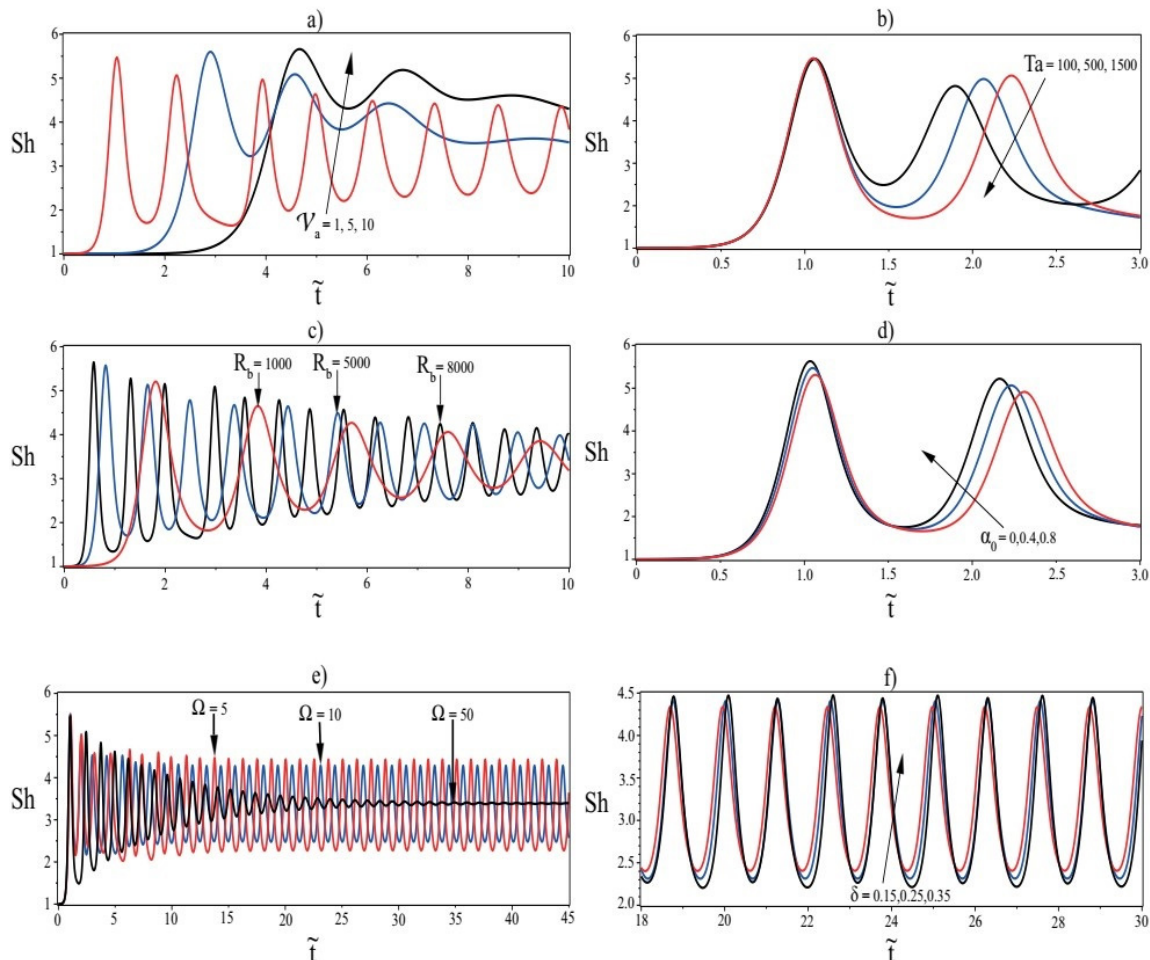

Figure 3. Dependence of the Nusselt number Nu on the time $\tilde{t}$ for a) $\mathcal{V}_a$, b) Ta, c) R_b, d) α_0, e) Ω, f) δ variations.

According to Figs. 3b and 4b, as the Taylor-Darcy number Ta increases, the value of the Nusselt Nu and Sherwood Sh numbers decreases, lowering the rate of heat and mass transfer and, as a result, stabilizing the system.

Figs. 3c and 4c show the effect of an increasing bioconvective Rayleigh-Darcy number R_b on heat and mass transfer. An increase in the bioconvective Rayleigh-Darcy number can be caused by an increase in the permeability of the porous medium or a decrease in the viscosity of the liquid medium. In both cases, this causes an increase in the velosity of convective flows, which promotes the transfer of heat and mass of microorganisms and therefore leads to destabilization of the system. This phenomenon eventually results in an increase in the Nusselt and Sherwood numbers over short time intervals, as shown in Figs. 3a and 4a.

Graphs in Figs. 3d and 4d demonstrate a significant influence of the shape of the microorganism on heat and mass exchange in the system, which is reflected in the temporary change in the Nusselt and Sherwood numbers. This physical phenomenon can be explained by considering how the shape of microorganisms affects their movement and interaction with liquid. In the case of spherical microorganisms $\alpha_0 = 0$ (represented by the red curve in Fig. 3d and 4d), their symmetrical shape ensures relatively unhindered movement in the liquid. This promotes improved heat transfer within the system, resulting in higher convective heat transfer rates and, therefore, higher Nusselt numbers. On the other hand, when microorganisms have a non-spherical or irregular shape $\alpha_0 = (0.4, 0.8)$ (represented by the blue and black curves in Fig. 3d and 4d), their movement in the liquid becomes more intense and complex. The presence of asymmetry in their shape can lead to a change in the flow regime. As a result, the process of convective heat transfer can be hindered, leading to lower heat transfer rates, lower Nusselt numbers, and, conversely, higher mass transfer rates (higher Sherwood numbers) compared to the case of spherical microorganisms.

Figs. 3e and 4e show the influence of the modulation frequency Ω on heat and mass exchange in the system. It can be noted that at lower modulation frequencies, especially in the low frequency case ($\Omega = 5$), higher heat and mass transfer rates are achieved compared to higher oscillation frequencies ($\Omega = 10$ and $\Omega = 50$). This suggests that lower modulation frequencies lead to more efficient heat transfer within the system. The observed trend is consistent with the results presented by Gresho and Sleigh [33] and Kopp et al. [48] in the context of conventional fluids, highlighting the importance of using low-frequency g-jitter to optimize the transfer process and improve heat transfer.

Figure 4. Dependence of the Sherwood number Sh on the time $\tilde{t}$ for a) $\mathcal{V}_a$, b) Ta, c) R_b, d) α_0, e) Ω, f) δ variations.

Weakly Nonlinear Biothermal Convection in a Porous Media Layer Under Rotation...   **EEJP. 1 (2024)**

Figs. 3f and 4f show the influence of the modulation amplitude δ on heat and mass exchange in the system. The study considers a range of δ values, specifically chosen to improve heat transfer, from 0.15 to 0.35. The graphs show how changing the modulation amplitude affects the characteristics of heat and mass transfer. It is obvious that higher modulation amplitudes lead to an increase in the rate of heat and mass exchange. By appropriately selecting the modulation amplitude, heat and mass transfer can be optimized, thereby improving overall system performance.
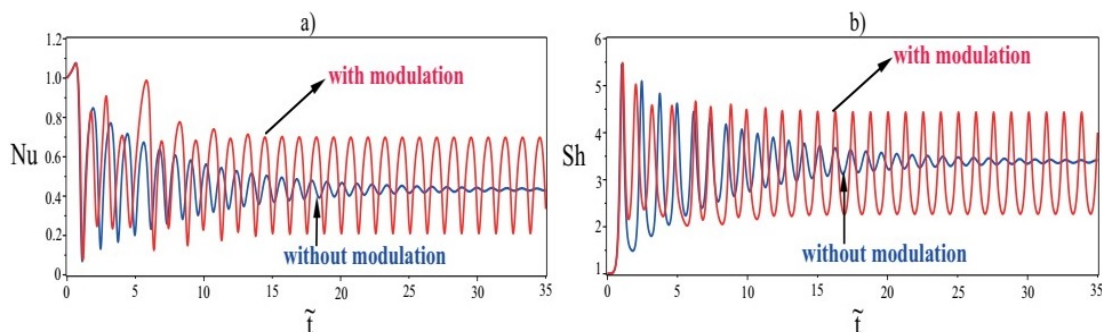
Figure 5. a) Variations of the Nusselt number $\mathrm{N}u(\tilde{t})$ in the absence of $\delta = 0$ and the presence of $\delta = 0.3, \Omega = 5$ modulation of the gravity field; b) variations of the Sherwood number $\mathrm{Sh}(\tilde{t})$ in the absence of $\delta = 0$ and the presence of $\delta = 0.3, \Omega = 5$ modulation of the gravity field.

In Figs. 5a and 5b, a comparison is presented between modulated and unmodulated systems. The graphs depict the characteristics of these two systems with regard to heat and mass transfer, as represented by the Nusselt and Sherwood numbers. In the unmodulated system, it is evident that the Nusselt number (Sherwood number) experiences a rapid increase for small values of the time parameter $\tilde{t}$. This initial surge in heat and mass transfer is followed by a phase of stabilization at higher $\tilde{t}$ values. This pattern suggests that, in the absence of gravitational field modulation, the process of heat and mass transfer eventually reaches a steady state. Conversely, the modulated system displays oscillatory behavior concerning Nusselt and Sherwood numbers. This signifies that heat exchange undergoes periodic fluctuations due to the modulation of the gravitational field. These fluctuations in the Nusselt and Sherwood numbers mirror the alternating enhancement and suppression of heat and mass exchange resulting from the gravitational field modulation.

7. CONCLUSIONS

In this research, we employed the Darcy-Brinkman model to explore the impacts of rotation, internal heating, and gravity modulation on biothermal convection within a porous medium saturated with a Newtonian fluid that includes gyrotactic microorganisms. Our analysis is based on the expansion of the perturbed parameters of the system using a truncated Fourier series. As a result of applying this approach, a non-autonomous system of nonlinear differential equations was obtained. An exact analytical solution to this system of equations was obtained for the stationary case. For small amplitudes of disturbances, i.e., within the framework of the linear theory of convective instability, we obtained the dispersion relation between the critical value of the Rayleigh number Ra_c and the wave number k_c. Based on the findings from the analysis of linear bio-thermal convective instability, the following conclusions can be drawn:

• Increasing the Darcy and Taylor numbers leads to an increase in the stability of the system.

• An increase in the modified bioconvective Rayleigh-Darcy number Ra_B, Peclet number Pe, and internal heating parameter R_i leads to destabilization of the system.

• Spherical gyrotactic microorganisms play a more significant role in fostering the onset of bio-thermal instability.

After conducting a numerical analysis of the resultant nonlinear system of equations, we drew several conclusions regarding the impact of gravitational modulation on biothermal convection in porous media:

• When the values of the parameters $\mathcal{V}_a$ and R_b are increased, a short-term growth in heat and mass transfer is observed.

• Increasing the Taylor number Ta has a stabilizing effect on the system, which delays the onset of convection and reduces heat and mass transfer.

• The spherical shape of the microorganisms contributes to a more efficient heat transfer process.

• Increasing the modulation frequency Ω leads to a decrease in the variations of the Nusselt and Sherwood numbers, resulting in suppressed heat and mass transfer.

• Increasing the modulation amplitude δ enhances heat and mass transfer.

Certainly, the examination of parameters like $\mathrm{Ta}, \mathrm{R}_b, \mathrm{Pe}, \alpha_0 \, \mathcal{V}_a, \, \Omega$, and δ offers valuable insights into their influence on the convection process. Through the manipulation of these parameters, it becomes feasible to amplify or control heat transfer in a porous medium saturated with a Newtonian fluid containing gyrotactic microorganisms. These

conclusions provide a foundation for designing more efficient heat transfer systems, formulating strategies to regulate convection, and enhancing thermal management across diverse applications.

ORCID

Michael I. Kopp, https://orcid.org/0000-0001-7457-3272, **Volodymyr V. Yanovsky,** https://orcid.org/0000-0003-0461-749X

REFERENCES

[1] D. Ingham, and L. Pop, *Transport Phenomena in Porous Media* (Elsevier, Oxford, 2005).
[2] D.A. Nield, and A. Bejan, "Internal Natural Convection: Heating from Below," in: *Convection in Porous Media*, (Springer, Cham, 2017). https://doi.org/10.1007/978-3-319-49562-0
[3] P. Vadasz, "Instability and convection in rotating porous media: A review," Fluids **4**, 147 (2019). http://dx.doi.org/10.3390/fluids4030147
[4] A.K. Agarwal, and A. Verma, "The effect of compressibility, rotation and magnetic field on thermal instability of Walters' fluid permeated with suspended particles in porous medium," Thermal Science **18**, 539-550 (2014). https://doi.org/10.2298/TSCI110805087A
[5] G. Padma, and S.V. Suneetha, "Hall effects on MHD Flow through Porous Medium in a Rotating Parallel Plate Channel," Int. J. Appl. Eng. Res. **13**, 9772-9789 (2018). https://www.ripublication.com
[6] P. Vasseur, and L. Robillard, "Natural convection in enclosures filled with anisotropic porous media," Trans. Phenom. Porous Media, 331-356 (1998). https://doi.org/10.1016/B978-008042843-7/50014-3
[7] M. Fahs, A. Younes, and A. Makradi, "A reference benchmark solution for free convection in a square cavity filled with a heterogeneous porous medium," Numer. Heat Transfer Part B Fundam. **67**, 437-462 (2015). https://doi.org/10.1080/10407790.2014.977183
[8] M. Zhao, S. Wang, S.C. Li, Q.Y. Zhang, and U.S. Mahabaleshwar, "Chaotic Darcy-Brinkman convection in a fluid saturated porous layer subjected to gravity modulation," Results in Physics, **9,** 1468-1480 (2018). https://doi.org/10.1016/j.rinp.2018.04.047
[9] T.S. Lundgren, "Slow Flow through Stationary Random Beds and Suspensions of Spheres," J. Fluid Mech. **51**, 273-299 (1972). http://dx.doi.org/10.1017/S002211207200120X
[10] D. Yadav, R. Bhargava, and G.S. Agrawal, "Boundary and internal heat source effects on the onset of Darcy-Brinkman convection in a porous layer saturated by nanofluid," Int. J. Therm. Sci. **60**, 244-254 (2012). https://doi.org/10.1016/j.ijthermalsci.2012.05.011
[11] D.A. Nield, and A.V. Kuznetsov, "The Onset of Convection in an Internally Heated Nanofluid Layer," J. Heat Transfer, **136**, 014501 (2014). https://doi.org/10.1115/1.4025048
[12] I.K. Khalid, N.F.M. Mokhtar, I. Hashim, Z.B. Ibrahim, and S.S.A. Gani, "Effect of Internal Heat Source on the Onset of Double-Diffusive Convection in a Rotating Nanofluid Layer with Feedback Control Strategy," Adv. Math. Phys. **2017**, 2789024. https://doi.org/10.1155/2017/2789024
[13] C. Jain, and V.S. Solomatov, "Onset of convection in internally heated fluids with strongly temperature-dependent viscosity," Phys. Fluids, **34**, 096604 (2022). https://doi.org/10.1063/5.0105170
[14] M. Devi, J. Sharma, and U. Gupta, "Effect of internal heat source on Darcy-Brinkman convection in a non-newtonian casson nanofluid layer," J. Porous Media, **25**, 17-35 (2022). https://doi.org/10.1615/JPorMedia.2022039506
[15] T.J. Pedley, N.A. Hill, and J.O. Kessler, "The growth of bioconvection patterns in a uniform suspension of gyrotactic microorganisms," J. Fluid Mech. **195**, 223-338 (1988). https://doi.org/10.1017/S0022112088002393
[16] N.A. Hill, T.J. Pedley, and J.O. Kessler, "Growth of bioconvection patterns in a suspension of gyrotactic microorganisms in a layer of finite depth," J. Fluid Mech. **208**, 509-543 (1989). https://doi.org/10.1017/S0022112089002922
[17] T.J. Pedley, and J.O. Kessler, "Hydrodynamic phenomena in suspensions of swimming microorganisms," Ann. Rev. Fluid Mech. **24**, 313-358 (1992). http://dx.doi.org/10.1146/ANNUREV.FL.24.010192.001525
[18] S. Childress, M. Levandowsky, and E.A. Spiegel, "Pattern formation in a suspension of swimming microorganisms: equations and stability theory," J. Fluid Mech. **69**, 591-613 (1975). https://doi.org/10.1017/S0022112075001577
[19] A V. Kuznetsov, and A. A. Avramenko, "Stability Analysis of Bioconvection of Gyrotactic Motile Microorganisms in a Fluid Saturated Porous Medium," Transp. Porous Media, **53**, 95-104 (2003). http://dx.doi.org/10.1023/A:1023582001592
[20] D.A. Nield, A.V. Kuznetsov, and A.A. Avramenko, "The onset of bioconvection in a horizontal porous-medium layer," Transp. Porous Media, **54**, 335-344 (2004). http://dx.doi.org/10.1023/B:TIPM.0000003662.31212.5b
[21] A.A. Avramenko, and A.V. Kuznetsov, "The Onset of Convection in a Suspension of Gyrotactic Microorganisms in Superimposed Fluid and Porous Layers: Effect of Vertical Throughflow," Transp. Porous Media, **65**, 159-176 (2006). http://dx.doi.org/10.1007/s11242-005-6086-3
[22] A.V. Kuznetsov, "The onset of thermo-bioconvection in a shallow fluid saturated porous layer heated from below in a suspension of oxytactic microorganisms," Eur. J. Mech. B/Fluids **25**, 223-233 (2006). http://dx.doi.org/10.1016/j.euromechflu.2005.06.003
[23] A.A. Avramenko, "Model of Lorenz instability for bioconvection," Dopov. Nac. akad. nauk Ukr. **10**, 68-76 (2010).
[24] E. Lorenz, "Deterministic nonperiodic flow," J. Atmos. Sci. **20**, 130-141 (1963). https://doi.org/10.1175/1520-0469(1963)020<0130:DNF>2.0.CO;2
[25] Y. Hwang, and T.J. Pedley, "Bioconvection under uniform shear: linear stability analysis," J. Fluid Mech. **738**, 522-562 (2014). https://doi.org/10.1017/jfm.2013.604
[26] N.P. Dmitrenko, "Main aspects of the process of bioconvection in nanofluids and porous media," Industrial Heat Engineering **39**(5), 19-25 (2017). https://doi.org/10.31472/ihe.5.2017.03
[27] Y.D. Sharma, and V. Kumar, "The effect of high-frequency vertical vibration in a suspension of gyrotactic micro-organisms," Mech. Res. Commun. **44**, 40-46 (2012). https://doi.org/10.1016/j.mechrescom.2012.06.001
[28] A.K. Kushwaha, Y.D. Sharma, and A. Sharma, "Stability analysis of Vibrational System of Shallow Layers repleted with Random Swimming Gyrotactic Microorganisms," Research Square, https://doi.org/10.21203/rs.3.rs-1814108/v1
[29] A. Garg, Y.D. Sharma, and S.K. Jain, "Stability analysis of thermo-bioconvection flow of Jeffrey fluid containing gravitactic microorganism into an anisotropic porous medium," Forces in Mechanics, **10**, 100152 (2023). https://doi.org/10.1016/j.finmec.2022.100152

[30] M. Zhao, S. Wang, H. Wang, and U.S. Mahabaleshwar, "Darcy-Brinkman bio-thermal convection in a suspension of gyrotactic microorganisms in a porous medium," Neural Comput. and Applic. **31**, 1061-1067 (2019). https://doi.org/10.1007/s00521-017-3137-y

[31] M.I. Kopp, V.V. Yanovsky, and U.S. Mahabaleshwar, "A Bio-Thermal Convection in a Porous Medium Saturated by Nanofluid Containing Gyrotactic Microorganisms Under an External Magnetic Field," East European Journal of Physics **4**, 23-47 (2022). https://doi.org/10.26565/2312-4334-2022-4-02

[32] M.I. Kopp, and V.V. Yanovsky, "Darcy-Brinkman bio-thermal convection in a porous rotating layer saturated by Newtonian fluid containing gyrotactic microorganisms," Ukr. J. Phys. **68**, 30-37 (2023). https://doi.org/10.15407/ujpe68.1.30

[33] P.M. Gresho, and R. Sani. "The effects of gravity modulation on the stability of a heated fluid layer," J. Fluid Mech. **40**, 783-806 (1970). https://doi.org/10.1017/S0022112070000447

[34] M.S. Malashetty, and I. Begum. "Effect of Thermal/Gravity Modulation on the Onset of Convection in a Maxwell Fluid Saturated Porous Layer," Transp. Porous Med. **90**, 889-909 (2011). https://doi.org/10.1007/s11242-011-9822-x

[35] P. Kiran, "Nonlinear thermal convection in a viscoelastic nanofluid saturated porous medium under gravity modulation," Ain Shams Engineering Journal, **7**, 639-651 (2016). https://doi.org/10.1016/j.asej.2015.06.005

[36] P. Kiran, "Gravity modulation effect on weakly nonlinear thermal convection in a fluid layer bounded by rigid boundaries," Int. J. Nonlinear Sci. Num. Simul. (2021). https://doi.org/10.1515/ijnsns-2021-0054.

[37] P. Kiran, "Nonlinear throughflow and internal heating effects on vibrating porous medium," Alex. Eng. J. **55**, 757-767 (2016). http://dx.doi.org/10.1016/j.aej.2016.01.012

[38] P. Kiran, "Throughflow and gravity modulation effects on heat transport in a porous medium," J. Appl. Fluid Mech. **9**, 1105-1113 (2016). https://doi.org/10.18869/acadpub.jafm.68.228.24682

[39] P. Kiran, S.H. Manjula, and R. Roslan. "Weak nonlinear analysis of nanofluid convection with g-jitter using the Ginzburg-Landau model," Open Physics, **20**, 1283-1294 (2022). https://doi.org/10.1515/phys-2022-0217

[40] S. H. Manjula, Palle Kiran, and S. N. Gaikwad. "Study of Heat and Mass Transfer in a Rotating Nanofluid Layer Under Gravity Modulation," J. Nanofluids **12**, 842-852 (2023). https://doi.org/10.1166/jon.2023.1971

[41] M.I. Kopp, and V.V. Yanovsky, "Effect of gravity modulation on weakly nonlinear bio-thermal convection in a porous medium layer," J. Appl. Phys. **134**, 104702 (2023). http://dx.doi.org/10.1063/5.0165178

[42] P. Kiran, and S.H. Manjula, "Weakly nonlinear bio-convection in a porous media under temperature modulation and internal heating," Research Square, (2023). https://doi.org/10.21203/rs.3.rs-3313311/v1

[43] R. Chand, and G.C. Rana, "On the onset of thermal convection in rotating nanofluid layer saturating a Darcy-Brinkman porous medium," International Journal of Heat and Mass Transfer, **55**, 5417-5424 (2012). https://doi.org/10.1016/j.ijheatmasstransfer.2012.04.043

[44] G.C. Rana, and R. Chand, "On the onset of thermal convection in a rotating nanofluid layer saturating a Darcy-Brinkman porous medium: a more realistic model," Journal of Porous Media, **18**, 629-635 (2015). https://doi.org/10.1016/j.ijheatmasstransfer.2012.04.043

[45] P.G. Siddheshwar, and C. Kanchana, "Unicellular unsteady Rayleigh-Benard convection in Newtonian liquids and Newtonian nanoliquids occupying enclosures: new findings," Int. J. Mech. Sci. **131**, 1061-1072 (2017). https://doi.org/10.1016/j.ijmecsci.2017.07.050

[46] R. Haberman, *Elementary Applied Partial Differential Equations with Fourier Series and Boundary Value Problems*, 4th ed. (Pearson/Prentice Hall, N.J., 2004).

[47] B.S. Bhadauria, and S. Agarwal, "Natural convection in a nanofluid saturated rotating porous layer: a nonlinear study," Transp. Porous Med. 87, 585-602 (2011). https://doi.org/10.1007/s11242-010-9702-9

[48] M.I. Kopp, A.V. Tur, and V.V. Yanovsky, "Weakly Nonlinear Magnetic Convection in a Nonuniformly Rotating Electrically Conductive Medium Under the Action of Modulation of External Fields," East Eur. J. Phys. 2, 5-37 (2020). https://doi.org/10.26565/2312-4334-2020-2-01

СЛАБОНЕЛІНІЙНА БІОТЕРМАЛЬНА КОНВЕКЦІЯ В ШАРІ ПОРИСТОГО СЕРЕДОВИЩА ПІД ВПЛИВОМ ОБЕРТАННЯ, ГРАВІТАЦІЙНОЇ МОДУЛЯЦІЇ ТА ДЖЕРЕЛА ТЕПЛА

Михайло Й. Копп[a], Володимир В. Яновський[a,b]

[a]*Інститут монокристаллов, Національна Академія Наук України*
пр. Науки 60, 61072 Харків, Україна
[b]*Харківський національний університет імені В.Н. Каразина*
майдан Свободи, 4, 61022, Харків, Україна

В цій роботі досліджено вплив гравітаційної модуляції на слабонелінійну біотермальну конвекцію в пористому шарі, що обертається. Розглядається шар пористого середовища, насиченого ньютонівською рідиною, що містить гіротактичні мікроорганізми і схильної до гравітаційної модуляції, обертання і внутрішнього нагрівання. Для аналізу лінійної стійкості досить уявлення обурень як нормальних мод, тоді як нелінійний аналіз включає усічений ряд Фур'є, що містить гармоніку нелінійної взаємодії. Побудовано шестивимірну нелінійну модель типу Лоренца, яка виявляє як симетрію відображення, так і дисипацію. Тепло- і масоперенос ми визначили з використанням слабкої нелінійної теорії, заснованої на уявленні усіченого ряду Фур'є. Додатково було досліджено поведінку нестаціонарних чисел Нуссельта та Шервуда шляхом чисельного вирішення рівнянь кінцевої амплітуди. Застосовуючи розкладання регулярних збурень за малим параметром до шестивимірної моделі рівнянь Лоренца з періодичними коефіцієнтами, ми отримали рівняння Гінзбурга-Ландау (ГЛ). Це рівняння визначає еволюцію кінцевої амплітуди виникнення конвекції. Амплітуда конвекції у немодульованому випадку визначається аналітично і служить еталоном для порівняння. У дослідженні вивчається вплив різних параметрів на систему, включаючи число Вадасза, модифіковане число Релея-Дарсі, число Тейлора, ексцентриситет клітини та параметри модуляції, такі як амплітуда та частота. Варіюючи ці параметри, у різних випадках ми проаналізували тепло і масопередачу, яка кількісно виражається числом Нуссельта і Шервуда. Встановлено, що амплітуда модуляції істотно впливає на посилення тепло і масовіддачі, тоді як частота модуляції зменшує вплив.

Ключові слова: *модель Дарсі-Брінкмана; біотермальна конвекція; гравітаційна модуляція; пористе середовище, що обертається; гіротактичний мікроорганізм*

IMPORTANCE OF REFLECTED SOLAR ENERGY LOADED WITH SWCNTs-MWCNTs/EG DARCY POROUS STRETCHED SURFACE: MIDRICH SCHEME

Gunisetty Ramasekhar[a]*, Sangapatnam Suneetha[b#], Vanipenta Ravikumar[c], Shaik Jakeer[d], Seethi Reddy Reddisekhar Reddy[e]

[a] Department of Mathematics, Rajeev Gandhi Memorial College of Engineering and Technology (Autonomous), Nandyal, 518501, Andhra Pradesh, India
[b] Department of Applied Mathematics Yogi Vemana University Kadapa, 516003, Andhra Pradesh, India
[c] Department of Mathematics, Annamacharya Institute of Technology and Sciences, (Autonomous), Rajampet, 516126, Andhra Pradesh, India
[d] School of Technology, The Apollo University, Chittoor, Andhra Pradesh, 517127, India
[e] Department of Mathematics, Koneru Lakshmaiah Education Foundation, Bowrampet, Hyderabad, Telangana, 500043, India
*Corresponding Authors e-mail: gunisettyrama@gmail.com, #e-mail suneethayvu@gmail.com
Received November 29, 2023; revised December 18, 2023; accepted December 30, 2023

Saving energy, shortening processing times, maximizing thermal efficiency, and lengthening the life of industrial equipment are all possible outcomes of heating and cooling optimization. In recent years, there has been a rise in interest regarding the development of high-efficiency thermal systems for the purpose of enhancing heat and mass movement. This study presents an investigation on the non-linear flow of a hybrid nanofluid comprising of Multi Walled Carbon Nanotubes (MWCNTs) and Single Walled Carbon Nanotubes (SWCNTs) over an extended surface, considering the effects of Magnetohydrodynamics (MHD) and porosity, with engine oil serving as the base fluid. Also, radiation and Darcy-Forchheimer flow is considered. The problem of regulating flow is transformed into ordinary differential equations (ODEs) by employing similarity variables. The Midrich Scheme is then used to implement a numerical solution to these equations in the program Maple. Through visual representations of fluid velocities and temperatures, the inquiry addresses several important factors, including magnetic parameters, porosity parameters, radiation parameters, Eckert numbers, inertia coefficients, and Biot numbers. The research has important implications in a number of real-world contexts. Due to its exceptional characteristics, such as reduced erosion, reduced compression drops difficulties, and greatly increased heat transfer rates, hybrid nanofluids are frequently used in heat exchangers. For instance, various cooling devices such as electromagnetic cooling systems, as well as heat exchangers including condensers, boilers, chillers, air conditioners, evaporators, coil preheaters, and radiators. Furthermore, it has the potential to be employed in pharmaceutical businesses and the field of biomedical nanoscience.

Keywords: *BVP Midrich scheme; MHD; Thermal radiation; Porous medium, Heat source; Darcy-Forchheimer flow; Hybrid nanofluid*
PACS: 44.05.+e, 44.30.+v, 44.40.+a, 47.10.ad.

INTRODUCTION

Because of its importance in a wide variety of engineering challenges and businesses, the issue of heat transfer continues to be one of the most hotly contested topics among scholars in the modern day. Nevertheless, water, oil, and glycol are commonly utilized in most applications, despite their poor thermal conductivity and inefficiency in facilitating heat transmission. To address this issue and enhance thermal efficiency, innovative fluid mediums, namely nano fluids and nanoparticles, are being created. Choi [1] was the first person to ever add metallic nanoparticles into base fluid for the purpose of increasing thermal conductivities and hence enhancing heat transfer. A few examples of real-world applications where nanofluids are employed to achieve higher levels of efficiency include the refrigerator, air conditioners, and other microelectronic goods as well as microcomputer processors. Researchers from all over the modern globe have been reporting their findings on the study of nano fluid, which has included both numerical and experimental research. Despite the significant advancements made in the field of nanofluids, contemporary researchers remain highly motivated and eager to explore novel fluid alternatives that surpass the thermal conductivity of nanofluids. Hybrid nanofluids, an advanced variation of nanofluids, have been developed to enhance performance and can serve as a suitable alternative to conventional nanofluids. Hybrid nanofluids consist of a combination of two modified types of nanoparticles. Compared to the base fluid and nanofluids made from a single type of nanoparticles, the hybrid nanofluid is predicted to have more advantageous thermal properties for heat transfer. Because of its superior performance, it is often referred to as a "next-generation fluid." Recently developed hybrid nanofluids have found widespread application in several fields of heat transmission. Microelectronics, microfluidics, transportation, manufacturing, medicine, military, acoustics, naval architecture, propulsion, and many more disciplines all fall under this broad category. The primary objective of utilizing hybrid nanofluids lies in the ability to strategically select an appropriate amalgamation of nanoparticles. This selection allows for the manipulation of the nanofluid, so augmenting the advantageous characteristics

associated with each particle type. Additionally, this approach serves to mitigate the drawbacks that arise from employing these particles individually, owing to the synergistic impact that arises from their combined utilization. The enhancement of thermal conductivity properties in hybrid nanofluids has garnered significant attention from researchers, leading to a substantial body of work focused on the practical applications of thermal transmission problems involving hybrid nanofluids. The investigation of heat transfer rate using hybrid nanofluid has emerged as a prominent field of study in recent years [2–6].

The thermo-physical and volume partitioning techniques are employed to ascertain the heat transport characteristics of nanomaterials. Nano fluids encompass a wide range of materials, including carbides, oxides, nitrides, fullerene, metals, and carbon nanotubes (CNTs), which are classified based on their size, form, and distinctive properties. The investigation of carbon nanotubes (CNTs) has been undertaken due to their heightened thermal conductivity properties. Carbon nanotubes, also known as CNTs, have a nanostructure resembling a barrel and are made up of numerous different allotropes of carbon. In the domains of health sciences, applied sciences, material sciences, energy, optics, natural sciences, and manufacturing, the morphological properties of carbon particles in spherical and tubular shapes are both intriguing and valuable. Single-walled carbon nanotubes (SWCNTs) and multi-walled carbon nanotubes (MWCNTs), which are differentiated from one another based on their structural properties, are the two unique categories that carbon nanotubes (CNTs) can be placed into. In 1991, Iijima [7] conducted a pioneering study on the application of CNTs in the examination of MWCNTs utilizing the Krastschmer and Huffman approach. The credit for the identification of SWCNTs is ascribed to Ajayan and Lijima in the year 1993 [8]. Over the past two decades, a substantial number of scholars have contributed a significant body of literature on the utilization of carbon nanotubes. The following selection of articles, ranging from references [9-16], may prove valuable for academic study purposes.

The field of fluid dynamics known as magnetohydrodynamic flow examines the magnetic properties of fluids that carry electricity and is a subfield of electrohydrodynamic flow. The application of magnetic fields in boundary layer flows serves the objective of causing separation of the boundary layer. A large number of researchers have included the impact of an external magnetic field effect into challenges involving hybrid nanofluid boundary layers. Magnetohydrodynamics, or MHD for short, offers a wide range of applications across a variety of business sectors and engineering subfields. Prominent applications of magnetohydrodynamic (MHD) technological innovations include controlled thermonuclear nuclear power plants, machines for refreshing shiny plates, power plants, circulatory control during surgical operations, magnetic endoscopy, magnetic devices utilized for cell separation, radiation therapy for cancer malignancy treatment, and magnetic targeting of medications. Magnetic endoscopy, magnetic cell separators, magnetic radiation therapy for tumors, and magnetic medication targeting are among further uses. In light of the aforementioned uses of the MHD, a significant number of researchers have investigated the MHD in the context of a variety of issues pertaining to fluid mechanics [17–19].

This study aim to examine the transport of hybrid nanofluid containing MWCNTs and SWCNTs over a stretched surface in presence of MHD and porosity with engine oil as base fluid. Also, radiation and Darcy-Forchheimer flow are taken into account. Notwithstanding the utility of the investigation, the flow model in question has not been formerly disseminated, and its flow features have not been subject to prior examination. The inquiry was prompted by the presence of multiple studies discussing the applications in industry and advancements of hybrid nanofluids. The mathematical model is solved by a computational approach known as the BVP Midrich method. The control problem can be effectively solved using Maple software, enabling the presentation of results through the use of figures and tables. This paper presents a qualitative analysis of the flow dynamics.

MATHEMATICAL MODELING

In addition to a stretched surface, a two-dimensional heat transfer representation is examined in a mixed-heat-dispersal (MHD) SWCNTs and MWCNTs hybrid nanofluid. Within the framework of the energy and temperature equation, thermal radiation is taken into account. As can be seen in Table 1, two distinct kinds of nanoparticles, namely SWCNTs and MWCNTs, are suspended in the base fluid Engine oil. The velocity components u and v are measured along the x-axis and the y-axis, respectively; the velocity is written as $u_w = ax$. Furthermore, the temperature of the sheet as well as the temperature of the free stream is represented by the symbols T_w, T_∞, respectively, which is demonstrated in Figure 1.

Table 1. Thermophysical properties of Engine oil, SWCNTs-MWCNTs hybrid nanofluid [22]

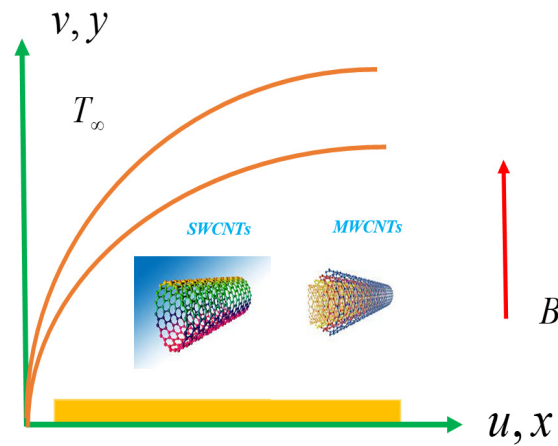| Property	Engine oil	SWCNTs	MWCNTs
Density ρ (kgm^{-3})	884.00	2600.00	1600.00
Specific heat C_p $(Jkg^{-1}K^{-1})$	1910.00	425.00	796.00
Heat conductivity k_f $(Wm^{-1}K^{-1})$	0.1440	6600.00	3000.0
Electrical conductivity σ $(\Omega m)^{-1}$	$10^{-6} - 2\times10^{-9}$	$10^{-16} - 10^{8}$	$10^{6} - 10^{7}$
Pr	6450		

Figure. 1. Geometry of the problem

The governing flow equations are constructed as [20][21]

$$\frac{\partial u}{\partial x} + \frac{\partial u}{\partial y} = 0,$$ (1)

$$u\frac{\partial u}{\partial x} + v\frac{\partial u}{\partial y} = \frac{\mu_{hnf}}{\rho_{hnf}}\left(\frac{\partial^2 u}{\partial y^2}\right) - \frac{\mu_{hnf}}{\rho_{hnf}}\frac{u}{K^*} - F^* u^2 - \frac{\sigma_{hnf}}{\rho_{hnf}}\left(B^2 u\right),$$ (2)

$$u\frac{\partial T}{\partial x} + v\frac{\partial T}{\partial y} = \frac{k_{hnf}}{\left(\rho c_p\right)_{hnf}}\left(\frac{\partial^2 T}{\partial y^2}\right) - \frac{1}{\left(\rho c_p\right)_{hnf}}\left(\frac{\partial q_r}{\partial y}\right) + \frac{Q_0}{\left(\rho c_p\right)_{hnf}}\left(T - T_\infty\right) + \frac{\sigma_{hnf}B^2}{\left(\rho c_p\right)_{hnf}}u^2.$$ (3)

By Rosseland approach, we have

$$q_r = -\frac{4\sigma^*}{3k^*}\frac{\partial T^4}{\partial y}.$$ (4)

By applying the Taylor's series expansion of T^4 about T_∞ and neglecting terms having higher order, we obtain

$$T^4 = 4T_\infty^{\,3}T - 3T_\infty^{\,4}.$$ (5)

Putting Eq. (5) in Eq. (3), we get

$$u\frac{\partial T}{\partial x} + v\frac{\partial T}{\partial y} = \frac{k_{hnf}}{\left(\rho c_p\right)_{hnf}}\left(\frac{\partial^2 T}{\partial y^2}\right) - \frac{1}{\left(\rho c_p\right)_{hnf}}\frac{16T_\infty^3}{3k^*}\frac{\partial^2 T}{\partial y^2} + \frac{Q_0}{\left(\rho c_p\right)_{hnf}}\left(T - T_\infty\right) + \frac{\sigma_{hnf}B^2}{\left(\rho c_p\right)_{hnf}}u^2.$$ (6)

The corresponding boundary conditions are:

$$u = u_w\left(x\right) = ax, v = 0, k_{hnf}\frac{\partial T}{\partial y} = h_f\left(T_f - T\right), \qquad at\ y = 0$$

$$u \to 0, T \to T_\infty \qquad\qquad\qquad\qquad as\ y \to \infty.$$ (7)

The following suitable self-similarity transformations are defined as:

$$u = axf'\left(\eta\right), v = -\sqrt{a\upsilon_f}f\left(\eta\right), \theta\left(\eta\right) = \frac{T - T_\infty}{T_f - T_\infty}, \eta = y\sqrt{\frac{a}{\upsilon_f}}.$$ (8)

Thermophysical properties of *hnf* are

$$R_1 = \frac{\mu_{hnf}}{\mu_f}, R_2 = \frac{\rho_{hnf}}{\rho_f}, R_3 = \frac{\left(\rho c_p\right)_{hnf}}{\left(\rho c_p\right)_f}, R_4 = \frac{k_{hnf}}{k_f}, R_5 = \frac{\sigma_{hnf}}{\sigma_f}.$$

$$R_1 = \frac{1}{(1-\phi_1)^{2.5}(1-\phi_2)^{2.5}},$$

$$R_2 = \left\{ (1-\phi_2)\left[(1-\phi_1) + \phi_1\left(\frac{\rho_{s_1}}{\rho_f}\right) \right] + \phi_2 \frac{\rho_{s_2}}{\rho_f} \right\},$$

$$R_3 = (1-\phi_2)\left[(1-\phi_1) + \phi_1\left(\frac{(\rho c_p)_{s_1}}{(\rho c_p)_f}\right) \right] + \phi_2 \frac{(\rho c_p)_{s_2}}{(\rho c_p)_f},$$

$$R_4 = \frac{k_{s_1} + 2k_{bf} - 2\phi_2(k_{bf} - k_{s_2})}{k_{s_2} + 2k_{bf} + \phi_2(k_{bf} - k_{s_2})} \times \frac{k_{s_1} + 2k_f - 2\phi_1(k_f - k_{s_1})}{k_{s_1} + 2k_f + \phi_1(k_f - k_{s_1})},$$

$$R_5 = \frac{\sigma_{s_2} + 2\sigma_{nf} - 2\phi_2(\sigma_{nf} - \sigma_{s_2})}{\sigma_{s_2} + 2\sigma_{nf} + \phi_2(\sigma_{nf} - \sigma_{s_2})} \times \frac{\sigma_{s_1} + 2\sigma_f - 2\phi_1(\sigma_f - \sigma_{s_1})}{\sigma_{s_1} + 2\sigma_f + \phi_1(\sigma_f - \sigma_{s_1})}.$$

(9)

In order to create the following dimensionless ODEs, Eqs. (2) and (6) are transformed using the ideal technique indicated in Eq (8).

$$\frac{R_1}{R_2}f''' + R_2\left(ff'' - (f')^2\right) - \frac{R_1}{R_2}Kf' - Frf'^2 - \frac{R_5}{R_2}Mf' = 0,$$

(10)

$$\theta''\left(R_4 + \frac{4}{3}Rd\right) + R_3 Prf\theta' + \frac{PrQ}{A_4}\theta + \frac{R_5}{R_3}MEc(f')^2 = 0.$$

(11)

The boundaries of the change are described as:

$$f(0) = 0, f'(0) = 1, R_4\theta'(0) = -Bi(1 - \theta(0))$$
$$f'(\infty) = 0, \theta'(\infty) = 0.$$

(12)

Note that $M = \frac{\sigma_f B^2}{\rho_f a}$ is the Magnetic field parameter, $Pr = \frac{\mu_f(c_p)_f}{k_f}$ is the Prandtl number, $Rd = \frac{4\sigma^* T_\infty^3}{k^* k_f}$ is the Radiation parameter, $Bi = \frac{h_f}{k_f}\sqrt{\frac{\upsilon_f}{a}}$ is the Biot number, $Ec = \frac{a^2 x^2}{c_p(T_f - T_\infty)}$ is the Eckert number, and $K = \frac{\upsilon_f}{aK^*}$ is the porosity parameter, $F^* = \left(\frac{C_d}{rK^{*1/2}}\right)$ non-uniform inertia coefficient, and $Fr = \frac{C_d}{\sqrt{K^*}}$ inertia coefficient, $Q = \frac{Q_0}{\Omega(\rho C_p)_f}$ heat absorption/generation coefficient.

The dimensional form of C_f, and Nu are expressed as

$$C_f = \frac{\tau_w}{\rho_f u_w^2}$$

(13)

Where shear stress τ_w is $\tau_w = \mu_{hnf}\left.\frac{\partial u}{\partial y}\right|_{y=0}$

$$Nu = \frac{xq_w}{k_f(T_w - T_\infty)}$$

(14)

Where heat flux q_w is $q_w = -k_{hnf}\left.\frac{\partial T}{\partial y}\right|_{y=0}$

The non-dimensional form of Eqs. (13–14) converts are

$$Re_r^{1/2}C_f = CF = R_1 f''(0),$$

(15)

$$Re_r^{-1/2}Nu_r = Nu = -R_4\theta'(0).$$

(16)

Where Re_r is the local Reynolds number.

SOLUTION METHODOLOGY

The nature of the ODE system (10–11) with BCs (12) is extremely nonlinear in its characteristics. For the purpose of dealing with these equations, we adopt a computational approach known as the BVP Midrich method see in Figure 2. Using Maple, we are able to solve the control problem. The midway method's standard operating procedure is laid out in detail below.

The following is a demonstration of the overall algorithm for the technique of midpoint collocation

$$\overline{Z}'(x) = F\left(x, \overline{Z}(x)\right), \quad \overline{Z}(x_0) = \overline{Z_0}, \tag{17}$$

In the explicit midpoint approach, also known as the Modified Euler method, the formula looks like this

$$\overline{Z_{n+1}} = \overline{Z_n} + hF\left(x_n + \frac{h}{2}, \overline{Z_n} + \frac{h}{2}F\left(x_n, \overline{Z_n}\right)\right), \tag{18}$$

The above equation h represents the step size and $x_n = (x_0 + nh)$.

The strategy that takes into account the implicit midpoint may be described as

$$\overline{Z_{n+1}} = \overline{Z_n} + hF\left(x_n + \frac{h}{2}, \ \overline{Z_n} + \frac{1}{2}\left(\overline{Z_n}, \overline{Z_{n+1}}\right)\right), \qquad n = 0,1,2,\dots \tag{19}$$

At each step size, the technique for locating the midpoint has a local error of order $O(h^3)$ whereas the global error is of order $O(h^2)$. When dealing with algorithms that are more quantifiable demanding, the algorithm-error decreases at a quicker rate as $h \to 0$ progresses, and the result gets more dependable.
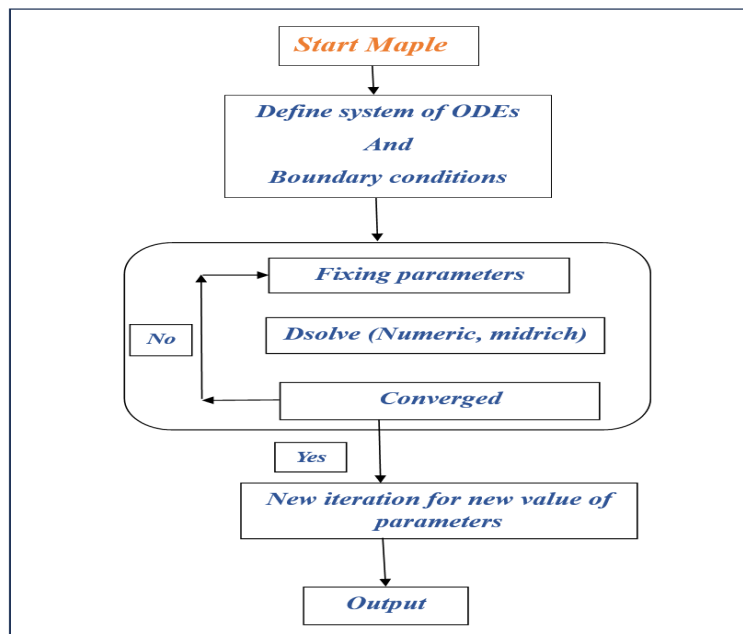
Figure 2. A flow chart pictogram of BVP Midrich technique

RESULTS AND DISCUSSION

The non-dimensional controlling flow model (10) – (11), which are subject to the boundary conditions (12), may be solved numerically with the assistance of Maple built in BVP Midrich scheme. We took the values of non-dimensional parameters and evaluated. Table 2, which illustrates the variances in skin friction coefficient, yields the exact solutions. The findings of both investigations were determined to be fairly accurate. Table 3, which demonstrates that various parameter values for CF. In the current part of the study, the authors go over the findings from the graphical narrative of the significant physical quantities in order to determine the quantitative fluctuation in relation to several important problem factors. To this end, writers have created graphs that define velocities, temperatures, Skin friction and heat transfer coefficient in order.

Table 2. Comparison table for various Prandtl numbers of the current study.

| Pr	Ali et al. [20]	Present results
0.7	0.4560	0.4552902
2.0	0.9113	0.9101351

Table 3. The quantitative results of the skin friction coefficient of different of values for *M, Fr* and *K* by fixing parameter values *Rd = Bi = 0.4,* and *Pr = Ec = 0.1.*

M	Fr	K	CF
0.1	0.4	0.5	1.026591
0.2	0.4	0.5	1.262674
0.3	0.4	0.5	1.004382
0.3	**0.1**	0.5	1.496002
0.3	**0.2**	0.5	1.172028
0.3	**0.3**	0.5	1.006005
0.3	0.4	**0.1**	0.958371
0.3	0.4	**0.2**	1.009034
0.3	0.4	**0.3**	1.045792

The influence of *M* on the velocity of MHD SWCNTs-MWCNTs/EG hybrid nanofluid is highlighted in Figure 3. Higher values of M cause some resistance in the fluid motion, as can be seen from the plot. The Lorentz forces, which are the resistive forces, increase in strength as M increases. when a result, when M increases, the Lorentz forces get stronger and slow down fluid motion.
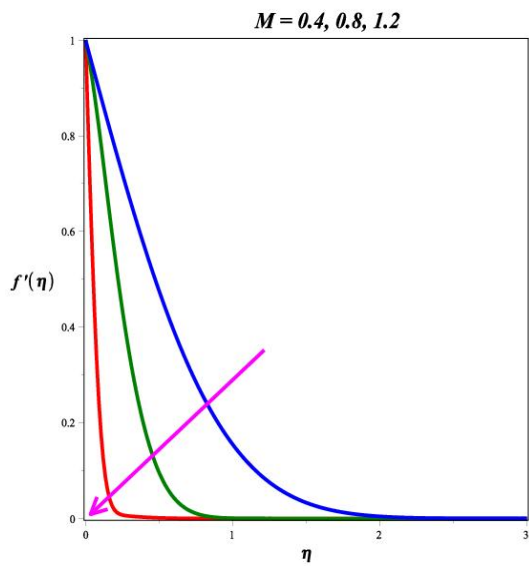
**Figure 3.** Pictogram of M on $f'(\eta)$
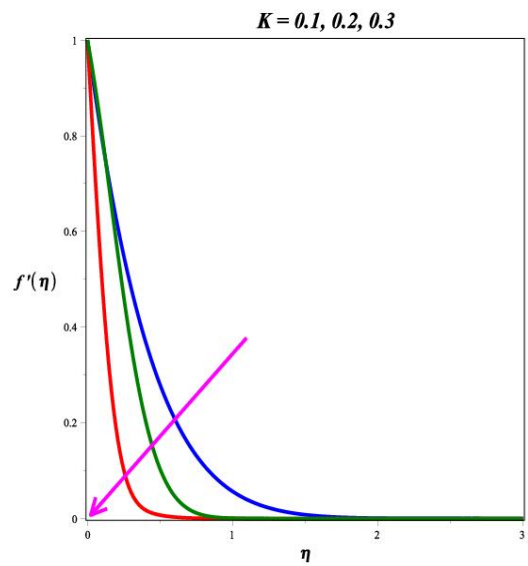
Figure 4. Pictogram of K on $f'(\eta)$
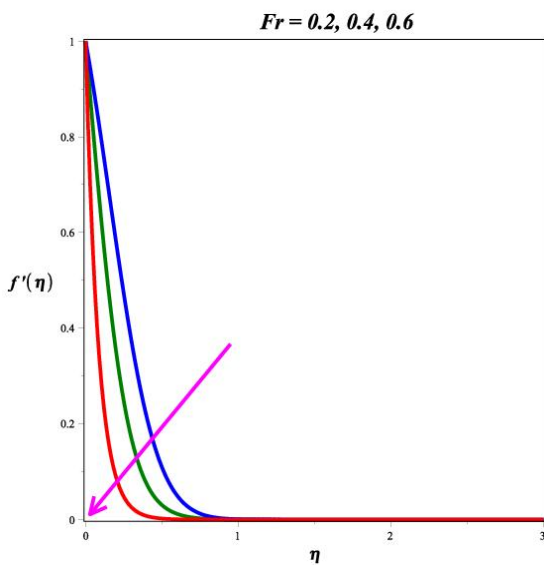
Figure 5. Pictogram of Fr on $f'(\eta)$
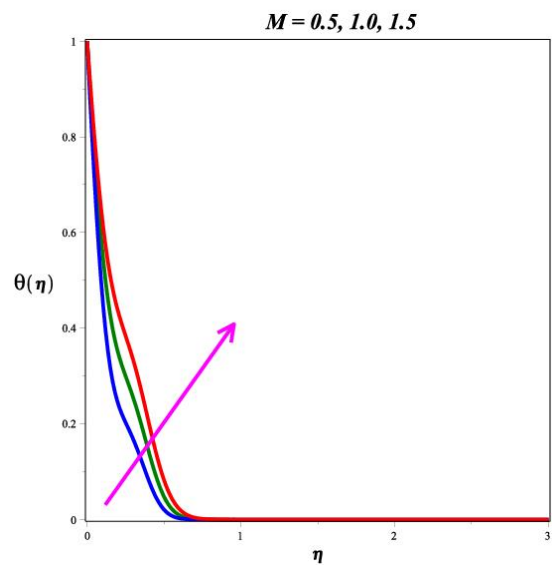
Figure 6. Pictogram of M on $\theta(\eta)$

Figure 4 show the influence of the porous parameter *K* on the velocity of hybrid nanofluid. Raise in K essentially increases the difficulty of boundary layer separation. Additionally, as the frictional drag force increases, the boundary layer flow is not supported. Consequently, a downward tendency in the velocity pattern is observed for higher K.

Figure 5 describes the behavior of Fr on $f'(\eta)$. Large local inertia coefficient values, which lower fluid speed and boundary layer thickness, are indicative of enhanced medium porosity. Higher Fr causes the pores to enlarge, which ultimately lowers the speed.

The effect of the magnetic parameter (M) on the temperature profile is depicted in Figure 6. Thermal energy strengthens the Lorentz force by motivating hybrid nanofluids to dissipate sub kinetic energy. In fact, as the magnetic factor increases, the size of the boundary layer's velocity profiles falls, leading to a raise in boundary layer temperature.
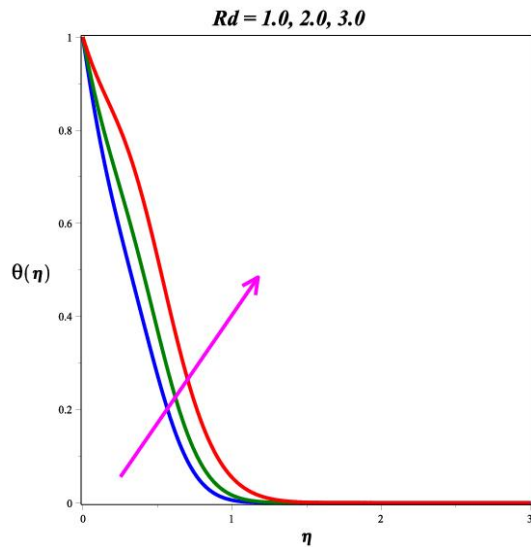
Figure 7. Pictogram of Rd on $\theta(\eta)$
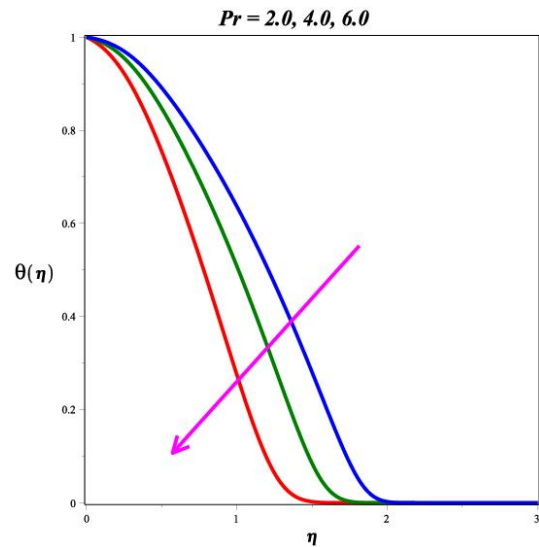
Figure 8. Pictogram of Pr on $\theta(\eta)$
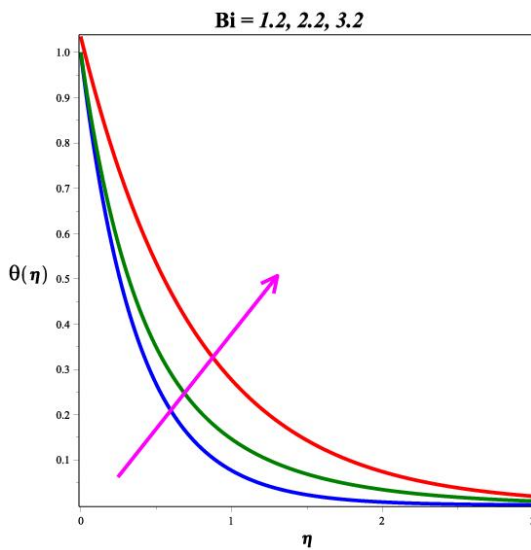
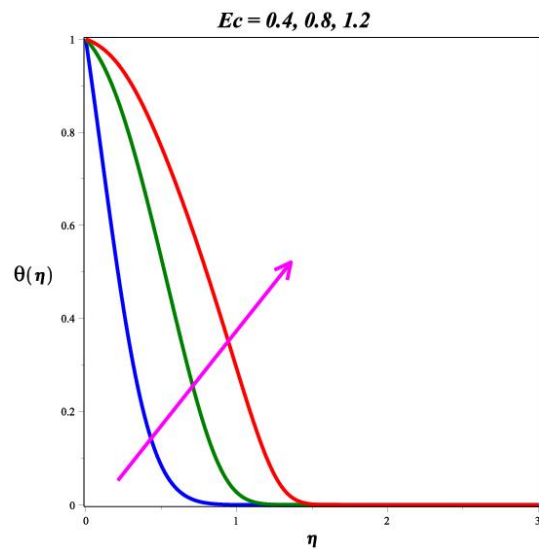**Figure 9.** Pictogram of Bi on $\theta(\eta)$

Figure 10. Pictogram of Ec on $\theta(\eta)$

Figure 7 depicts the effect of various radiation parameter (Rd) values on the temperature of hybrid nanofluid. Kinetic energy, or the energy required to cause moving atoms in matter to rotate, is derived from heated surfaces and is known as electromagnetic energy. The graph unequivocally demonstrates that better heat transmission results from raising the radiation parameter. A thicker thermal barrier layer is produced when the Rd parameter is raised because more heat is transported into the liquid. The temperature rises as the radiation parameter increases because the mean absorption coefficient drops. Thermal radiation has a positive physical effect on the medium's thermal diffusibility, which increases the temperature profile. Physically, higher temperature and a thicker thermal boundary layer are correlated with increased thermal radiation parameters.

The temperature for various amounts of Pr is revealed in Figure 8. It is clear that as Pr increases, the temperature parameter decreases. The boundary layer of thermal energy is thicker and the rate of heat transmission decreases for smaller Pr. Typically, Pr is employed in heat transfer-related applications to determine the width of the thermal and also the momentum border layers. This is due to the fact that when the Prandtl number increases, the thermal diffusion rate drops.

Figure 9 is aimed at presenting the variation in temperature with Biot number. The convective boundary property at the surface is connected to the Biot number. As the Biot number rises, the temperature gradient close to the surface also rises, raising the temperature there and, consequently, the thickness of the thermal boundary layer, as seen in Figure 9 the thermal resistance of a body as measured by its Biot number is the ratio of its internal thermal resistance to its surface thermal resistance.

Figure 10 describes the plot of temperature counter to the Eckert number Ec. The production of thermal energy increases with the existence of Ec in nanofluid, becoming more intense, improving temperature distributions, and therefore increasing thermal layer thickness. This is because frictional heating causes an increase in heat energy in the flow, which the viscosity of nanofluids stores and converts into internal energy when heated. From the same figure, it is noticed that the temperature is maximum near the walls when compared with the middle of the channel. Since Ec is proportional to the enthalpy of heat and to the kinetic energy of particles, an increase in Ec results in greater kinetic energy for the particles by decreasing the enthalpy actor, and thus an increase in temperature. Figure 11 depicts the inspiration of Q on energy outline. For the higher numeric values of the Q in energy profile enhanced. Physically, when heat generation rises, so does the inherent energy of liquid particles, resulting in a rise in the temperature outline.
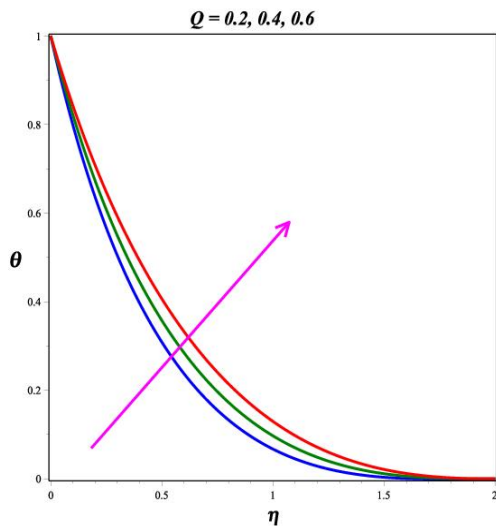

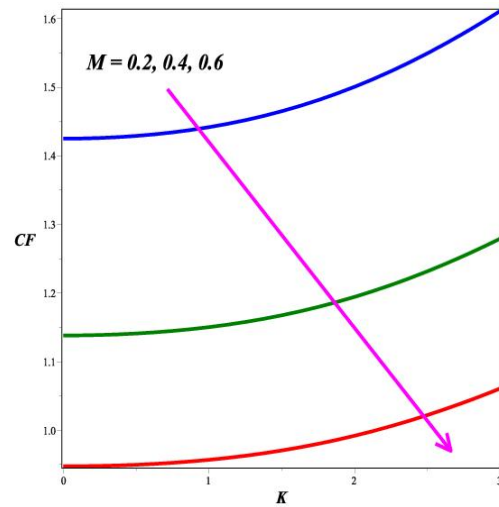**Figure 11.** Pictogram of Q on $\theta(\eta)$

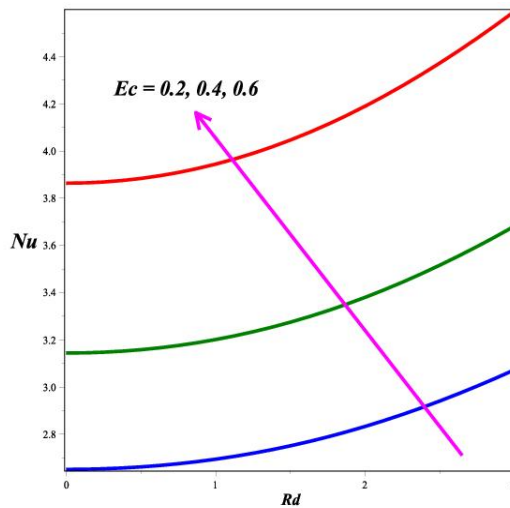**Figure 12.** Sway of K and M on CF

Figure 13. Sway of Rd and M on Nu

The skin friction coefficient diminutions when growing the values of a magnetic parameter, similarly the skin friction increases when increasing porosity parameter is revealed in Figure 12. The effect of the radiation parameter and the Eckert number on the Nusselt number is shown in Figure 13. Increasing the Eckert number results in a corresponding rise in the Nusselt number and the radiation parameter. Plots or graphs of contours are frequently employed in the field of fluid dynamics for the purpose of visualizing and analyzing numerous characteristics included inside a liquid, including its speed, pressure, energy, and concentration. For the higher values of the magnetic parameter case, we are observing on decreasing tendency which is presented in Figures 14 and 15, while the opposite nature we noticed on Nusselt number profile and it is demonstrated in Figures 16 and 17.

The various values of *M, K, Fr* were presented in Figures 18, 19, and 20. Rising porosity liquid medium leads to reduced magnetic field for the movement of fluids, as seen in the graph. A decreased heat transfer rate is seen for moving sheet. Streamlines have significance in the study of fluids and technology for many different reasons. Streamlines illustrate movement of fluids characteristics. They demonstrate fluid particle movement and path throughout period. This simplifies unpredictable interpretation.
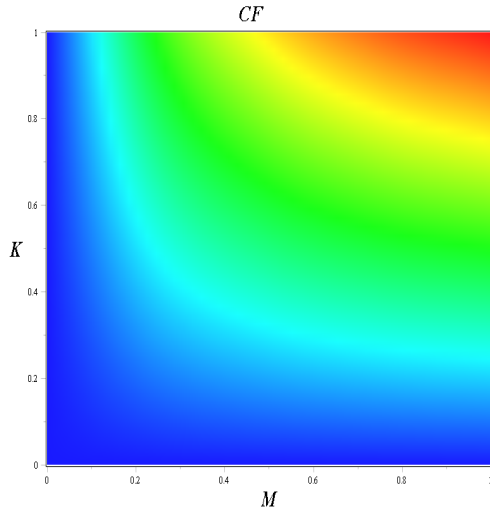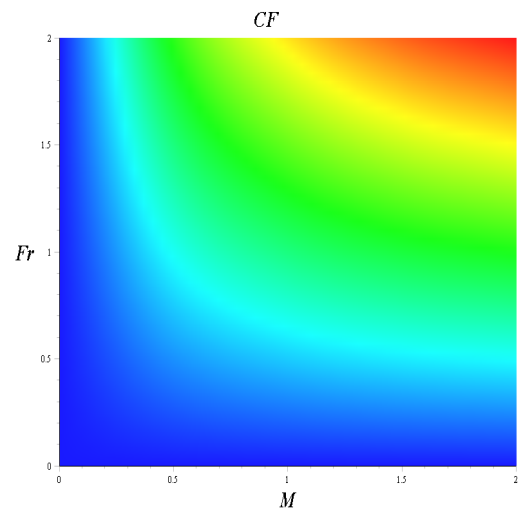

Figure 14. Sway of *K and M* on *CF*

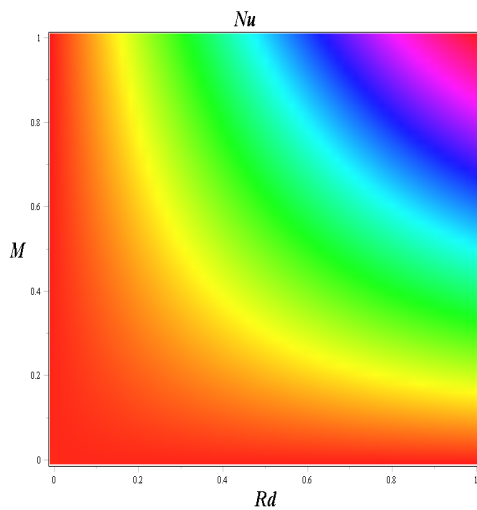**Figure 15.** Sway of *Fr and Rd* on *CF*

Figure 16. Sway of *Fr and Rd* on *Nu*
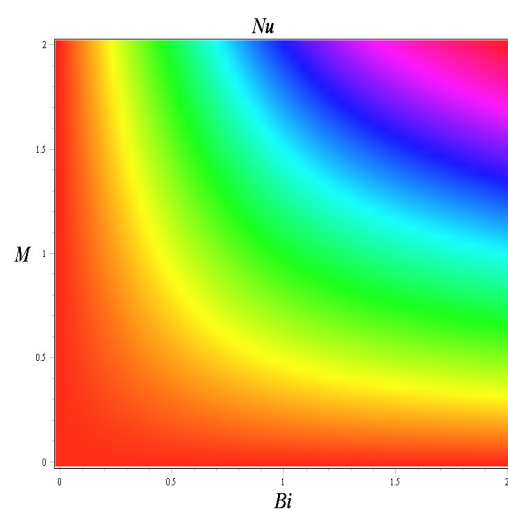
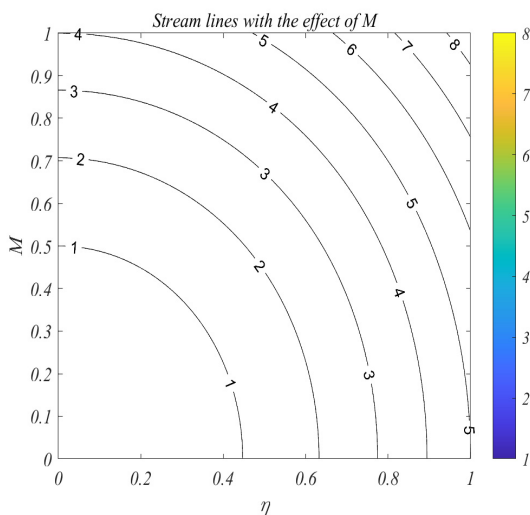**Figure 17.** Sway of *Fr and Rd* on *Nu*

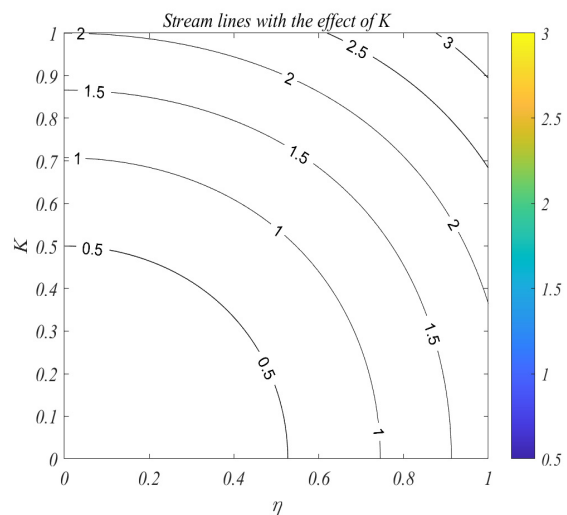**Figure 18.** Stream lines for *M*

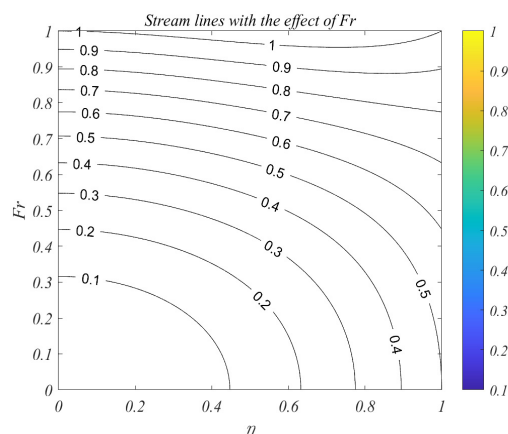

Figure 19. Stream lines for *K*

Figure 20. Stream lines for Fr

CONCLUSIONS

The current research study explored the numerical solution for MHD of SWCNTs-MWCNTs /Engine oil hybrid nanofluid over a Stretching surface. The Numerical method (BVP Midrich scheme) was used to solve the issue of velocity, temperature and the outcome was truly solution to the model. The results are presented in a variety of graphical formats, including a two-dimensional plot, Contour plots, and streamlines.

The research produced a number of interesting findings, which are listed below:

1. The high local inertia coefficient values, which lower both the fluid velocity and the boundary layer thickness.
2. Thermal radiation has a positive physical effect on the medium's thermal diffusibility, which increases the temperature profile of the hybrid nanofluid.
3. The temperature gradient at the surface rises with a rise in the Biot number, raising the temperature there and, consequently, the thickness of the thermal boundary layer.
4. When the value of Ec is increased, it results in an elevation in the kinetic energy of particles due to a decrease in the enthalpy factor. This increase in kinetic energy subsequently leads to a rise in temperature.
5. By enhancing the values of the Eckert number, increases the Nusselt number and the radiation parameter.
6. As the values of the radiation parameter and magnetic field parameter are increased, the rate of skin friction increases.
7. Magnetic parameter strength draws electrical conductivity molecules more towards to the main stream is observed on streamlines plots.

ORCID

 Gunisetty Ramasekhar, https://orcid.org/0000-0002-3256-3145; **Sangapatnam Suneetha,** https://orcid.org/0000-0001-6627-6446
 Vanipenta Ravikumar, https://orcid.org/0000-0001-9598-8717; **Shaik Jakeer,** https://orcid.org/0000-0002-6350-1457
 Seethi Reddy Reddisekhar Reddy, https://orcid.org/0000-0001-5501-570X

REFERENCES

[1] S.U. Choi, and J.A. Eastman, *Enhancing Thermal Conductivity of Fluids with Nanoparticles, Technical Report*, (Argonne National Lab. Argonne, IL, USA, 1995).
[2] A. Venkateswarlu, S. Suneetha, M.J. Babu, J.G. Kumar, C.S.K. Raju, and Q. Al-Mdallal, "Significance of Magnetic Field and Chemical Reaction on the Natural Convective Flow of Hybrid Nanofluid by a sphere with viscous dissipation: A statistical Approach," Nonlinear Engineering, **10**, 563–573 (2021). https://doi.org/10.1515/nleng-2021-0047
[3] A.B. Vishalakshi, R. Mahesh, U.S. Mahabaleshwar, A.K. Rao, L.M. Pérez, and D. Laroze, "MHD Hybrid Nanofluid Flow over a Stretching/Shrinking Sheet with Skin Friction: Effects of Radiation and Mass Transpiration," Magnetochemistry, **9**, 118 (2023). https://doi.org/10.3390/magnetochemistry9050118
[4] P.S. Reddy, P. Sreedevi, and A.J. Chamkha, "Hybrid Nanofluid Heat and Mass Transfer Characteristics Over a Stretching/Shrinking Sheet with Slip Effects," Journal of Nanofluids, **12**, 251–260 (2023). https://doi.org/10.1166/jon.2023.1996
[5] U. Farooq, M. Tahir, H. Waqas, T. Muhammad, A. Alshehri, and M. Imran, "Investigation of 3D flow of magnetized hybrid nanofluid with heat source/sink over a stretching sheet," Sci. Rep. **12**(1), 12254 (2022). https://doi.org/10.1038/s41598-022-15658-w
[6] M. Nadeem, I. Siddique, J. Awrejcewicz, *et al., "*Numerical analysis of a second-grade fuzzy hybrid nanofluid flow and heat transfer over a permeable stretching/shrinking sheet," Sci. Rep. **12**, 1631 (2022). https://doi.org/10.1038/s41598-022-05393-7
[7] S. Iijima, "Helical microtubules of graphitic carbon," Nature, **354**, 56–58 (1991). https://doi.org/10.1038/354056a0
[8] P.M. Ajayan, and S. Lijima, "Capillarity-induced filling of carbon nanotubes," Nature, **361**, 333–334 (1993). https://doi.org/10.1038/361333a0
[9] K. Subbarayudu, S. Suneetha, P.B.A. Reddy, and A.M. Rashad, "Framing the activation energy and binary chemical reaction on CNT's with Cattaneo-Christov heat diffusion on Maxwell Nano fluid in the presence of non-linear thermal radiation," Arabian journal of Science and Engineering, **44**, 10313–10325 (2019). https://doi.org/10.1007/s13369-019-04173-2

[10] L. Wahidunnisa, S. Suneetha, S.R.R. Reddy, and P.B.A. Reddy, "Comparative study on electromagnetohydrodynamic SWCNT-water dusty nanofluid in the presence of radiation and Ohmic heating," Proceedings of the Institution of Mechanical Engineers, Part E: Journal of Process Mechanical Engineering, **235**(4), 950-958 (2021). https://doi.org/10.1177/0954408920985735

[11] S. Suneetha, L. Wahidunnisa, A. Divya, and P.B.A. Reddy, "Electrical magnetohydrodynamic flow of kerosene oil-based carbon nanotube's Maxwell nanofluid in the presence of non-linear radiation and Cattaneo-Christov heat diffusion: Applications in aerospace industry," Proc. Mech. E, Part E: J. Process Mechanical Engineering, **237**, 1670–1678 (2022). https://doi.org/10.1177/09544089221125100

[12] G. Ramasekhar, and P.B. Reddy, "Numerical analysis of significance of multiple shape factors in Casson hybrid nanofluid flow over a rotating disk," International Journal of Modern Physics B, **37**(12), 2350113 (2023). https://doi.org/10.1142/S0217979223501138

[13] R. Tabassum, A. Al-Zubaidi, S. Rana, R. Mehmood, and S. Saleem, "Slanting transport of hybrid (MWCNTs-SWCNTs/H2O) nanofluid upon a Riga plate with temperature dependent viscosity and thermal jump condition," International Communications in Heat and Mass Transfer, **135**, 106165 (2022). https://doi.org/10.1016/j.icheatmasstransfer.2022.106165

[14] E. Tayari, L. Torkzadeh, D. Domiri Ganji, et al., "Investigation of hybrid nanofluid SWCNT–MWCNT with the collocation method based on radial basis functions," Eur. Phys. J. Plus. **138**, 3 (2023). https://doi.org/10.1140/epjp/s13360-022-03601-x

[15] A.M. Obalalu, M.A. Memon, and O.A. Olayemi, et al., "Enhancing heat transfer in solar-powered ships: a study on hybrid nanofluids with carbon nanotubes and their application in parabolic trough solar collectors with electromagnetic controls," Sci. Rep. **13**, 9476 (2023). https://doi.org/10.1038/s41598-023-36716-x

[16] Z. Shah, A. Tassaddiq, S. Islam, A.M. Alklaibi, and I. Khan, "Cattaneo–Christov heat flux model for three-dimensional rotating flow of SWCNT and MWCNT nanofluid with Darcy–Forchheimer porous medium induced by a linearly stretchable surface," Symmetry, **11**(3), 331 (2019). https://doi.org/10.3390/sym11030331

[17] G. Ramasekhar, and P.B.A. Reddy, "Entropy generation on Darcy-Forchheimer ow of copper-aluminium oxide/water hybrid nanofluid over a rotating disk: Semi-analytical and numerical approaches," Scientia Iranica. Transaction F, Nanotechnology, **30**(6), 2245-2259 (2023). https://doi.org/10.24200/sci.2023.60134.6617

[18] I. Rashid, T. Zubair, and M.I. Asjad, "Tag-Eldin E.M. The Influence of Aligned MHD on Engine Oil-Based Casson Nanofluid with Carbon Nanotubes (Single and Multi-Wall) Passing through a Shrinking Sheet with Thermal Radiation and Wall Mass Exchange," Micromachines (Basel), **13**(9), 1501 (2022). https://doi.org/10.3390/mi13091501

[19] S.R.R. Reddy, P.B.A. Reddy, and S. Suneetha, "Magnetohydro Dynamic Flow of Blood in A Permeable Inclined Stretching Viscous Dissipation, Non-Uniform Heat Source/Sink and Chemical Reaction," Frontiers in Heat and Mass Transfer, **10**(22), 1-10 (2018). https://doi.org/10.5098/hmt.10.22

[20] M. Ramzan, F. Ali, N. Akkurt, et al., "Computational assesment of Carreau ternary hybrid nanofluid influenced by MHD flow for entropy generation," J. Magn. Magn. Mater. **567**, 170353 (2023). https://doi.org/10.1016/j.jmmm.2023.170353

[21] G. Ramasekhar, and P.B.A. Reddy, "Entropy generation on EMHD Darcy-Forchheimer flow of Carreau hybrid nano fluid over a permeable rotating disk with radiation and heat generation: Homotopy perturbation solution," Proc. Inst. Mech. Eng. Part E, J. Process Mech. Eng. **237**(4), 1179–1191 (2022). https://doi.org/10.1177/09544089221116575

[22] S. Ahmad, S. Nadeem, N. Muhammad, and A. Issakhov, "Radiative SWCNT and MWCNT nanofluid flow of Falkner–Skan problem with double stratification," Phys. A, Stat. Mech. Appl. **547**, 124054 (2020). https://doi.org/10.1016/j.physa.2019.124054

ВАЖЛИВІСТЬ ВІДБИТОЇ СОНЯЧНОЇ ЕНЕРГІЇ, ДЛЯ НАВАНТАЖЕНОЇ SWCNTs-MWCNTs/EG, ПОРИСТОЇ РОЗТЯГНУТОЇ ПОВЕРХНІ DARCY: СХЕМА МІДРІХА

Рамасекхар Гунісетті[a], Сангапатнам Сунітха[b], Ваніпента Равікумар[c], Шайк Джакер[d], Сіті Редді Реддісекар Редді[e]

[a] Кафедра математики, Меморіальний коледж інженерії та технологій імені Раджива Ганді (автономний), Нандьял, 518501, Андхра-Прадеш, Індія

[b] Департамент прикладної математики Університет Йогі Вемана Кадапа, 516003, Андхра-Прадеш, Індія

[c] Департамент математики, інститут технологій і наук Аннамачарья, (автономний), Раджампет, 516126, Андхра-Прадеш, Індія

[d] Школа технологій, Університет Аполло, Читтор, Андхра-Прадеш, 517127, Індія

[e] Департамент математики, Освітня фундація Конеру Лакшмайя, Боурампет, Хайдарабад, Телангана, 500043, Індія

Економія енергії, скорочення часу обробки, максимізація термічної ефективності та подовження терміну служби промислового обладнання – усі можливі результати оптимізації опалення та охолодження. Останніми роками зріс інтерес до розробки високоефективних теплових систем з метою підвищення тепло- та масопереміщення. У цьому дослідженні представлено дослідження нелінійного потоку гібридної нанофлюїду, що складається з багатостінних вуглецевих нанотрубок (MWCNT) і одностінних вуглецевих нанотрубок (SWCNT) над розтягнутою поверхнею, враховуючи вплив магнітогідродинаміки (MHD) і пористості, з масляним двигуном, яке служить базовою рідиною. Також враховується радіація та потік Дарсі-Форхгеймера. Задача регулювання потоку перетворюється на звичайні диференціальні рівняння за допомогою змінних подібності. Схема Мідріча потім використовується для реалізації чисельного розв'язку цих рівнянь у програмі Maple. За допомогою візуального представлення швидкостей і температур рідини запит стосується кількох важливих факторів, включаючи магнітні параметри, параметри пористості, параметри випромінювання, числа Еккерта, коефіцієнти інерції та числа Biot. Дослідження має важливі наслідки в багатьох контекстах реального світу. Завдяки своїм винятковим характеристикам, таким як зменшення ерозії, зменшення труднощів падіння при стисненні та значно підвищена швидкість теплопередачі, гібридні нанофлюїди часто використовуються в теплообмінниках. Наприклад, різні охолоджувальні пристрої, такі як електромагнітні системи охолодження, а також теплообмінники, включаючи конденсатори, котли, чиллери, кондиціонери, випарники, змійовики попереднього нагрівання та радіатори. Крім того, він має потенціал для використання у фармацевтичному бізнесі та в галузі біомедичної нанонауки.

Ключові слова: *схема BVP Midrich; МГД; теплове випромінювання; пористе середовище, джерело тепла; потік Дарсі-Форхгеймера; гібридний нанофлюїд*

HYSTERESIS AND BISTABILITY BIFURCATION INDUCED BY COMBINED FLUID SHEAR-THICKENING AND DOUBLE-DIFFUSIVE CONVECTION IN SHALLOW POROUS ENCLOSURES FILLED WITH NON-NEWTONIAN POWER-LAW FLUIDS

◉Saleh Khir[a,b,c], ◉Redha Rebhi[a,b]*, ◉Mohamed Kezrane[a,c], Mohamed Naceur Borjini[d]

[a]*Department of Mechanical Engineering, University of Medea, Medea 26000, Algeria*
[b]*LERM-Renewable Energy and Materials Laboratory, University of Medea, Medea 26000, Algeria*
[c]*Laboratoire de Mécanique Physique et Modélisation Mathématique (LMP2M), Université Yahia Fares de Médéa,
Quartier Ain Dheb, Médéa 26000, Algérie*
[d]*Université de Monastir, Ecole Nationale d'Ingénieurs de Monastir, Laboratoire de Métrologie et des Systems Énergétiques,
5019 Monastir, Tunisia*
Corresponding Author e-mail: rebhi.redha@gmail.com
Received January 8, 2024; revised January 22, 2024; accepted January 31, 2024

This paper presents a numerical study of the linear and non-linear stability of thermosolutal convection within a porous medium saturated by a non-Newtonian binary fluid. The power-law model is utilized for modeling the behavior of the working medium. The given statement implies that the horizontal boundaries experience thermal and solutal flow rates, whereas the vertical walls are impermeable and thermally isolated. The relevant factors that govern the problem being investigated are the Rayleigh number, R_T, the power-law index, n, the cavity aspect ratio, A, the Lewis number, Le, and the buoyancy ratio, N. An analytical solution is obtained for shallow enclosures ($A >> 1$) using the parallel flow approximation and a modified form of the Darcy equation. By solving the entire set of governing equations, a numerical investigation of the same phenomenon was conducted. One of the most intriguing discoveries from this research is that it identifies a bi-stability phenomenon, this particular phenomenon signifies the existence of two stable solutions. The results obtained from both methods demonstrate a good level of agreement across a diverse range of these governing parameters.

Keywords: *Bi-stability; Thermosolutal convection; Power-law fluid; Porous layer; non-Newtonian binary fluid*
PACS: 47.55.P-, 47.50.Gj, 44.30.+v, 83.60.Rs, 47.20.Ky, 02.70.Bf

1. INTRODUCTION

In recent decades, natural convection of heat and mass transfer has been characterized by fluid flows driven by buoyancy effects due to temperature and concentration gradients applied at different diffusion rates. This phenomenon is frequently encountered in nature and has many applications in the fields of science and technology, geothermal systems, heat exchangers, cooling systems, heat exchangers, microchannels, solar energy collectors, non-Newtonian chemical processes, and many others [1-3]. Over the last few decades, most studies carried out on Newtonian double-diffusive convection in closed geometries have focused on simple geometries such as a rectangular cavity or a rectangular porous layer heated from below from the side. However, in many of the fields mentioned, the fluids used are non-Newtonian in nature. A few limited studies have been carried out on natural of power-law fluids in two- and three-dimensional enclosures [4-6].

Natural convection in rectangular enclosures with differentially heated vertical walls and adiabatic horizontal walls is one of the most studied configurations for Newtonian flows [7, 8]. In fact, Newtonian behavior at higher shear rates with dynamic viscosity dependencies as a function of temperature has been reported, as has pseudoplasticity at lower shear rates. Non-Newtonian fluids, i.e., those that go against Newton's law of viscosity, have been widely used in many industries, such as food, petrochemicals, pharmaceuticals, etc. However, when it comes to rheology, non-Newtonian fluids have been widely used. With regard to rheology, non-Newtonian fluids can be classified into Bingham plastic fluids, pseudoplastic fluids and dilatant fluids. In addition, non-Newtonian fluid models can be divided into time-dependent, time-independent and viscoelastic models [9-12]. Moraga et al. [13] studied the 3D natural convection heat transfer of a non-Newtonian power-law fluid in a container placed in an enclosure. The container was filled with a non-Newtonian power-law fluid and surrounded by air. Their results included isotherms and streamlines at different values of Ra for each Newtonian and non-Newtonian power-law fluid. Jahanbakhshi et al. [14] studied the influence of the magnetic field on the natural convection of a non-Newtonian fluid in an L-shaped cavity. They found that the rate of heat transfer increased for shear-thinning fluids and decreased for shear-thickening fluids. They also found that the Nusselt number decreases with increasing Pr when the fluid shear-thins. Lamsaadi et al. [15] have numerically simulated the natural convection of a non-Newtonian fluid in a vertical cavity. Their results show that a shear-thinning fluid contributes to fluid flow and a shear-thickening fluid reduces it. Shear-thinning fluid also increases heat transfer. Makayssi et al. [16] presented an analytical and numerical experimental study of natural double-diffusion convection in a shallow two-dimensional horizontal enclosure. These authors concluded that the characteristics of fluid flow, heat and mass transfer appear to be highly sensitive to the flow behavior index, n. Thus, compared to the Newtonian case (n = 1), shear-thinning

behavior (0 < n < 1) enhances fluid flow as well as convective heat and mass transfer. Kefayati [17] considered non-Newtonian fluid in a square enclosure and discussed the effect of Reynold's and magnetic field inclination angle on fluid flow. Zyła et al. [18] carried out a rheological study on nanofluids containing a mixture of nanodiamond and graphite with different ash fractions. They also studied a mixture of nanodiamond and graphite with different ash fractions. Non-Newtonian behavior and viscoelastic structure were also observed. The transient buoyant convection of a non-Newtonian fluid in a square enclosure, heated differentially from the vertical, has been studied numerically by Kim et al. [19]. Getachew et al. [20] have described the flow type and heat and mass transfer patterns of double-diffusive inside a porous enclosure saturated with a non-Newtonian fluid of power using scaling arguments, verifying the results obtained by experimental. Moradi et al. [21] have carried out an experimental study of heat transfer rate enhancement of multi-walled carbon nanotube nanofluids in a double-pipe heat exchanger with aluminium porous media. Jena et al. [22] have studied the double-diffusive free convection of a non-Newtonian Ostwald-De Waele fluid inside a 2D cavity with partially active vertical walls. Lounis et al. [23] studied the impact of Dufour and Soret effects on double-diffusive convection in an inclined square enclosure using the Carreau-Yasuda model to model the rheological behavior of a non-Newtonian fluid. Their main conclusion is that for different values of the power-law index, the Lewis number increases heat and mass exchange. Rebhi et al. [24, 25] investigated the convection generated in porous cavities containing a binary fluid and discovered that the drag parameters had a significant impact on the stability and onset of subcritical and Hopf bifurcation. Rebhi et al. [26] studied Rayleigh-Bénard thermosolutal convection instabilities in shallow enclosures with finite aspect ratios that influenced by the rheological behavior of non-Newtonian fluids. They showed that the bistable convection regime exists for every aspect ratio of the enclosure, regardless of the type of thermal and solutal boundary conditions. Bihiche et al. [27] analyzed the effect of buoyancy ratio on natural convection and on heat and mass transfer rates in a horizontal rectangular enclosure filled with a non-Newtonian power-law fluid. The emergence and development of double-diffusive convection for both aiding and opposing flows were also studied.

Consequently, natural convection in rectangular/square cavities filled with porous layers saturated with a non-Newtonian fluid has been studied by many researchers [28-30]. Nield et al. [31] studied the effect of high heterogeneity on the occurrence of vertical density gradient-induced convection in soil. On the occurrence of convection induced by a vertical density gradient in a saturated porous medium governed by Darcy's law. Devakar et al. [32] have simulated the flow of non-Newtonian fluids in a straight, uniform square duct through a porous medium. They observed that the velocity and volumetric flow rate decrease with increasing torque stress and porosity parameters. Uphill et al. [33] studied the flow of nanofluids in porous media. They showed that nanofluids containing particles smaller than the size of water are more efficient in porous media. Lakshmi et al. [34] studied the effect of Soret and Dufour diffusion on natural convection in a saturated porous medium. The results indicate that the Nusselt number increases linearly with increasing Dufour parameter to facilitate buoyancy. Numerical study of Soret and Dufour effects on the natural convection flow of a vertical plate with power-law heat flux embedded in a porous medium is studied by Tsai and Huang [35]. Zhu et al. [36] have numerically studied the natural double-diffusive convection of power-law fluids in a porous cube using a generalized non-Darcy model. They found that the impact of different power law indices on convection is mainly manifested in rheological properties, showing that shear-thinning fluids are more efficient at enhancing heat and mass transfer than shear-thickening fluids. Madhua et al. [37] investigated new entropy generation characteristics in the fully developed heat transport of a non-Newtonian Carreau fluid in an inclined microchannel. They found that the velocity is maximal at the center of the microchannel when using increasing values of Grashof number Gr, while entropy production is maximal at the center of the channel. Ben Khelifa et al. [38] have derived an analytical solution to characterize the onset of motion, heat and mass convection for a binary power law fluid in a shallow porous enclosure. The occurrence of nonlinear convection in a horizontal porous layer saturated with a shear-acting fluid is studied by Bensilakhal et al. [39]. The most interesting results of their study are the demonstration of the existence of a bi-stability phenomenon, i.e., the existence of two steady-state solutions, which had not previously been observed in the convection of non-Newtonian fluids.

Many studies have focused on the effect of the shear-thinning of non-Newtonian fluids, which attracts more attention when it comes to heat transfer problems. The Marangoni in a shallow rectangular cavity of a power-law fluid was studied by Naimi [40]. Chen [41] examined the influence of Marangoni convection for a power-law liquid film on an unsteadily stretching aluminium foil. Lamsaadi [42] studied the natural convection of non-Newtonian power-law fluids subjected to transverse temperature gradients inside a horizontal rectangular space. These authors noted the combined effect of heat flow ratio, power-law index and Rayleigh number on flow intensity and heat transfer rates. Lamsaadi et al. [43] have shown that the depends only on the nominal Rayleigh number Ra and the power-law index, n, for large values of the aspect ratio and the nominal Prandtl number Pr. Habibi et al. [44] described the natural laminar convection of a non-Newtonian fluid between two horizontal eccentric square ducts under equilibrium conditions. Recently, Alloui et al. [45] analyzed the onset of fluid motion for power-law fluids. It was shown that, for shear-thinning fluids, the onset of convection is subcritical. For shear-thickening fluids, convection occurs at a supercritical Rayleigh number of zero. Khali et al. [46] studied double-diffusive convection in a power-law fluid. The results indicate that the fluid structure is more important for thermal base flow. Ohta et al. [47] have numerically investigated transient heat transfer in a square cavity heated from below and cooled from above. For shear-thinning fluids, the Sutherby model was used. Their study also reveals an increasing magnitude of shear-thinning, based on a transient analysis of the natural convection of shear-thinning-fluids in rectangular enclosures with differential heating. Hojjat [48] described Reynolds and Prandtl numbers for non-Newtonian fluids; the coefficient index and power-

law index are very important in determining the Reynolds number and initial velocity of the fluid at the tube inlet. Reynolds and Prandtl numbers are described as follows for non-Newtonian fluids. Solomatov and Barr [49, 50] have numerically investigated the occurrence of convection in non-Newtonian power-law fluids under the effect of temperature-dependent viscosity. The authors summarize their results in terms of simple scaling relations.

The primary focus of this investigation centered on the phenomenon of thermosalutal convection within a horizontal porous layer filled with a non-Newtonian fluid, subjected to heating and salting from below. The non-Newtonian fluid behavior was accurately characterized through the implementation of the power-law model, accepting a diverse range of fluid types, including shear-thinning ($n < 1$), shear-thickening ($n > 1$), and Newtonian fluids ($n = 1$). Employing a time-accurate finite difference method, the comprehensive nonlinear governing equations were numerically resolved. Additionally, an analytical solution for shallow enclosures was derived. The outcomes of this study significantly contributed to an enhanced comprehension of the impact of various governing parameters on diverse convective bifurcations. Notably, the shapes of bifurcation branches underwent substantial alterations, particularly in scenarios involving opposing double-diffusive flows. The most noteworthy revelation was the emergence of bistability bifurcation with increasing shear-thickening behavior of the fluid, leading to the occurrence of two distinct and stable solutions under identical flow conditions, a phenomenon hitherto unobserved in the context of Newtonian fluids.

2. PROBLEM DEFINITION AND MATHEMATICAL FORMULATION

The problem under study is sketched in Figure 1. It's a tow-dimensional horizontal shallow cavity filled with non-Newtonian binary fluids saturated porous media. Choose an appropriate coordinate system where the x', y' are the longitudinal and transversal axis, respectively. The enclosure is of height H' and length L'. The short vertical end walls are thermally insulated, while the horizontal walls are submitted to constant heat flux, q', and solutal flux, J'. In accordance with previous statements made by Pascal [51, 52], the model of laminar flow of a non-Newtonian power-law fluid through a porous medium is explained as follows:

$$\nabla p' = -\frac{\mu'_a}{K} V' \tag{1}$$

where

$$\mu'_a = \varepsilon \left(u'^2 + v'^2 \right)^{\frac{n-1}{2}}, \quad \text{and} \quad \varepsilon = 8^{\frac{n+1}{2}} \left(K\phi \right)^{\frac{n-1}{2}} \left(n/(1+3n) \right)^n (2h)^{-1} \tag{2}$$
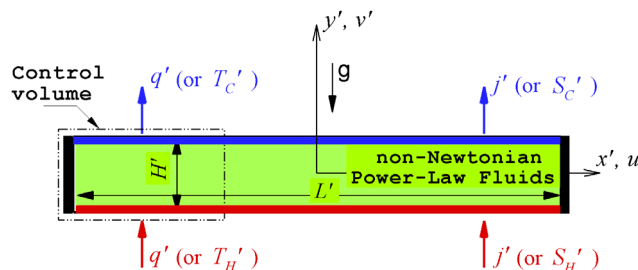

Figure 1. Sketch of the enclosure and coordinates system.

where V' is the superficial velocity, ϕ and K the porosity and the permeability of the porous medium respectively, μ'_a, the apparent viscosity, h the consistency index and n the power-law index. In the above model the rheological parameters h and n are assumed to be temperature independent.

The equations governing the heat flux q' and matter flux j', with respect to the thermal and solute gradients in the binary fluid mixture, are expressed by De Groot and Mazur [53], as follow:

$$\vec{q}' = -k\nabla T', \quad \vec{j}' = -\rho D\nabla S' \tag{3}$$

Herein, where T' and S' represent respectively the temperature and the concentration of the fluid at a point in the system, k and D represent the thermal conductivity and molecular diffusion coefficient of the species, respectively.

If we make the assumption that the flowing fluid and the porous medium are in local thermodynamic equilibrium throughout, with constant properties for both the fluid and the porous medium, and apply the Boussinesq approximation, which has been used in the past by many authors Amari et al. [29], Bian et al. [54, 55], and Benhadji and Vasseur [28]. The equations that govern the current problem can be expressed as follows:

$$\nabla . \vec{V}' = 0 \tag{4}$$

$$\nabla p' = -\frac{\mu'_a}{K} \vec{V}' - \rho_0 \vec{g} \left[1 - \beta'_T \left(T' - T'_0 \right) - \beta'_S \left(S' - S'_0 \right) \right] \tag{5}$$

$$\left(\rho C \right)_p \frac{\partial T'}{\partial t'} + \left(\rho C \right)_f J(\Psi', T') = k\nabla^2 T' \tag{6}$$

$$\phi \frac{\partial S'}{\partial t'} + J(\Psi', S') = D\nabla^2 S' \tag{7}$$

where ρ the density of the non-Newtonian fluid. T'_0, S'_0 and ρ_0 represent the temperature, concentration, and mass density of reference, g the gravitational acceleration, $(\rho C)_f$ and $(\rho C)_p$ are the heat capacities of fluid and saturated porous medium, and $\alpha = k/(\rho C)_f$ the thermal diffusion coefficient. β'_T, β'_S are respectively the thermal and solutal expansion coefficients. They are defined by

$$\beta'_T = -\frac{1}{\rho_0}\left(\frac{\partial \rho}{\partial T}\right)_{P',S'}, \quad \beta'_S = -\frac{1}{\rho_0}\left(\frac{\partial \rho}{\partial S}\right)_{P',T'} \tag{8}$$

By using H', α/H', $\Delta T' = q'H'/k$, and $S = S'/\Delta S'$ to scale length, velocity, temperature, and concentration, respectively, and eliminating the pressure term from Equation (5) through standard methods, it can be demonstrated that the dimensionless governing equations can be formulated as follows

$$\nabla^2 \Psi = -\mu_a^{-1}\left[\frac{\partial \Psi}{\partial y}\frac{\partial \mu_a}{\partial y} + \frac{\partial \Psi}{\partial x}\frac{\partial \mu_a}{\partial x} + R_T\left(\frac{\partial T}{\partial x} + N\frac{\partial S}{\partial x}\right)\right] \tag{9}$$

$$\nabla^2 T = \frac{\partial T}{\partial t} + \frac{\partial \Psi}{\partial y}\frac{\partial T}{\partial x} - \frac{\partial \Psi}{\partial x}\frac{\partial T}{\partial y} \tag{10}$$

$$Le^{-1}\nabla^2 S = \xi\frac{\partial S}{\partial t} + \frac{\partial \Psi}{\partial y}\frac{\partial S}{\partial x} - \frac{\partial \Psi}{\partial x}\frac{\partial S}{\partial y} \tag{11}$$

$$\mu_a = \left[\left(\frac{\partial \Psi}{\partial x}\right)^2 + \left(\frac{\partial \Psi}{\partial y}\right)^2\right]^{\frac{n-1}{2}} \tag{12}$$

The dimensionless parameters who were extracted from Eqs. (9)-(11) are $R_T = K\rho g\beta'_T\Delta T'/\mu$ is a thermal Rayleigh number, the Lewis number $Le = \alpha/D$, the buoyancy ratio $N = \beta'_S\Delta S'/\beta'_T\Delta T'$, $\varepsilon = \phi/\sigma$ the normalized porosity, with $\sigma = (\rho C)_p/(\rho C)_f$ is the heat capacity ratio, and Ψ is a dimensionless stream function defined as

$$u = \frac{\partial \Psi}{dy}, \quad v = -\frac{\partial \Psi}{dx} \tag{13}$$

Remember that it is possible to improve the Newtonian expressions by simply set $n=1$ and $\mu_a = 1$. The non-dimensional boundary conditions at the enclosure walls are as follows

$$\Psi = \frac{\partial \Psi}{\partial y} = 0, \quad \frac{\partial T}{\partial y} = \frac{\partial S}{\partial y} = -1 \text{ at } y = \pm 1/2 \tag{14}$$

$$\Psi = \frac{\partial \Psi}{\partial x} = 0, \quad \frac{\partial T}{\partial x} = \frac{\partial S}{\partial x} = 0 \text{ at } x = \pm A/2 \tag{15}$$

where $A = H'/L'$ is the cavity aspect ratio.

The problem definition is rendered complete by the simultaneous consideration of Eqs. (9)-(13) along with the boundary conditions, as denoted by Eqs. (14) and (15). It is important to note that the solution to this problem is intrinsically dependent on the values of the parameters R_T, A, Le, N and n.

From an engineering perspective, the focus lies in the calculation of heat and mass transfer rates expressed through local and average Nusselt and Sherwood numbers, denoted as Nu_x, Nu_m, Sh_x, and Sh_m, respectively. In the current notation, the computation of Nu_x, Nu_m, Sh_x, and Sh_m is performed as follows:

$$\left.\begin{array}{l} Nu_x^{-1} = T_{(x,-1/2)} - T_{(x,1/2)} \quad ; \quad Sh_x^{-1} = S_{(x,-1/2)} - S_{(x,1/2)} \\[2mm] Nu_m = A^{-1}\int\limits_{-A/2}^{+A/2} Nu_x dx \quad ; \quad Sh_m = A^{-1}\int\limits_{-A/2}^{+A/2} Sh_x dx \end{array}\right\} \tag{16}$$

where the integral is performed using Simpson's method.

3. NUMERICAL SOLUTION

For simple geometry problems Fig. 1, the finite difference method used to numerically solve the governing equations (9)-(11). The energy and concentration equations are discretized with a second-order centered scheme. For each time step the implicit method with alternating directions (ADI) gives rise to two tri-diagonal matrix systems to be solved, one

resulting from the implicit discretization in x and the other of the implicit discretization in y. The (ADI) method divides the time step into two equal parts, in the first half-time step, the system is implicitly in x but explicitly in y and in the second half-time step, the system is implicitly in y and explicitly in x. For each time step, the solution is obtained by scanning the computational domain in the x direction then in y-direction. Knowing the fields of temperature and concentration at time $(n + 1)\Delta t$, to solve the discretized motion equation at each time step successive over relaxation method (SOR) is used which is an explicit method directly giving the value of Ψ to the instant $(n + 1)\Delta t$. The convergence criterion for solving Eq. (9) is provided.

$$\frac{\sum_i \sum_j \left|\Psi_{i,j}^{k+1} - \Psi_{i,j}^k\right|}{\sum_i \sum_j \left|\Psi_{i,j}^k\right|} \leq 10^{-6} \tag{17}$$

The selection of mesh size is a careful consideration aimed at striking a suitable balance between computational efficiency and result accuracy. The approach involves grid refinement iteratively until the numerical solution converges, with a reasonable accuracy threshold, to the analytical solution developed in the subsequent section. This convergence is achieved under the prescribed values for A, Le, N, n, and R_T. As indicated in Table 1, a uniform grid of dimensions 221x141 proves to be well-suited for accurately modeling the flow, temperature, and concentration fields within a cavity between 6 and 10. The chosen time-step sizes for simulations range between 10^{-6} and 10^{-3}.

Table 1. Convergence tests for specified parameters, $A = 6$, $Le = 5$, $N = -0.1$, $R_T = 100$, and $n = 1.2$.

	Numerical solution				Analytical
Grids	40x20	100x60	160x100	220x140	solution
Ψ_0	3.0342	2.9574	2.9462	2.9397	2.9269
Nu	2.9153	3.0033	3.0219	3.0254	3.0280
Nu_m	2.7292	2.8213	2.8404	2.8442	-
Sh	5.0314	5.3053	5.3772	5.4060	5.4358
Sh_m	5.1010	5.3920	5.4691	5.4997	-
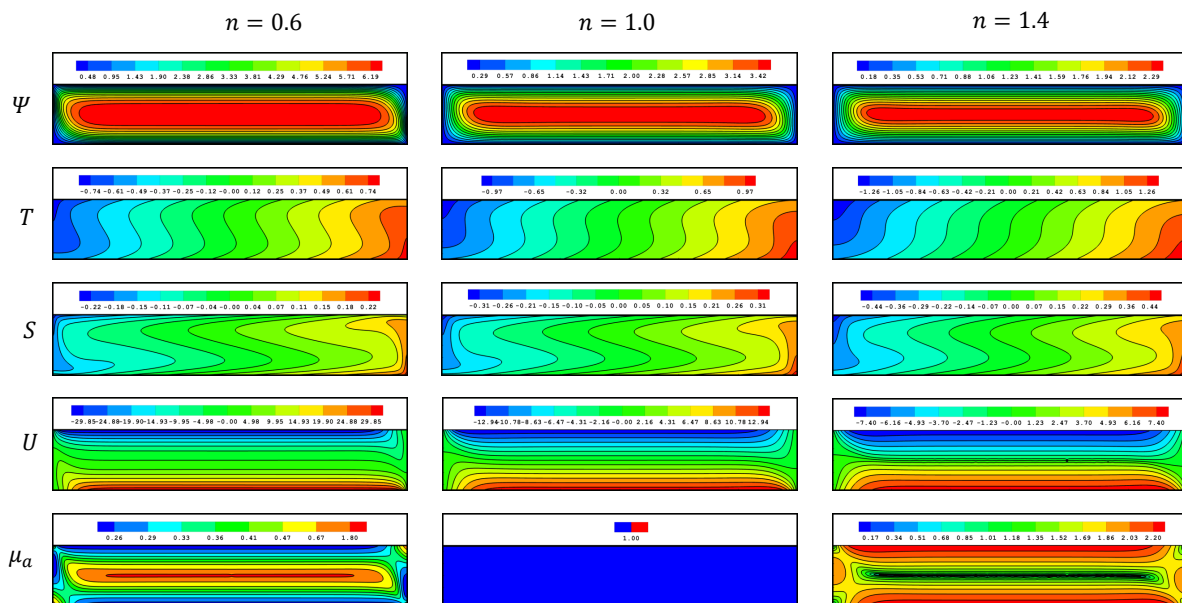
Figure 2. Contours of streamlines, Ψ, Temperature, T, Concentration, S, horizontal velocity, U, and apparent viscosity, μ_a, for $R_T = 100$, $Le = 5$, $N = -0.1$ and various values of n

Figure 2 present the contours of streamlines, Ψ, temperature, T, concentration, S, horizontal velocity, U, and apparent viscosity, μ_a, obtained numerically, for two different liquids with power-law index of n = 0.6 and 1.4 and for a Newtonian fluid (n = 1), at $R_T = 100$, $Le = 5$, and $N = -0.1$. The streamlines are uniformly distributed with designated increments, $\Delta\Psi$, spanning from zero at the boundaries to the maximum value, Ψ_{max}, at the center. The isotherms and isoconcentration lines are uniformly distributed between the successive positions of the peak temperature T_{max} and maximum concentration S_{max} situated lower edge of the right vertical wall. On the other hand, the minimum temperature T_{min} and minimum concentration S_{min} are situated along the upper edge of the left vertical wall. Notably, the dimensionless temperature and concentration at the cavity's center are both normalized to zero. Furthermore, owing to the centrosymmetry inherent in the problem, the minimum and maximum temperatures, as well as concentrations, exhibit equivalent magnitudes but with opposite signs. The horizontal velocity lines are uniformly distributed from the maximum velocity, U_{max}, located on the lower horizontal wall and the minimum velocity, U_{min}, on the upper horizontal wall. The

apparent viscosity lines are uniformly distributed with specified increments $\Delta\mu_a$ between the minimum value, μ_{amin}, on the center of cavity and the extremum value, μ_{amax}, on the center when $n = 0.6$, this is the opposite of $n = 1.4$, and it's clearly constant ($\mu_a = 1$) when $n = 1$. The numerical findings depicted in Figure 2 validate the theoretical assumption made in the analytical solution, indicating that the flow patterns within the central region of the cavity remain parallel regardless of the power-law index, n. It is important to note. However, that the scope of this current investigation is confined to the examination of unicellular convection exclusively.

To validate the accuracy of the current numerical solutions, Tables 2 and 3 presents the obtained numerical results, including the center stream function, Ψ_0, value, as well as the local Nusselt, Nu, and Sherwood, Sh, numbers. A comprehensive comparison with the findings reported by Amari et al. [29] and Ben Khelifa et al. [38] reveals a very good level of agreement.

Table 2. Comparison of Ψ_0, and Nu with previous numerical studied of Amari et al. [29] for $N = 0$, $Le = 5$, and various values of n, with horizontal cavity.

n		Analytical	Amari et al. [29] study	Present study	Present study vs analytical	Present study vs Amari et al. [29]
			$A = 6$ and $R_T = 100$			
0.6	Ψ_0	6.701	6.762	6.742	0.61%	0.30%
	Nu	6.000	5.997	5.929	1.19	1.14
1.0	Ψ_0	3.708	3.708	3.706	0.05	0.05
	Nu	3.750	3.750	3.737	0.35	0.35
1.4	Ψ_0	2.448	2.468	2.474	1.06	0.24
	Nu	2.553	2.553	2.558	0.20	0.20

Table 3. Comparison of Ψ_0, Nu and Sh with previous numerical studied of Ben Khelifa et al. [38] for $N = 0.2$, $Le = 10$, and various values of n, with horizontal cavity.

n		Analytical solution	Present study	Present study vs analytical	Ben Khelifa et al. [38]	Present study vs Ben Khelifa et al. [38]
			$A = 6$ and $R_T = 25$			
0.6	Ψ_0	2.54	2.55	0.39%	2.60	1.94%
	Nu	3.22	3.22	0.00	3.27	1.54
	Sh	7.22	7.30	1.10	7.25	0.69
1.0	Ψ_0	1.47	1.47	0	1.48	0.68
	Nu	1.81	1.81	0	1.81	0
	Sh	5.75	5.75	0	5.75	0
1.6	Ψ_0	1.00	1.02	1.98	1.01	0.99
	Nu	1.36	1.37	0.73	1.64	18.09
	Sh	4.98	4.97	0.20	4.98	0.20

4. ANALYTICAL SOLUTION

An analytical solution for the full governing equations, (9)-(11) is in general impossible, except for certain cases and assumptions for which the equations simplify considerably. In the case of a porous layer of large aspect ratio ($A \gg 1$) with active walls exposed to constants fluxes of heat and mass, it is possible to find an approximate analytical solution. This last, obtained using the concept of parallel flow, the generated flow becomes relatively parallel along the long walls of the cavity, which of course makes it possible to neglect the component of the velocity perpendicular to these walls.

The streamlines, at the center of the cavity, become parallel to the *x*-axis. In other words, the current function Ψ becomes a function of the y ordinate only. We can then write:

$$\Psi(x, y) = \Psi(y) \tag{18}$$

The temperature and concentration profiles are given by the sum of two terms, the first one defining a linear longitudinal variation and the other giving the transverse distribution:

$$\left.\begin{array}{l} T(x, y) = C_T x + \theta_T(y) \\ S(x, y) = C_S x + \theta_S(y) \end{array}\right\} \tag{19}$$

where C_T and C_S are constants expressing temperature and concentration gradients along the *x*-direction.

Substituting approximations (18) and (19) in the governing equations (9)-(11) and assuming steady state of flows, the heat and mass fluxes, we get the following ordinary differential equations:

$$\frac{d}{dy}\left[\frac{d\Psi}{dy}\left|\frac{d\Psi}{dy}\right|^{n-1}\right] = -\Lambda \tag{20}$$

where: $\Lambda = R_T (C_T + NC_S)$

$$\frac{d^2\theta_T}{dy^2} = C_T \frac{d\Psi}{dy} \tag{21}$$

$$\frac{d^2\theta_S}{dy^2} = C_S Le \frac{d\Psi}{dy} \tag{22}$$

Solution of Eqs. (20)-(22) satisfying the boundary conditions given by Eq. (14) are:

$$\Psi(y) = -(m)^{-1} [\Lambda]^{1/n} \left[|y|^m - (1/2)^m \right] \tag{23}$$

$$T(y) = C_T x \; - \; [\Lambda]^{1/n} (m)^{-1} C_T y \left[(m+1)^{-1} |y|^m - (1/2)^m \right] - y \tag{24}$$

$$S(y) = C_S x \; - \; [\Lambda]^{1/n} (m)^{-1} Le C_S y \left[(m+1)^{-1} |y|^m - (1/2)^m \right] - y \tag{25}$$

where: $m = 1 + 1/n$.

The expression of the velocity distribution u along y derived from the stream function is:

$$u(y) = - [\Lambda]^{1/n} |y|^{1/n} \tag{26}$$

The concept of parallel flow loses its viability due to the turning flow at the end of perpendicular walls. However, in the case of thermal and mass conditions in the end walls, the value of constant temperature and concentration gradients, C_T and C_S respectively are determined by considering the arbitrary control volume of Fig. 1, the energy and material balances in the control volume at any x-direction are written according to the following forms:

$$C_T = \int_{-1/2}^{+1/2} \theta_T u \, dy \; ; \; C_S = Le \int_{-1/2}^{+1/2} \theta_S u \, dy \tag{27}$$

By substituting the temperature, concentration and velocity Eqs. (24)-(26) into Eqs. (27), we get the following expression:

$$(m+1)^{-1} (1/2)^m [\Lambda]^{1/n} \left[1 - (1/2)^{m-1} (2m+1)^{-1} C_T [\Lambda]^{1/n} \right] - C_T = 0 \tag{28}$$

$$Le(m+1)^{-1} (1/2)^m [\Lambda]^{1/n} \left[1 - (1/2)^{m-1} (2m+1)^{-1} C_S Le[\Lambda]^{1/n} \right] - C_S = 0 \tag{29}$$

Equations (28) and (29) has been solved numerically for C_T and C_S using the method of Newton-Raphson.

From Eqs. (24), (25) and (16), the Nusselt and Sherwood numbers are given by:

$$Nu^{-1} = 1 - [\Lambda]^{1/n} (m+1)^{-1} C_T (1/2)^m \tag{30}$$

$$Sh^{-1} = 1 - [\Lambda]^{1/n} (m+1)^{-1} C_S Le (1/2)^m \tag{31}$$

5. LINEAIR STABILITY ANALYSIS

In this section, an investigation into the stability of the steady state is conducted. The overall convective solution encompasses a foundational solution (Ψ_b, T_b, S_b) with a perturbation solution (Ψ_p, T_p, S_p).

In the context of an infinite horizontal fluid layer, the perturbation solution for the stream function, temperature, and concentration field can be formulated as follows:

$$\left. \begin{array}{l} \Psi_p(x,y,t) = \Psi_0 e^{pt+i\alpha x} F(x,y) \\ T_p(x,y,t) = \theta_0 e^{pt+i\alpha x} G(x,y) \\ S_p(x,y,t) = \phi_0 e^{pt+i\alpha x} H(x,y) \end{array} \right\} \tag{32}$$

In this formulation, $F(x,y)$, $G(x,y)$, and $H(x,y)$ represent the spatial profiles of the perturbation for the stream function, temperature, and concentration, respectively. p characterizes the growth rate of the perturbation, α is a real number which designates the wave number. The variables Ψ_0, θ_0, and ϕ_0 denote infinitesimal unknown perturbation amplitudes for the stream function, temperature, and concentration.

In order to assess the stability of the rest state solution, a tiny perturbation is introduced, allowing the complete solution to be expressed as follows:

$$\left.\begin{array}{l} \Psi(x,y,t) = \Psi_b(x,y) + \Psi_p(x,y,t) \\ T(x,y,t) = T_b(x,y) + T_p(x,y,t) \\ S(x,y,t) = S_b(x,y) + S_p(x,y,t) \end{array}\right\} \quad (33)$$

The apparent viscosity, denoted as μ_a, can be further decomposed as:

$$\mu_a = \mu_{a,b} + \mu_{a,p} \quad (34)$$

Here, $\mu_{a,p}$ and $\mu_{a,b} = \left(\dfrac{\partial \Psi_b}{\partial y}\right)^{n-1}$ represent the perturbation and basic apparent viscosity, respectively.

The linearized form of the perturbed apparent viscosity is expressed as follows:

$$\mu_{a,p} = (n-1)\left(\frac{\partial \Psi_b}{\partial y}\right)^{n-1}\frac{\partial \Psi_p}{\partial y} \quad (35)$$

Upon substituting equations (32)-(35) into equations (9)-(11) and neglecting the second-order nonlinear terms, the resulting linearized stability equation is as follows:

$$(nD^2 - \alpha^2)(D\Psi_b)^{n-1} f + n(n-1)(D\Psi_b)^{n-2} D^2\Psi_b Df = -R_T(g + Nh) \quad (36)$$

$$(C_T D - i\alpha DT_b)f + \left(\alpha^2 + i\alpha D\Psi_b - D^2\right)g = -pg \quad (37)$$

$$(C_S D - i\alpha DS_b)f + \left(Le^{-1}\alpha^2 + i\alpha D\Psi_b - Le^{-1}D^2\right)h = -p\xi h \quad (38)$$

where:

$$\psi_0 F = f, \quad \theta_0 G = g, \quad \phi_0 G = h, \quad D = \frac{d}{dy} \quad (39)$$

By employing the variational formulation through the Galerkin technique, the integrated linear equations are derived as follows:

$$[K_\psi]\{f\} = R_T\left([B_\psi]\{g\} + N[B_\psi]\{h\}\right) \quad (40)$$

$$[B_\theta]\{f\} + [K_\theta]\{g\} = -p[M_\theta]\{g\} \quad (41)$$

$$[B_\phi]\{f\} + [K_\phi]\{h\} = -P\varepsilon[M_\phi]\{h\} \quad (42)$$

The constants $[K_\psi]$, $[B_\psi]$, $[C_\psi]$, $[B_\theta]$, $[K_\theta]$, $[M_\theta]$, $[B_\phi]$, $[K_\phi]$, and $[M_\phi]$ can be determined through the computation of the following Galerkin integral

$$[B_\psi]^e = \int_{-1}^{1} i\alpha N_j N_i \frac{\Delta y}{2} d\eta$$

$$[B_\theta]^e = \int_{-1}^{1}\left(C_T \frac{\partial N_j}{\partial \eta} - i\alpha\frac{\partial T_b}{\partial \eta}N_j\right)N_i d\eta$$

$$[B_\phi]^e = \int_{-1}^{1}\left(C_s \frac{\partial N_j}{\partial \eta} - i\alpha\frac{\partial S_b}{\partial \eta}N_j\right)N_i d\eta$$

$$[K_\psi]^e = \int_{-1}^{1}\left(n\left(\frac{\partial \Psi_b}{\partial \eta}\right)^{n-1}\left(\frac{2}{\Delta y}\right)^{n-1}\frac{\partial N_j}{\partial \eta}\frac{\partial N_i}{\partial \eta} - n(n-1)\left(\frac{\partial \Psi_b}{\partial \eta}\right)^{n-2}\frac{\partial^2 \Psi_b}{\partial \eta^2}\left(\frac{2}{\Delta y}\right)^{n-1}N_j \frac{\partial N_i}{\partial \eta} + \right.$$
$$\left. \alpha^2 \left(\frac{\partial \Psi_b}{\partial \eta}\right)^{n-1}\left(\frac{\Delta y}{2}\right)^{n-2}N_j N_i\right) d\eta$$

$$[K_\theta]^e = \int_{-1}^{1}\left(\frac{\Delta y}{2}\alpha^2 N_j N_i + i\alpha\frac{\partial \Psi_b}{\partial \eta}N_j N_i + \frac{2}{\Delta y}\frac{\partial N_j}{\partial \eta}\frac{\partial N_i}{\partial \eta}\right)d\eta$$

$$[K_\phi]^e = \int_{-1}^{1}\left(\frac{\Delta y}{2}\alpha^2 N_j N_i + i\alpha Le\frac{\partial \Psi_b}{\partial \eta}N_j N_i + \frac{2}{\Delta y}\frac{\partial N_j}{\partial \eta}\frac{\partial N_i}{\partial \eta}\right)d\eta$$

$$[M_\theta]^e = [M_\phi]^e = \int_{-1}^{1}N_j N_i \frac{\Delta y}{2}d\eta$$

The perturbation boundary conditions are specified by:

$$Df = f = 0 \quad \text{at} \quad x = \pm\frac{A}{2} \quad \text{and} \quad y = \pm\frac{1}{2} \tag{43}$$

$$Dg = Dh = 0 \quad \text{at} \quad x = \pm\frac{A}{2} \tag{44}$$

6. RESULTS AND DISCUSSION

The results of this study focus on the effect of the power-law index, n, the Rayleigh number, R_T, the buoyancy ratio, N, and the Lewis number, Le, on the bistability convective flows, heat and mass transfer behaviors, and on the thresholds of the onset of various convective bifurcations in a porous layer, as predicted by the analytical solution. The findings have been confirmed through numerical analysis of the complete governing equations. The primary revelation in this research involves identifying a convective bistability phenomenon occurs from the interactional effect between the slower diffusing component and the shear-thickening fluids ($n > 1$) properties. The study encompasses both numerical and analytical outcomes, which fall within the following typical ranges: 0.6 to 1.4 for 'n,' 1.0 to 20.0 for 'Le,' and -0.2 to 0.2 for 'N.'

Our research is primarily concerned with the onset of bifurcation. Consequently, we restrict our analysis to Rayleigh numbers R_T of relatively modest magnitudes, specifically $R_T \leq 100$, in close proximity to the critical points. Furthermore, in order to establish the presence of bistability in convection across various aspect ratio and thermal and solutal boundary conditions, we systematically vary the parameter 'A' within the range of 6 to 10, while adopting Neumann boundary conditions. This approach serves to generalize the conditions under which bistability in convection phenomena can manifest. Our initial investigation focuses on a shallow enclosure, benefiting from the availability of an analytical solution to provide guidance in this context.

Figures 3(a)-(d) show the horizontal velocity, U, apparent viscosity, μ_a, temperature, T, and (d) concentration, S, profiles at the center of the layer ($x = 0$) for $R_T = 100$, $Le = 5$, $N = -0.1$, and various values of n. the results are presented for $-0.5 \leq y \leq 0.5$. The analytical solution, represented by solid lines, aligns closely with the numerical results, denoted by solid circles, demonstrating a favorable agreement between the present analytical solution and the numerical solution. Figure 3(a) reveals a discernible decrease in velocity with increasing values of the power-law index, n, and highlights that the maximum velocity values occur at the boundaries. This behavior stems from the modeling of the porous medium in accordance with Darcy's law, permitting fluid slip at the solid boundary.
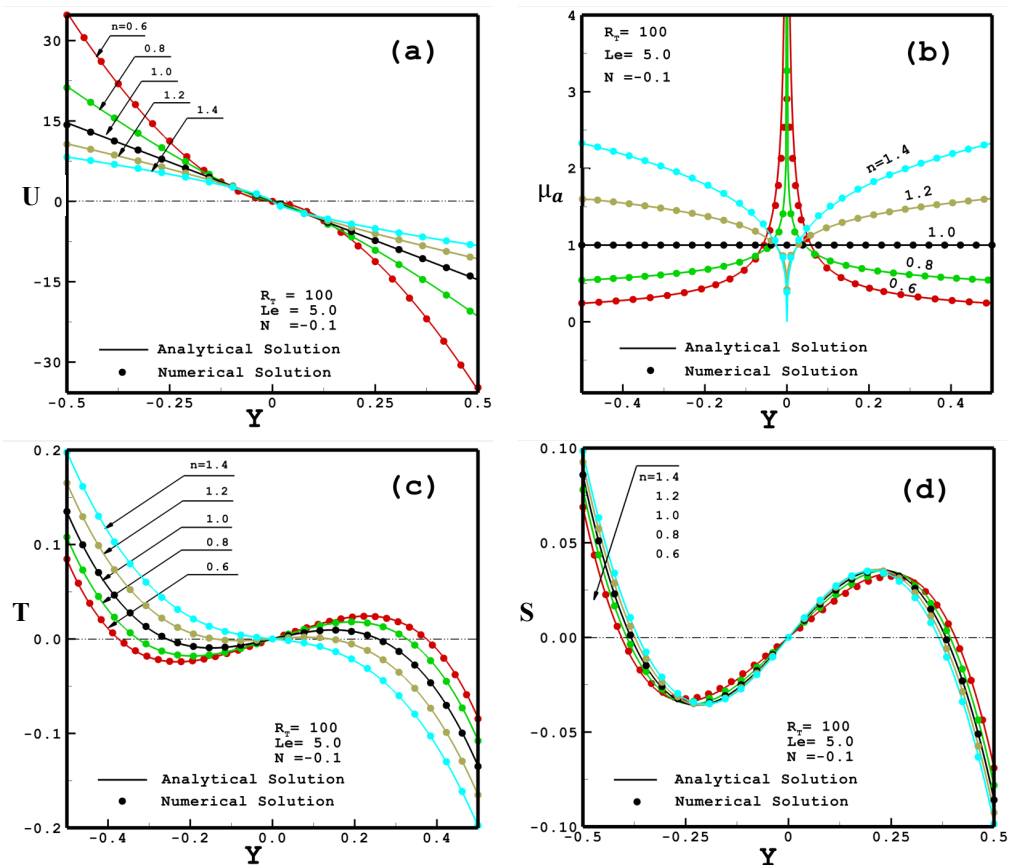
Figure 3. Effect of the power-law index, n, on (a) the horizontal velocity, U, (b) apparent viscosity, μ_a, (c) temperature, T, and (d) concentration, S

Notably, for a Newtonian fluid, the velocity distribution follows a linear pattern, in agreement with the findings of Amari et al. [29] and Vasseur et al. [56]. The depiction of apparent viscosity in Figure 3(b) elucidates a diminishing trend as the power-law index, n, decreases. This signifies a reduction in the significance of convective motion when the fluid exhibits shear-thickening behavior ($n > 1$). Conversely, contrasting effects are observed for shear-thinning fluids ($n < 1$), as evidenced in Figure 3(b). These observed phenomena align with the findings reported by Amari et al. [29], Dharmadhikari and Kale [57], as well as Chen and Chen [58, 59], and it's clearly constant ($\mu_a = 1$) in the case of Newtonian fluid ($n = 1$). In Figures 3(c) and 3(d), it is observed that the temperature and concentration profiles exhibit an augmentation with increasing values of the power-law index, n. Additionally, all curves maintain a constant slope at $y = -0.5$ and $y = 0.5$, attributed to the imposition of a constant heat and mass flux on the horizontal walls.
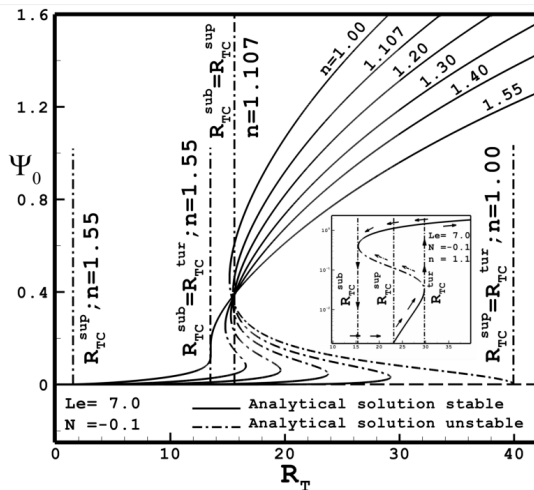

Figure 4. Bifurcation diagram in terms of Ψ_0 as the function of R_T and n

As an introductory exploration into the identification of bistability in convection, we present a graphical representation with an algorithmic scale in zoomed image Figure 4, illustrating the bistability bifurcation concerning flow intensity as a function of the Rayleigh number. The figure encompasses three distinct Rayleigh number thresholds, each bearing significance. Specifically, it is well-established that, in the context of a negative buoyancy ratio ($N < 0$), a threshold similar to that of subcritical flows emerges, denoted as R_{TC}^{sub}. This threshold may manifest either below or above the supercritical threshold, R_{TC}^{sup}. Furthermore, an additional threshold, referred to as R_{TC}^{tur}, consistently surpassing R_{TC}^{sup}, delineates a hypothetical backward bifurcation, symbolized by a dashed-dotted arrow. This backward bifurcation exhibits a transition from low to high finite amplitude convective states, forming an "S"-shaped bifurcation pattern.

The phenomenon of bistability bifurcation, achieved through systematic variations in Rayleigh numbers in both ascending and descending sequences, engenders a hysteresis loop. Within this loop, high and low convective states persist concurrently under identical flow boundary conditions and governing parameters.

In Figure 4, we depict three distinctive bistability regimes. The first of these regimes, referred to as the subcritical regime, manifests when the subcritical threshold R_{TC}^{sub} is significantly lower than the supercritical threshold R_{TC}^{sup}, specifically when, n, is less than 1.107. The second regime, known as the transcritical regime, materializes when R_{TC}^{sub} equal R_{TC}^{sup}, denoting a condition where, n, equals 1.107. The third regime, termed the supercritical regime, emerges when R_{TC}^{sub} considerably exceeds R_{TC}^{sup}, signifying, n, values greater than 1.107. Across all three of these regimes, the characteristic "S" shaped bistability bifurcation remains intact, resulting in the coexistence of two distinct and stable convective states. Notably, the bistability in convection ceases to exist when the lower and upper bifurcation points, R_{TC}^{sub} and R_{TC}^{tur}, converge (i.e., when n equal 1.55), giving rise to a well-defined inflection convection state characterized by a sharp increase in heat and solute transfer rates.

Table 4 provides a comprehensive presentation of the critical Rayleigh numbers denoting the onset of motion (R_{TC}^{sub}, R_{TC}^{tur} and R_{TC}^{sup}) as a function of the power-law index, n. A discernible trend emerges from the table, underscoring the notable influence of the power-law index, particularly in the context of thickening fluids. It is remarkable that such an influence does not manifest in the case of shear-thinning fluids, highlighting a significant distinction in the behavior of bistability convection.
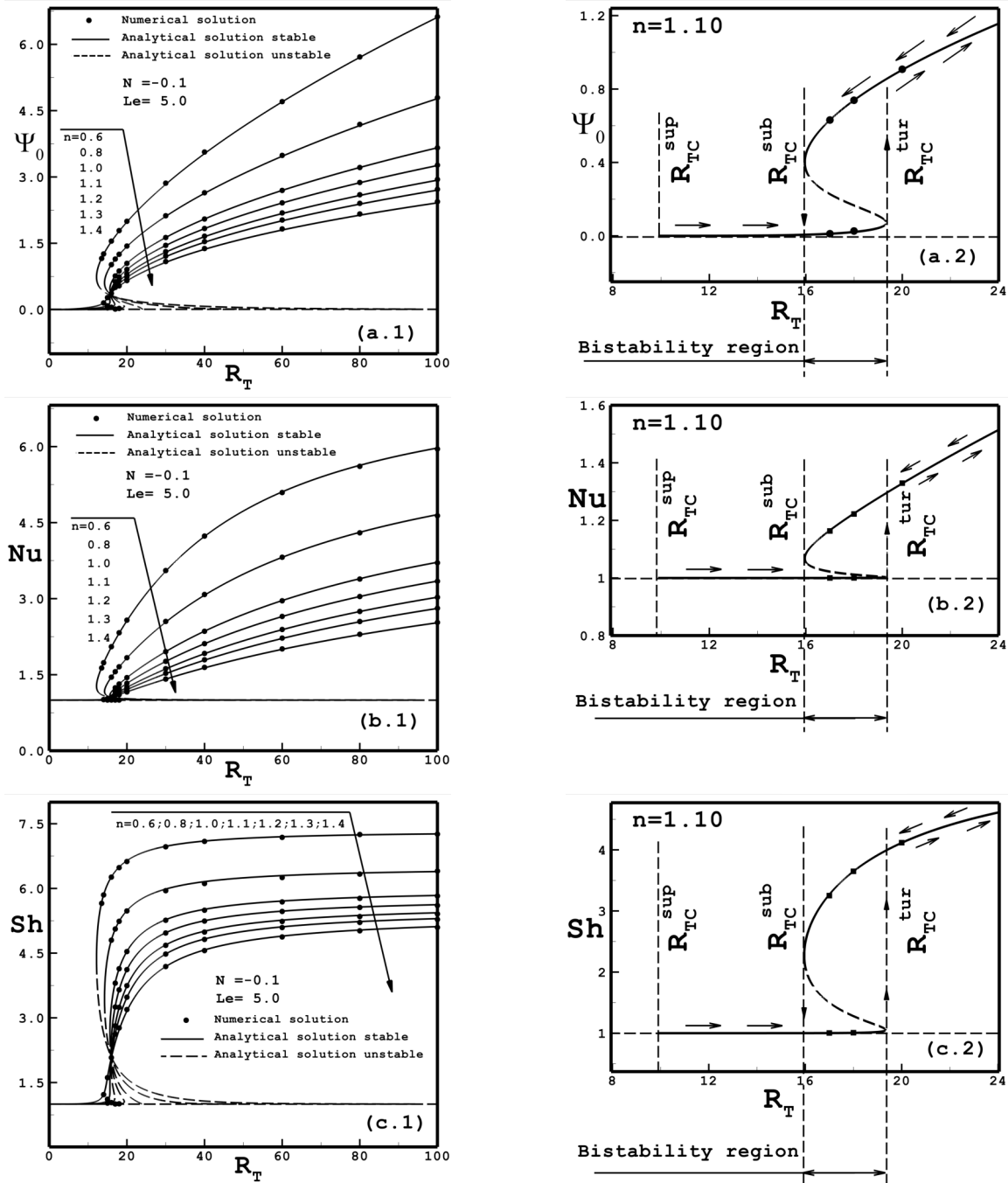
In Figure 5, characteristic bifurcation diagrams are presented, illustrating the dependencies of Ψ_0, Nu, and Sh on R_T and n under the specified conditions of $Le = 5$ and $N = -0.1$. The outcomes encompass a range of power-law index, spanning from $n = 0.6$ to 1.4. The curves featured in the plots represent the predictions derived from the present analytical/numerical nonlinear models. The solid lines denote the stable branches, while the long-dashed lines signify unstable branches.

Table 4. Dependence of R_{TC}^{sub}, R_{TC}^{tur} and R_{TC}^{sup} on n for $Le = 7.0$ and $N = -0.1$.

n	R_{TC}^{sub}	R_{TC}^{tur}	R_{TC}^{sup}
0.6	11.95	...	1314.69
0.8	13.90	...	232.48
1.0	15.17	40.00	40.00
1.1	15.46	29.72	16.47
1.2	15.50	23.77	6.75
1.3	15.28	19.62	2.76
1.4	14.80	16.59	1.12

Figure 5. Bifurcation diagram as a function of R_T and n: (a) flow intensity Ψ_0, (b) Nusselt number Nu, and (c) Sherwood number, Sh

The numerical solutions derived from the full governing equations are represented by solid circles. Notably, Good agreement is observed between the results of these two nonlinear theories. The profile obtained for a Newtonian fluid $n = 1.0$ corresponds to convection induced by the imposition of a constant heat and mass flux on the horizontal boundaries of the system. This configuration leads to the emergence of a saddle-node bifurcation at a subcritical Rayleigh number, denoted as $R_{TC}^{sub} = 15.63$. The determination of the subcritical Rayleigh number involved a numerical search within the analytical model, where the value of R_T was identified such that the inverse of the derivative of Ψ_0 with respect to R_T equaled zero. With an increasing in the power-law index, denoted as n, the bifurcation behavior undergoes a notable transformation contingent upon the magnitude of power-law index. Across the range of cases spanning from $1 < n < 1.3$, the bifurcation curve exhibits the distinctive presence of two turning saddle-node points (R_{TC}^{sub} and R_{TC}^{tur}). These points connect the two stable branches, delineated by an intervening unstable branch represented by long-dashed lines. The upper stable branch, originating from R_{TC}^{sub}, aligns with the conventional subcritical bifurcation observed earlier for $n = 1$. Conversely, the lower stable branch, commencing at R_{TC}^{sup}, corresponds to a supercritical bifurcation. However, it is noted that the latter exist within the interval of $R_{TC}^{sup} \leq R_T \leq R_{TC}^{tur}$. Under these circumstances, a bistability regime manifests

itself between the two thresholds ($R_{TC}^{sub} \leq R_T \leq R_{TC}^{tur}$). Beyond the supercritical Rayleigh number, R_{TC}^{sup}, the outcomes derived from the numerical solution of the full governing equations suggest that, when initiating computations from the initial rest state conditions, the solution traces a hysteresis loop as illustrated by arrows in the zoom included in Figure 5(a.2; b.2 and c.2). Corresponding heat and solute transfer rates are presented in Figures 5(b) and 5(c). Under the specified conditions of $N = -0.1$ and $Le = 5$, the presence of bistability bifurcation is confirmed within the power-law index range of $1 < n < 1.3$. Notably, for $n \leq 1$, the observed bifurcation assumes a subcritical.
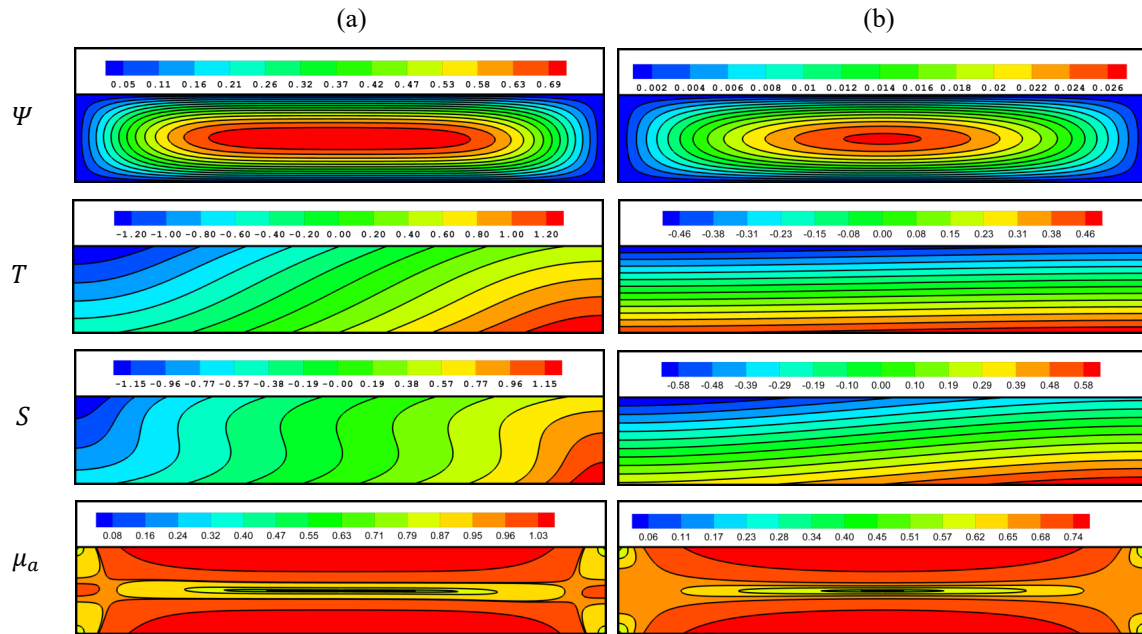
Figure 6. Contours of streamlines, Ψ_0, temperature, T, concentration, S, and apparent viscosity μ_a.

Within the zone of bistability, Figure 6 showcases the solutions at $R_T = 18$, obtained through the numerical resolution of the comprehensive governing equations. These visual representations encompass streamlines, isotherms, isoconcentrates, and apparent viscosities, presented in a sequential order from top to bottom. The solution portrayed in Figure 6(b), attributed to the lower branch, originates from the initiation of numerical calculations using the initial rest state conditions. However, the solution related to the upper branch, Figure 6(a), is exclusively attained by following the delineated hysteresis path on the curve for $n = 1.1$, with an increase in the power-law index, the region of bistability contracts, as evidenced by the outcomes derived for $n = 1.1$, and diminishes entirely as the fluid became more and more shear-thickening, exemplified in instances with $n = 1.3$. In such circumstances, a resultant pitchfork-type bifurcation emerges, characterized by the transition from the rest state to a convective regime, occurring at a supercritical Rayleigh number, R_{TC}^{sup}.

Table 5 gives the critical values of the Rayleigh numbers characterizing the onset of motion (R_{TC}^{sup}, R_{TC}^{sup}, and R_{TC}^{tur}) as a function of the power-law index, n. This table clearly indicates that bistability convection was significantly affected by the power-law index, n.

Table 5. Dependence of R_{TC}^{sub}, R_{TC}^{tur} and R_{TC}^{sup} on n for $Le = 5.0$ and $N = -0.1$.

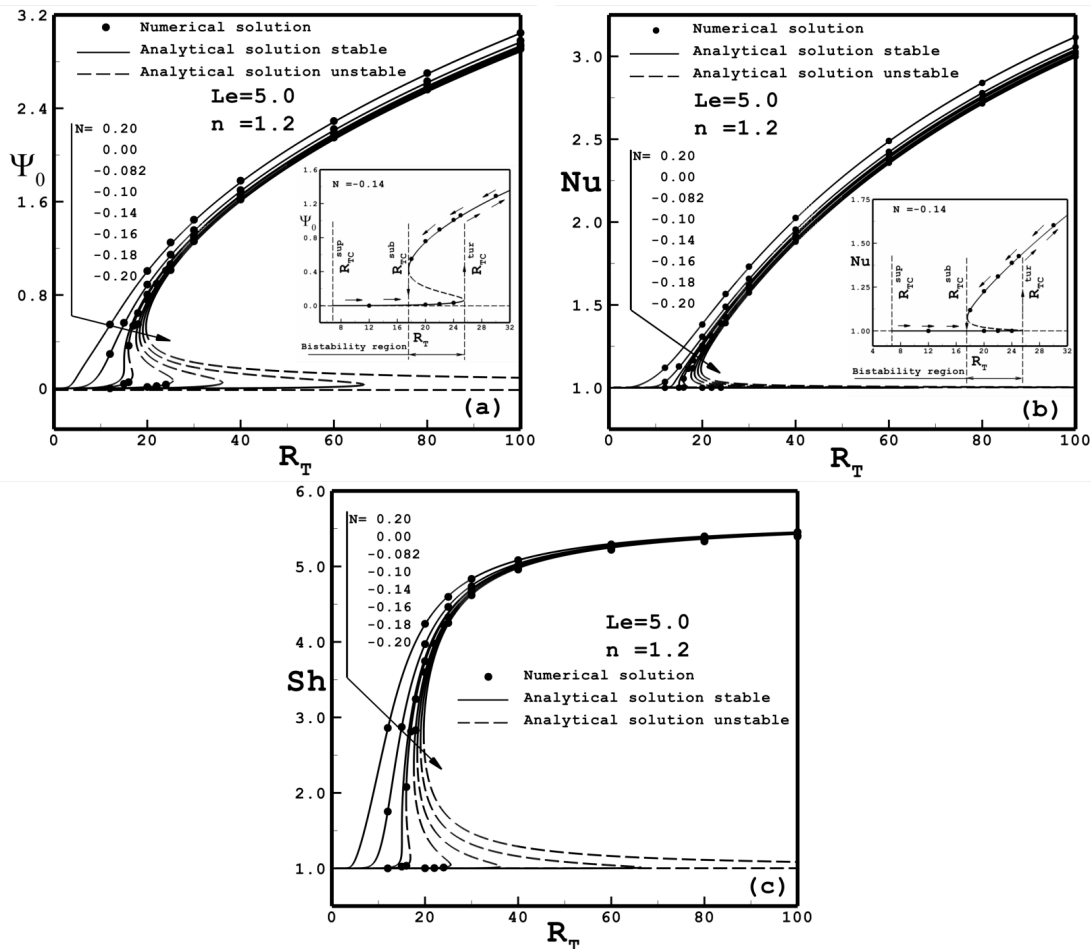| n	R_{TC}^{sub}	R_{TC}^{tur}	R_{TC}^{sup}
0.6	12.18	…	788.90
0.8	14.24	…	139.50
1.0	15.63	24.00	24.00
1.1	15.96	19.33	9.88
1.2	15.96	16.87	4.05
1.3	15.63	15.63	1.98
1.4	…	…	0.67

In Figure 7, a stability diagram is presented to illustrate the influence of the power-law index denoted as, n, and the buoyancy ratio, N, on critical Rayleigh numbers that govern the onset of subcritical R_{TC}^{sub} and supercritical R_{TC}^{sup} convection, as well as an additional critical point denoted as R_{TC}^{tur}, which corresponds to a turning saddle-node point where a backward bifurcation occurs, resulting in a transition from lower to higher convective states. These findings are presented within the context of $Le = 5.0$. Upon initial examination, it becomes evident that R_{TC}^{sub}, R_{TC}^{sup} and R_{TC}^{tur} exhibit significant decreases as the buoyancy ratio, N, increases. This decrease can be attributed to the collaborative influence of shear-thickening behavior and the slower diffusing solute, which collectively augment the subcritical convection phenomenon.
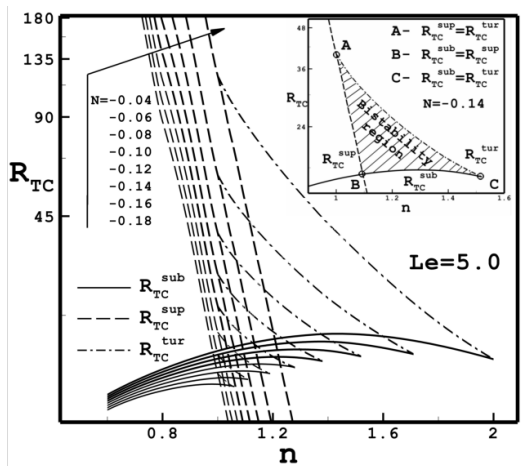
Figure 7. Buoyancy ratio, N, and power-law index, n, effects on the critical Rayleigh numbers (R_{TC}^{sub}, R_{TC}^{tur}, and R_{TC}^{sup})

When the buoyancy ratio N approaches or exceeds approximately -0.02, a bistability convection regime becomes evident. This region is distinctly outlined as a triangular area, as depicted in the zoomed image in Figure 7 for the case of $N = -0.14$. Notably, it becomes evident that bistability convection exclusively occurs in the context of shear-thickening fluid ($n > 1$) and opposing flow conditions where ($N < 0$), This is the opposite of what reported by Rebhi et al. [26], where the bistability occurs in the context of shear-thinning fluid ($n < 1$) and aiding flow conditions where ($N > 0$). For a specific buoyancy ratio value of $N = -0.14$, the graph clearly demonstrates that the subcritical regime, R_{TC}^{sub} is observed to be the lowest among the three critical values i.e., ($R_{TC}^{sub} < R_{TC}^{sup} < R_{TC}^{tur}$). a co-dimension two point emerges within the transcritical regime where $R_{TC}^{sup} = R_{TC}^{sub} = 17.26$, for a power-law index, with $n = 1.107$, indicated as point (B) in the zoomed image. This transcritical regime extends until $n = 1.52$, where $R_{TC}^{sup} = R_{TC}^{tur} = 16.89$, indicated as point (C), and a point (A) demonstrates a weak dependence on the power-law index $n = 1$ and $R_{TC}^{sup} = R_{TC}^{tur} = 40$. The boundaries of the bistability region are delineated by the triangle (ABC) as illustrated in the zoomed image. In summary, as the buoyancy ratio value with ($N < 0$) decreases, the value of the power-law index n increases, the presence of bistability becomes increasingly evident, regardless of n exceeding 1.0. However, it is noteworthy that the extent of the bistability region exhibits significant sensitivity to the buoyancy ratio, N, and the power-law index, n, expanding as N, and n decreases (refer to Figure 7 and Figure 5 for the range $-0.04 \leq N \leq -0.18$, and $1 < n < 3$). It is pertinent to observe that as shear-thickening behavior becomes more pronounced, it promotes Newtonian thermosolutal subcritical convection $n = 1$, leading to a notable reduction in the threshold for subcritical convection.


Figure 8. Bifurcation diagram as a function of R_T and N: (a) flow intensity Ψ_0, (b) Nusselt number Nu, and (c) Sherwood number Sh.

A more comprehensive depiction of the impact of buoyancy ratio, N, and Rayleigh number, R_T, on Ψ_0, Nu, and Sh is presented in Figure 8 for $Le = 5$ and $n = 1.2$. The outcomes are derived for varying buoyancy ratio values from 0.2 to -0.2. As evident from Figures 8(a)–8(c), for a given Rayleigh number, both the intensity of convection, Ψ_0, and the ensuing heat, Nu, and solute, Sh, transfer rates exhibit a decline as the buoyancy ratio, N, diminishes. The plot notably illustrates the influence of N on the existence of various bifurcation curves, as elucidated in Figure 8. Consequently, a decrease in the buoyancy ratio, N, leads to the evolution of bifurcation curves from subcritical to supercritical behavior. Overall, the influence of N on the onset of motion (R_{TC}^{sup}, R_{TC}^{sub}, and R_{TC}^{tur}) is elucidated in Figure 7. Under the specified conditions of a power-law index, $n = 1.2$, and a Lewis number, $Le = 5$, the presence of bistability bifurcation is confirmed within the buoyancy ratio range of $N =$-0.18 to -0.082, (i.e., under opposing flow conditions $N < 0$), Notably, for $N = -0.2$, the observed bifurcation assumes a subcritical.
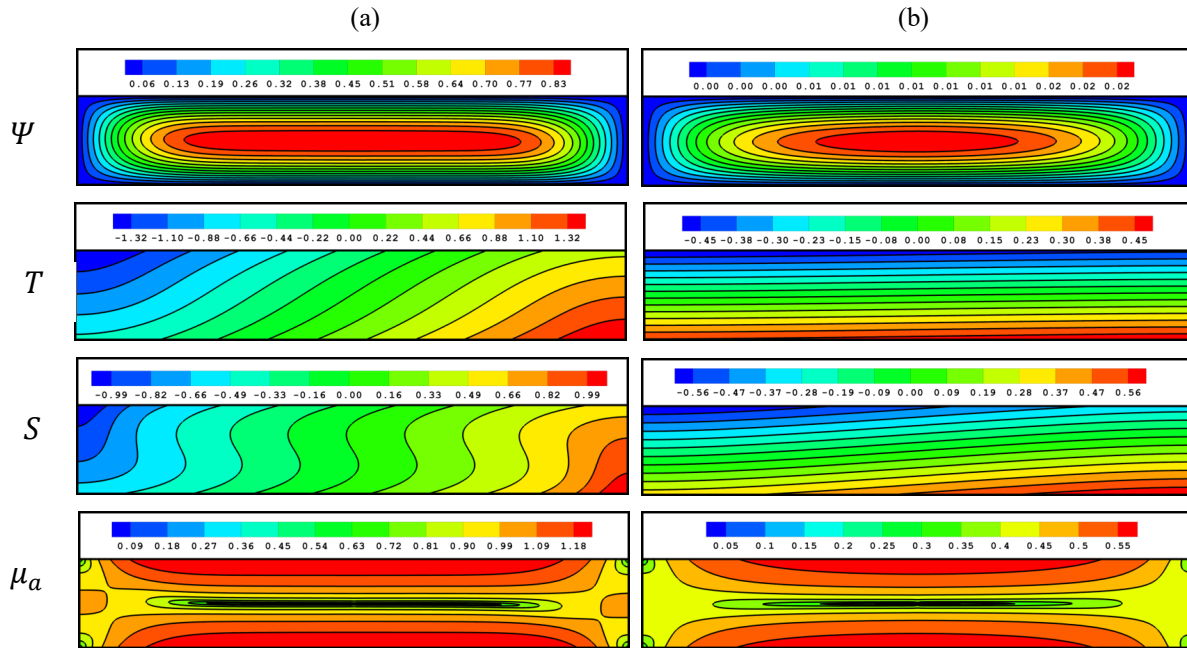
Figure 9. Contours of streamlines, Ψ_0, temperature, T, concentration, S, and apparent viscosity μ_a.

In the region characterized by bistability, the solutions corresponding to $R_T = 22$, derived from the numerical solution of the comprehensive governing equations, are depicted in Figure 9. These graphical representations sequentially present streamlines, isotherms, isoconcentrates, and apparent viscosities from top to bottom. The solution illustrated in Figure 9(b), representing the lower branch, is obtained by initializing the numerical computations with the rest state as the initial conditions. Conversely, the solution for the upper branch, as shown in Figure 9(a), is exclusively acquired by tracing the hysteresis path delineated on the curve for $N = -0.14$. As the buoyancy ratio becomes large, the bistability region shrinks, as shown by the results obtained for $N = -0.14$, and it completely disappears when the buoyancy ratio becomes very large, as displayed for thermal convection $N = 0$ and for the aiding flow ($N > 0$). For this situation, the resulting pitchfork type bifurcation, characterized by a transition from the rest state to a convective regime, takes place at a supercritical Rayleigh number, R_{TC}^{sup} .

Table 6 provides the critical Rayleigh numbers, delineating the onset of motion (R_{TC}^{sup}, R_{TC}^{sub}, and R_{TC}^{tur}), as functions of the buoyancy ratio, N. This table clearly indicates the impact of the buoyancy ratio, N, on bistability convection.

Table 6. Dependence of R_{TC}^{sub}, R_{TC}^{tur} and R_{TC}^{sup} on N for $Le = 5.0$ and $n = 1.2$.

N	R_{TC}^{sub}	R_{TC}^{tur}	R_{TC}^{sup}
0.20	...	...	1.01
0.00	...	...	2.02
-0.082	15.04	15.04	3.43
-0.10	15.96	19.33	9.88
-0.14	17.61	25.51	6.75
-0.16	18.35	36.14	10.13
-0.18	19.05	66.49	20.27
-0.20	19.73	...	$+\infty$

In Figure 10, a stability diagram is presented to illustrate the influence of the power-law index denoted as, n, and the Lewis number, Le, on critical Rayleigh numbers discus in figure 7. These findings are presented within the context of $N = -0.1$. Upon initial examination, it becomes evident that the bistability region presented in zoomed image Figure

10.a decrease as the Lewis number, Le, decrease until a value of $Le = 2.4$, where $R_{TC}^{sub}=R_{TC}^{sup}=R_{TC}^{tur}$ and $n = 1$, when the values of Le exceeds approximately 10 the bistability regime disappear the invers of Rebhi et al [26]. For this interval of Lewis number, Le, and with an increasing of Le, the domain of n expands and remains above 1.
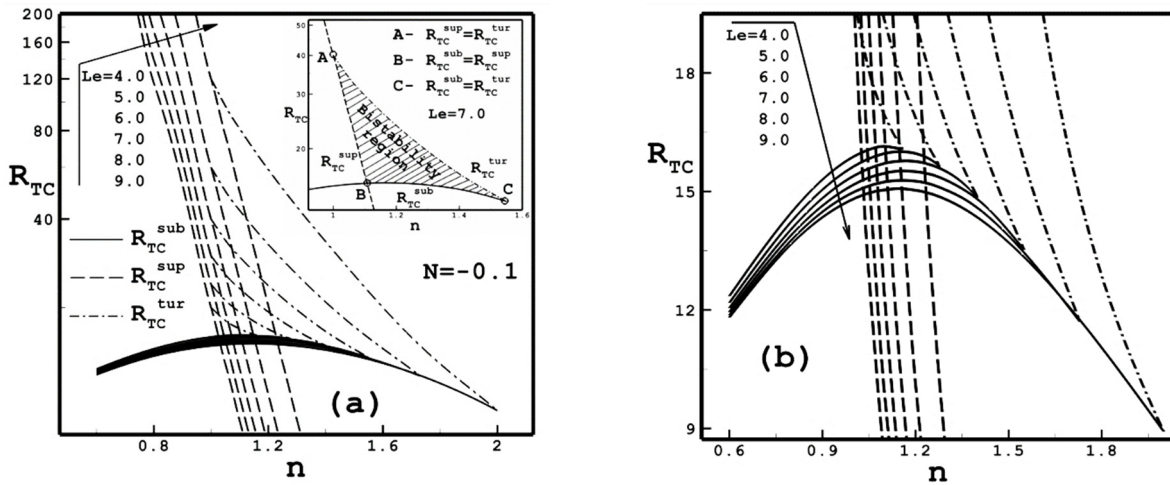

Figure 10. Effect of Lewis number, Le, and Power-law index, n, on the critical Rayleigh numbers (R_{TC}^{sub}, R_{TC}^{tur}, and R_{TC}^{sup})
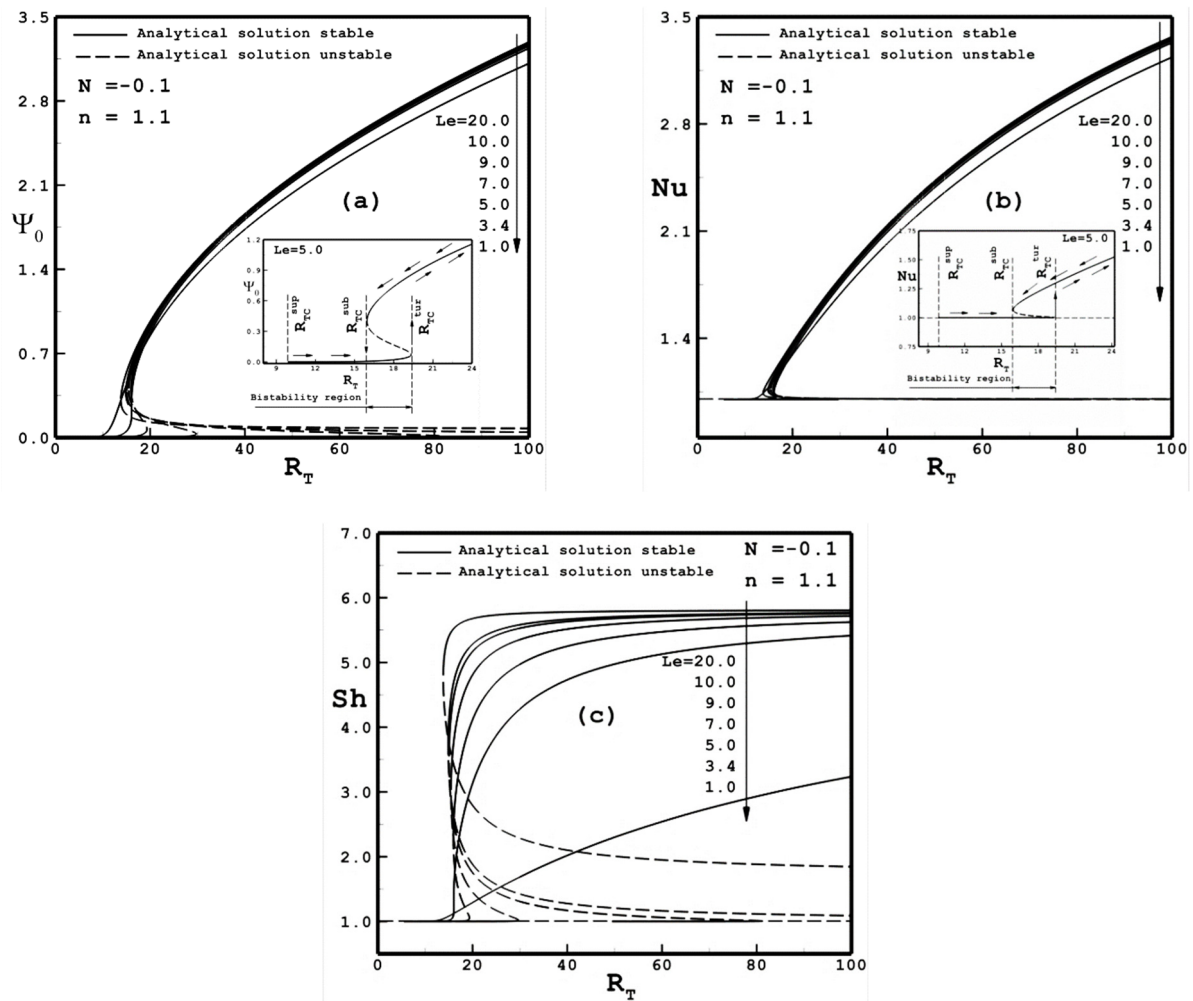

Figure 11. Bifurcation diagram as a function of R_T and Le: (a) flow intensity Ψ_0, (b) Nusselt number Nu, and (c) Sherwood number Sh

An alternative perspective on the influence of the Lewis number, Le, on Ψ_0, Nu, and Sh, with fixed parameters $n = 1.1$ and $N = -0.1$, is delineated in Figure 11. Within the defined range of governing parameters, the analytical model predicts that the occurrence of bistability bifurcation is not exist when the Lewis number is below 3.4. As the Lewis

number progressively increases, the bistability region manifests and undergoes significant expansion, persisting within the range below 10, indicative of thermal diffusion dominant over mass diffusion. The graphical representation in Figure 11 provides insight into the notable impact of the magnitude of the Lewis number on the characteristic "S"-bifurcation shape within the bistability region. Specifically, the "S"-bifurcation curve becomes increasingly conspicuous with higher Lewis numbers (i.e., $Le = 7$ and 9). At the subcritical bifurcation point, the flow exhibits finite amplitude, marking a discernible transition from a rest state to a convective state. This transition is characterized by a sudden and substantial augmentation in flow intensity, Nusselt, and Sherwood numbers. Such enhancements are attributed to a pronounced reduction in the apparent viscosity, as depicted in Figures 11(a)–11(c).

Table 7 shows the impact of the Lewis number, Le, on the critical Rayleigh numbers (R_{TC}^{sub}, R_{TC}^{tur}, and R_{TC}^{sup}) for $n = 1.1$, and $N = -0.1$. It was found that the bistability regime occurs when Lewis number, Le, values are within the domain]3.4;10[.

Table 7. Dependence of R_{TC}^{sub}, R_{TC}^{tur} and R_{TC}^{tur} on Le for $n = 1.1$ and $N = -0.1$.

Le	R_{TC}^{sub}	R_{TC}^{tur}	R_{TC}^{sup}
1.0	…	…	5.49
3.4	16.07	16.07	7.51
5.0	15.96	19.33	9.88
7.0	15.46	29.72	16.47
9.0	15.04	81.14	49.41
10.0	14.87	…	$+\infty$
20.0	13.81	…	$+\infty$

7. CONCLUSIONS

In this paper, the problem of thermosalutal convection of power-law fluid saturated porous media contained in a horizontal enclosure subject to vertical constant fluxes of heat and solute, has been investigated analytically and numerically. The effect of the thermal Rayleigh number R_T, the power-law index n, buoyancy ratio N, Lewis number Le, and the aspect ratio of the cavity, A, on the onset of linear and nonlinear convective motion, as well as heat and mass transfer rates. for the case of a shallow enclosure $A \gg 1$, an analytical solution, based on the parallel flow approximation, has been formulated. The results show good agreement between the numerical and analytical solutions, and a strong influence of the governing parameters on the onset of convective motion and the resulting convective heat and mass transfer rates.

In the first part, results are presented for the velocity, apparent viscosity, temperature and concentration fields, revealing a significant sensitivity to the power law-index n. It is shown that an increase in the power-law index (dilatant fluids) enhances the apparent viscosity while a decrease (pseudoplastic fluids) reduces it, and it's constant for the case of Newtonian fluid ($n = 1$), it is observed that the temperature and concentration profiles exhibit an augmentation with increasing values of the power-law index, n.

It was observed that the intensity of convection Ψ_0 and the resulting heat Nu and mass Sh transfer rates experienced enhancement with a decrease in the value of n, and N, while reduces it when Le decrease.

The resulting nonlinear solution indicated that the threshold of finite amplitude motion occurred at a supercritical Rayleigh number (R_{TC}^{sup}), which considerably decreased upon increasing the power-law index n, and N, and Le decrease.

Specifically, the manifestation of bistability convection phenomena, denoted by the coexistence of two distinct stable solutions under identical flow and boundary conditions, is contingent upon specific values of n, N, and Le. Notably, this phenomenon is associated with the characteristics of a dilatant fluid ($n > 1$) and opposing buoyancy forces ($N < 0$). The bistability bifurcation was observed to traverse three saddle-node points, corresponding to the thresholds R_{TC}^{sub}, R_{TC}^{sup}, and R_{TC}^{tur}. This bifurcation exhibited three branches, resulting in an "S" shape curve. The first branch bifurcated forward from R_{TC}^{sup} to R_{TC}^{tur}, the second bifurcated backward from R_{TC}^{tur} to R_{TC}^{sub} but was deemed unstable, and a third stable branch bifurcated forward from R_{TC}^{sub}. Furthermore, it was demonstrated that this bistability phenomenon could manifest irrespective of the aspect ratio of the enclosure and the types of thermal and solutal boundary conditions.

In the case of opposing convective flows, there was a collaborative influence of both shear-thinning and slow-diffusing solute effects, resulting in the augmentation of subcritical convective flows. Conversely, for aiding convective flows, a cooperative impact of shear-thickening and slow-diffusing solute effects was observed, leading to the enhancement of supercritical convective flows.

The occurrence of bistability convection was attributed to the cooperative counteracting influences within the fluid system. Specifically, the dilatant fluid. Simultaneously, the slower diffusing component in the binary mixture tended to maintain uniformity within the core region of the system while establishing a pronounced solute gradient near the walls.

ORCID
Saleh Khir, https://orcid.org/0009-0004-6018-1453; **Redha Rebhi**, https://orcid.org/0000-0003-3019-9156
Mohamed Kezrane, https://orcid.org/0009-0001-3558-4128

REFERENCES
[1] A.A. Mohamad, Num. Heat Transf. Part A, **27**, 6 (1995). https://doi.org/10.1080/10407789508913727
[2] G. H. R. Kefayati, Energy. **107** (2016). https://doi.org/10.1016/j.energy.2016.05.044
[3] R. Bennacer, and D. Gobin. Int. J. Heat Mass Transf. **39**,13 (1996). https://doi.org/10.1016/0017-9310(95)00350-9
[4] G.H. R. Kefayati, Int. J. Heat Mass Transf. **89** (2015). https://doi.org/10.1016/j.ijheatmasstransfer.2015.05.058
[5] Q.Y. Zhu, et al., Int. J. Heat Mass Transf. **104**, (2017). https://doi.org/10.1016/j.ijheatmasstransfer.2016.09.018
[6] P. Kennedy, and R. Zheng. *Flow analysis of injection molds*, (Carl Hanser Verlag GmbH Co KG, 2013), pp. I–XXIX.
[7] G. De-Vahl Davis, Int. J. Numer. Methods Fluids. **3**, 3 (1983). https://doi.org/10.1002/fld.1650030305
[8] O. Aydin et al., Int. J. Heat Mass Transf. **42**,13 (1999). https://doi.org/10.1016/S0017-9310(98)00319-6
[9] Y. Liu, and Y. Hu, Nanoscale Res. Lett. **12**, 446 (2017). https://doi.org/10.1186/s11671-017-2185-7
[10] M. Omid, et al., Physics reports. **790**, (2019). https://doi.org/10.1016/j.physrep.2018.11.004.
[11] S. Fatih, and H.F. Öztop, Int. J. Heat Mass Transf. **129**, (2019). https://doi.org/10.1016/j.ijheatmasstransfer.2018.09.101
[12] P.A. Hajatzadeh, et al., Ener. Conv. Manage. **198**, (2019). https://doi.org/10.1016/j.enconman.2019.111886
[13] N.O. Moraga, et al., Int. J. Thermal Sci. **107**, (2016). https://doi.org/10.1016/j.ijthermalsci.2016.04.007
[14] A.A. Jahanbakhshi, et al., J. Therm Anal Calorim. **133**, (2018). https://doi.org/10.1007/s10973-018-7219-6
[15] M. Lamsaadi, et al., Num. Heat Transf, Part A: Applications, **49**,10 (2006). https://doi.org/10.1080/10407780500324988
[16] T. Makayssi, et al., Ener. Conv. Manage, **49**, 8 (2008). https://doi.org/10.1016/j.enconman.2008.02.008
[17] G.H.R. Kefayati, Computers & Fluids. **114**, (2015), https://doi.org/10.1016/j.compfluid.2015.02.009
[18] G. Żyła, et al., Diamond and Related Materials, **74**, (2017). https://doi.org/10.1016/j.diamond.2017.02.008
[19] G.B. Kim, et al., Int. J. Heat Mass Transf. **46**,19 (2003). https://doi.org/10.1016/S0017-9310(03)00149-2
[20] D. Getachew, et al., Journal of Thermophysics and Heat Transfer. **12**, 3 (1998). https://doi.org/10.2514/2.6357
[21] A. Moradi, et al., J. Therm Anal Calorim. **137**, 5 (2019). https://doi.org/10.1007/s10973-019-08076-0
[22] S.K, Jena, et al., Journal of the Taiwan Institute of Chemical Engineers. **51**, (2015). https://doi.org/10.1016/j.jtice.2015.01.007
[23] S. Lounis, et al., CFD Letters. **14**, 3 (2022). https://doi.org/10.37934/cfdl.14.3.96118
[24] R. Rebhi, et al., Int. J. Heat Mass Transf. **100**, (2016). https://doi.org/10.1016/j.ijheatmasstransfer.2016.04.060
[25] R. Rebhi, et al., J. Fluid Mech. **812**, (2017). https://doi.org/10.1017/jfm.2016.787
[26] R. Rebhi, et al., Physics of Fluids. **33**, 7 (2021), https://doi.org/10.1063/5.0051058
[27] K. Bihiche, et al., J. Non-Newt. Fluid Mech. **283**, (2020). https://doi.org/10.1016/j.jnnfm.2020.104349.
[28] K. Benhadji, and P. Vasseur. Int. Comm. Heat Mass Transfer. **28**,6 (2001). https://doi.org/10.1016/S0735-1933(01)00280-9
[29] B. Amari, et al., Wärme- und Stoffübertragung. **29**, 3 (1994). https://doi.org/10.1007/BF01548603
[30] G.H.R. Kefayati, Int. J. Heat Mass Transf. **94**, (2016). https://doi.org/10.1016/j.ijheatmasstransfer.2015.11.043
[31] D.A. Nield, et al., Transp Porous Med. **83**, (2010). https://doi.org/10.1007/s11242-009-9455-5
[32] M. Devakar, et al., J. Assoc. Arab Univ. Basic Appl. Sci. **23**, (2017). https://doi.org/10.1016/j.jaubas.2016.04.001
[33] S.J. Uphill, et al., Colloid Surf. A. **460**, (2014). https://doi.org/10.1016/j.colsurfa.2014.05.008
[34] A.L.N. Narayana, et al., Journal of Porous Media. **12**,10 (2009). https://doi.org/10.1615/JPorMedia.v12.i10.40
[35] R. Tsai, and J.S. Huang, Comp. Mater. Sci. **47**, 1 (2009). https://doi.org/10.1016/j.commatsci.2009.06.009
[36] Q.Y. Zhu, et al., Int. J. Heat Mass Transf. **104**, (2017). https://doi.org/10.1016/j.ijheatmasstransfer.2016.09.018
[37] M. Madhu, et al., Int. Comm. Heat Mass Transfer. **117**, (2020). https://doi.org/10.1016/j.icheatmasstransfer.2020.104761
[38] N. Ben Khelifa, et al., J. Non-Newt. Fluid Mech, **169-170**, (2012). https://doi.org/10.1016/j.jnnfm.2011.11.002
[39] S. Bensilakhal, et al., J. Advanced Research in Fluid Mechanics and Thermal Sciences. **101**, 1 (2023). https://doi.org/10.37934/arfmts.101.1.137159.
[40] M. Naimi, et al., Engineering Computations. **17**, 6 (2000), https://doi.org/10.1108/02644400010340570
[41] C.H. Chen, et al., Physics Letters A. **370**, 1 (2007), https://doi.org/10.1016/j.physleta.2007.05.024
[42] M. Lamsaadi, et al., Num. Heat Transf. Part A: Applications. **53**, 2 (2007), https://doi.org/10.1080/10407780701454055
[43] M. Lamsaadi, et al., Ener. Conv. Manage. **47**, 15-16 (2006), https://doi.org/10.1016/j.enconman.2005.10.028
[44] M. H. Matin, et al., J. Non-Newt. Fluid Mech. **197**, (2013), https://doi.org/10.1016/j.jnnfm.2013.02.002
[45] Z.Z. Alloui, et al., J. Non-Newt. Fluid Mech. **196**, (2013), https://doi.org/10.1016/j.jnnfm.2013.01.008
[46] S. Khali, et al., Journal of Thermophysics and Heat Transfer. **36**, 2 (2022), https://doi.org/10.2514/1.T6405
[47] M. Ohta, et al., Numerical Heat Transfer: Part A: Applications. **41**, 4 (2002), https://doi.org/10.1080/104077802317261218
[48] M. Hojjat, et al., Int. Comm. Heat Mass Transfer. **38**, 2 (2011), https://doi.org/10.1016/j.icheatmasstransfer.2010.11.019
[49] S.V. Solomatov, and A.C. Barr, Phys. Earth Planet. Int. **155**, 1-2 (2006), https://doi.org/10.1016/j.pepi.2005.11.001
[50] V.S. Solomatov, and A. C. Barr, Phys. Earth Planet. Int. **165**, 1-2 (2007), https://doi.org/10.1016/j.pepi.2007.06.007
[51] H. Pascal, Int. J. Numer. Analy. Methods Geomech. **7**, 3 (1983), https://doi.org/10.1002/nag.1610070303
[52] H. Pascal, Int. J. Engng Sci. **24**, 9 (1986), https://doi.org/10.1016/0020-7225(86)90157-6
[53] S.R. De Groot, and P. Mazur, *Non-equilibrium thermodynamics*, (Courier Corporation, 2013)
[54] W. Bian, et al., Chem. Eng. Commun. **129**, 1 (1994), https://doi.org/10.1080/00986449408936252
[55] W. Bian, et al., Int. J. heat and fluid flow. **15**, 5 (1994), https://doi.org/10.1016/0142-727X(94)90052-3
[56] P. Vasseur, et al., Num Heat Transf. **15**, 2 (1989), https://doi.org/10.1080/10407788908944686
[57] R.V. Dharmadhikari, and D.D. Kale. Chem. Eng. Sci. **40**, 3 (1985), https://doi.org/10.1016/0009-2509(85)85113-7
[58] H.T. Chen, and C.K. Chen. J. Heat Transfer. **110**, 1 (1988), https://doi.org/10.1115/1.3250462
[59] H.T. Chen, and C.K. Chen. Int. Comm. Heat Mass Transfer. **15**, 5 (1988), https://doi.org/10.1016/0735-1933(88)90051-6

ГІСТЕРЕЗИС ТА БІФУРКАЦІЯ БІСТАБІЛЬНОСТІ, ІНДУКОВАНА КОМБІНОВАНИМ ЗСУВНИМ ЗГУЩЕННЯМ РІДИНИ ТА ПОДВІЙНОЮ ДИФУЗІЙНОЮ КОНВЕКЦІЄЮ В МІЛКОПОРИСТИХ КОРПОРАТАХ, ЗАПОВНЕНИХ НЕНЬЮТОНІВСЬКИМИ СТЕПЕНЕВИМИ РІДИНАМИ

Салех Хір[a,b,c], Редха Ребхі[a,b], Мохамед Кезране[a,c], Мохамед Насер Борджині[d]

[a]Департамент машинобудування, Університет Медеа, Медеа 26000, Алжир
[b]LERM-Лабораторія відновлюваної енергії та матеріалів, Університет Медеа, Медеа 26000, Алжир
[c]Лабораторія фізичної механіки та математичного моделювання (LMP2M), Університет Яхья Фарес у Медеа, район Айн-Деб, Медеа 26000, Алжир
[d]Університет Монастіра, Національна школа інженерів Монастіра, Лабораторія метрології та енергетичних систем, 5019 Монастір, Туніс

У цій статті представлено чисельне дослідження лінійної та нелінійної стійкості терморозчинної конвекції в пористому середовищі, насиченому неньютонівською бінарною рідиною. Для моделювання поведінки робочого середовища використовується степенева модель. Наведене твердження має на увазі, що горизонтальні межі відчувають теплові потоки та швидкості розчину, тоді як вертикальні стінки є непроникними та термічно ізольованими. Відповідними факторами, які керують проблемою, що досліджується, є число Релея, R_T, індекс степеневого закону, n, співвідношення розмірів порожнини, A, число Льюїса, Le, і коефіцієнт плавучості, N. Аналітичне рішення отримано для неглибокі камери ($A \gg 1$) з використанням наближення паралельного потоку та модифікованої форми рівняння Дарсі. Розв'язавши всю систему керівних рівнянь, було проведено чисельне дослідження самого явища. Одним із найбільш цікавих результатів цього дослідження є те, що воно ідентифікує явище бістабільності, яке означає існування двох стабільних розчинів. Результати, отримані за допомогою обох методів, демонструють хороший рівень узгодженості в різноманітному діапазоні цих керівних параметрів.

Ключові слова: *бістабільність; терморозчинна конвекція; степенева рідина; пористий шар; неньютонівська подвійна рідина*